SUPPLEMENTARY INFORMATION

Crystalline and Amorphous MOFs Based on an Amphiphilic Cyclic Stereoregular p-Carboxyphenylsiloxane: Synthesis, Structures and Properties

Sergey P. Kutumov,[a] Dmitry N. Kholodkov,[a] Irina K. Goncharova,[a] Anna N. Vologzhanina,[a] Alexander D. Volodin,[a] Alexander A. Korlyukov,[a] Pavel V. Dorovatovskii,[b] Alexey S. Kashin,[c] Roman A. Novikov,[c] Valery G. Vlasenko,[d] Ilia A. Pankin,[e] Alexander A. Guda,[e] Ashot V. Arzumanyan*[a,f]

[a] A.N. Nesmeyanov Institute of Organoelement Compounds, Russian Academy of Sciences, 28 Vavilov St., bld. 1, Moscow 119991, Russian Federation.

[b] National Research Center "Kurchatov Institute" 1 Acad. Kurchatov Sq., Moscow 123182, Russian Federation

[c] N.D. Zelinsky Institute of Organic Chemistry Russian Academy of Sciences 47 Leninsky Pr., Moscow 119991, Russian Federation

[d] Institute of Physics Southern Federal University 194 Stachki ave., Rostov-on-Don 344090, Russian Federation

[e] The Smart Materials Research Institute Southern Federal University 178/24 Sladkov Str., Rostov-on-Don 344090, Russian Federation

[f] A.V. Topchiev Institute of Petrochemical Synthesis Russian Academy of Sciences 29 Leninsky Prospect, Moscow 119991, Russian Federation

Corresponding Author: *A.V.A. e-mail: aav@ineos.ac.ru

Table of contents:

S1. Materials and methods

General Information

All the starting materials were purchased from Acros, Sigma Aldrich and Chemcraft Ltd companies. Solvents were dried and purified according to standard procedures.

GPC analysis was performed on the "Shimadzu" (Japan, Germany), the detector - refractometer RID - 20A, the column – Phenogel 5u 1000Å (Size (300 x 7,8 mm)); standart – polystyrene, eluent – THF; temperature - 40°C; speed of flow 1 ml/sec.

^{1}H, ^{13}C, ^{29}Si NMR spectra were recorded using a Bruker Avance 400 NMR spectrometer in CDCl$_3$, (CD$_3$)$_2$CO, chemical shifts are referenced to residual chloroform (7.26 ppm, ^{1}H) and DMSO-d6 (2.50 ppm, ^{1}H). Chemical shifts are reported in ppm, multiplicities are indicated by s (singlet), d (doublet), t (triplet), q (quartet), m (multiplet) and br (broad).

Environmental stability of materials was studied using Jeio Tech TH-ME-025 Temperature and Humidity Chamber.

IR spectra were obtained using an IR spectrometer with a Fourier transformer Bruker "Tensor 37". Spectra were taken from KBr pellets.

FTIR spectra for activation dynamics studies were recorded in diffuse reflectance mode (DRIFT spectra) with an MCT detector throughout the entire treatment procedure, using the Praying Mantis Low-Temperature Reaction Chamber (Harrick Scientific Products Inc., New York, USA) installed in the Bruker Vertex 70 spectrometer (Bruker, Billerica, MA, USA). The background spectrum was collected for outgassed KBr powder placed in the reaction chamber. Measurements were performed in the range from 5000 to 550 cm–1 with a resolution of 1 cm–1 and 39 scans (1 min per spectrum), and the data were automatically transformed into absorption units using the Kubelka–Munk function.

TGA measurements were performed on Shimadzu DTG-60H at a heating rate of 10°C/min under both air and argon atmospheres.

Routine crystal growth and transformation was observed using USB Digital Magnifying Camera 50-500 X (Focus range 15-40 mm).

Single crystal XRD (SCXRD)

Single crystal X-ray studies of **B**, **B1**, **B2**, **G**, **H**, and **F** were carried out in Center for molecule composition studies of INEOS RAS with APEX3 software [1]. The data were then integrated with SAINT. SADABS program was used for scaling, empirical absorption corrections and the generation of data files for structure solution and refinement. The X-ray data for **B3**, **C**, **E** and **D**, were collected at Belok station of synchrotron radiation source of National research centre "Kurchatov institute" using Madtb goniostat. The XDS [2] software was utilized for reduction of collected datasets.

The structures were solved by dual-space algorithm and refined in anisotropic approximation for non-hydrogen atoms against $F^2(hkl)$. Hydrogen atoms of methyl, methylene and aromatic fragments were calculated according to those idealized geometry and refined with constraints applied to C-H and N-H bond lengths and equivalent displacement parameters ($U_{eq}(H) = 1.2U_{eq}(X)$, X - central atom of XH_2 group; $U_{eq}(H) = 1.5U_{eq}(Y)$, Y - central atom of YH_3 group). All structures were solved with the ShelXT [3] program and refined with the ShelXL [4] program. Molecular graphics was drawn using OLEX2 [4] program. The solvent contributions to the structure factors in the crystals were calculated and removed with *Solvent Mask* tool in OLEX2 program [5].

References:

1. Bruker (2016). APEX3, RLATT, CELL_NOW, TWINABS, SAINT-Plus and SADABS. Bruker AXS Inc., Madison, Wisconsin, USA.

2. (a) Kabsch W. (2010). XDS. Acta Cryst. D66, 125-132 (b) Kabsch W. (2010). Integration, scaling, space-group assignment and post refinement. Acta Cryst. D66, 133-144.

3. Sheldrick G.M. (2015). SHELXT - Integrated space-group and crystal-structure determination. Acta Cryst. A71, 3-8.

4. Sheldrick G.M. (2015). Crystal structure refinement with SHELXL. Acta Cryst. C71, 3-8.

5. Dolomanov O.V., Bourhis L.J., Gildea R.J, Howard J.A.K., Puschmann H. (2009). J. Appl. Cryst. 42, 339-341.

Powder XRD (PXRD)

The synchrotron PXRD data were recorded at X-ray structural analysis beamline (XSA) of Kurchatov Synchrotron Radiation Source [1] at room temperature. Monochromatic radiation with a wavelength of 0.75 Å was used. The sample was placed in a cryoloop of 200 μm in size and rotated around the horizontal axis during the measurement, which made it possible to average the diffraction patterns according to the orientations of the sample. The diffraction patterns were collected by the 2D Rayonix SX165 detector, which was located at a distance of 250 mm with a 18° tilt angle, Debye-Scherrer (transmission) geometry was used with a 400 μm beam size. The 2θ range was 0.94–59.8° with a step size of 0.00994°. The exposure time was 10 min. The two-dimensional diffraction patterns obtained on the detector were further integrated to the standard form of the dependence of the intensity on the scattering angle I(2θ) using Dionis software [2]. To calibrate the sample–detector distance the polycrystalline LaB6 (NIST SRM 660a) was used as a standard with the known position of the diffraction peaks.

References:

1. Svetogorov, R. D.; Dorovatovskii, P. V.; Lazarenko, V. A. Belok/XSA Diffraction Beamline for Studying Crystalline Samples at Kurchatov Synchrotron Radiation Source. Crystal Research and Technology 2020, 55 (5), 1900184. DOI: 10.1002/crat.201900184.

2. Svetogorov, R.D. Dionis—Diffraction Open Integration Software, 2018.

X-ray absorption spectroscopy (XAS)

Cu K-edge XAS spectra were measured at the beamline "Structural Materials Science" using the equipment of Kurchatov Synchrotron Radiation Source (Moscow, Russia) [1]. The storage ring with an electron beam energy of 2.5 GeV and a current of 80–100 mA was used as the source of radiation. All the spectra were collected in the transmission mode using a Si(111) channel-cut monochromator. Three ionization chambers were used to monitor the intensity of the X-ray beam before and after the sample, and after the reference foil for energy calibration. Sample of MOF **B** was placed in liquid tight cuvette without destroying crystals and wetted in pyridine solution (the amount sufficient to cover all crystals by without liquid excess). Powder samples of MOFs **B4** and **B5** were pelletized.

A double-shell Fourier approach was applied for EXAFS data analysis. Background subtraction, normalization, energy alignment, and extraction of $\chi(k)$ oscillatory functions were performed in the Athena program of the Demeter package [2]. Further analysis in Artemis program included calculation of theoretical amplitudes and phases by the FEFF6 code [3] and fitting in the R-range from 1.0 to 2.2 Å of the Fourier-transformed data k^3-weighted $\chi(k)$ applying Δk Hanning window from 3 to 13.0 Å^{-1} with the width of the window slope dk = 1 Å^{-1}. The fitting parameters were the first shell Cu-O/N interatomic distances, Debye-Waller factor (σ^2), zero energy shift (ΔE_0). The value of passive electron reduction factor (S_0^2) was fixed by fitting reference $Cu(OAc)_2$ sample. The fits for **B4** and **B5** were performed for several possible coordination numbers of Cu-Cu and Cu-O/N and the best combination was reported in the text. Number of parameters for fit didn't exceed the number of independent points N_{ind}, defined as

$$N_{ind}=(2\Delta r\Delta k/\pi)+1 \tag{1}$$

where Δk – is the region of EXAFS spectrum in k-space used for the Fourier analysis, Δr – is the region in R-space for the Fourier filtration.

References:

1. Chernyshov A.A., Veligzhanin A.A., Zubavichus Y.V. Structural Materials Science end-station at the Kurchatov Synchrotron Radiation Source: Recent instrumentation upgrades and experimental results. Nuclear Instruments & Methods in Physics Research Section A: Accelerators Spectrometers Detectors and Associated Equipment, 2009, 603, 95-98.

2. Ravel B., Newville M. ATHENA, ARTEMIS, HEPHAESTUS: data analysis for X-ray absorption spectroscopy using IFEFFIT. Journal of Synchrotron Radiation, 2005, 12, 537-541.

3. Zabinsky S.I., Rehr J.J., Ankudinov A., Albers R.C., Eller M.J. Multiple-scattering calculations of X-ray absorption spectra. Physical Review B, 1995, 52, 2995-3009.

In situ X-ray study of crystallization

Crystallization at r.t. for MOF **B** was studied *in situ* by means of time-resolved X-rays diffraction acquired on single droplets of reagents placed inside of special cell dedicated for *in situ* protein crystallization studies [1]. The experiment was carried out at BioMUR beamline of KISI-Kurchatov synchrotron source [2, 3]. Monochromatic X-ray beam (0.1445 nm, 8.58 keV) with spot size 1.7 x 1.2 mm were used to measure 2D scattering patterns using Pilatus3 1M pixel detector (Dectris, Swiszerland) placed at the distance 730.0 mm, being separated from the cell by the cylindric vacuum chamber. The cell is equipped with mica windows which barely attenuate X-rays at given wavelengths and do not produce any diffraction features (See **Figure S1.1**).
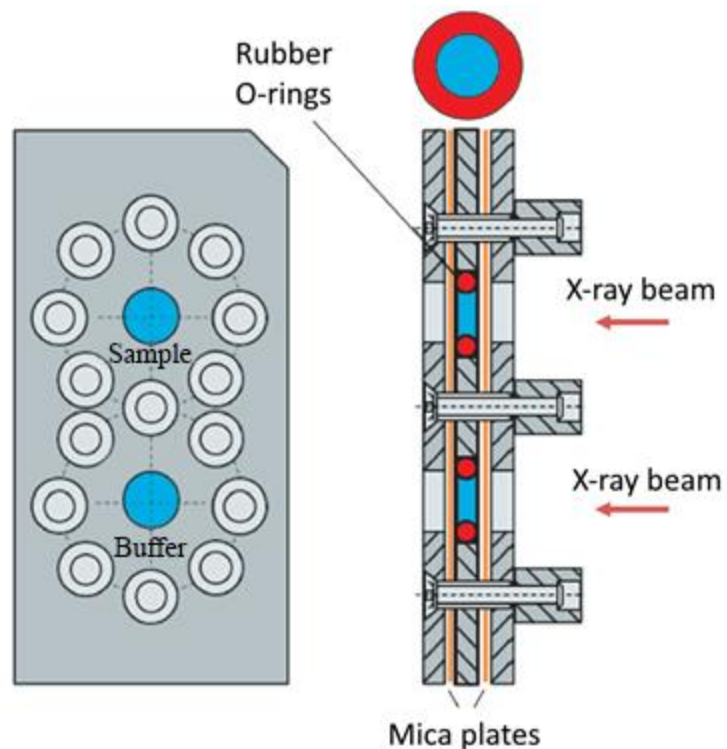
Figure S1.1 Schematic representation of the cell used for *in situ* monitoring of MOF **B** crystallization at BioMUR beamline of KISI-Kurchatov synchrotron source. The cell initially dedicated to SAXS *in situ* monitoring of proteins crystallization, so it is equipped with two equivalent cavities (18 µL each) for liquid samples, places in the internal area of O-ring used for sealing and preventing the contact with metallic basement. The figure reproduced from [1].

References:

1. Ilyina K.B., Konarev P.V., Sukhanov A.E., Volkov V.V., Marchenkova M.A., Peters G.S., Pisarevsky Y.V., Shishkov V.A. A new sealed cell with microliter cavities for temperature measurements of solution structure by small-angle X-ray scattering. Pribory i tehnika èksperimenta, 2024, 3, 91-99. DOI: 10.31857/S0032816224030122.

2. G.S. Peters, O.A. Zakharchenko, P.V. Konarev, Y.V. Karmazikov, M.A. Smirnov, A.V. Zabelin, E.H. Mukhamedzhanov, A.A. Veligzhanin, A.E. Blagov, M.V. Kovalchuk. The small-angle X-ray scattering beamline BioMUR at the Kurchatov synchrotron radiation source. Nuclear Instruments and Methods in Physics Research Section A: Accelerators, Spectrometers, Detectors and Associated Equipment, 2019, 945, 162616.

3. G.S. Peters, Y.A. Gaponov, P.V. Konarev, M.A. Marchenkova, K.B. Ilina, V.V. Volkov, Y.V. Pisarevsky, M.V. Kovalchuk. Upgrade of the BioMUR beamline at the Kurchatov synchrotron radiation source for serial small-angle X-ray scattering experiments in solutions. Nuclear Instruments and Methods in Physics Research Section A: Accelerators, Spectrometers, Detectors and Associated Equipment, 2022, *1025*, 166170.

MAS SSNMR

Solid-state NMR (SSNMR) experiments were recorded on a Bruker AVANCE III WB 400 MHz spectrometer equipped with 4.0 mm DVT MAS BB/HF probe (15 kHz) and 2.5 mm DVT MAS BB/HF probe (35 kHz) (^{1}H – 400.1 MHz, ^{13}C – 100.6 MHz, ^{29}Si – 79.5 MHz, ^{81}Br – 100.25 MHz). Samples were spun at 11–14 kHz (4.0 mm probe) and 26–34 kHz (2.5 mm probe) at the magic angle (MAS) using ZrO_2 rotors. ^{1}H MAS spectra were recorded using single-pulse sequence with 30° pulse at 14 kHz (4.0 mm probe) and 34 kHz (2.5 mm probe) with a recycle delay of 5 sec. Wideline ^{13}C MAS SSNMR spectra were recorded using three different methodologies (CP; single-pulse sequence with HPDEC; and Spin-Echo) with a wide spectral sweep (typically 600 kHz) to detect wide signals from paramagnetic Cu-MOF. A number of optimization experiments with variation of parameters and pulse powers were performed to search any wide signals in the range of at least 1200 to -500 ppm. Below only the final optimized parameters for recording the informative part of the spectra are given. ^{13}C-CP/MAS spectra were recorded with a recycle delay of 1.0 sec, short acquisition time of ~7 ms, contact time of 3 msec at 13 kHz. ^{13}C-single-pulse-HPDEC MAS spectra were recorded with a recycle delay of 1.75 sec and short acquisition time of ~7 ms at 13 kHz. ^{13}C Solid Spin-Echo experiments were performed using Hahn-Echo MAS synchronized pulse sequence with a spinning rate of 11–13 kHz with a recycle delay of 1.75 s, short acquisition time of ~7 ms (under high-power proton decoupling conditions), spin echo times of 72.4 μs (1 rotor period at 13 kHz), 177.3 μs (2 rotor periods at 11 kHz), 303.2 μs (4 rotor periods at 13 kHz), and 359.1 μs (4 rotor periods at 11 kHz), high-power 90-degree ^{13}C pulses of 3.0 us and 145 W with RF field of 83.3 kHz, and exponential apodization with LB 60 to 600 for processing or magnitude mode. 2D ^{13}C–^{1}H CP-FSLG-HETCOR spectra were recorded at 13 kHz MAS (4.0 mm probe) in a rotor-synchronized mode using 1000 usec CP contact time with RF field 98 kHz for FSLG. ^{29}Si MAS spectra were recorded at 11 kHz using CP pulse sequence under HPDEC conditions with a recycle delay of 7.5 sec and contact time of 6 msec. 2D ^{29}Si–^{1}H CP-FSLG-HETCOR spectra were recorded

at 12 kHz MAS (4.0 mm probe) in a rotor-synchronized mode using 1500 usec CP contact time with RF field 98 kHz for FSLG. The ^{13}C, ^{29}Si, and 2D HETCOR spectra were recorded under high-power proton decoupling conditions using "spinal64". Chemical shifts for ^{1}H and ^{13}C are relative to external adamantane sample; ^{29}Si chemical shifts were calculated to this scale and were checked using DSS sample. Magic angle was calibrated precisely to the spinning side bands in ^{81}Br spectra of the KBr sample.

SEM and X-ray microanalysis (EDX)

Prior to measurements, the samples were mounted on a 1 inch aluminum specimen stub using conductive carbon-filled plasticine or conductive carbon double-sided tape and coated with a thin film (15 nm) of carbon. Observations were carried out using a Hitachi SU8000 field-emission scanning electron microscope (FE-SEM). Images were acquired in the secondary electron mode at a 10 kV accelerating voltage. An Oxford Instruments X-Max 80 energy dispersive spectrometer was used for X-ray microanalysis (EDX-SEM) and measurements were carried out at a 15 kV accelerating voltage.

TEM

Prior to measurements, the samples were deposited on the 3 mm carbon-coated copper grids (200 mesh). The morphology of the samples was studied using a Hitachi HT7700 transmission electron microscope. Images were acquired in bright-field TEM mode at 100 kV accelerating voltage.

Surface Area and Porous Structure

Express one-point estimation of S_{BET} surface area was performed using Sorbi MS device. The porous structure of **B5** was analyzed using the nitrogen adsorption technique on a Top 200 Surface Area and Pore Size Analyzer (Altamira Instruments, China) gas sorption analyzer at 77 K. Initially, the compound was activated under a dynamic vacuum at 200 °C for 6 h. The nitrogen adsorption−desorption isotherms were measured within the range of relative pressures from 10^{-6} to 0.995. The specific surface area was calculated from the data obtained using the conventional BET and BJH models.

Ligand **A** was synthesized according to previously published procedures with slight modifications:

Sodium *cis*-tetratolylcyclotetrasiloxanolate and its trimethylsilyl derivative[a]:
Step 1. Tolyltriethoxysilane (10.02 g, 39.4 mmol), n-butanol (66 ml), sodium hydroxide (1.732 g, 43.3 mmol) and water (0.709 ml, 39.4 mmol) were stirred under reflux until the reaction mass became transparent, and then stirred for an additional hour. The white crystals were collected by filtration after storage of reaction mixture in a freezer (-18 °C) for a few days and dried for 4-6 hours under vacuum at 4 mbar to afford 7.52 g of a white crystalline product.
Step 2. A reaction flask was charged with 288 ml toluene, trimethylchlorosilane (12.90 g, 118.7 mmol) and pyridine (7.51 g, 95 mmol) and cooled to -78 °C. Then, white crystals (7.52 g) obtained in previous step were added stepwise under stirring. The reaction mass was stirred at room temperature for 24 h and precipitate was filtered off. The filtrate was washed till neutral pH and dried over sodium sulfate. The solvent was removed in vacuum and the residue was distilled using Kugelrohr (target fraction boiling point is over 200 °C at 1-2 mbar) to give 6.18 g (70%, based on starting tolyltriethoxysilane) of a white crystalline cyclosiloxane precursor. Purity of product was confirmed by GPC and NMR analysis.

Cis-tetra(*p*-carboxyphenyl)cyclotetrasiloxane A[b]:
Cyclosiloxane precursor (2.8 g, 3.12 mmol), solvent (19.6 ml, 0.45/0.45/0.1 AcOH/DCE/hexafluoroisopropanol or AcOH/CHCl$_3$/hexafluoroisopropanol), N-hydroxyphtalimide (0.603 g, 3.74 mmol) and cobalt(II) acetate tetrahydrate (0.07 g, 0.28 mmol) were sequentially charged into round bottom flask, flushed with dry oxygen for 1-2 minutes and stirred under static dry oxygen atmosphere at 30 °C for 24 hours. Solvent was removed using rotary evaporator, then solid residue was mostly dissolved and ultrasonicated in 19.6 ml of EtOH for 30 minutes. Resulting suspension was diluted by solution of sodium bicarbonate (1.1 g, 21 ml of water) and filtered. Hydrochloric acid (1.64 ml of conc. HCl diluted by 78 ml of water) was added to filtrate, precipitate was collected by filtration and dried under vacuum at 4 mbar for 4-6 hours. Dried precipitate was dissolved in THF (10 ml) and hexane (50-80 ml) was added until slimy brown fraction is precipitated. Solute was decanted and charged with hexane till crystallization begins, then left intact for 2-3 days. Crystalline product was collected by filtration and recrystallized again to afford 1.76 g (56 %) of ligand **A**. Purity of product was confirmed by NMR analysis.

[a] A. A. Anisimov, P. V. Zhemchugov, S. A. Milenin, A. S. Goloveshkin, U. S. Tsareva, I. S. Bushmarinov, A. A. Korlyukov, R. U. Takazova, Y. A. Molodtsova, A. M. Muzafarov and O. I. Shchegolikhina, Journal of Organometallic Chemistry, 2016, 823, 103-111.

[b] I. Goncharova, A. Arzumanyan [M]-/Organo-Catalyzed Aerobic Functionalization of Alkylaryl-Siloxanes: Synthesis Carboxy-, Carbonyl- and Hydroxy-Aryl-Siloxanes, 2024, https://doi.org/10.26434/chemrxiv-2024-l9j07.

S2. Screening of Crystallization Conditions and Preparation of MOFs **B-H**

Table S2.1. Solubility of ligand A Under Ambient Conditions

Solvent	Solubility (1 mg A / 0.1 ml)	Solubility (1 mg A / 1 ml solv)
H_2O	-	-
AcOH	+	+
DMF	+	+
DMSO	+	+
Pyr	+	+
AcMe	+	+
MeOH	+	+
EtOH	+	+
i-PrOH	+	+
n-BuOH	+	+
THF	+	+
1,4-Dioxane	+	+
MeCN	partial	+
Et_2O	+	+
$CHCl_3$	partial	+
CH_2Cl_2	partial	partial
Toluene	partial	opalescent solution
Hexane	-	-

**Table S2.2. The Effect of Solvent on MOF B Crystal Formation Under Solvothermal Conditions**
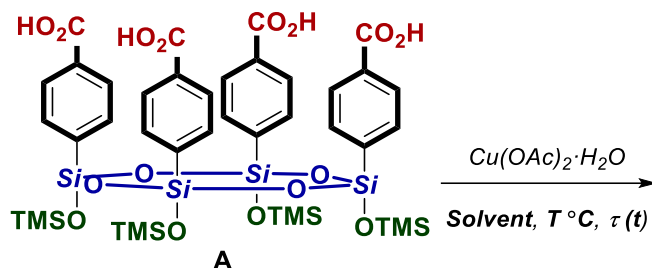
Reaction conditions: Solution of **A** (0.010 g, 0.00000983 mol, 1 eq. in 0.5 ml **Solvent**) was simply added to solution of Cu(OAc)₂·H₂O (0.00393 g, 0.0000197 mol, 2 eq. in 0.5 ml **Solvent**) in Schott Duran GL14 tube and left intact at **T °C** till formation of precipitate was observed.

Solvent	*T*, °C	**Experiment duration**	**Time of precipitation *t***	**Result**	**Product color**[d]
DMF	100	3 d	~ 1 d	Amorphous precipitate[a]	
DMF	100	3 d	-	Homogeneous solution[b]	N/D
DMF	100	3 d	~ 1 d	Amorphous precipitate[c]	
DMF	100	3 d	< 1 min	Gel-like precipitate	
0.9 DMF / 0.1 H₂O	100	3 d	< 1 min	Gel-like precipitate	
DMSO	100	3 d	< 1 min	Gel-like precipitate	
0.9 DMSO / 0.1	100	3 d	< 1 min	Gel-like precipitate	
Pyr	115	6 d	< 1 min	Amorphous precipitate	
Pyr	100	3 d	~ 1 d	Amorphous precipitate	
0.9 Pyr / 0.1 H₂O	100	3 d	< 3 h	Amorphous precipitate	
NMP	100	3 d	< 1 min	Gel-like precipitate	
0.9 NMP / 0.1 H₂O	100	3 d	< 1 min	Amorphous precipitate	
DMAc	100	3 d	< 1 min	Gel-like precipitate	
0.9 DMAc / 0.1	100	3 d	< 1 min	Amorphous precipitate	

[a] Cu(NO₃)₂·3H₂O; [b] CuCl₂ or [c] Cu(OBz)₂ were used instead of Cu(OAc)₂·H₂O; [d] color of wet product in reaction mixture

Table S2.3. The Effect of Solvent on MOF B Crystal Formation Under Ambient Conditions
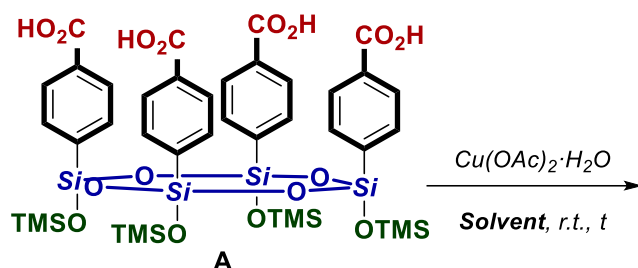
Reaction conditions: Solution of **A** (0.010 g, 0.00000983 mol, 1 eq. in 0.5 ml **Solvent**) was simply added to solution of Cu(OAc)$_2$·H$_2$O (0.00393 g, 0.0000197 mol, 2 eq. in 0.5 ml **Solvent**) in snap cap vial (15 ml, ND22) and left intact till formation of precipitate was observed.

Solvent	Time of precipitation *t*	Result	Product color
AcOH	-	Homogeneous solution	N/D
DMSO	< 1 min	Gel-like precipitate	
DMF	< 1 min	Gel-like precipitate	
Pyr	< 1 min (~ 30 min - 2 h)	Precipitate (and crystals later)	
0.75 Pyr / 0.25 H$_2$O	30 min - 2 h	Single crystals	
AcMe	< 1 min	Gel-like precipitate	
MeOH	< 1 min	Gel particles (bulk precipitate, see	
EtOH	< 1 min	Bulk amorphous precipitate	
0.75 EtOH / 0.25 1,4-Dioxane	< 30 min	Gel-like precipitate	
0.5 EtOH / 0.5 1,4-Dioxane	< 1 min	Gel	
0.5 EtOH / 0.5 THF	< 1 min	Gel	
THF	~ 1-2 min	Gel	
1,4-Dioxane	< 1 min	Gel-like precipitate	
0.95 1,4-Dioxane / 0.05 H$_2$O	< 1 min	Amorphous precipitate	
0.75 1,4-Dioxane / 0.25 EtOH	< 30 min	Gel	
0.25 1,4-Dioxane / 0.75 EtOH	< 30 min	Opaque gel	
MeCN	< 1 min	Amorphous precipitate	

[a] reaction conditions that were used for further research of amorphous MOFs due to superior volume of precipitate among other results
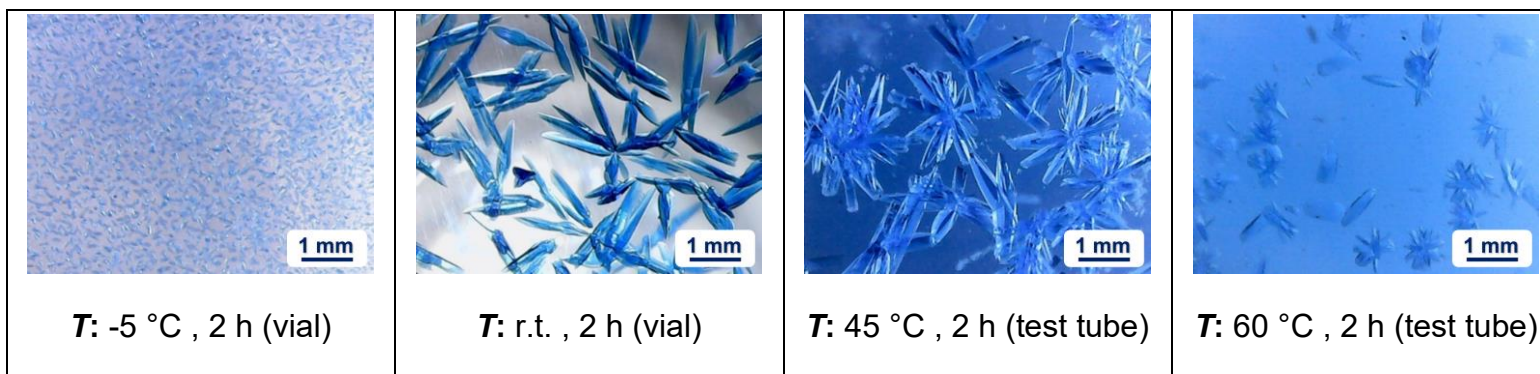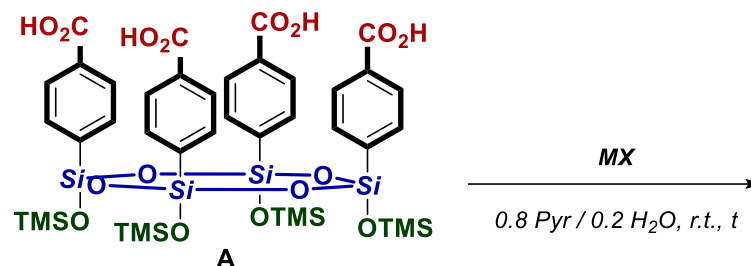
Table S2.4. The Effect of Solvent Composition on MOF B Crystal Formation
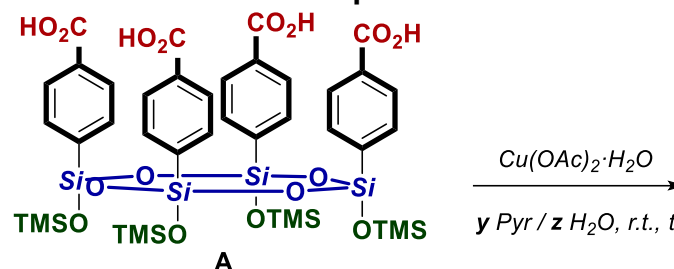
Reaction conditions: Solution of **A** (0.010 g, 0.00000983 mol, 1 eq. in 0.5 ml **y** *Pyr /* **z** H_2O) was simply added to solution of Cu(OAc)$_2$·H_2O (0.00393 g, 0.0000197 mol, 2 eq. in 0.5 ml **y** *Pyr /* **z** H_2O) in snap cap vial (15 ml, ND22) and left intact till formation of precipitate was observed.

y *Pyr /* **z** H_2O *(V/V)*	**Time of precipitation** *t*	**Result**
Pyr	< 1 min (crystal grow ~ 30 min - 2 h)	Amorphous precipitate, crystals
0.9 Pyr / 0.1 H_2O	30 min - 2 h	Single crystals
0.8 Pyr / 0.2 H_2O	30 min - 2 h	Single crystals[a]
0.75 Pyr / 0.25 H_2O	30 min - 2 h	Single crystals
0.5 Pyr / 0.5 H_2O	< 2 h	Crystalline precipitate

[a] optimal parameters for SCXRD analysis

Table S2.5. The Effect of Solvent Loading on MOF B Crystal Formation
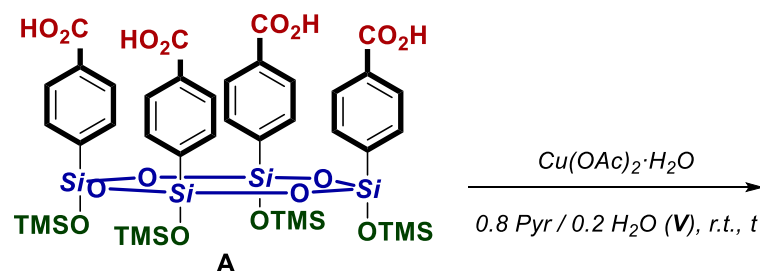
Reaction conditions: Solution of **A** (0.010 g, 0.00000983 mol, 1 eq. in **V/2** ml 0.8 Pyr / 0.2 H_2O) was simply added to solution of Cu(OAc)$_2$·H_2O (0.00393 g, 0.0000197 mol, 2 eq. in **V/2** ml 0.8 Pyr / 0.2 H_2O) in snap cap vial (15 ml, ND22) and left intact till formation of precipitate was observed.

V, ml	Time of precipitation t	Result
10	~ 2 h	Single crystals
5	~ 2 h	Single crystals
2	30 min - 2 h	Single crystals
1	30 min - 2 h	Single crystals[a]
0.5	30 min - 2 h	Single crystals
0.25	30 min - 2 h	Single crystals

[a] following conditions were chosen for further research mainly because of optimal solubility of reagents and best stability of sample towards slow solvent evaporation in standard 15 ml snap cap vials

Table S2.6. The Effect of Temperature on MOF B Crystal Formation
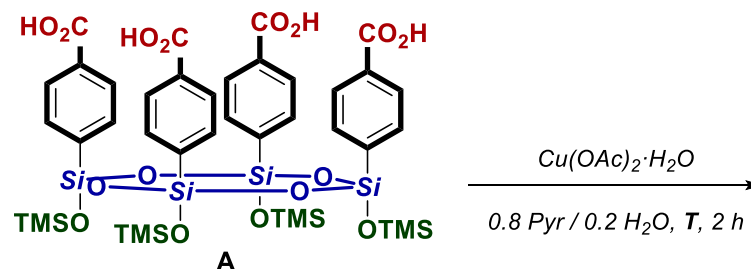
Reaction conditions: Solution of **A** (0.010 g, 0.00000983 mol, 1 eq. in 0.5 ml 0.8 Pyr / 0.2 H_2O) was simply added to solution of Cu(OAc)$_2$·H_2O (0.00393 g, 0.0000197 mol, 2 eq. in 0.5 ml 0.8 Pyr / 0.2 H_2O) in snap cap vial (15 ml, ND22) or Schott Duran GL14 tube (if **T** > r.t.) and left intact at **T °C** for 2 hours.

T, °C	Result
-25	Amorphous precipitate
-5	Small crystals
r.t	Single crystals
45	Single crystals
60	Crystals
120	Amorphous precipitate

| **T**: -5 °C , 2 h (vial) | **T**: r.t. , 2 h (vial) | **T**: 45 °C , 2 h (test tube) | **T**: 60 °C , 2 h (test tube) |

Table S2.7. The Effect of Metal Precursor on MOF B Crystal Formation

Reaction conditions: Solution of **A** (0.010 g, 0.00000983 mol, 1 eq. in 0.5 ml 0.8 Pyr / 0.2 H_2O) was simply added to solution of **MX** (0.0024 - 0.0075 g, 0.0000197 mol,[a] 2 eq. in 0.5 ml 0.8 Pyr / 0.2 H_2O) in snap cap vial (15 ml, ND22) and left intact till formation of precipitate was observed.

MX	M/A Ratio (mol/mol)	Time of precipitation t	Result
CuCl	4	10-12 h	Single crystals
CuBr	4	10-12 h	Single crystals
CuI	4	10-12 h	Single crystals
CuCl$_2$	2	-	Homogeneous solution
CuBr$_2$	2	~ 1 d	Non-uniform crystals
Cu(NO$_3$)$_2$·3H$_2$O	2	-	Homogeneous solution
Cu(OAc)$_2$	2	30 min - 2 h	Single crystals
Cu(OAc)$_2$·H$_2$O	2[a]	30 min - 2 h	Single crystals (regular size)
	2[b]	30 min - 2 h	Single crystals (smaller size)
	6[c]	~ 2 h	Single crystals (regular size)
	10[d]	< 1 d	Single crystals (regular size)
Cu(OBz)$_2$	2	30 min - 2 h	Single crystals
Cu(AcAc)$_2$	2	< 21 d	Small amount of crystals
Cu(C$_2$O$_4$)$_2$	2	< 21 d	Single crystals

[a] These conditions are referred as standard conditions for **MOF B** crystals growth further in the text. [b] 5X scaling of reagents loading.
[c] Experiments with 3X (0.0118 g, 0.0000590 mol) and [d] 5X (0.0196 g, 0.0000983 mol) loadings of Cu(OAc)$_2$·H$_2$O were carried out to evaluate the effect of metal/ligand ratio
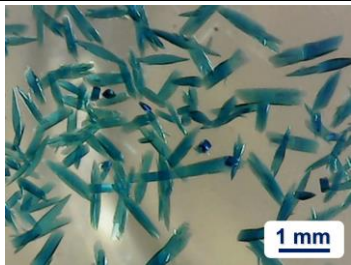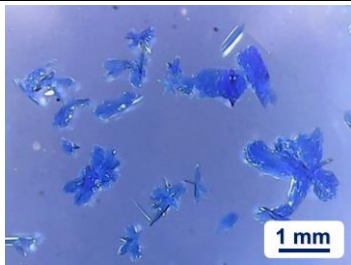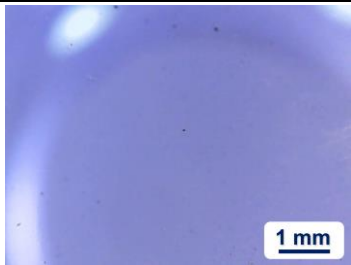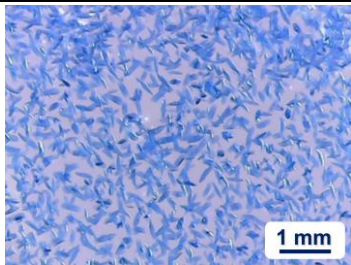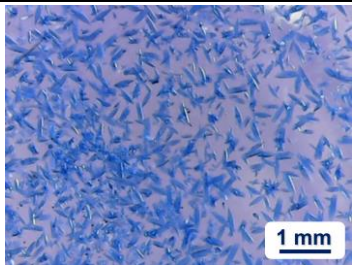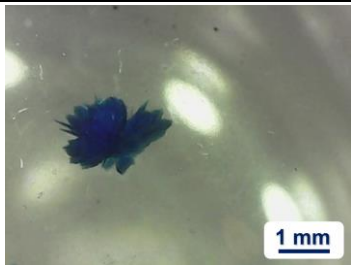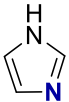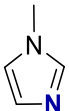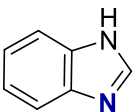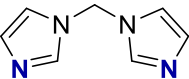
MX: CuCl

MX: CuBr

MX: CuI

MX: $CuCl_2$

MX: $CuBr_2$

MX: $Cu(NO_3)_2 \cdot 3H_2O$

MX: $Cu(OAc)_2$

MX: $Cu(OAc)_2 \cdot H_2O$

MX: $Cu(OBz)_2$

MX: $Cu(AcAc)_2$

MX: $Cu(C_2O_4)_2$

Table S2.8. The Effect of Nitrogen-containing Base Additive on MOF B Crystal Formation

Reaction conditions: Solution of **A** (0.010 g, 0.00000983 mol, 1 eq.) and nitrogen-containing base **[N]** (0.0013 - 0.0046 g, 0.0000197 mol, 2 eq.) in 0.5 ml 0.8 Pyr / 0.2 H_2O was simply added to solution of Cu(OAc)$_2$·H_2O (0.00393 g, 0.0000197 mol, 2 eq. in 0.5 ml 0.8 Pyr / 0.2 H_2O) in snap cap vial (15 ml, ND22) and left intact till formation of precipitate was observed.

[N]	**Time of precipitation _t_**	**Result**
	~ 1 d	Small amount of deformed crystals
	< 2 h	Single crystals (same habit as for crystals grown with absence of **[N]**)
	< 2 h	Single crystals (same habit as for crystals grown with absence of **[N]**)
	< 2 h	Single crystals (same habit as for crystals grown with absence of **[N]**)
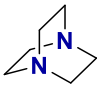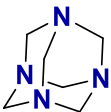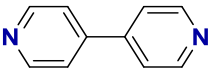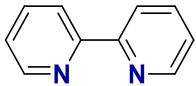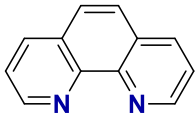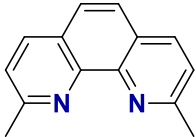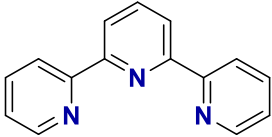
Structure	Time	Result
	< 2 h	Single crystals (bigger size, same habit as for crystals grown with absence of *[N]*)
	< 2 h	Single crystals (bigger size, same habit as for crystals grown with absence of *[N]*)
	~ 2 h	Single crystals (bigger size, habit and structure is identical to crystals grown with absence of *[N]*)
	-	Homogeneous solution
	-	Homogeneous solution
	-	Homogeneous solution
	-	Homogeneous solution

Table S2.9. Other M(II)-Metal Precursors in Standard Conditions of MOF B Crystals Formation. MOFs C-F
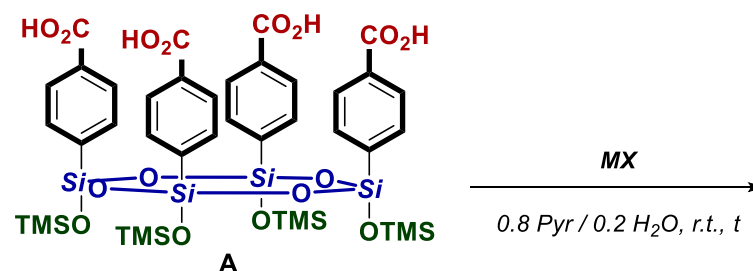
Reaction conditions: Solution of **A** (0.010 g, 0.00000983 mol, 1 eq. in 0.5 ml 0.8 Pyr / 0.2 H_2O) was simply added to solution of **MX** (0.0008 - 0.0063 g, 0.0000197 mol, 2 eq. in 0.5 ml 0.8 Pyr / 0.2 H_2O) in snap cap vial (15 ml, ND22) and left intact till formation of precipitate was observed.

MX	Time of precipitation t	Result
MgO	10-18 h	Thin crystal-like fibers[a]
Mg(OAc)$_2$	10-18 h	Thin crystal-like fibers[a]
Ca(NO$_3$)$_2$·4H$_2$O	< 7 d	Polycrystalline precipitate
Mn(OAc)$_2$·4H$_2$O	< 1 min (< 7 d)	Suspension (precipitate)
Fe(OAc)$_2$	< 1 min	Emulsion
Co(OAc)$_2$·4H$_2$O	1 d	Lamellar single crystals (**MOF C**)[b]
Ni(OAc)$_2$·4H$_2$O	2 h - 1 d	Crystal-like lamellar plates[a]
Zn(OAc)$_2$·2H$_2$O	1 d	Cubic single crystals (**MOF D**)[b]
Cd(OAc)$_2$·2H$_2$O	1 d	Radial single crystals (**MOF E**)
Hg(OAc)$_2$	1 d	Bladed single crystals (**MOF F**)

[a] Aggregates were not suitable for SCXRD analysis

[b] Further investigation of selected reaction conditions was performed to generalize the approach
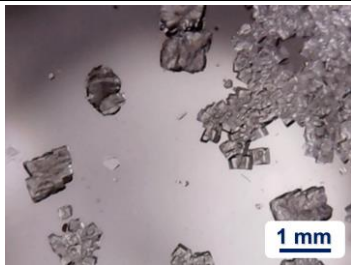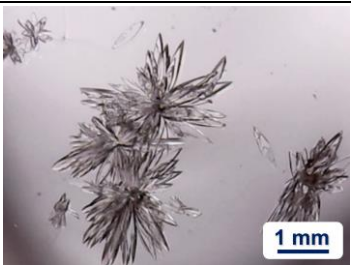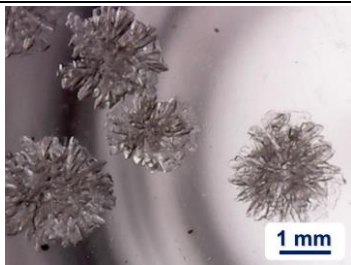
MX: Mg(OAc)$_2$

MX: Co(OAc)$_2$·4H$_2$O

MX: Ni(OAc)$_2$·4H$_2$O

MX: Zn(OAc)$_2$·2H$_2$O

MX: Hg(OAc)$_2$


MX: Cd(OAc)$_2$·2H$_2$O

Table S2.10. Other M(III)-Metal Precursors in Standard Conditions of MOF B Crystals Formation
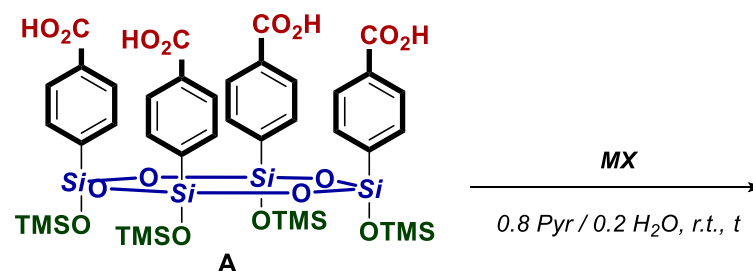
Reaction conditions: Solution of **A** (0.010 g, 0.00000983 mol, 3 eq. in 0.5 ml 0.8 Pyr / 0.2 H_2O) was simply added to solution of **MX** (0.0030 - 0.0053 g, 0.0000131 mol, 4 eq. in 0.5 ml 0.8 Pyr / 0.2 H_2O) in snap cap vial (15 ml, ND22) and left intact till formation of precipitate was observed.

MX	Time of precipitation t	Result
$Cr(OAc)_3$	-	Green homogeneous solution
$Mn(OAc)_3 \cdot 2H_2O$	< 1 min	Dark amorphous precipitate
$Fe(NO_3)_3 \cdot 9H_2O$	< 1 min	Colorless suspension
$La(OAc)_3 \cdot 1.5H_2O$	< 1 min	Colorless suspension
$Ce(OAc)_3 \cdot H_2O$	< 1 min	Colorless suspension
$Eu(OAc)_3 \cdot H_2O$	< 1 min	Colorless suspension
$Dy(OAc)_3 \cdot 4H_2O$	< 1 min	Colorless suspension
$Lu(OAc)_3 \cdot 3H_2O$	< 1 min	Colorless suspension

Table S2.11. Screening of Crystal Formation Conditions of MOF C. The Effect of Solvent
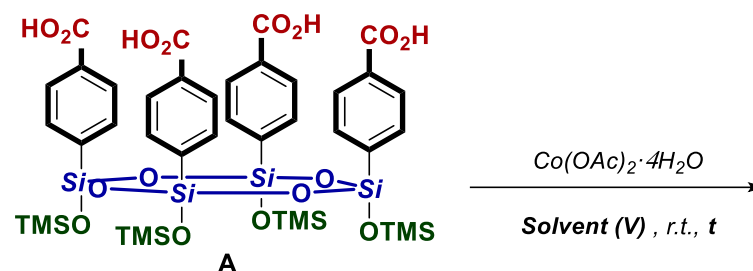
Reaction conditions: Solution of **A** (0.010 g, 0.00000983 mol, 1 eq. in 0.5**V** of **Solvent**) was simply added to solution of Co(OAc)$_2$·4H$_2$O (0.0049 g, 0.0000197 mol, 2 eq. 0.5**V** of **Solvent**) in snap cap vial (15 ml, ND22) and left intact till formation of precipitate was observed.

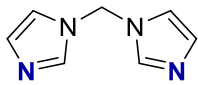| *Solvent (V≈V$_{sol1}$+V$_{sol2}$), ml*	**Time of precipitation *t***	**Result[b]**
AcOH, 1 ml	-	Homogeneous solution
DMSO, 1 ml	< 1 min	Amorphous precipitate
DMF, 1 ml	< 1 min	Gel-like precipitate
DMF / H$_2$O, 0.9 ml / 0.1 ml	< 1 min	Amorphous precipitate
Pyr, 1 ml	< 1 min	Amorphous precipitate
Pyr / H$_2$O, 0.8 ml / 0.2 ml	1 d	Single crystals
AcMe / MeOH, 1 ml / 0.2 ml [a]	< 1 min	Amorphous precipitate
MeOH, 1 ml	7-17 d	Crystal-like aggregates
EtOH / MeOH, 1 ml / 0.1 ml [a]	< 1 min	Amorphous precipitate
i-PrOH / MeOH, 1 ml / 0.2 ml [a]	< 1 min	Amorphous precipitate
n-BuOH / H$_2$O, 0.8 ml / 0.2 ml	< 11 d	Crystal-like aggregates
THF / MeOH, 1 ml / 0.05 ml [a]	-	Homogeneous solution
THF / H$_2$O, 0.5 ml / 0.5 ml	< 3 d	Amorphous precipitate
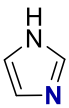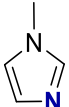
[a] This amount of methanol is necessary to improve salt solubility in a chosen solvent

[b] The reaction products are predominantly colored pink (precipitates) or reddish-pink (aggregates)

Table S2.12. The Effect of Nitrogen-containing Base Additive on MOF C Crystal Growth

Reaction conditions: Solution of **A** (0.010 g, 0.00000983 mol, 1 eq.) and nitrogen-containing base **[N]** (0.0013 - 0.0046 g, 0.0000197 mol, 2 eq.) in 0.5 ml 0.8 Pyr / 0.2 H_2O was simply added to solution of Co(OAc)$_2$·4H$_2$O (0.0049 g, 0.0000197 mol, 2 eq. in 0.5 ml 0.8 Pyr / 0.2 H_2O) in snap cap vial (15 ml, ND22) and left intact till formation of precipitate was observed.

[N]	Time of precipitation *t*	Result
	< 3 d	Single crystals
	< 3 d	Single crystals (same habit as for crystals grown with absence of *[N]*)
	< 3 d	Single crystals (same habit as for crystals grown with absence of *[N]*)
	< 3 d	Single crystals (same habit as for crystals grown with absence of *[N]*)
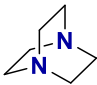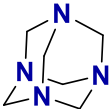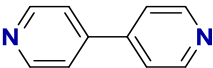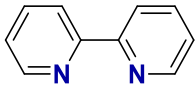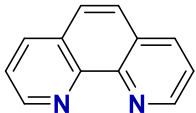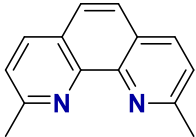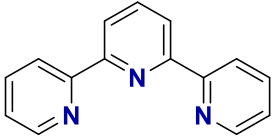
	< 3 d	Single crystals (habit and structure is identical to crystals grown with absence of [N])
	< 3 d	Single crystals (same habit as for crystals grown with absence of [N])
	~ 2 h	Single crystals
	-	Homogeneous solution
	-	Homogeneous solution
	-	Homogeneous solution
	-	Homogeneous solution

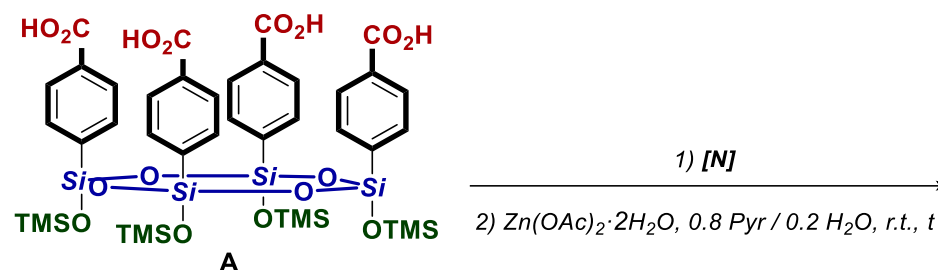**Table S2.13. Screening of Crystal Formation Conditions of MOF D. The Effect of Solvent**
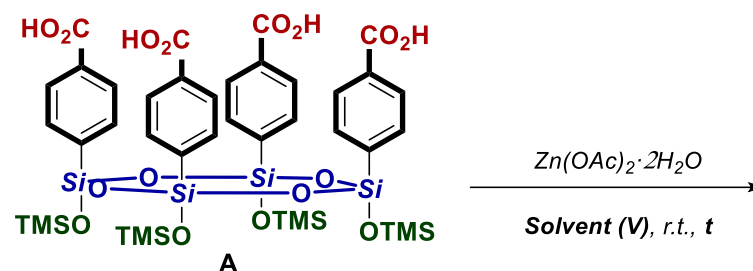
Reaction conditions: Solution of **A** (0.010 g, 0.00000983 mol, 1 eq. in 0.5**V** of **Solvent**) was simply added to solution of Zn(OAc)$_2$·2H$_2$O (0.0043 g, 0.0000197 mol, 2 eq. in 0.5**V** of **Solvent**) in snap cap vial (15 ml, ND22) and left intact till formation of precipitate was observed.

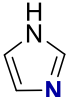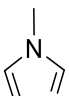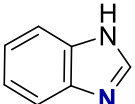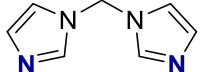| Solvent (V≈V$_{sol1}$+V$_{sol2}$), ml	Time of precipitation t	Result[b]
DMF, 1 ml	< 1 min	Amorphous precipitate
DMF / H$_2$O, 0.9 ml / 0.1 ml	< 1 min	Amorphous precipitate
DMSO, 1 ml	< 1 min	Amorphous precipitate
Pyr, 1 ml	< 1 min	Amorphous precipitate
Pyr / H$_2$O, 0.8 ml / 0.2 ml	< 1 d	Single crystals
MeOH, 1 ml	< 1 min	Amorphous precipitate
EtOH, 1 ml	< 1 min	Amorphous precipitate
n-BuOH / H$_2$O, 1 ml / 0.2 ml [a]	< 1 min	Amorphous precipitate
THF / MeOH, 1 ml / 0.05 ml [a]	< 1 min	Amorphous precipitate

[a] This amount of methanol or water is necessary to improve salt solubility in a chosen solvent

[b] The reaction products are predominantly colorless

Table S2.14. The Effect of Nitrogen-containing Base Additive on MOF D Crystal Growth

Reaction conditions: Solution of **A** (0.010 g, 0.00000983 mol, 1 eq.) and nitrogen-containing base **[N]** (0.0013 - 0.0046 g, 0.0000197 mol, 2 eq.) in 0.5 ml 0.8 Pyr / 0.2 H$_2$O was simply added to solution of Zn(OAc)$_2$·2H$_2$O (0.0043 g, 0.0000197 mol, 2 eq. in 0.5 ml 0.8 Pyr / 0.2 H$_2$O) in snap cap vial (15 ml, ND22) and left intact till formation of precipitate was observed.

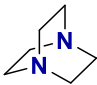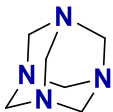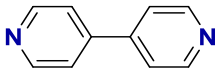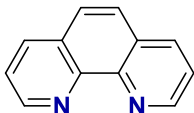| *[N]*	Time of precipitation *t*	Result
	-	Homogeneous solution
	< 21 d	Small amount of polycrystalline aggregates on surface of solution
	< 7 d	Polycrystalline precipitate
	< 2 d	Polycrystalline aggregates on surface of solution
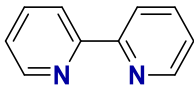
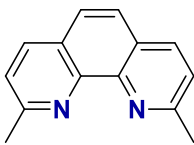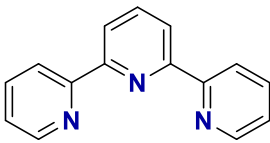|		
	< 21 d	Small amount of single crystals and polycrystalline aggregates on surface of solution
	< 21 d	Small amount of single crystals and polycrystalline aggregates on surface of solution
	-	Homogeneous solution
	-	Homogeneous solution
	< 7 d	Amorphous precipitate
	< 7 d	Amorphous precipitate
	< 1 min	Amorphous precipitate

Table S2.15. The Effect of Metal Precursor on MOFs D and H Crystal Growth
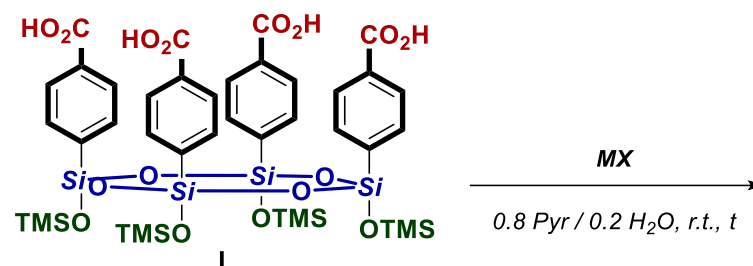
Reaction conditions: Solution of **A** (0.010 g, 0.00000983 mol, **I** eq. in 0.5 ml **x** Pyr / **y** H_2O) was simply added to solution of **MX** (0.0041 - 0.006 g, 0.0000197 or 0.0000131 mol, **mx** eq. in 0.5 ml **x** Pyr / **y** H_2O) in snap cap vial (15 ml, ND22) and left intact till formation of precipitate was observed.

MX	I/mx Ratio	x Pyr / y H_2O	Time t	Result
$Zn(OAc)_2 \cdot 2H_2O$	1/2	0.8 / 0.2	< 1 d	Single crystals (**MOF D**)
$Zn(OPiv)_2$	1/2	0.8 / 0.2	< 4 d	Single crystals (same structure as for **MOF D**)
$Zn_4O(OAc)_6$	3/2	0.8 / 0.2	< 6 d	Single crystals (same structure as for **MOF D**)
$Li_2Zn_2(OPiv)_6(Pyr)_2$	2/1	0.8 / 0.2	< 2 h	Single crystals (**MOF H**)
$Li_2Zn_2(OPiv)_6(Pyr)_2$	3/2	0.7 / 0.3	< 2 h	Single crystals (same structure as for **MOF D**)

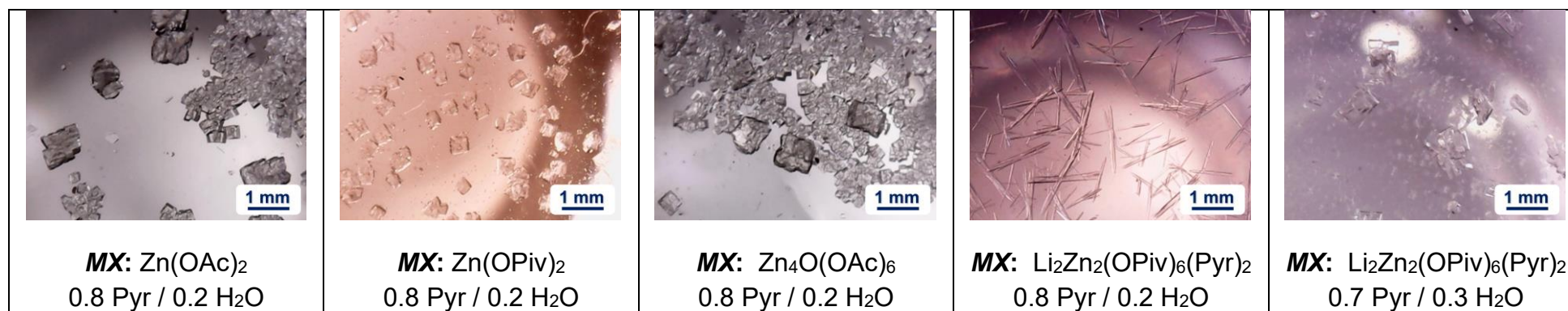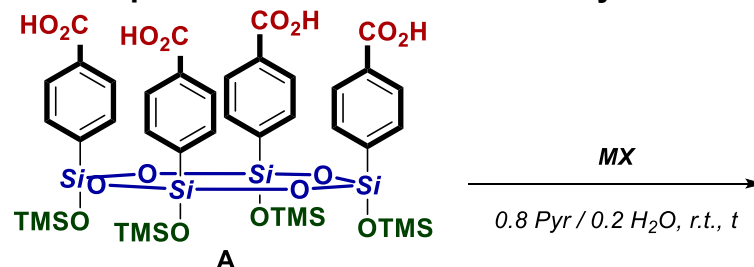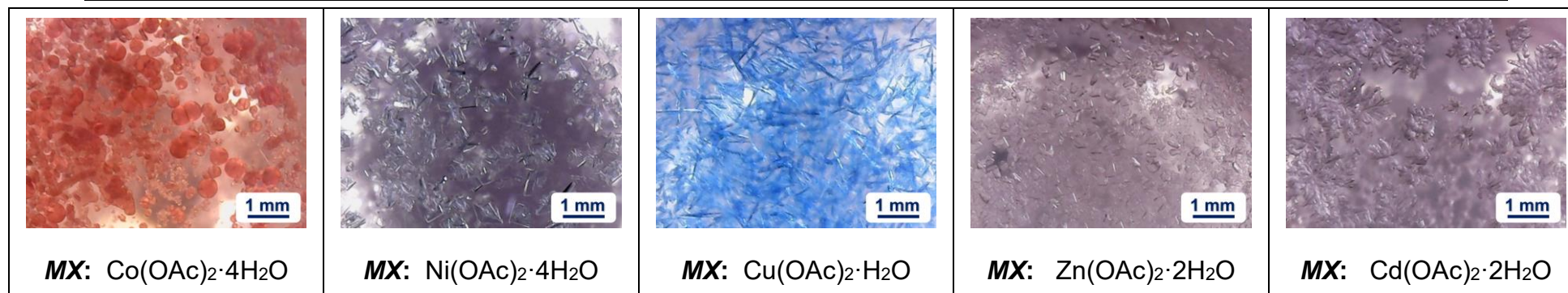|				
MX: $Zn(OAc)_2$ 0.8 Pyr / 0.2 H_2O	**MX:** $Zn(OPiv)_2$ 0.8 Pyr / 0.2 H_2O	**MX:** $Zn_4O(OAc)_6$ 0.8 Pyr / 0.2 H_2O	**MX:** $Li_2Zn_2(OPiv)_6(Pyr)_2$ 0.8 Pyr / 0.2 H_2O	**MX:** $Li_2Zn_2(OPiv)_6(Pyr)_2$ 0.7 Pyr / 0.3 H_2O

Table S2.16. The Effect of Sequential Solvent Addition on Crystal Growth of MOFs B-E and G

Reaction conditions: Solution of **A** (0.010 g, 0.00000983 mol, 1 eq. in 0.25 ml 0.8 Pyr / 0.2 H_2O) was simply added to solution of **MX** (0.0039 – 0.052 g, 0.0000197 mol, 2 eq. in 0.25 ml 0.8 Pyr / 0.2 H_2O) in snap cap vial (15 ml, ND22). Then 0.125 ml of H_2O and 0.375 ml of Pyr were sequentially added to reaction mixture. Mixture left intact till formation of precipitate was observed.

MX	Time *t*	*t* between H_2O and Pyr addition	Result[a]
$Co(OAc)_2 \cdot 4H_2O$	<1-2 h	Less than 5-10 sec	Single crystals (**MOF G**)
$Ni(OAc)_2 \cdot 4H_2O$	<1-2 h	Less than 5-10 sec	Single crystals (same habit as for Ni-A)
$Cu(OAc)_2 \cdot H_2O$	<1-2 h	Less than 5-10 sec	Single crystals (same habit as for **MOF B**)
$Zn(OAc)_2 \cdot 2H_2O$	<1-2 h	Less than 5-10 sec	Single crystals (same habit as for **MOF D**)
$Cd(OAc)_2 \cdot 2H_2O$	<1-2 h	Less than 5-10 sec	Single crystals (same habit as for **MOF E**)

MX: $Co(OAc)_2 \cdot 4H_2O$ *MX*: $Ni(OAc)_2 \cdot 4H_2O$ *MX*: $Cu(OAc)_2 \cdot H_2O$ *MX*: $Zn(OAc)_2 \cdot 2H_2O$ *MX*: $Cd(OAc)_2 \cdot 2H_2O$

[a] despite faster average crystal formation in comparison to standard conditions, method have such major disadvantages as unstable reproducibility, high dependence of the shape and size of crystals on the time interval between the addition of water and pyridine – bigger interval (>10-15 sec) results in formation of smaller crystals or polycrystalline aggregates

S3. Stability of *as-synthesized* MOFs to solvent exchange. MOFs **B4**, **B4'** preparation

Table S3.1. Screening of Solvents for Sequential Solvent Exchange on Example of MOF B

MOF B was chosen as model for solvent exchange procedure among other MOFs due to its best reproducibility, uniform and fast crystal growth.

Standard[a] procedure for solvent exchange (result of last exchange step is shown in table):

Step 1: 0.5 ml of solvent was added to as-synthesized MOF in mother liquor then left intact for 24 h;
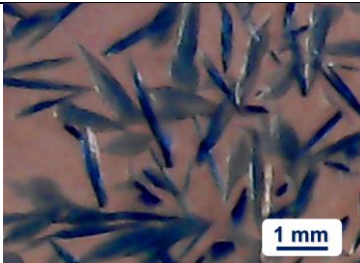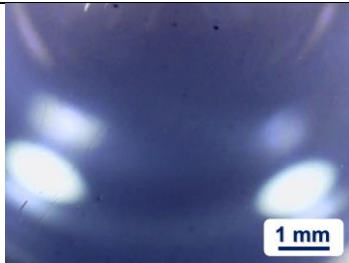
Step 2: 1 ml of solvent was added to reaction mixture then left intact for 24 h;

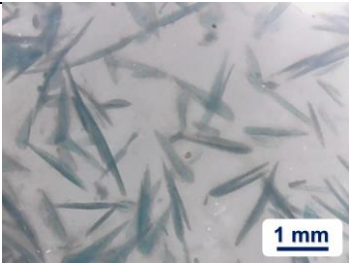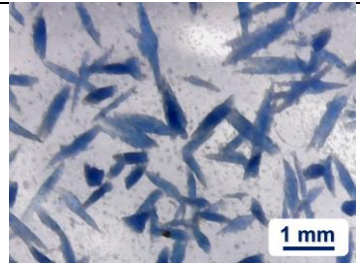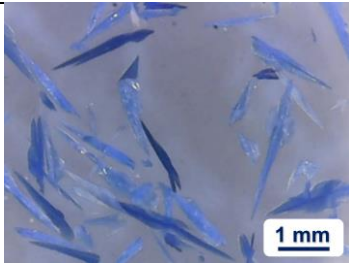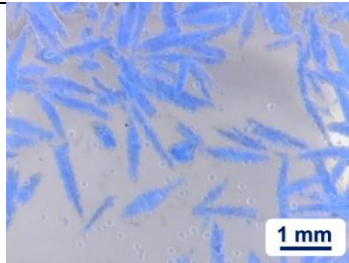Step 3: 1 ml of mixture liquor was withdrawn and 1 ml of solvent was added then left intact for 24 h;

Step 4: 2 ml of mixture liquor was withdrawn and 2 ml of solvent was added then left intact for 24 h.

If it was possible, Step 4 was repeated.

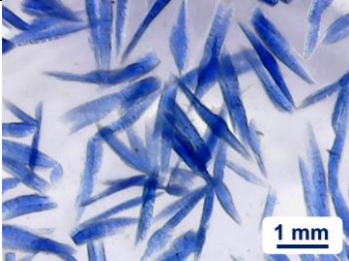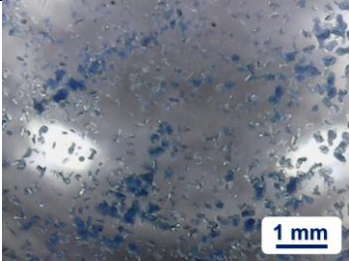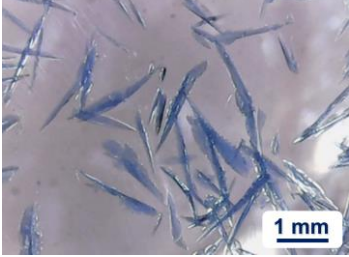[a] applied for crystals, derived from standard conditions (per 10 mg of ligand A)

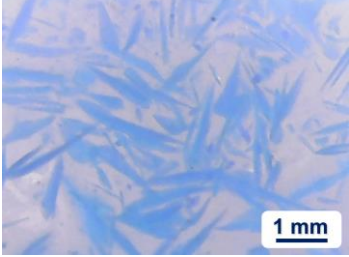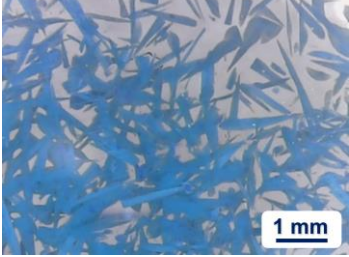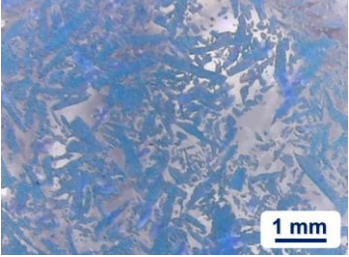| Solvent	Mother liquor	H_2O	AcOH	DMSO
Max exchange step	-	> 4	< 1 (full dissolution)	< 2
Results				
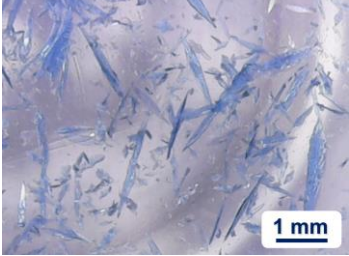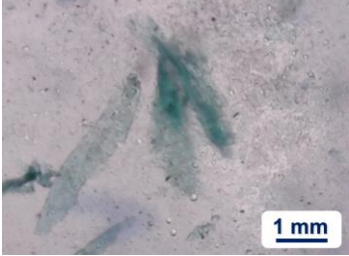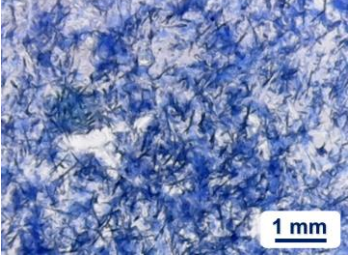
Solvent	DMAc	AcMe	MeOH	EtOH
Max exchange step	< 4	< 4	< 2	< 4
Results				
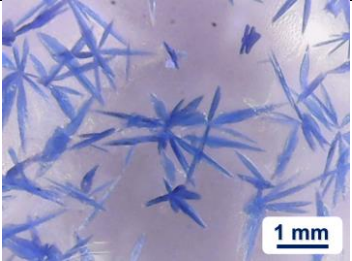
Solvent	*i*-PrOH	*n*-BuOH	THF	1,4-Dioxane
Max exchange step	4	< 2	< 2	< 3
Results				

Solvent	Glycerol	2-Methoxyethanol	Ethylene glycol	MeCN
Max exchange step	4 (too viscous for $scCO_2$)	< 4	< 4	< 4
Results				

Solvent	DMC	MTBE	DCM	Et_2O
Max exchange step	4	4	< 4	< 3
Results				

Solvent	Hexane	Et₃N	Pyr	NMP
Max exchange step	< 4 (phase separation)	< 2	> 4	< 2
Results				

Least visible changes occurred when mother liquor was exchanged to isopropanol, methyl *tert*-butyl ether, dimethylcarbonate (DMC) or initial solvent components (water and pyridine). However, only isopropanol- and pyridine-exchanged samples were suitable for supercritical CO_2 activation without loss of shape and integrity of solvated crystals.

S4. Stability of *as-synthesized* MOFs to solvolysis in the presence of nitrogen-contaning organic bases. MOFs **B1**, **B2** and **B3** preparation
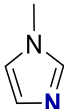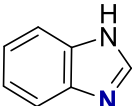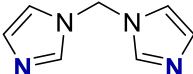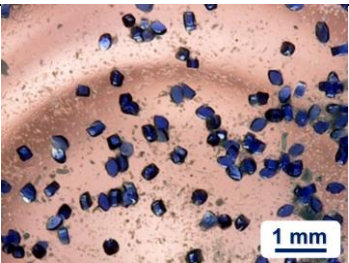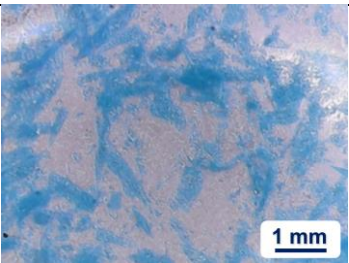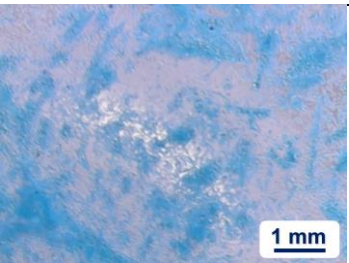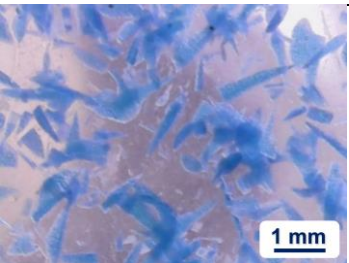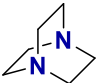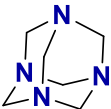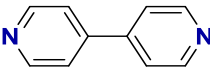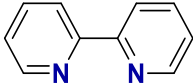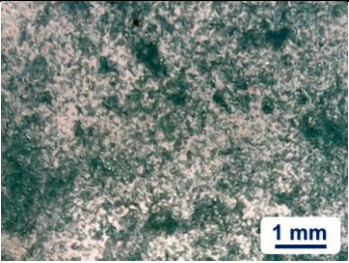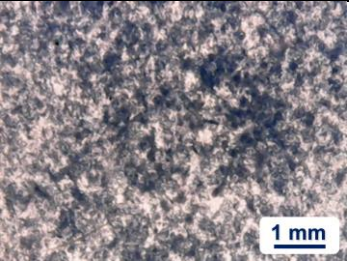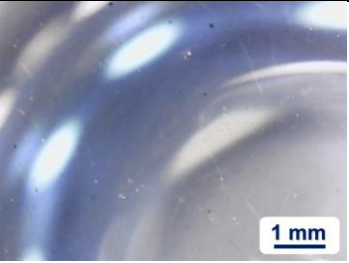
Table S4.1. Stability of MOF B to Solvolysis in Presence of Nitrogen-contaning Organic Bases

As-synthesized MOF B → 1) Mother liqour evacuation
2) **[N]**, **Solvent**, r.t., **t**

Standard conditions for solvolysis test in presence of nitrogen-containing base: mother liquor of as-synthesized **MOF B** was evacuated[a] and solution of nitrogen-containing base **[N]** (0.0013 - 0.0046 g, 0.0000197 mol, 2 eq. in 1 ml of polar **Solvent**) was added. Degradation/transformation of crystals was checked for at least 7 days.[b]
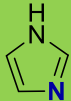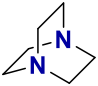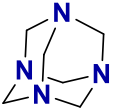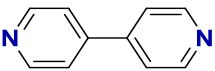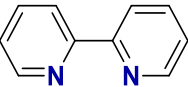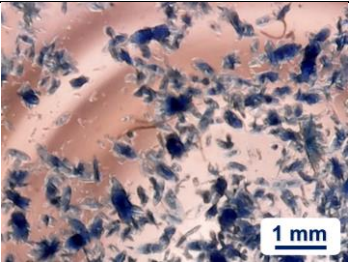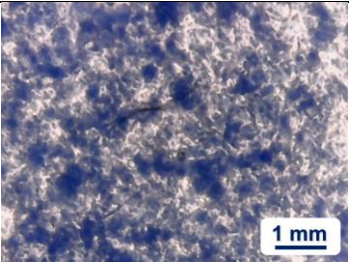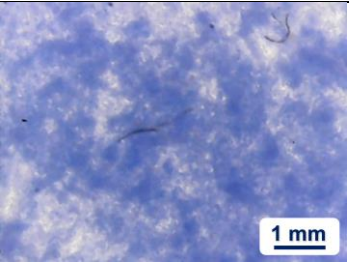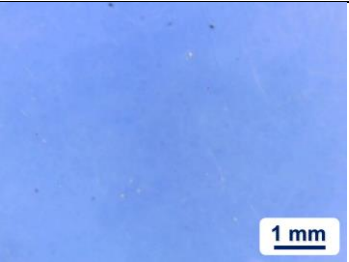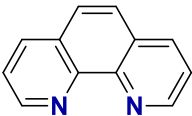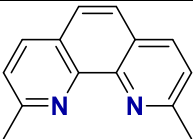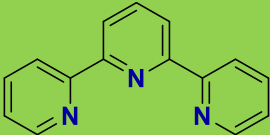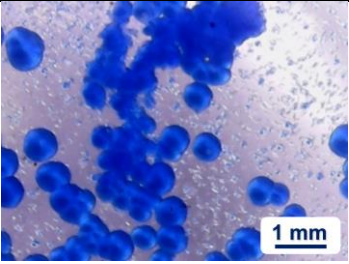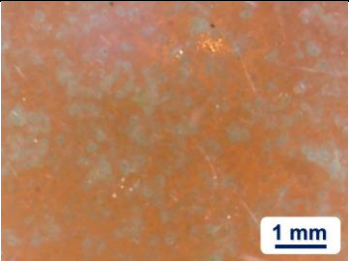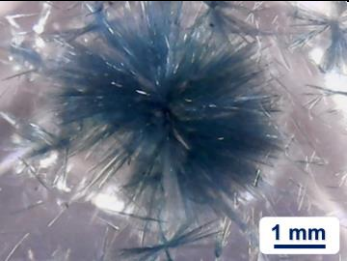
[a] Evacuation of mother liquor was carried out to lower pyridine/base ratio
[b] These conditions are referred as standard conditions for solvolysis in presence of nitrogen-containing organic base further in the text

Solvent	MeOH			
[N]	(imidazole)	(1-methylimidazole)	(benzimidazole)	(1,1'-methylenebis-imidazole)
Time t	7 d	7 d	7 d	7 d
Results				
[N]	(DABCO)	(hexamethylenetetramine)	(4,4'-bipyridine)	(2,2'-bipyridine)
Time t	7 d	7 d	7 d	7 d
Results				
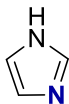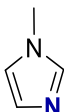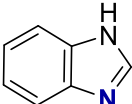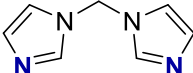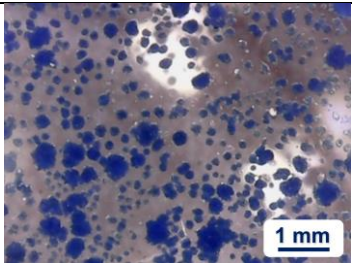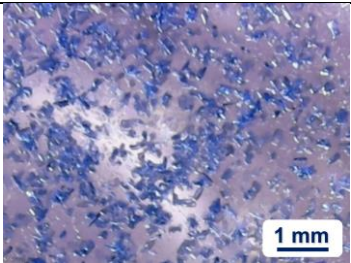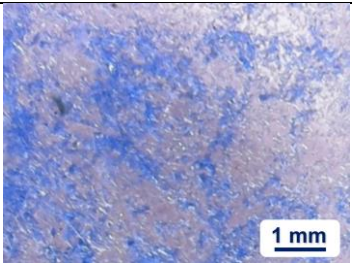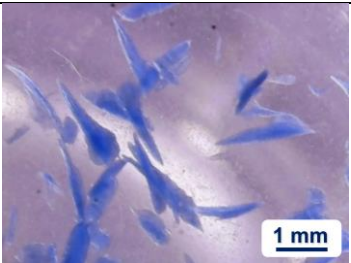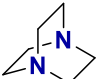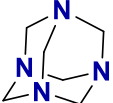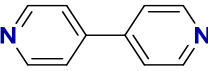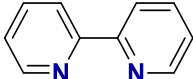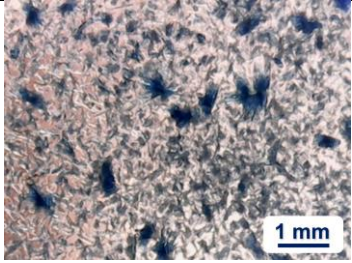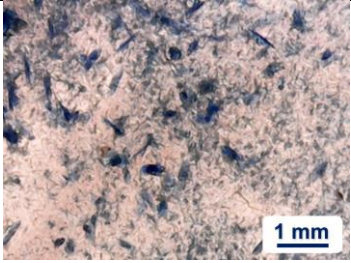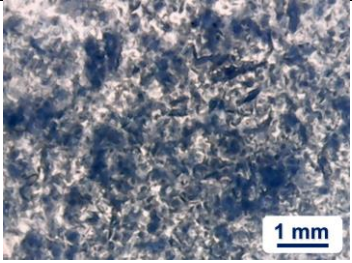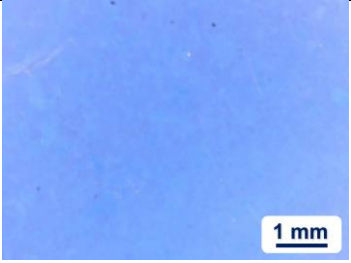
Solvent	MeOH		
[N]			
Time t	7 d	7 d	7 d
Results			
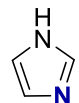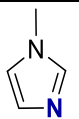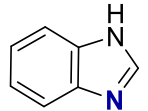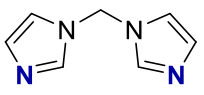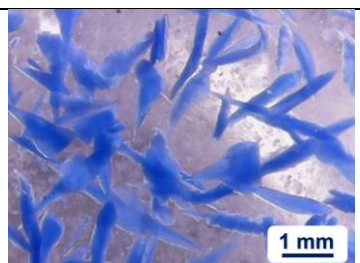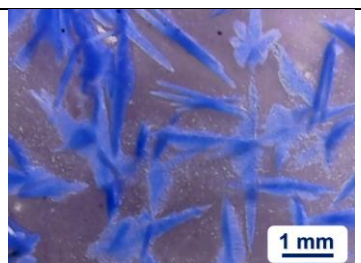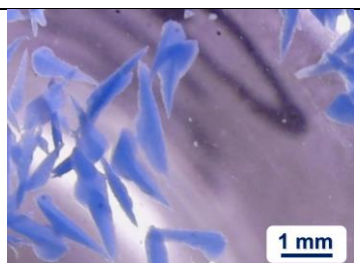
Solvent	EtOH			
[N]				
Time t	7 d	7 d	7 d	7 d
Results				
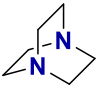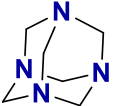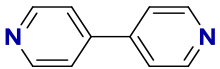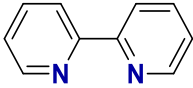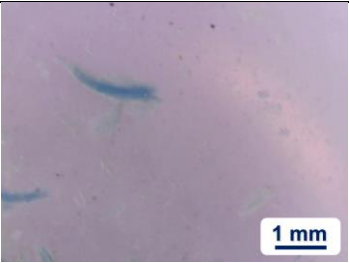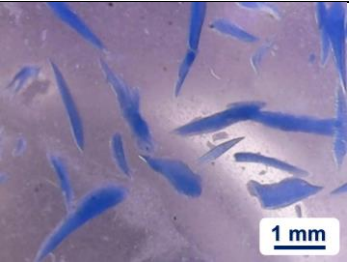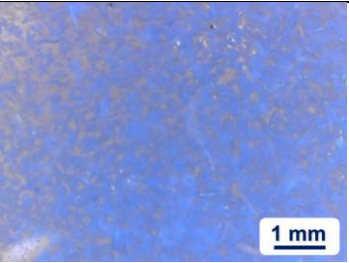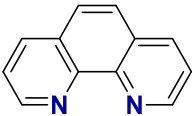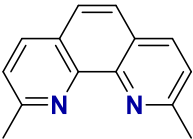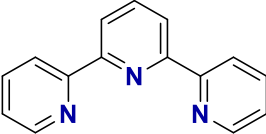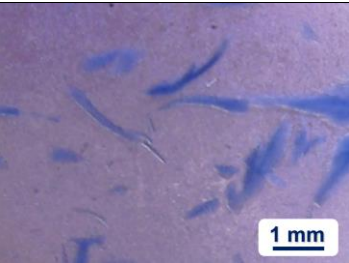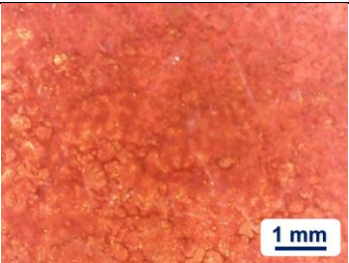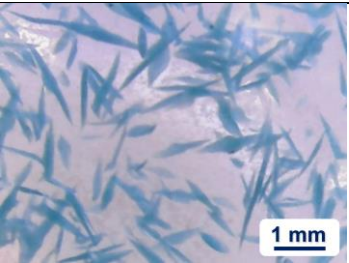
Solvent	EtOH			
[N]				
Time t	**7 d**	**7 d**	**7 d**	**7 d**
Results				
[N]				
Time t	**7 d**	**7 d**	**7 d**	
Results				
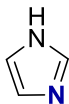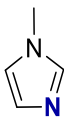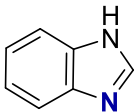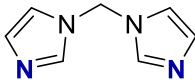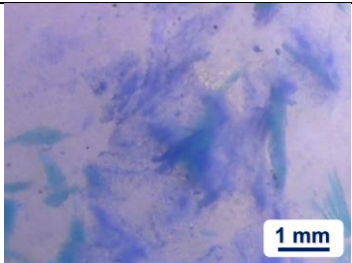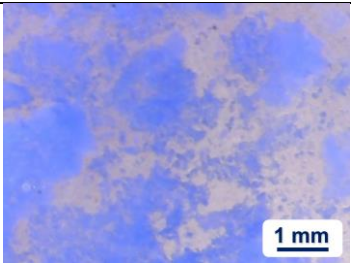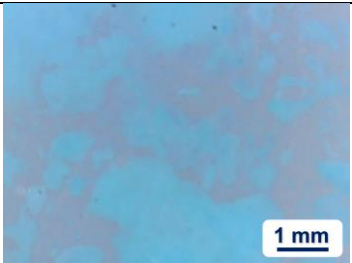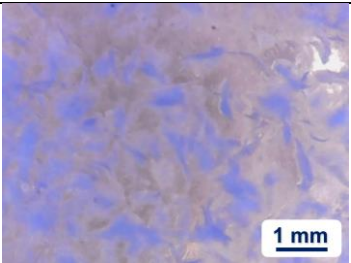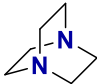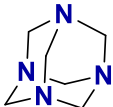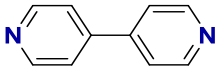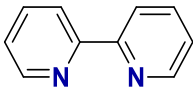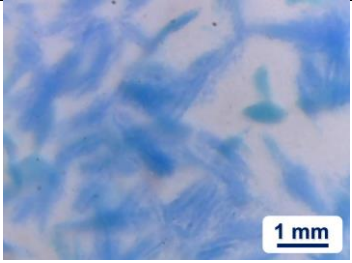
Solvent	i-PrOH			
[N]				
Time t	**7 d**	**7 d**	**7 d**	**7 d**
Results				
[N]				
Time t	**7 d**	**7 d**	**7 d**	**7 d**
Results				
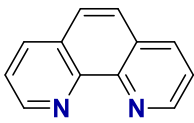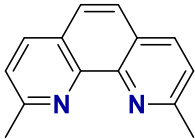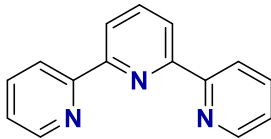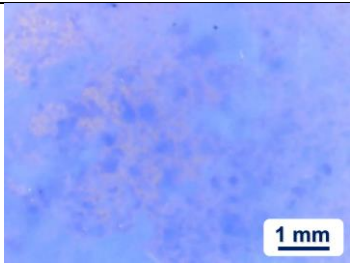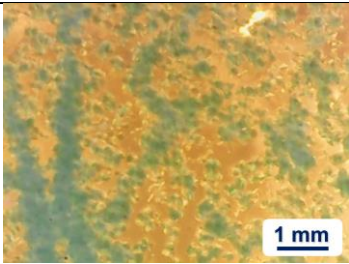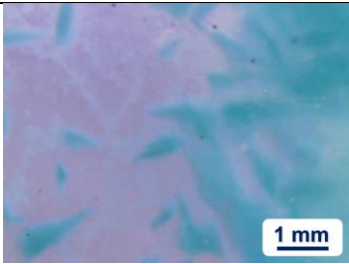
Solvent	*i*-PrOH		
[N]			
Time t	**7 d**	**7 d**	**7 d**
Results			
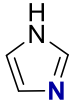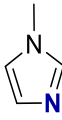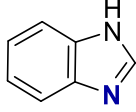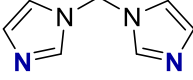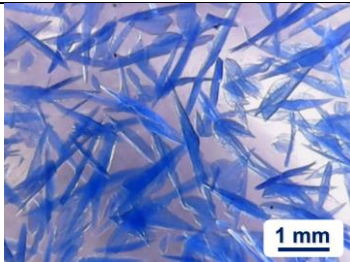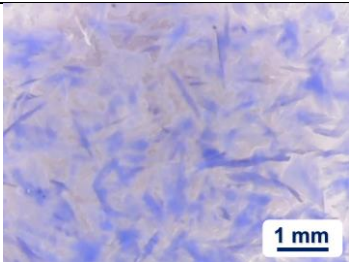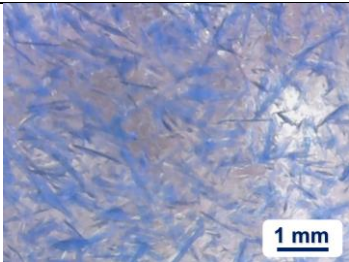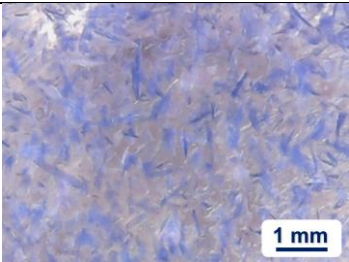
Solvent	AcMe			
[N]				
Time t	**7 d**	**7 d**	**7 d**	**7 d**
Results				

Solvent	AcMe			
[N]				
Time t	**7 d**	**7 d**	**7 d**	**7 d**
Results				
[N]				
Time t	**7 d**	**7 d**	**7 d**	
Results				

Solvent	THF			
[N]	imidazole	1-methylimidazole	benzimidazole	1,1'-methylenebis(imidazole)
Time t	**7 d**	**7 d**	**7 d**	**7 d**
Results	1 mm	1 mm	1 mm	1 mm
[N]	DABCO	hexamethylenetetramine	4,4'-bipyridine	2,2'-bipyridine
Time t	**7 d**	**7 d**	**7 d**	**7 d**
Results	1 mm	1 mm	1 mm	1 mm
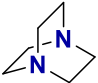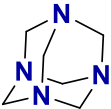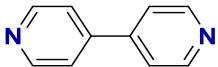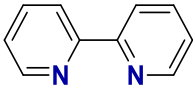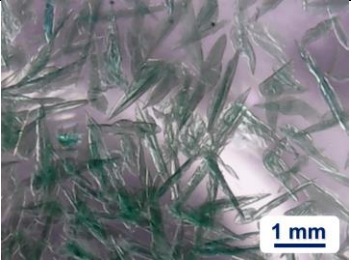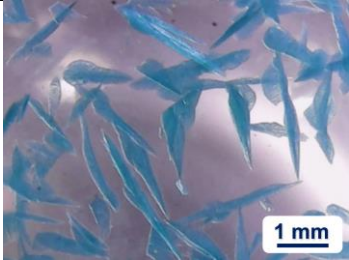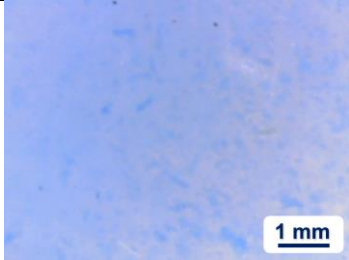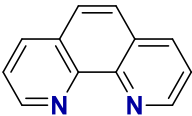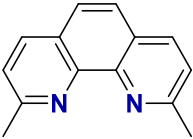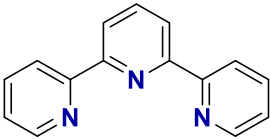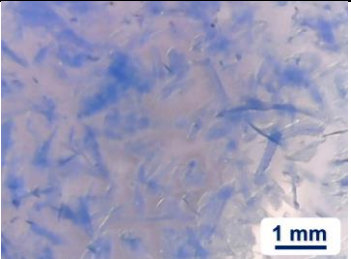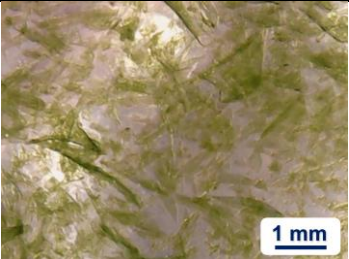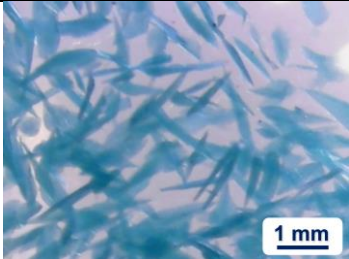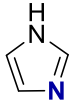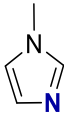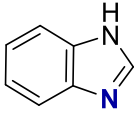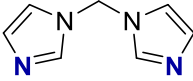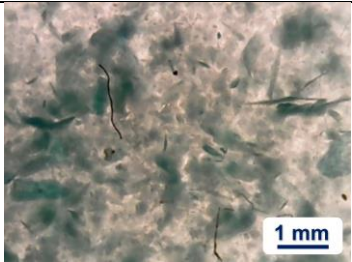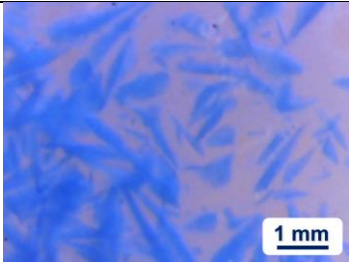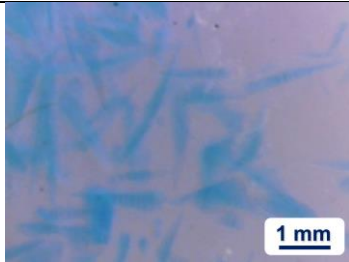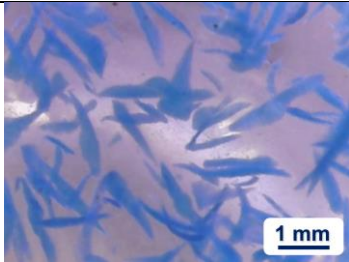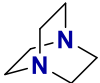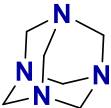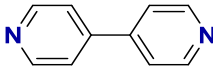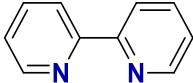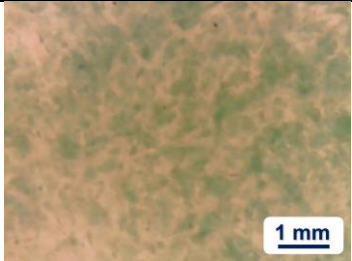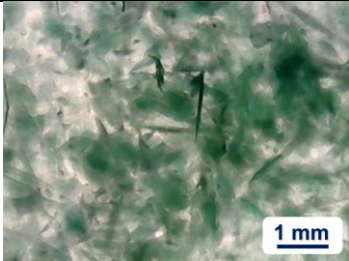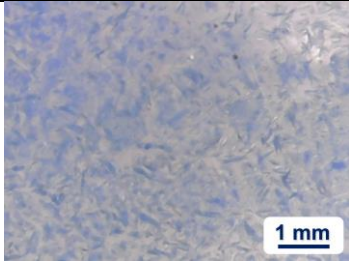
Solvent	THF		
[N]			
Time t	7 d	7 d	7 d
Results			
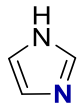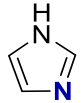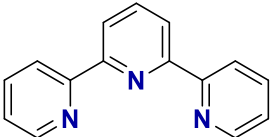
Solvent	1,4-Dioxane			
[N]				
Time t	7 d	7 d	7 d	7 d
Results				

Solvent	1,4-Dioxane			
[N]				
Time t	7 d	7 d	7 d	7 d
Results				
[N]				
Time t	7 d	7 d	7 d	
Results				

Solvent	DMF			
[N]	imidazole	1-methylimidazole	benzimidazole	1,1'-methylenebis(imidazole)
Time t	**7 d**	**7 d**	**7 d**	**7 d**
Results				
[N]	DABCO	hexamethylenetetramine	4,4'-bipyridine	2,2'-bipyridine
Time t	**7 d**	**7 d**	**7 d**	**7 d**
Results				
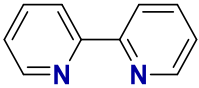
Solvent	DMF		
[N]	1,10-phenanthroline	2,9-dimethyl-1,10-phenanthroline	2,2':6',2''-terpyridine
Time t	7 d	7 d	7 d
Results			

In most cases visible degradation of **MOF B** was observed, but in certain conditions we were able to obtain crystalline aggregates of degradation products. Reaction conditions used to obtain single crystals of degradation products are summarized:

Name	**[N], Solvent**	Time of crystallization *t*	Deviation from standard conditions
MOF B1	imidazole MeOH	~ 4-7 d	-
MOF B2	imidazole EtOH	~ 4-6 d	After mother liquor evacuation, 1 ml of ethanol was added to crystals and mixture is ultra-sonicated for 5 min, followed by addition of 2 eq. of **[N]** in 0.1 ml of ethanol.
MOF B3	2,2':6',2''-terpyridine EtOH	< 7 d	3 eq. of **[N]** was used instead of 2 eq.

| B1 [N]/Solv: ImH, MeOH | B2 [N]/Solv: ImH, EtOH | B3 [N]/Solv: Terpy, EtOH |
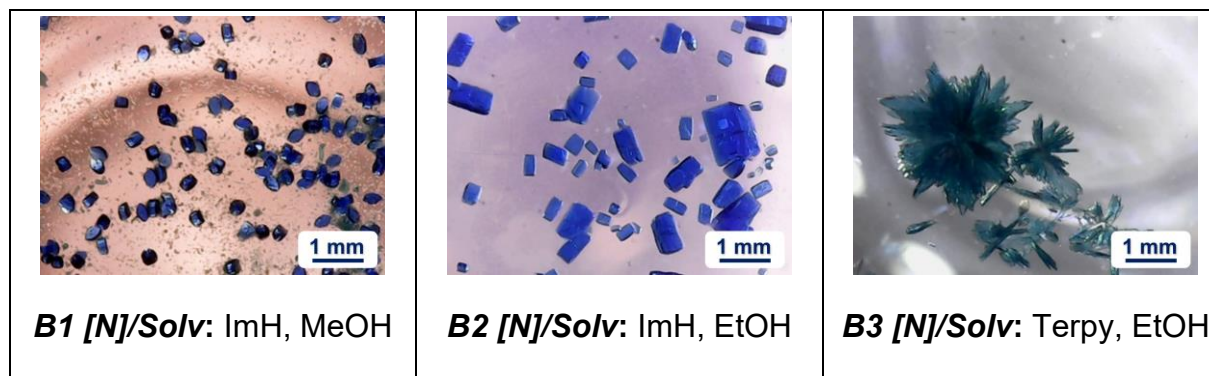
Same stability tests were carried out for **MOF C** and **MOF D** crystal samples. In most cases, crystals degraded to amorphous precipitates. Suitable for SCXRD single crystals of degradation products were obtained in following conditions:

Name	[N], Solvent	Time of crystallization t	Deviation from standard conditions
Zn-A (complex)	DMF	~ 30 - 90 d	-

[N]/Solv: 2,2'-bpy, DMF
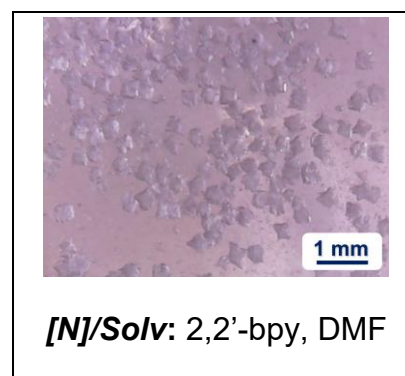
S5. Hydrolytic stability of *as-synthesized* MOFs

S5.1. Hydrolytic stability of *as-synthesized* MOF B

Conditions for hydrolytic stability test: 0.5 ml of water was added to *as-synthesized* **MOF B** in mother liquor and left intact till visible changes are observed. No significant changes in shape/integrity/size of crystals are detected in 7 d.

S5.2. Hydrolytic stability of *as-synthesized* MOF B in absence of mother liquor

Conditions for hydrolytic stability test: mother liquor of *as-synthesized* **MOF B** was evacuated and 0.5 ml of water was added, then test mixture left intact till visible changes are observed. No significant changes in shape/integrity/size of crystals are detected in 7 d. Upon mother liquor exchange with a fresh portion of solvent no change of solvent's color and crystals integrity is observed over 7 d indicating that leaching of copper (II) ions is insignificant.

Table S5.1. Hydrolytic stability of *as-synthesized* MOF B in absence of mother liquor at elevated temperatures

Conditions for hydrolytic stability test: mother liquor of *as-synthesized* **MOF B**[a] was evacuated and 1 ml of water was added, then test mixture was heated to T °C till visible changes are observed.
[a] Obtained in standard conditions for **MOF B** crystals growth in Schott Duran GL14 tubes

T, °C	Visible changes t	Result
45	-	No significant changes in shape/integrity/size of crystals are detected in 7 d
60	-	No significant changes in shape/integrity/size of crystals are detected in 7 d
100	< 3 h	Amorphization of crystals occurs in less than 3 h

S6. Activation and hydrolytic stability of *activated* MOFs.
MOFs **B4**, **B4'**, **B5** preparation

S6.1. General procedure for activation of MOFs

Sample prepared for activation (through solvent exchange procedure or initial use of low-boiling solvent suitable for supercritical drying) was dried in supercritical carbon dioxide (scCO$_2$) to obtain corresponding activated materials. Excess of solvent was lowered to the level for precipitate still was covered before drying procedure. Drying conditions: P = 250 atm., CO$_2$ flow = 2 ml / min, T = 45 °C, t $_{drying}$ = 6 - 8 h, t $_{decompression}$ = 4 h.

S6.2. Synthesis of MOF B4

Solution of **A** (0.050 g, 0.0000492 mol, 1 eq. in 2.5 ml 0.8 Pyr / 0.2 H$_2$O) was simply added to solution of Cu(OAc)$_2$·H$_2$O (0.0196 g, 0.0000983 mol, 2 eq. in 2.5 ml 0.8 Pyr / 0.2 H$_2$O) in snap cap vial (50 ml, ND28) and left intact till the end of crystal growth (2-24 h). Then reaction mixture was solvent exchanged (1st step: +2.5 ml of i-PrOH; 2nd step: +5 ml of i-PrOH; 3rd step: -5 ml of solute, +5 ml of i-PrOH, according to Table S17) over 3 days and subjected to supercritical drying. Yield after additional thermal/vacuum activation (100 °C, 20 mbar, 2 h) and subsequent storage in air (2 h)^a: 0.052 g (85 %). Anal. Calcd. for C$_{40}$H$_{64}$Cu$_2$O$_{22}$Si$_8$: C, 38.48; H, 5.17; Cu, 10.18; Si, 17.99. Found: C, 38.45; H, 5.16; Cu, 10.19; Si, 18.01.

S6.3. Synthesis of MOF B4'

Solution of **A** (0.050 g, 0.0000492 mol, 1 eq. in 2.5 ml 0.8 Pyr / 0.2 H$_2$O) was simply added to solution of Cu(OAc)$_2$·H$_2$O (0.0196 g, 0.0000983 mol, 2 eq. in 2.5 ml 0.8 Pyr / 0.2 H$_2$O) in snap cap vial (50 ml, ND28) and left intact till the end of crystal growth (2-24 h). Then reaction mixture was solvent exchanged (1st step: +2.5 ml of Pyr; 2nd step: +5 ml of Pyr; 3rd step: -5 ml of solute, +5 ml of Pyr; 4th and 5th step: -10 ml of solute, +10 ml of Pyr; according to Table S17) over 5 days and subjected to supercritical drying. Yield after additional thermal/vacuum activation (100 °C, 20 mbar, 2 h) and subsequent storage in air (2 h)^a: 0.049 g (80 %). Anal. Calcd. for C$_{40}$H$_{64}$Cu$_2$O$_{22}$Si$_8$: C, 38.48; H, 5.17; Cu, 10.18; Si, 17.99. Found: C, 38.53; H, 5.20; Cu, 10.15; Si, 17.96.

S6.4. Synthesis of MOF B5

Solution of **A** (0.050 g, 0.0000492 mol, 1 eq. in 2.5 ml MeOH) was simply added to solution of Cu(OAc)$_2$·H$_2$O (0.0196 g, 0.0000983 mol, 2 eq. in 2.5 ml MeOH) in snap cap vial (5 ml, ND18) and left intact till the end of precipitation (2-24 h). Then reaction mixture was subjected to supercritical drying.^{b} Yield after additional thermal/vacuum activation (100 °C, 20 mbar, 2 h) and subsequent storage in air (2 h)^a: 0.058 g (95 %). Anal. Calcd. for C$_{40}$H$_{64}$Cu$_2$O$_{22}$Si$_8$: C, 38.48; H, 5.17; Cu, 10.18; Si, 17.99. Found: C, 38.50; H, 5.18; Cu, 10.17; Si, 17.97.

^{a} After this treatment, the solvate molecules/ligands at the Cu-centers are replaced by water molecules ([Cu]·3H$_2$O)
^{b} It should be noted that color of freshly obtained **B5** can vary from a deep and rich shade of green with a light gray-blue undertone to light, shiny, grayish-green, cool color with metallic effect but it has no significant effect on color change process of **B5**

S6.5. Hydrolytic stability of *activated* materials

Conditions for hydrolytic stability test: 0.5 ml of water was added to **B4** or **B5** (10 mg) and left intact till visible changes are detected. No wetting of activated sample occurs, in case of **B5** sample floats on surface of liquid. These results correspond to aforementioned results of hydrolytic stability tests of *as-synthesized* MOFs.

S6.6. Environmental stability of B5

Sample of thermally activated (100 °C, 20 mbar, 2 h) and subsequently stored in air (2 h) **B5** in vial was introduced into environmental chamber for 4-8 hours. Humidity (from 20 to 90% RH) and temperature (from 30 to 70 °C) were varied over course of the test. No significant weight gain in comparison with starting **B5** loading was detected even in most harsh conditions (90% RH, 70 °C). Sample was reactivated (100 °C, 20 mbar, 2 h), stored for 2 h in air and analyzed using IR and PXRD methods (*see below*, Figures S7.9-7.10 and Section S11.2, Supp. Inf.).

S7. Properties of activated materials

Section S7.1

Table S7.1.1. Bulk density and surface characteristics of activated materials B4 and B5

Supercritical CO_2 activation procedure is shown in **S6.1**. Further thermal activation was applied to evaluate efficiency of $scCO_2$ drying.

Mat.	Reaction solvent	Exchange solvent	Drying (T °C)	Additional thermal activation	Bulk density, g/cm^3	S_{BET}, m^2/g
B4	Pyr / H$_2$O	i-PrOH	scCO$_2$	-	0.28	15[a]
	Pyr / H$_2$O	i-PrOH	scCO$_2$	20 mbar, 200 °C, 2 h	0.32	16[a]
B4'	Pyr / H$_2$O	Pyr	scCO$_2$	-	0.25	7[a]
B5	MeOH	-	scCO$_2$	-	0.011	~ 200[a]
	MeOH	-	scCO$_2$	20 mbar, 100 °C, 2 h	0.015	~ 200-300[a]
	MeOH	-	scCO2	20 mbar, 200 °C, 2 h	0.013	~ 200-300[a]
	MeOH	-	scCO$_2$	Dynamic vacuum, 200 °C, 6 h	0.01	~ 350[b]

[a] S_{BET} was estimated using nitrogen sorption one-point analysis on Sorbi MS device

[b] S_{BET} surface area was estimated using Top 200 Surface Area and Pore Size Analyzer (*see below*, Section S15, Supp. Inf.)
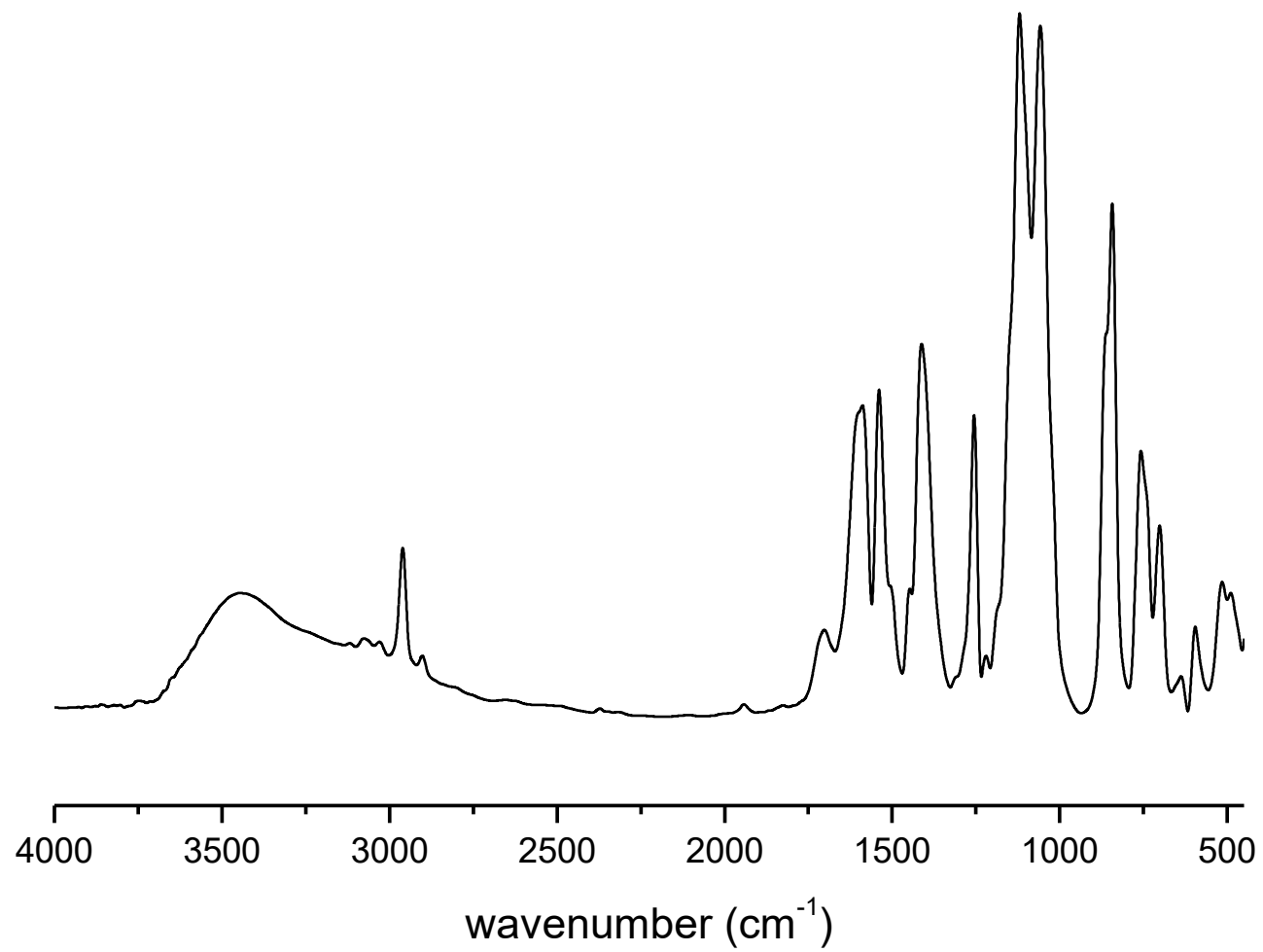
Figure S7.1.1. IR of B4
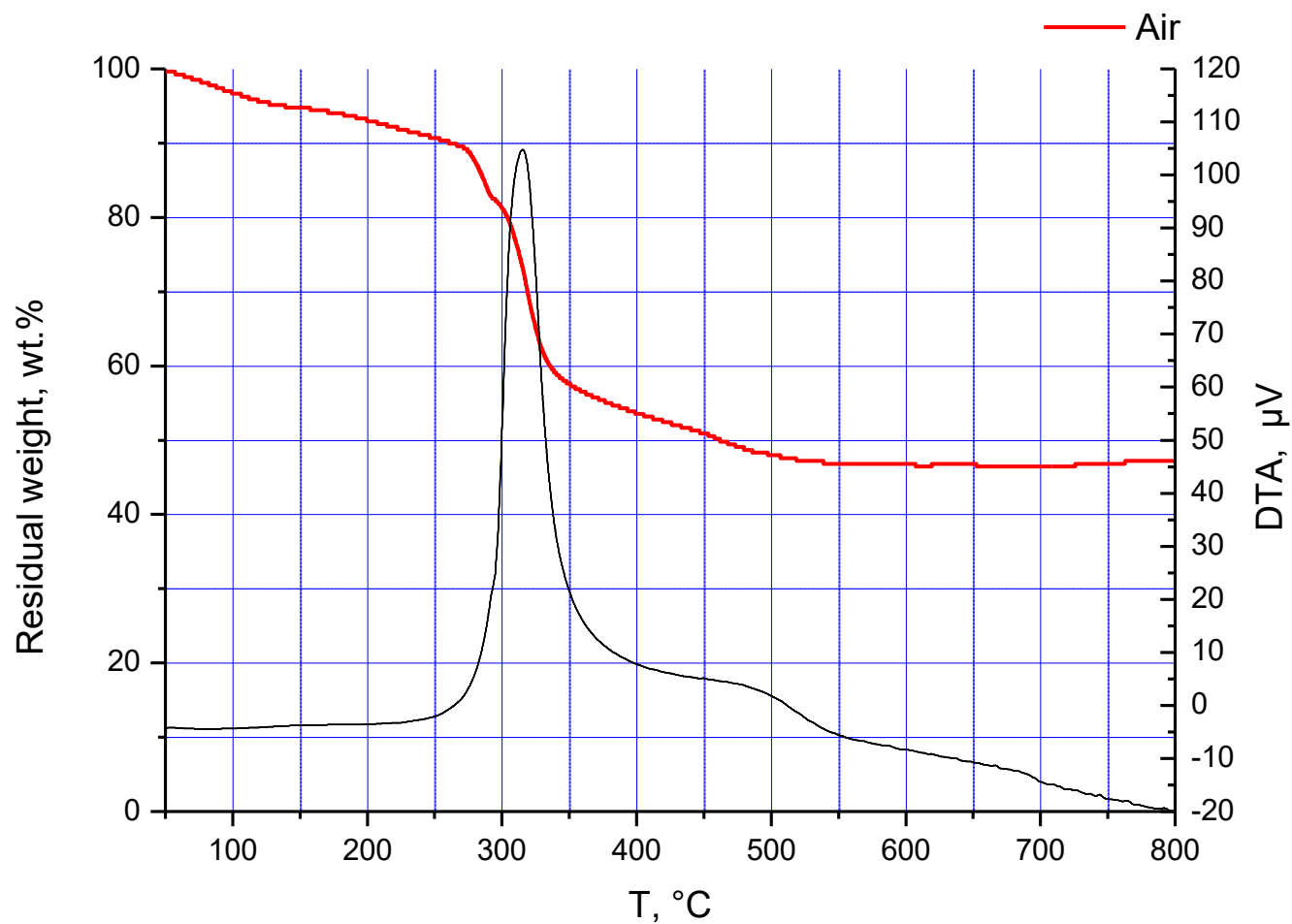
Figure S7.1.2. TGA (Air) of B4

Weight loss up to ~270 °C corresponds to water and residual isopropanol molecules in coordination sphere of Cu-SBU. Thermal decomposition of material starts at ~270 °C as it can be observed via weight loss on TGA graph and thermal effect on DTA graph.
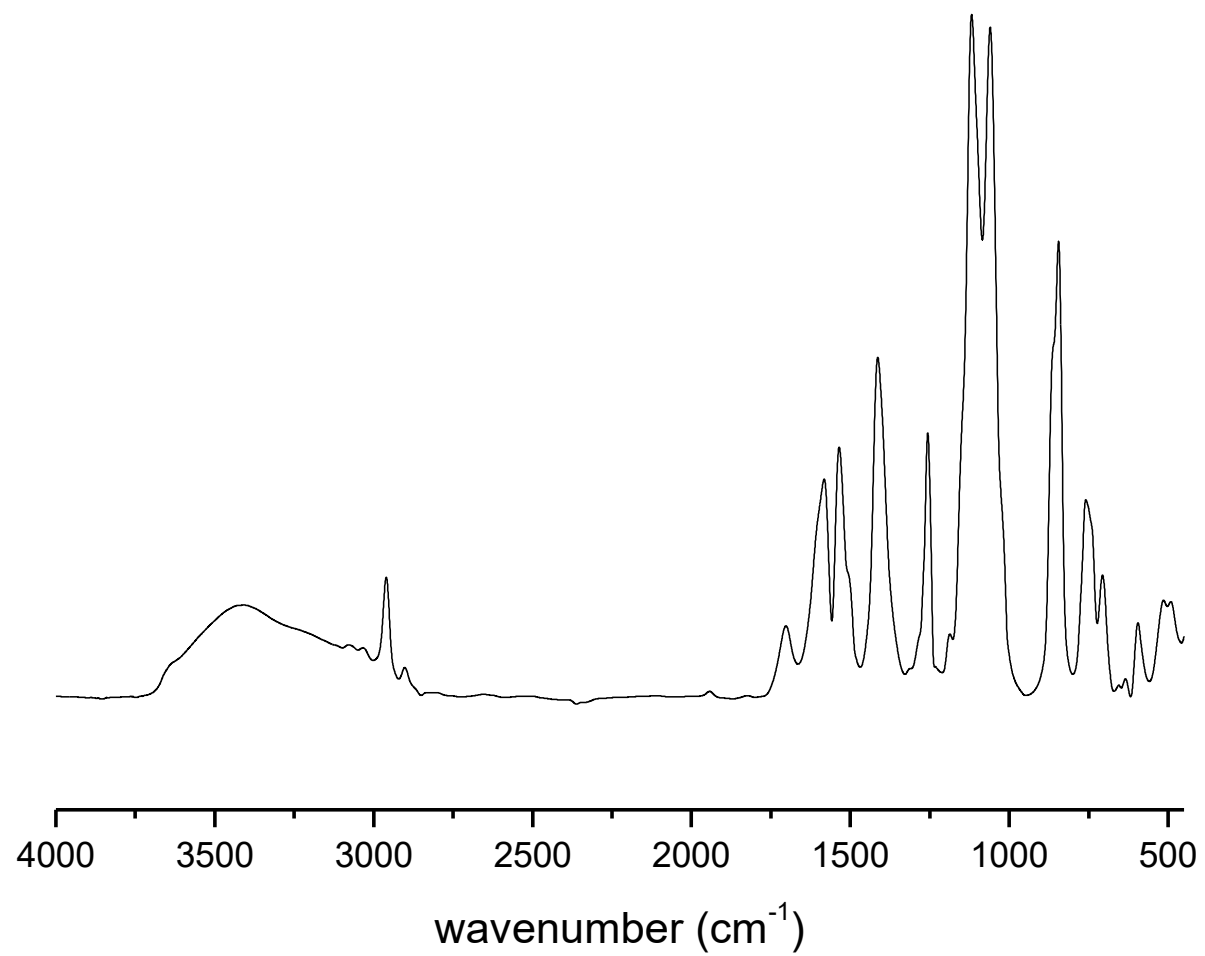
Figure S7.1.3. IR of B4'
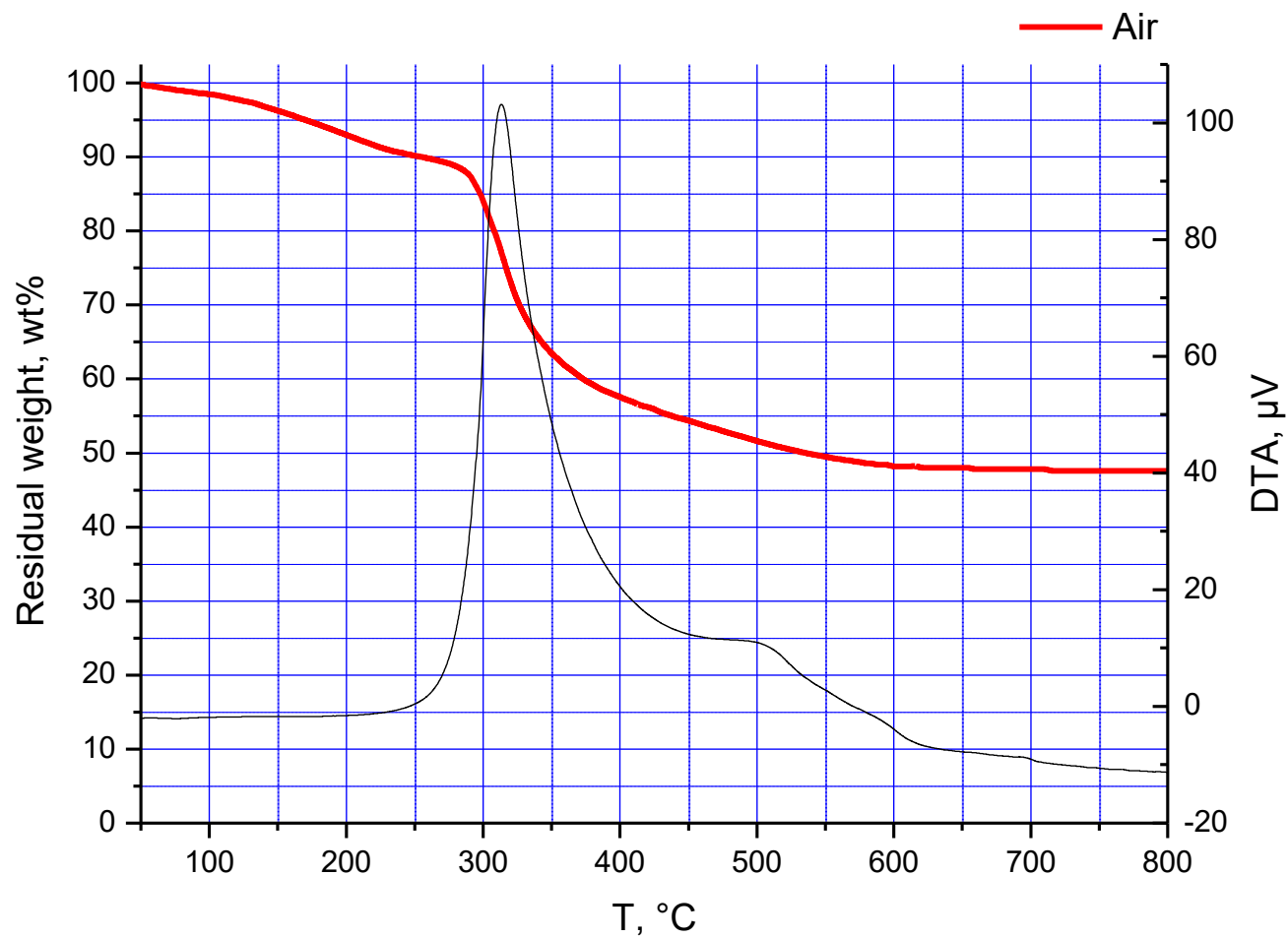
Figure S7.1.4. TGA (Air) of B4'

Weight loss up to ~270 °C corresponds to water and residual pyridine molecules in coordination sphere of Cu-SBU. Thermal decomposition of material starts at ~270 °C as it can be observed via weight loss on TGA graph and thermal effect on DTA graph.
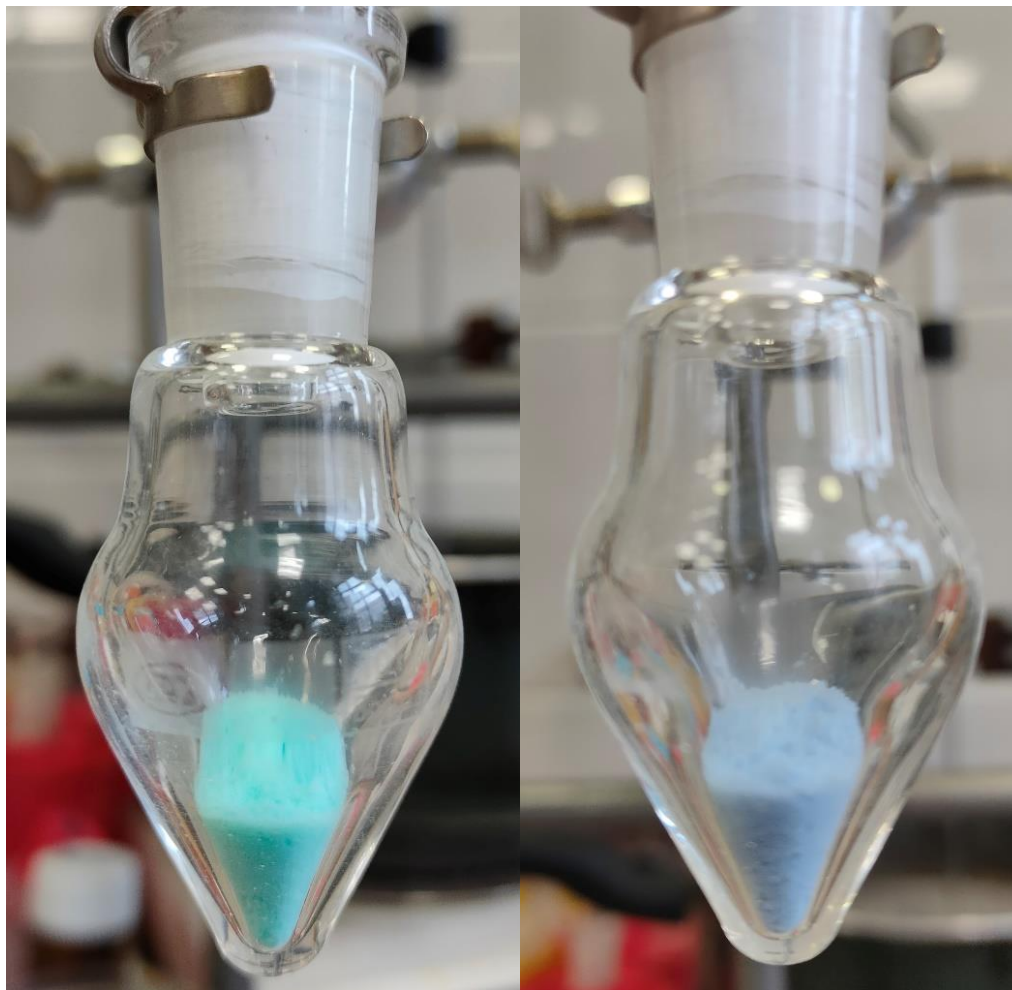
Figure S7.1.5. Color change of B5 – activated by scCO$_2$ (left) and after additional thermal activation (100 °C, 20 mbar, 2 h) (right)
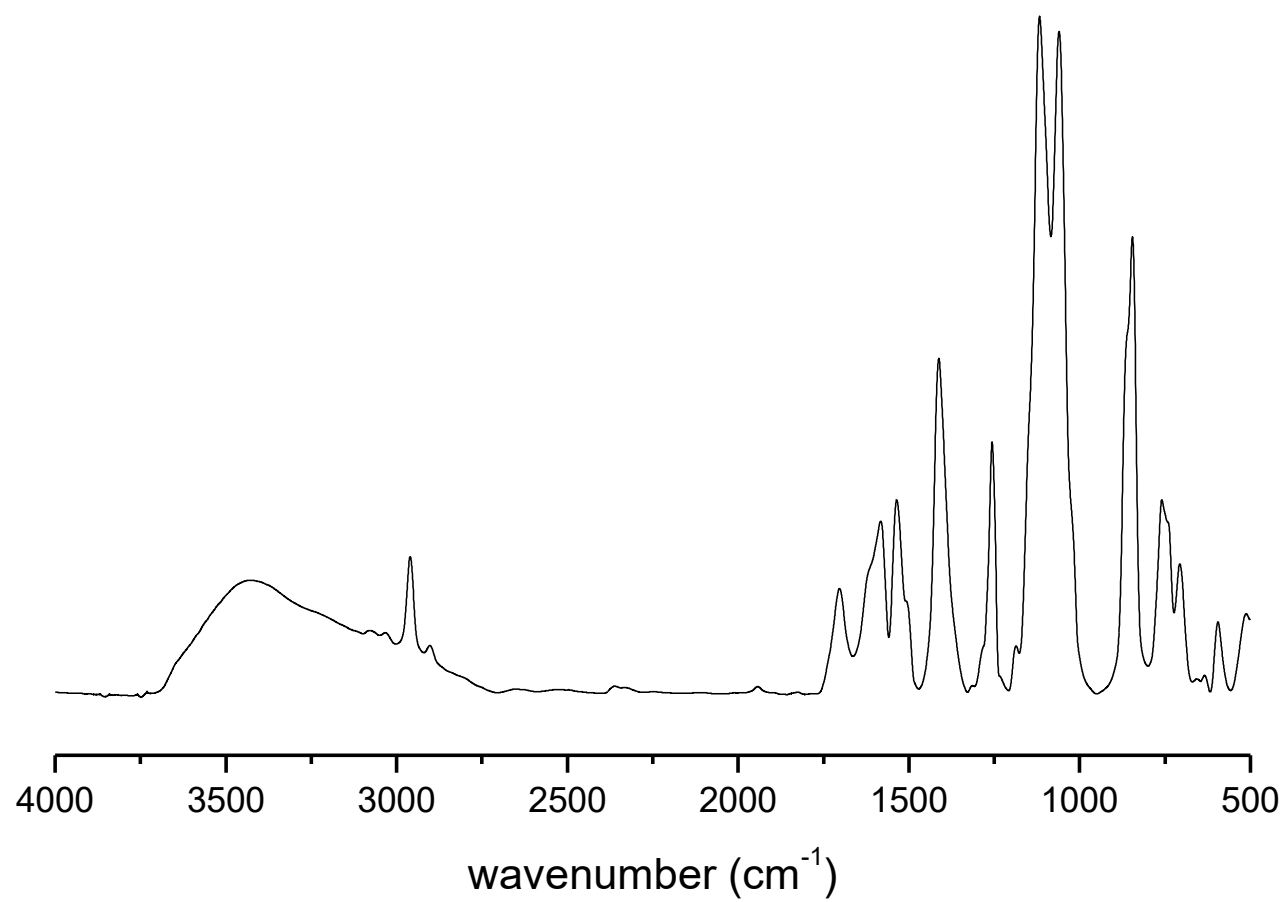
Figure S7.1.6. IR of B5
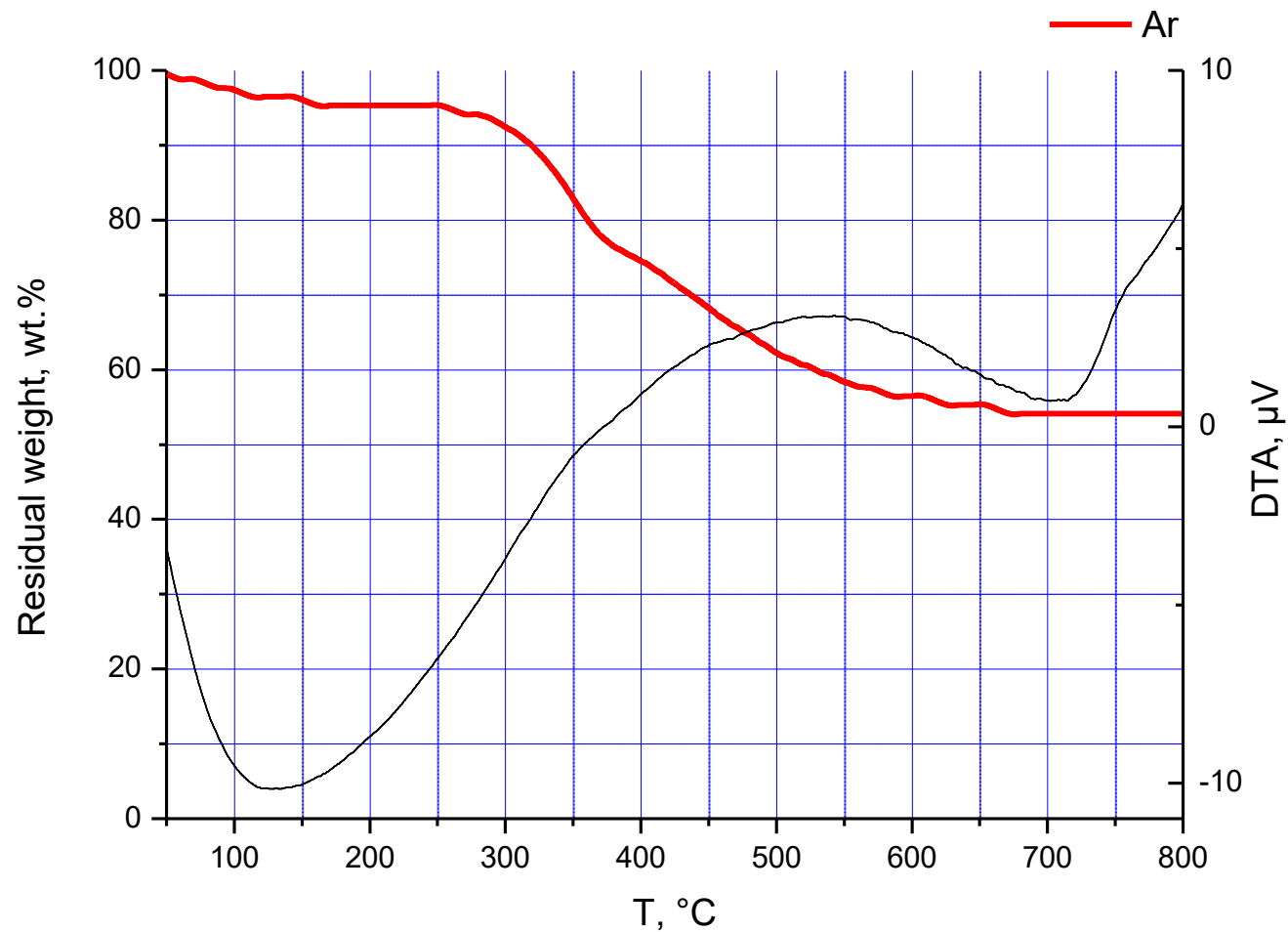
Figure S7.1.7. TGA (Ar) of B5

Wavy anomaly on graph can be attributed to the dusty nature of **B5** powder emerging in the gas flow of TG device. Weight loss mainly up to ~160 °C corresponds to water and residual methanol molecules in coordination sphere of Cu-SBU. Thermal decomposition of material starts at ~300 °C as it can be observed via weight loss on TGA graph.
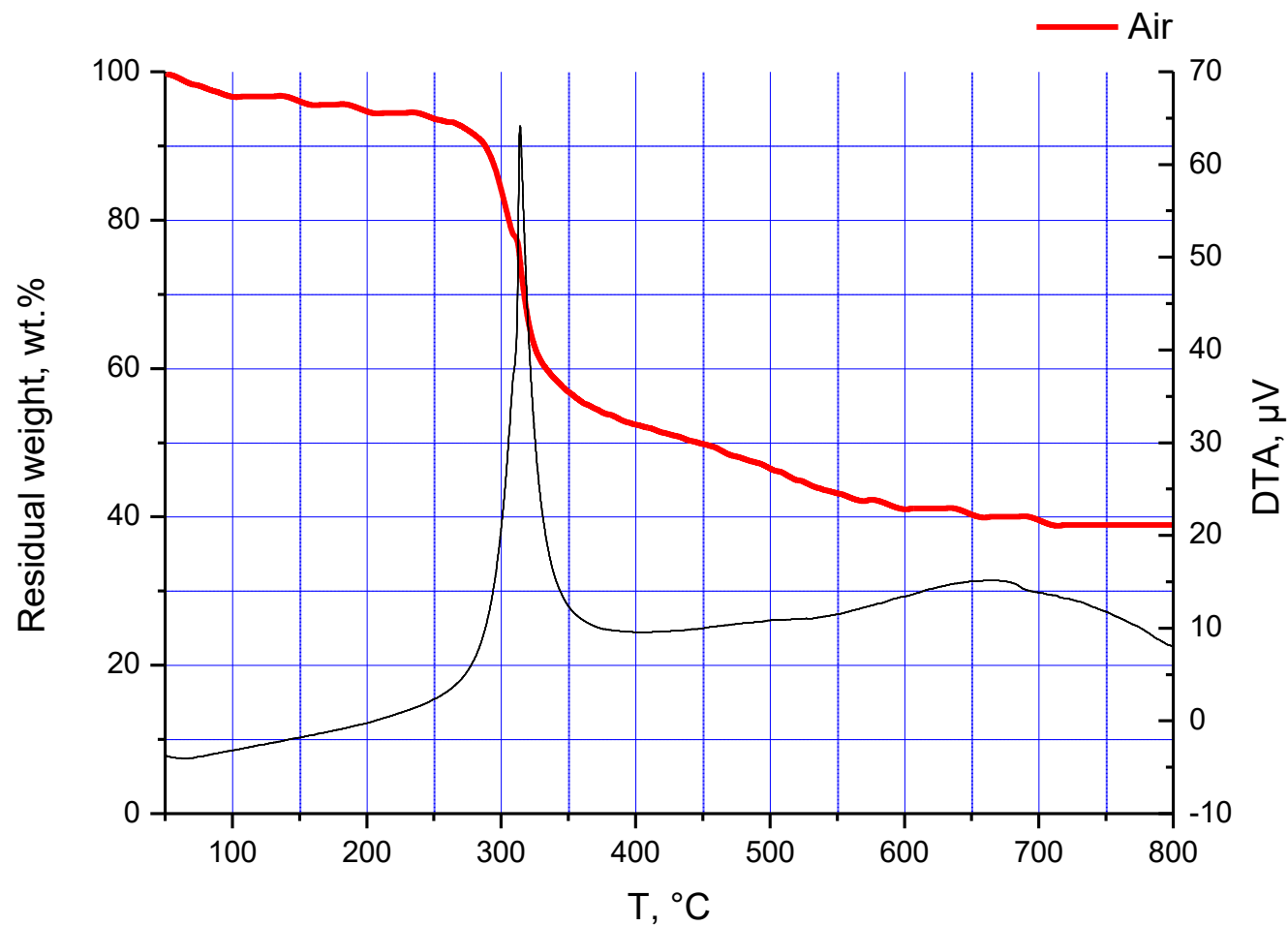
Figure S7.1.8. TGA (Air) of B5

Wavy anomaly on graph can be attributed to the dusty nature of **B5** powder emerging in the gas flow of TG device. Weight loss mainly up to ~160 °C corresponds to water and residual methanol molecules in coordination sphere of copper. Thermal decomposition of material starts at ~290-300 °C as it can be observed via weight loss on TGA graph and thermal effect on DTA graph.
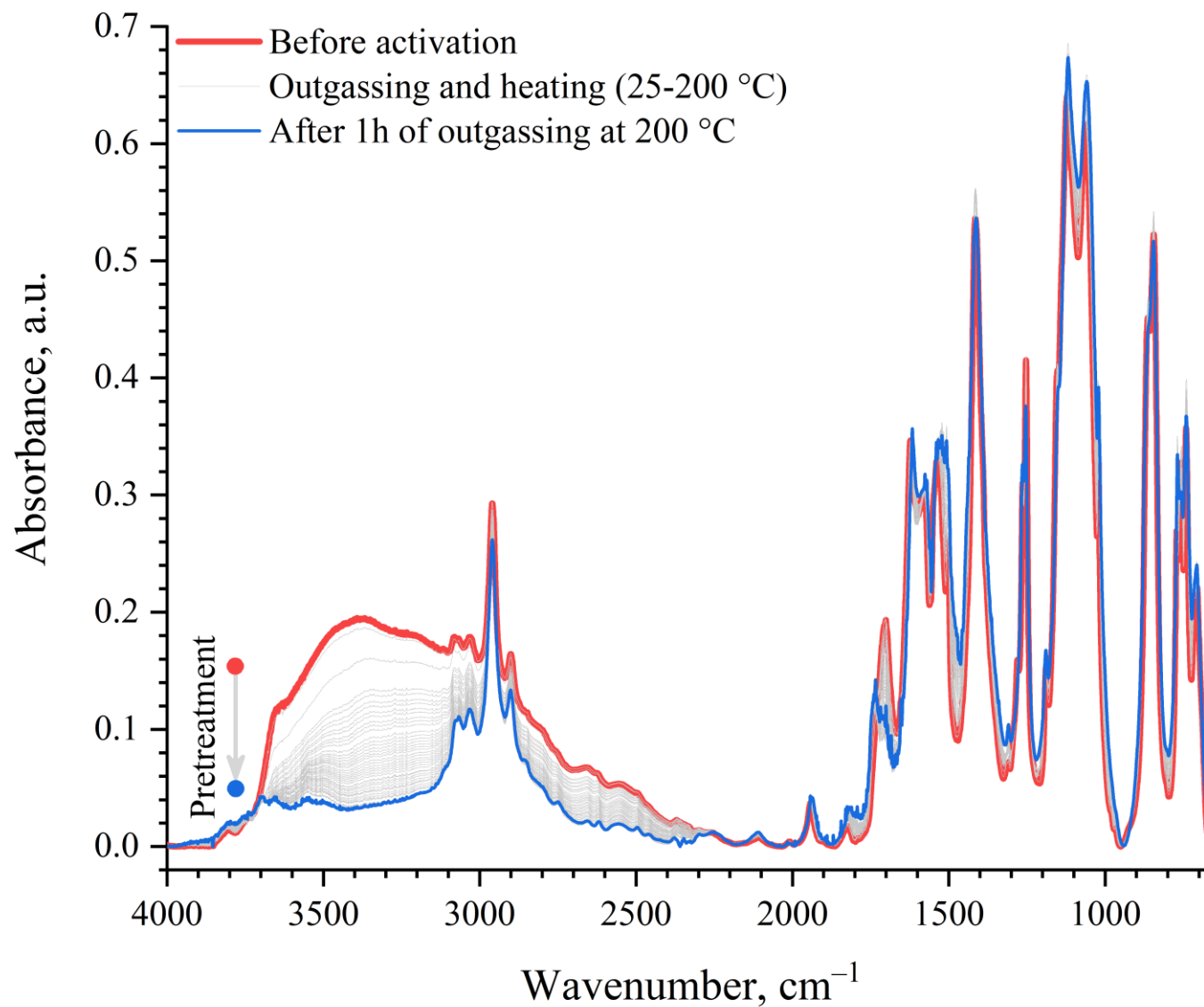
Figure S7.1.9. IR studies of B5 activation dynamics

To prevent sample displacement during vacuuming, 18 mg of the sample was mixed with 18 g of KBr. The treatment procedure was as follows: the sample was heated from room temperature to 200 °C at a ramp rate of 5 °C/min, then it was outgassed for 60 min, and cooled back to room temperature.
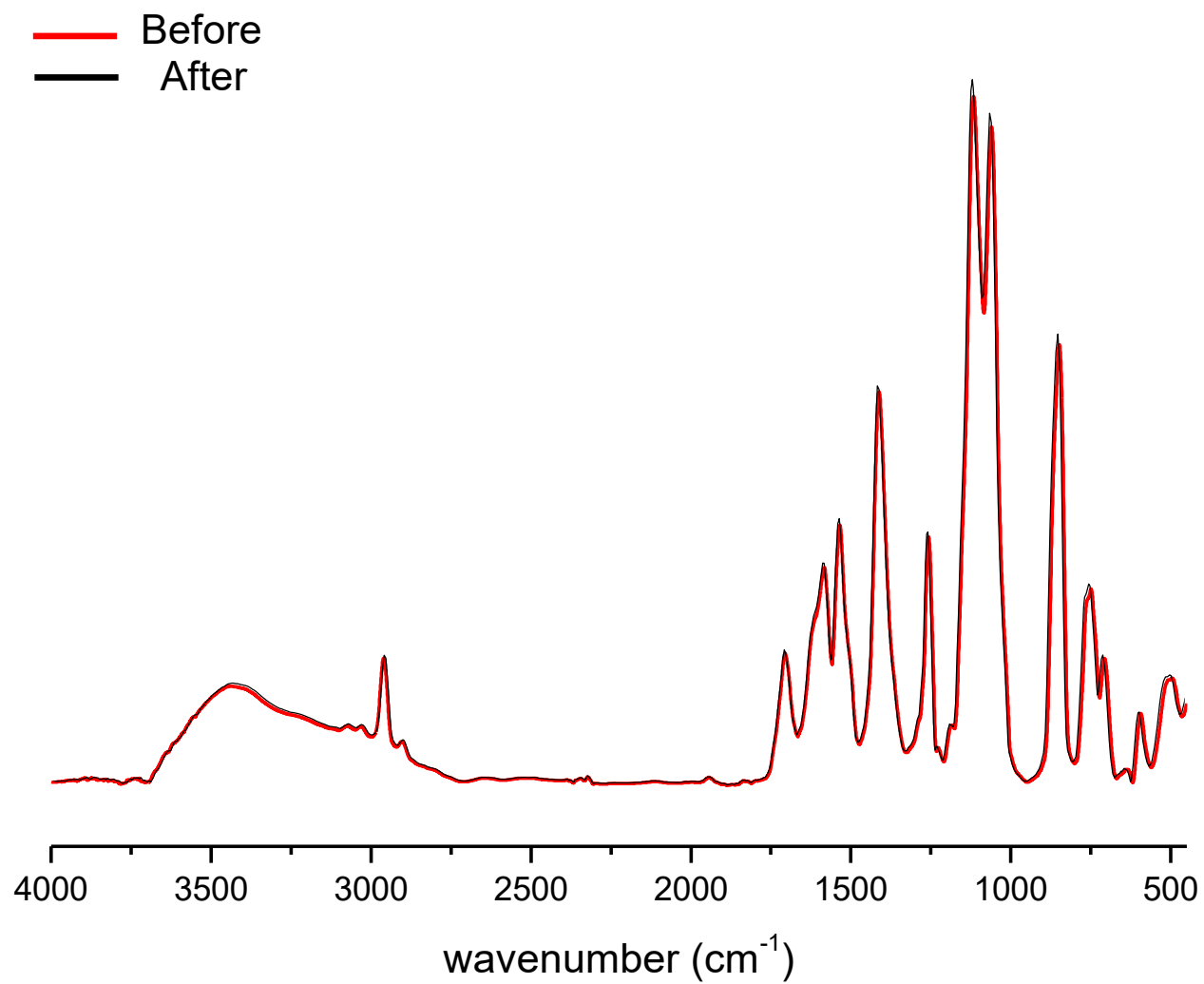
Figure S7.1.10. IR of B5 before and after environmental chamber

Both samples were thermally activated (100 °C, 20 mbar, 2 h) and subsequently stored in air (2 h) prior to IR experiment to negate impact of water excess.
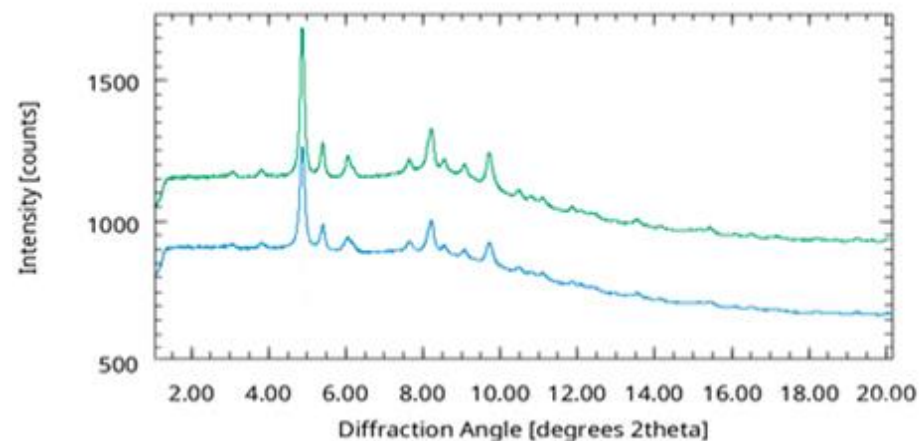
Figure S7.1.11. Comparison of PXRD patterns of B5 before (green) and after environmental chamber (blue)

Both samples were thermally activated (100 °C, 20 mbar, 2 h) and subsequently stored in air (2 h) prior to PXRD experiment to negate impact of water excess. Blue PXRD pattern corresponding for experiment in environmental chamber with the highest relative humidity (RH = 90%).

Section S7.2

Table S7.2.1. The Effect of Reduced Pressure on Color Change of B5 at Room Temperature
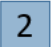
Conditions of experiment: the pressure in the vessel containing 10 mg of the activated by scCO$_2$ drying **B5** was sequentially reduced (100 mbar per step, interval between steps ~15 min) using rotary evaporator (bath temperature 30 °C) until change of color was clearly detected.

Gas	Color change gradient / pressure							Comments / Result
Air	1000-900 mbar	900-800 mbar	800-700 mbar	700-600 mbar	600-500 mbar	500-400 mbar	400-300 mbar	The most contrasting color change can be determined visually by bare eye at 300 mbar

Rapid color change of **B5** sample (5-10 seconds) is observed when pressure is lower than 200 mbar.

Table S7.2.2. The Effect of Temperature on Color Change of B5. Comparison with HKUST-1

Conditions of experiment: sealed flask containing 10 mg of the activated by scCO$_2$ drying **B5** (**1**) was heated using oil bath at corresponding temperature for 2 minutes (**2**). **B5** sample can withstand more than 60 cycles of heating and atmospheric water sorption (RH = 20%) without significant loss of color change ability.

T, °C	B5 color before (**1**) / after (**2**)	Comments / Result
60	[1] [2]	-
70	[1] [2]	-
80	[1] [2]	Color change of **B5** can be detected after 5-10 seconds of heating. Saturation of B5 color is reached.
90	[1] [2]	-
100	[1] [2]	-

HKUST-1 upon heating up to 150-200 °C (at 1 atm) changing its color to bright violet in 0.5–1 h. Under reduced pressure (1-5 mbar at r.t) same color change is not observed. HKUST-1 was synthesized using previously reported method: M. Schlesinger, S. Schulze, M. Hietschold, M. Mehring, Microporous and Mesoporous Materials, 2010, 132(1-2), 121-127 (Entry 2.2.4).

Table S7.2.3. The Effect of Atmosphere Composition on Color Change of (activated) B5

Conditions of experiment: the pressure in the evacuated vessel containing 10 mg of the activated by both scCO$_2$ drying and thermal activation (200 °C, 20 mbar, 2 h) **B5** (**1**) was brought to atmospheric pressure by immersing the sample in a gas atmosphere using balloon filled with the corresponding gas. Sample then left intact for 2-4 hours (**2**).
[a] sample was immersed in flow of dry argon for 2-4 hours

Gas	Color before (**1**) / after (**2**)	Comments / Result
Ar (dry)	1 2	No significant change of color is detected
Ar (dry)[a]	1 2	No significant change of color is detected
O$_2$ (dry)	1 2	No significant change of color is detected
CO (dry)	1 2	No significant change of color is detected
CO$_2$ (dry)	1 2	No significant of color is detected
C$_2$H$_2$ (wet, <1 wt% of water)	1 2	After sample was immersed in gas atmosphere, the top layer of sample rapidly changed its color from **1** to **2**. Color gradient from **1** to **2** is observed throughout the entire volume after 1 day of experiment. Partial color change in excess of acetylene in presence of water can be referred to water adsorption by the activated material.

Table S7.2.4. The Effect of Atmosphere Composition on Color Change of (not activated) B5

Conditions of experiment: 10 mg of the activated by scCO$_2$ drying **B5** (**1**) sample was immersed in atmosphere of corresponding gas. Then color change of material was investigated (**2**).
[a] color change was observed after S$_{BET}$ nitrogen sorption test.
Test cycle consists of:
   A) Gas composition reveal (N$_2$ $P/P_0 \sim$ 9-20%, 1 atm)
   B) Nitrogen adsorption (-195 °C, few minutes, gas flow)
   C) Nitrogen desorption (-80 °C, few minutes, gas flow)
[b] sample was immersed in flow of dry gas for 15-20 minutes
[c] sample was immersed in flow of dry gas for 2-4 hours, then back to atmosphere; cycle was repeated for 2-3 times

Gas	Pressure	Color before (**1**) / after (**2**)	Comments / Result
N$_2$/He (dry)[a]	1 atm	1 2 3	After sample was immersed back in air atmosphere at r.t., material rapidly changed its color back to the original (**3**)
N$_2$ (dry)[b]	1 atm	1 2	Color change (from **1** to **2**) is barely observed
Ar (dry)[b]	1 atm	1 2	Color change (from **1** to **2**) is barely observed
O$_2$ (dry)[b]	1 atm	1 2	Color change (from **1** to **2**) is barely observed
Ar (dry)[c]	1 atm	1 2	Color gradient (from **1** to **2**) is observed; in each further cycle color gradient shifts towards pristine color (**1**), indicating that dry gas flow less effective as reactivation method compared to thermal reactivation
O$_2$ (dry)[c]	1 atm	1 2	Color gradient (from **1** to **2**) is observed; in each further cycle color gradient shifts towards pristine color (**1**), indicating that dry gas flow less effective as reactivation method compared to thermal reactivation
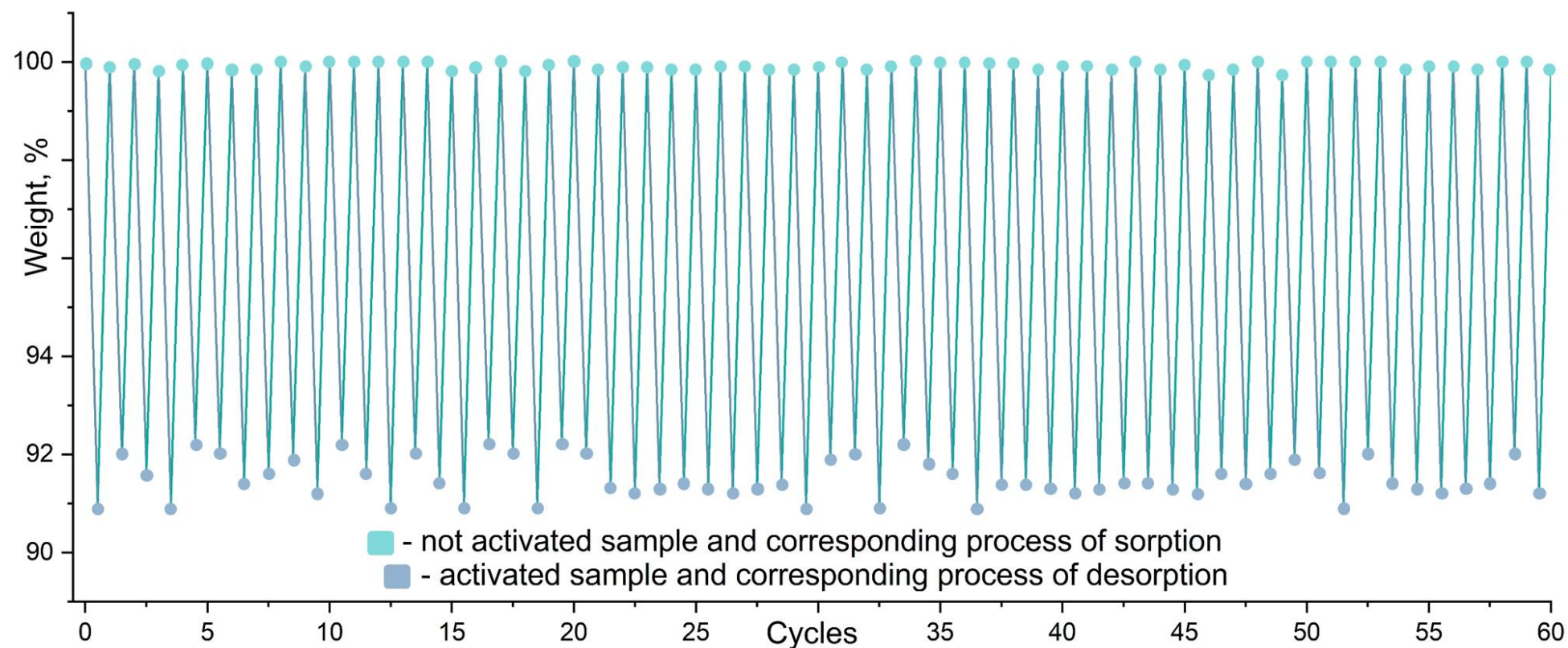
Figure S7.2.1. Weight loss dynamics of B5 sample under activation conditions.

Desorption of coordinated on Cu-centres water can be achieved by heating the sample of **B5** (50 mg, prepared by same procedure as sample for elemental analysis – Section S6, entry S6.4, Supp. Inf.) to 80 °C under atmospheric pressure. Sorption of water by activated **B5** proceeds even at low relative humidity (RH = 20%) at room temperature. **B5** can withstand more than 60 cycles of sorption-desorption with retention of its structure (confirmed using PXRD, SSNMR). Typical sorption-desorption cycle takes up about 10-15 minutes, with desorption proceeding within 30 seconds.

S8. Catalytic properties of **B5**

S8.1. Chan-Lam Coupling

Reaction scheme:

PhB(OH)$_2$ + 1.2 imidazole (HN$\diagup$N) $\xrightarrow[\text{MeOH, MS 3Å, 50 °C, 24 h}]{\text{5 mol\% B5, O}_2}$ N-phenylimidazole
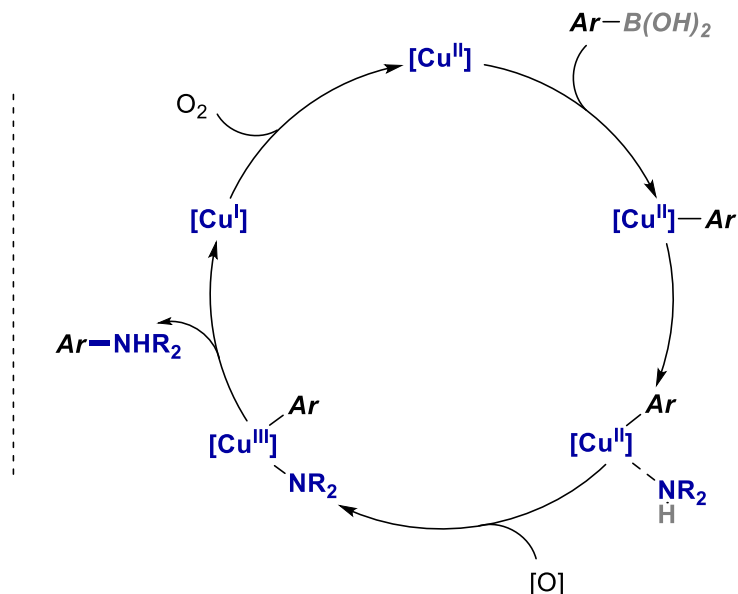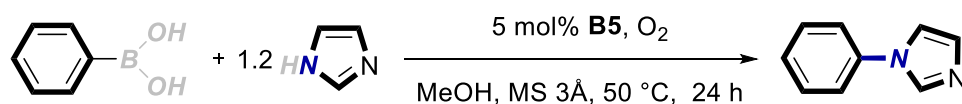
Proposed Mechanism of [Cu]-Catalyzed Chan-Lam cross-coupling. [Cu] = MOA B5

Reaction conditions: to the mixture of activated by both scCO$_2$ drying and thermal activation **B5** (0.0143 g, 0.0000125 mol, 5 mol%) and 1 ml of MeOH in 25 ml round-bottom flask were subsequently added phenylboronic acid (0.0305 g, 0.00025 mol), imidazole (0.0204 g, 0.0003 mol, 1.2 eq.), freshly activated powder of molecular sieves 3Å (0.05 g) and 1 ml of MeOH. Then reaction flask was capped with calcium chloride tube and reaction mixture was heated to 50 °C while stirring for 24 hours. Solvent was evaporated and residue was extracted with hexane (3×5 ml) under ultrasonication. Extract was filtered through PTFE Hydrophilic Syringe Filter 0.45µm and solvent was evaporated to give product as colorless viscous liquid. Yield: 0.0306-0.0324 g (85-90%).

Catalyst recycling procedure: residue (B5 and MS 3Å) was dried under vacuum (20 mbar) for 3-4 hours so the addition of fresh molecular sieves for the next catalytic cycle is not needed.

S8.2. Hydrosilane oxidation
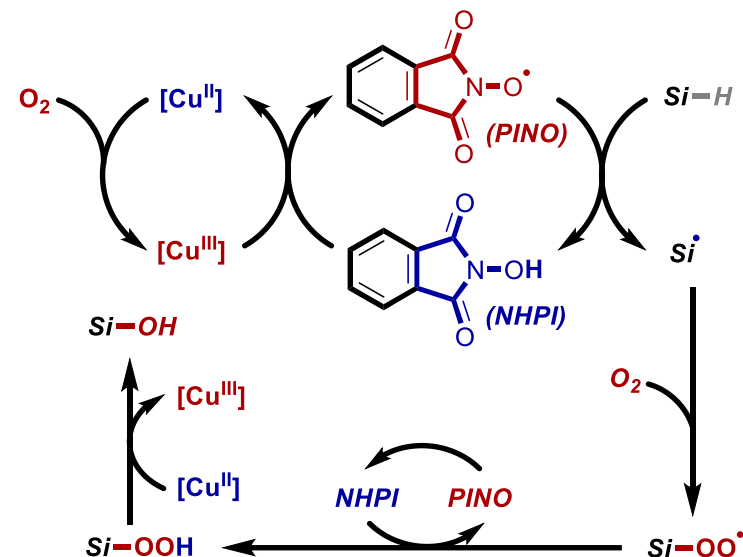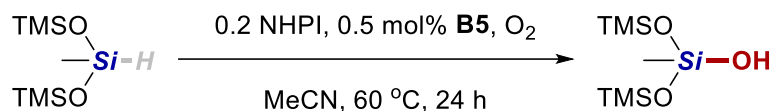
Proposed Mechanism of [Cu]-/NHPI-Catalyzed Aerobic Oxidation of Si-H to Si-OH. [Cu] = MOA B5

Reaction conditions: 1,1,1,3,5,5,5-heptamethyltrisiloxane (0.1 g, 0.00045 mol), N-hydroxyphtalimide (0.0145 g, 0.00009 mol, 0.2 eq.), activated by both scCO$_2$ drying and thermal activation **B5** (0.0026 g, 0.00000225, mol, 0.5 mol%) and 1 ml of MeCN were charged into Schott Duran GL14 tube and heated to 60 °C while stirring under static oxygen atmosphere (balloon) for 24 hours. Yield (estimated by GLC): 0.085-0.0907 g (80-85%).

Catalyst recycling procedure: reaction mixture was centrifugated and solute was decanted. Solid residue was dried under vacuum (20 mbar) for 3-4 hours.

S9. Synthesis and properties of **B5@PDMS**-composite

S9.1. Synthesis of composite B5@PDMS

$M_w \approx 5000$ Da

Reaction conditions: **B5** (0.002 g, 0.00000175 mol, 0.0117 g per 1 g of reaction mixture, ~ 1.18 wt% in reaction mixture) was added to the mixture of 1,3-divinyltetramethyldisiloxane (0.0695 g, 0.000373 mol) and hydride-containing polymer (0.101 g, 0.0000202 mol) in Eppendorf tube or 1 ml plastic syringe and stirred till the uniform distribution of MOA. Then solution of Karstedt's catalyst (0.0000146 g of [Pt], 0.0000000747 mol of [Pt], 0.85 μl of 2% [Pt] solution in *m*-xylene) was added under stirring. Reaction mixture was left intact at 30 °C till the end of crosslinking (~ 1.5 hours). In case of poor mechanical stability, sample was left intact for additional 12 hours of aging in air.

Activation/reactivation procedure: **B5@PDMS** was heated at 100 °C under vacuum (4 mbar) for 1-1.5 hours.

Water vapor treatment: vial with perforated cap containing **B5@PDMS** was subjected to water vapor treatment in isolated chamber containing water for 24 hours at r.t. Then **B5@PDMS** was reactivated following the procedure mentioned above.

Figure S9.1.1. Color change of vapor-treated (left) and reactivated (right) B5@PDMS

S9.2. Comparison of distribution of B5 and HKUST-1 in PDMS-precursor mixture

To evaluate stability of distribution of **B5** in precursor mixture, **B5**-containing reaction mixture was left intact for 2 hours before charging with catalyst. For comparison, experiment with same molal amounts of **HKUST-1** was unsuccessful because of poor dispersibility of this MOF in reaction mixture even after prolonged shaking and ultrasonication. Moreover, dispersed part of **HKUST-1** was readily precipitated in less than 5 minutes after treatment, while **B5**-containg mixture maintained even distribution of **B5** for at least 2 hours.

[a] HKUST-1 was synthesized using previously reported method and activated under vacuum (4 mbar) while heating (~ 150 °C):

M. Schlesinger, S. Schulze, M. Hietschold, M. Mehring, Microporous and Mesoporous Materials, 2010, 132(1-2), 121-127 (Entry 2.2.4).
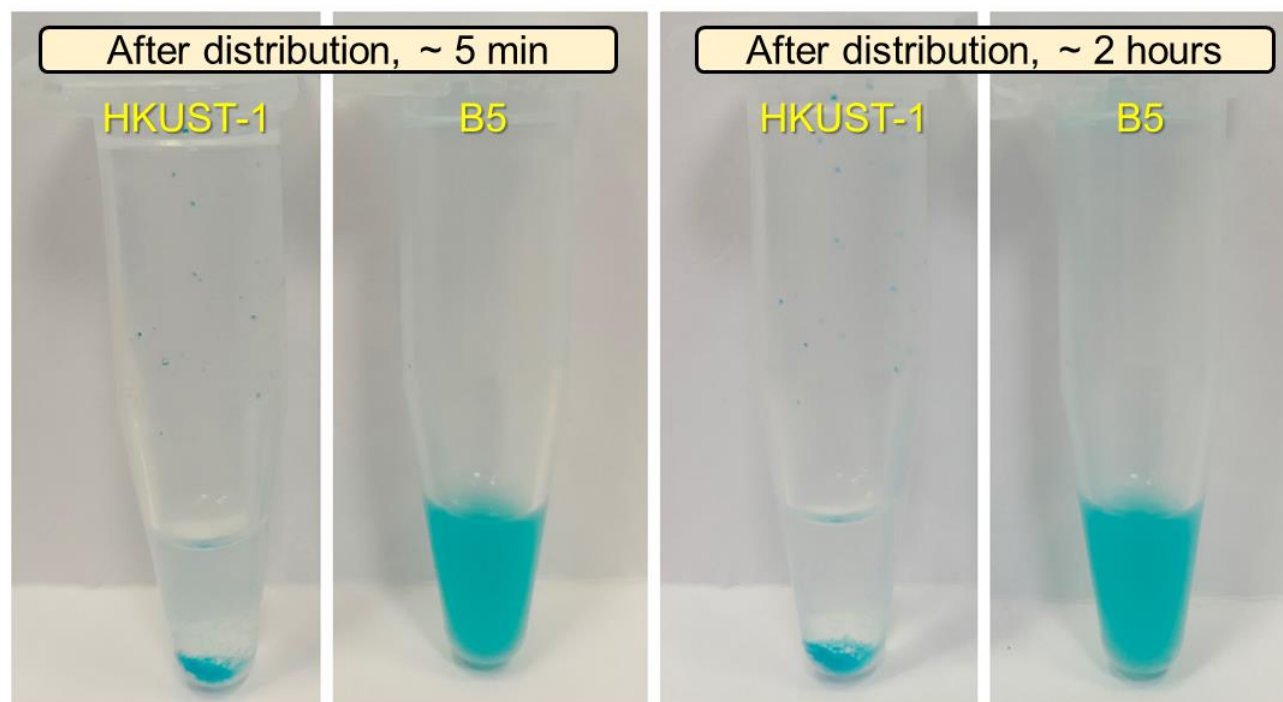
Figure S9.2.1. Time-depending distribution of B5 and HKUST-1 in B5@PDMS precursor mixture

S10. Microfluidic synthesis of MOF **B**

It is often difficult to scale up the synthesis of MOFs, especially under solvothermal conditions, due to problems associated with heat and mass transfer and control of the resulting solvent vapor pressure. Highly efficient microfluidic systems were suggested as a solution.[1-6] Since active crystal growth under solvothermal conditions begins only at elevated temperatures, the precursors are mixed at r.t. (either in a syringe or in a separate mixing unit before the droplet generator). Our attempts to implement similar schemes failed: MOF crystals began to grow at r.t. even at the stage of mixing two precursors before the droplet generator (retention time ~14 min). We suggested a principal setup for the microfluidic production of MOF **B** (Figure S10.1 *A*). It consists of a droplet generator (Figure S10.1 *B*) and a delay line (made of polytetrafluoroethylene, PTFE), which allowed crystalline MOF **B** to be obtained at r.t. within 30 min.
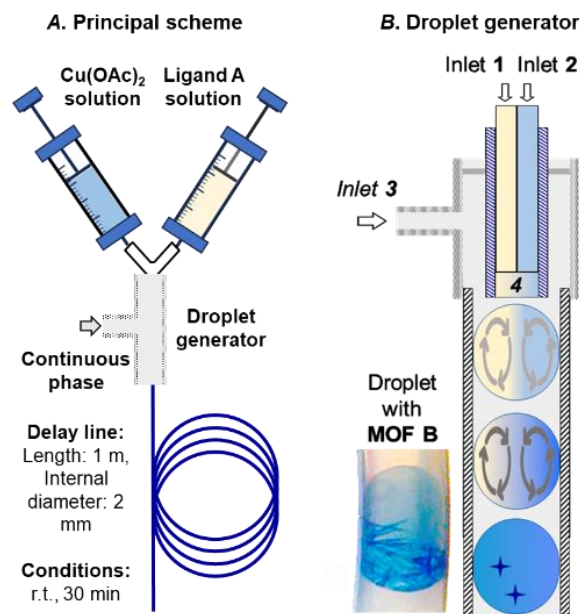
Figure S10.1. Microfluidic synthesis of MOF B in droplets. *A*. Principal scheme. *B*. Droplet generator: 1 – inlet of Ligand **A** solution, 2 – inlet of Cu(OAc)$_2$ solution, 3 – inlet of continuous phase (PDMS), 4 – mixing area

The operational principle of the droplet generator is co-flow focusing[7, 8] allowing the continuous immiscible phase (polydimethylsiloxane, PDMS) to cut the Pyr/H$_2$O phase (with reagents) from a nozzle of the tube. It was fundamentally important that ligand **A** and Cu(OAc)$_2$ were mixed in device element **4** (Figure S10.1 *B*) right before contacting with the continuous PDMS phase. Without mixing area (**4**) solutions did not mix evenly. It was also important to make device element **4** as short as possible (5-10 mm), so the retention time (~1 sec) was enough for reagents mixing, and not enough for the needle to be clogged with the crystals formed. The droplets formed in this

way were stable and reliably encapsulated the resulting MOF **B** crystals, thus preventing the delay line from clogging with the crystalline product.

Since PDMS is a non-toxic and, most importantly, highly hydrophobic and non-volatile medium, it can be easily separated from Pyr/H_2O and crystalline MOF **B** by simple decantation and can be used repeatedly. In addition, the effective heat and mass transfer in the flow regime makes it possible to scale up the process and achieve uniform results (crystal shape and size, reaction time, etc.), which is not always possible in a batch reactor.

Crystalline products in flow conditions are better be synthesized in biphase mode, so the products are encapsulated in mother liquor droplet, which flows in immiscible continuous phase. In order to develop a device for continuous-flow synthesis of MOFs in Pyr/H_2O medium at r.t. preliminary experiments were carried out to determine the most suitable continuous phase. As was shown, alkanes (hexane, cyclohexane, decane, *etc.*) and polydimethylsiloxane (PDMS) do not mix with Pyr/H_2O-phase. Synthesis of **MOF B** was used as model example (Table S6). In batch, crystals were formed in biphase mode using hexane, decane or PDMS within 0.5-1 h.

A device, consisting of mixing line, droplet generator and delay line was proposed (Figure S10.2). In such a device, solution of **A** (0.10 g, 0.0000983 mol, 1 eq. in 5 ml 0.8 Pyr / 0.2 H_2O, 0.5 ml/h flowrate) was mixed with solution of $Cu(OAc)_2 \cdot H_2O$ (0.0393 g, 0.000197 mol, 2 eq. in 5 ml 0.8 Pyr / 0.2 H_2O, 0.5 ml/h flowrate) in Y-connector and in a mixing line (PTFE tube, 1 mm internal diameter, 30 cm length, retention time 14 min). Resulting solution was injected into a flow of a continuous phase (hexane or PDMS, 1.5 ml/h flowrate). Thus generated droplets were allowed to flow in a delay line (PTFE, 2 mm internal diameter, 1 m length, 75 min retention time).
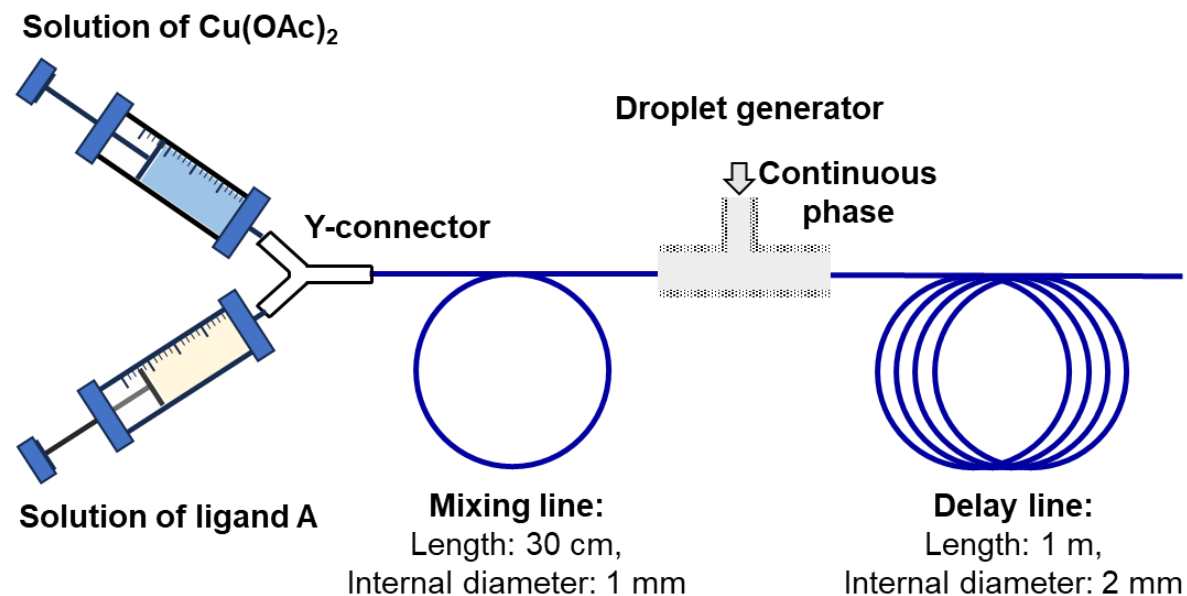
Figure S10.2. Microfluidic device for MOFs synthesis

Droplets were generated by co-flow focusing using specially assembled droplet-generator (Figure S10.3). The operational principle of the droplet generator is co-flow focusing allowing the continuous immiscible phase (hexane or PDMS) to cut the Pyr/H_2O phase (with reagents) from a nozzle of the tube. It was fundamentally important that ligand **A** and $Cu(OAc)_2$ were mixed evenly, so the reactants ratio was as in optimized batch conditions.
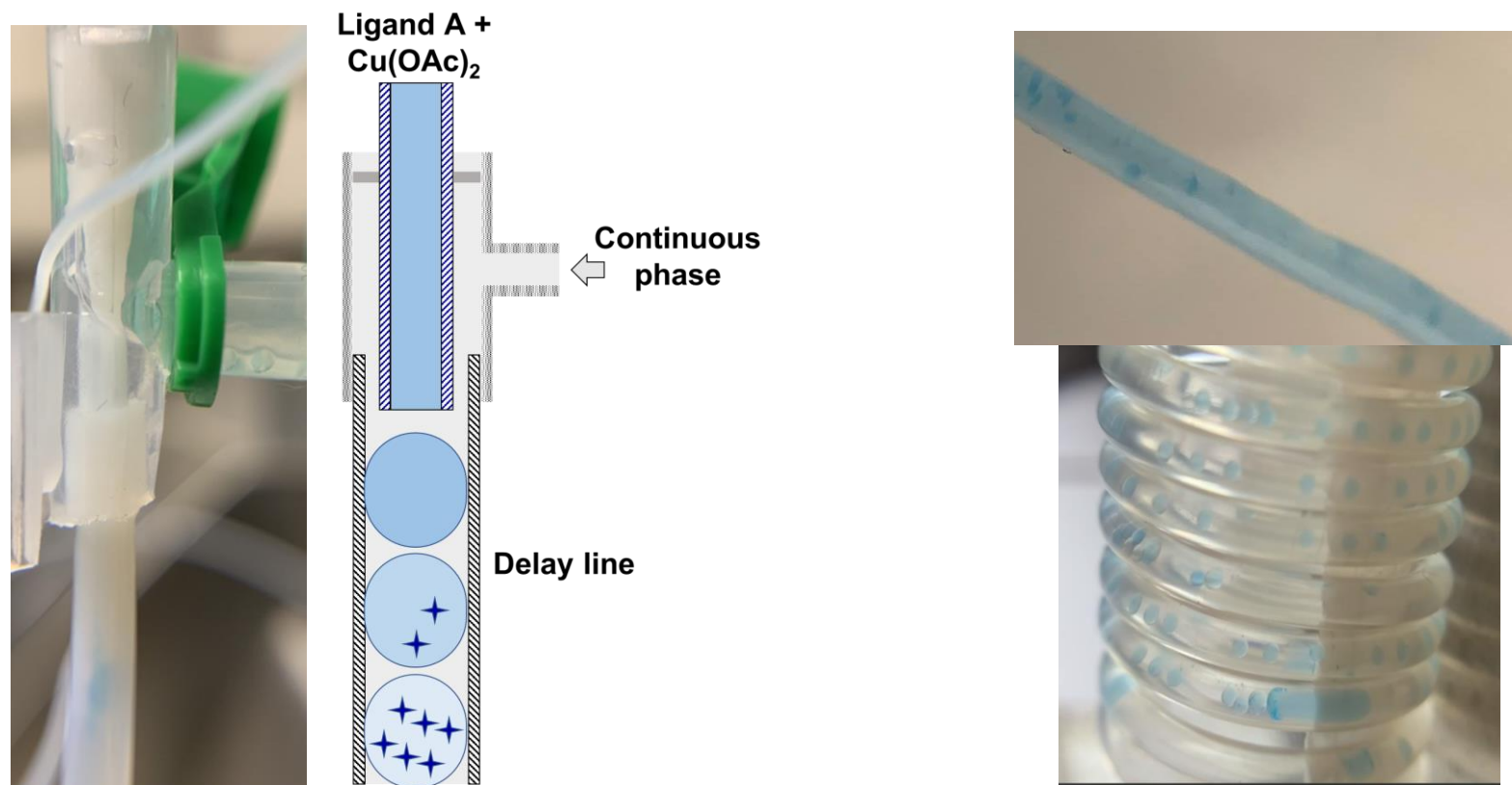
Figure S10.3. Microfluidic device for MOFs synthesis (left) and found problems (right)

Several problems were noticed (Figure 10.3, right):
- MOF crystals began to grow at r.t. even at the stage of mixing two precursors before the droplet generator (in the mixing line, Figure S10.1.);
- In hexane droplets formed were different in size and not stable. They had high tendency to aggregate.

To address these problems, PDMS was used as continuous phase and droplet generator was modified (Figure S10.4), so the mixing line was as short as possible (3-5 mm), so the retention time (~1 sec) was enough for reagents mixing, and not enough for the needle to be clogged with the crystals formed.
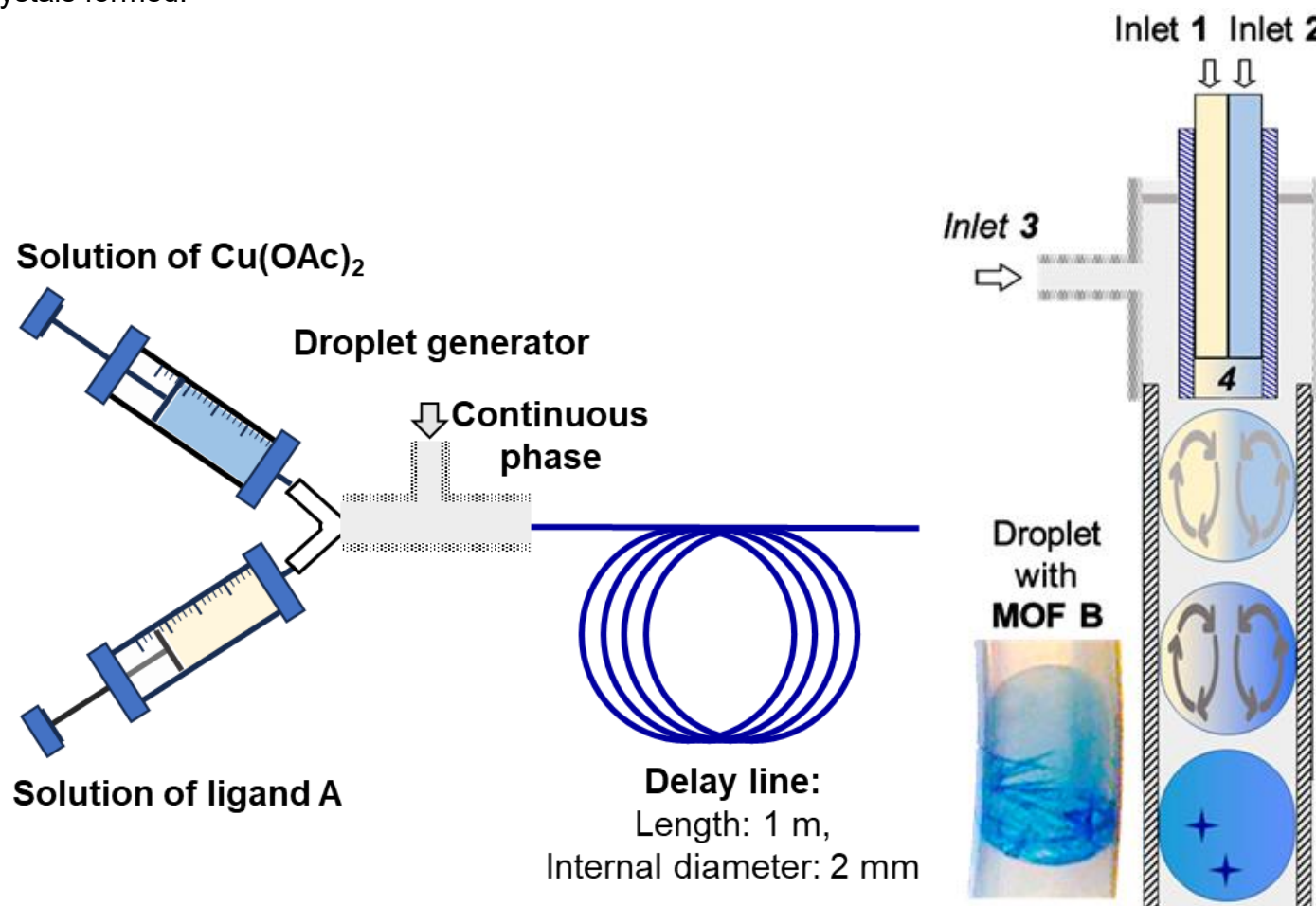
Figure S10.4. Microfluidic device for MOFs synthesis (left) and modified droplet generator (right)

This modification was successful; droplets were formed and survived the delay line. After an optimization, following conditions were selected which allowed the most efficient synthesis of **MOF B** in microfluidic device (Figure S10.5):

Ligand **A** solution flowrate: 1 ml/h

Cu(OAc)$_2$ solution flowrate: 1 ml/h

PDMS flowrate 2 ml/h

Retention time: 30 min

Room temperature

Nucleation was observed at 1/3 of the delay line (10 min retention time)

Figure S10.5. Set-up and droplets formed in optimal conditions

Up-scaled flow synthesis of MOF B4': solution of **A** (0.14 g, 0.000138 mol, 1 eq. in 7 ml 0.8 Pyr / 0.2 H_2O, 1 ml/h flowrate) was mixed with solution of $Cu(OAc)_2 \cdot H_2O$ (0.055 g, 0.000275 mol, 2 eq. in 7 ml 0.8 Pyr / 0.2 H_2O, 1 ml/h flowrate) in Y-connector and in a mixing line (PTFE tube, 1 mm internal diameter, 1 cm length). Resulting solution was injected into a flow of a continuous phase (PDMS, 2 ml/h flowrate). Thus generated droplets were allowed to flow in a delay line (PTFE, 2 mm internal diameter, 1 m length, 30 min retention time). Then reaction mixture was solvent exchanged (1st step: +7 ml of Pyr; 2nd step: +14 ml of Pyr; 3rd step: -14 ml of solute, +14 ml of Pyr; 4th and 5th step: -28 ml of solute, +28 ml of Pyr) over 5 days and subjected to supercritical drying. Yield of **B4'** was 85% (after additional thermal/vacuum activation (100 °C, <50 mbar, 3 h) and subsequent storage in air (2 h)).

References:

1.   Ameloot, R., et al., *Interfacial synthesis of hollow metal–organic framework capsules demonstrating selective permeability.* Nature Chemistry, 2011. **3**(5): p. 382-387.
2.   Kim, K.-J., et al., *High-rate synthesis of Cu–BTC metal–organic frameworks.* Chemical Communications, 2013. **49**(98): p. 11518-11520.
3.   Faustini, M., et al., *Microfluidic Approach toward Continuous and Ultrafast Synthesis of Metal–Organic Framework Crystals and Hetero Structures in Confined Microdroplets.* Journal of the American Chemical Society, 2013. **135**(39): p. 14619-14626.
4.   Balachandran, Y.L., X. Li, and X. Jiang, *Integrated Microfluidic Synthesis of Aptamer Functionalized Biozeolitic Imidazolate Framework (BioZIF-8) Targeting Lymph Node and Tumor.* Nano Letters, 2021. **21**(3): p. 1335-1344.
5.   Wu, H.-Y., et al., *Continuous and ultrafast MOF synthesis using droplet microfluidic nanoarchitectonics.* Journal of Materials Chemistry A, 2023. **11**(17): p. 9427-9435.
6.   Kim, J.-O., et al., *Large-area synthesis of nanoscopic catalyst-decorated conductive MOF film using microfluidic-based solution shearing.* Nature Communications, 2021. **12**(1): p. 4294.
7.   Dewandre, A., et al., *Microfluidic droplet generation based on non-embedded co-flow-focusing using 3D printed nozzle.* Scientific Reports, 2020. **10**(1): p. 21616.
8.   Tereshchenko, A.A., et al., *Heterophase Pt/EG-catalyzed hydrosilylation in droplet microfluidics: Spectral monitoring and efficient 3D-printed reactors.* Chemical Engineering Journal, 2024. **498**: p. 155016.

S11. X-Ray analysis

S11.1. XRD

Although connectivity of cations and anions as well as their molar ratio are similar in the majority of complexes, these form complexes of different periodicity and topology of underlying nets (**Table S11.1.1**). This fact is in accordance with effect of local coordination on topology of nets mentioned before [1]. All complexes are either 1D, or 2D coordination polymers. Topology of their underlying nets was estimated by means of ToposPro package [2] using simplification procedure described in Refs. [3]. Particularly, uncoordinated, chelate, terminal and two-coordinated bridge ligands were not taken into account. Three-, four-, five- or six-coordinated anions were simplified to the centers of gravity keeping connectivity with metal atoms unchanged. Positions of metal atoms were taken as nodes only if these are three-coordinated or act as two-coordinated linkers in 1D complexes. Two-coordinated cations in layered structures were removed from consideration keeping connectivity between anions as nodes. On **Figure S11.1.1** underlying nets of some complexes are given. Note, that several complexes realize the square lattice (**sql**) or honeycomb (**hcb**) topologies of their underlying nets which are the most widespread among layered coordination polymers [4]. At the same time, rare 3,4,5L117 topology is also observed in MOF **G**. In two of complexes metal atoms realize the "lantern" disposition or connected by a bridge water molecule, thus, their underlying nets can be additionally obtained using the "cluster representation", where a pair of atoms is taken as a node of the network. In this representation topologies of **G** and **H** complexes are, respectively, **fes** and the ladder (4,4)(0,2). The anion can also be simplified to a square or a triangle in accordance with its coordination mode; and in this case a series of augmented nets can be constructed. These are also listed in **Table S11.1.1** and demonstrated on **Figure S11.1.1**. For example, **fes** net is the augmented net for **sql** one (MOF **C**). To sum up, a variety of topologies observed in the complexes demonstrates a great potential of the tetratopic ligand **A** for construction of various coordination polymers and MOFs with different topologies.

Table S11.1.1. Topological classification of coordination polymers based on ligand A.

Datablock name	MOF	Cation	Coordination mode[a]	Topology[b]			Dimensionality
				Standard representation	Cluster representation	Augmented representation	
xe159	**B**	Cu(II)	K^4	**sql**	-	**fes**	2D
spk6161	**B1**	Cu(II)	K^4	**sql**	-	**fes**	2D
spk6212	**B2**	Cu(II)	K^4	2,4C4	-	(4,4)(0,2)	1D
spk7724	**B3**	Cu(II)	T^3	2C1	-	2,3C2	1D
co253k_a	**C**	Co(II)	K^4	**sql**	-	**fes**	2D
znmof_a	**D**	Zn(II)	K^4	2,4C4	-	(4,4)(0,2)	1D
spk9156fin	**E**	Cd(II)	K^4	2,2,2,4,4C2	-	$\{4.5^2\}^4\{5\}$	1D
spk3062	**F**	Hg(II)	K^4	**hcb**	-	3,3L3	2D
xe1552	**G**	Co(II)	K^{41}	3,4,5L117	**fes**	$\{3.4.5\}^2$ $\{3.6.7.12^2.13\}$ $\{4.12^2\}\{4.6.7\}$	2D
spk6122	**H**	Zn(II) Li(I)	T^3	3,6C1	(4,4)(0,2)	3,3,3C3	1D

[a] Coordination modes are given in terms of notation described in Ref. [5], and are depicted on **Figure S11.1.1**. [b] Notation is given in accordance with [6]. [c] In standard representation metal atoms and siloxanes are considered as nodes of a net. [d] In cluster representation metal clusters, if any, connected by bridge water

molecules are considered as one node as well as anions. [e] In augmented representation each silicon and metal atoms are considered as nodes.

M-units for B-H (see also below, Figures S11.1.2-S11.1.14)

Structure of **B** is based on the single type of mononuclear Cu-units (nodes) with square pyramidal coordination geometry. Two carboxylate groups are located in the trans positions of square base and coordinated in a monodentate mode. Two pyridine molecules are located in the trans positions of square base and one in the remaining pyramidal top position.

Structure of **B1** is based on two types of mononuclear Cu-units (nodes). The first one has square pyramidal coordination geometry. Two carboxylate groups are located in the trans positions of square base and coordinated in a monodentate mode. One pyridine and one imidazole molecules occupy remaining positions of square base and one methanol molecule occupies top pyramidal position. The second type of Cu-unit has square planar geometry. Two carboxylate groups are located in trans positions in a monodentate mode, remaining sites are occupied by one pyridine and one imidazole.

Structure of **B2** is based on three types of mononuclear Cu-units (nodes). All nodes have square pyramidal coordination geometry with different tendency to distortion towards trigonal bipyramidal form due to hydrogen bonding and disordered ligands. Square base occupied by one pyridine and one imidazole molecule in trans positions while the rest trans positions are occupied by two carboxylate fragments, coordinated in a monodentate mode. In the first type remaining top pyramidal position is occupied by water molecule. The second and the third types of node are variations of one node with different chemical occupancy. The remaining top pyramidal position in the second type is occupied by ethanol molecule with chemical occupancy 70%, in the third type remaining position is occupied by pyridine molecule with chemical occupancy 30%.

Structure of **B3** is based on two types of mononuclear Cu-units while only one can be considered as node. Both has square pyramidal geometry with terpy occupies 3 of 4 coordination sites of the base of pyramid and one carboxylate fragment in a monodentate mode occupy the top. Remaining base site is occupied either by carboxylate fragment in a monodentate mode (node) or water molecule (non-binding Cu-unit).

Structure of **C** is based on the single type of mononuclear Co-units (nodes) with octahedral coordination geometry. Two carboxylate fragments are located in the trans equatorial positions in a monodentate mode. Remaining equatorial positions are occupied by one water and one pyridine while both axial positions are occupied by two pyridine molecules.

Structure of **D** is based on mononuclear Zn-units (nodes) with tetrahedral coordination geometry. Two carboxylate fragments are coordinated in a monodentate mode while two pyridine molecules occupy remaining sites.

Structure of **E** is based on the single type of mononuclear Cd-units (nodes) with pentagonal bipyramidal coordination geometry. Two carboxylate fragments are located in the equatorial positions in a bidentate mode while remaining sites are occupied by three pyridine molecules.

Structure of **F** is based on two types of mononuclear Hg-units (nodes). The first one has trigonal bipyramidal coordination geometry with two carboxylate located at the equatorial positions in a monodentate mode while remaining sites are occupied by three pyridine molecules. The second type possesses have the same composition but has trigonal prismatic coordination geometry due to one carboxylate switching from a monodentate mode to bidentate.

Structure of **G** is based on the single type of binuclear Co-units (SBU). Both cobalt(II) in unit have the same octahedral coordination geometry and ligand composition. Two of three equatorial carboxylate fragments are bridge between cobalt(II) centers and exist in cis positions. Exo-axial and remaining equatorial sites are occupied by pyridine molecules. Endo-axial site is occupied by bridging water molecule.

Structure of **H** is based on the single type of binuclear heterometallic Zn/Li-units (SBU). Both zinc(II) and lithium have tetrahedral coordination geometry giving a rise to asymmetrical «paddle-wheel»-like SBUs. Three carboxylate fragments bridge zinc(II) and lithium. Remaining zinc(II) site is occupied by one pyridine while remaining lithium site is occupied by water molecule.
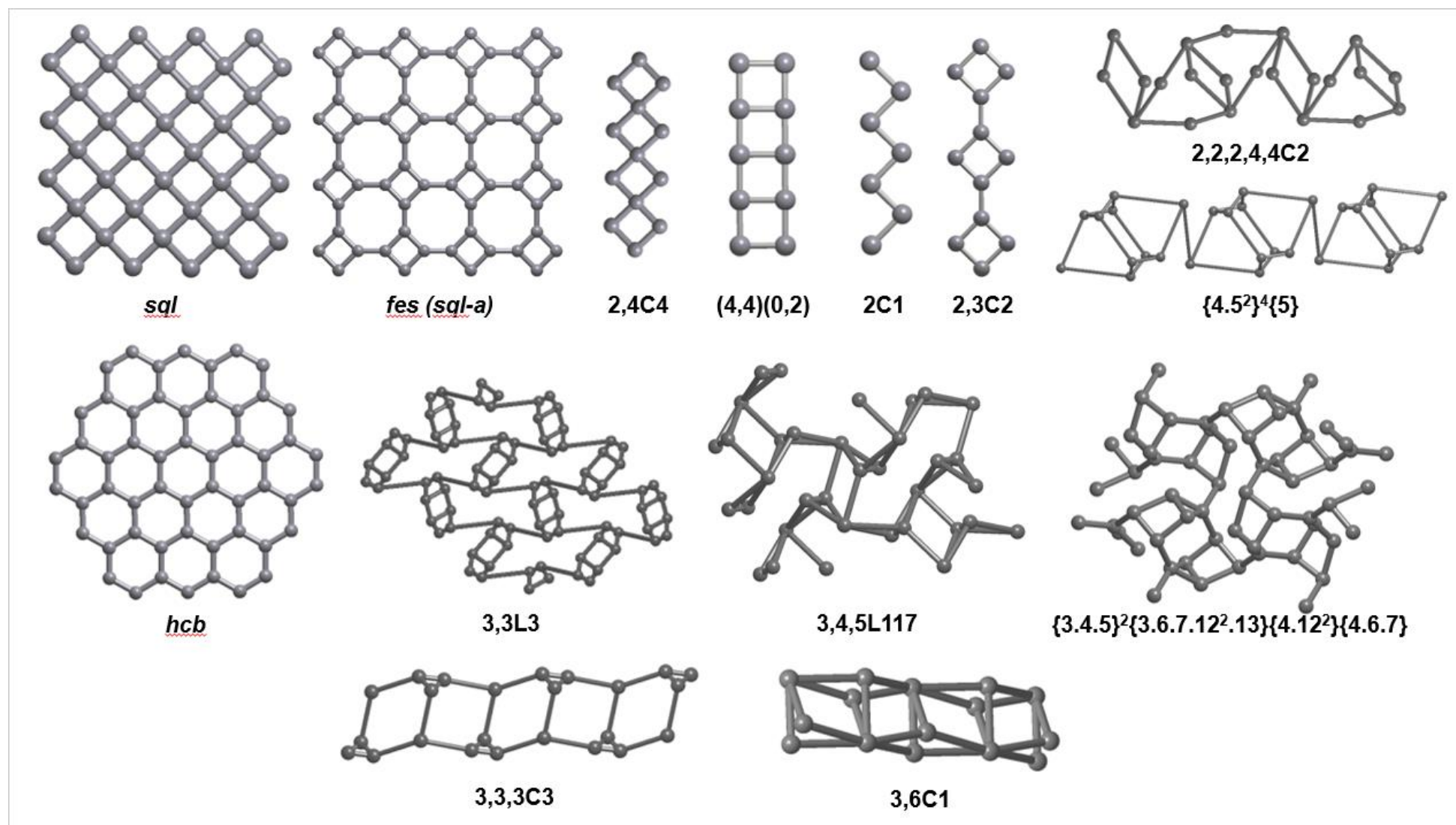
Figure S11.1.1. Motifs obtained by simplification of complexes to their underlying nets

References:

[1]. (a) Alexandrov E.V., Shevchenko A.P., Asiribc A.A., Blatov V.A. New knowledge and tools for crystal design: local coordination versus overall network topology and much more. CrystEngComm. 2015, 17, 2913-2924. (b) Zorina-Tikhonova E.N., Chistyakov A.S., Novikova V.A., Knyazev D.A., Gogoleva N.V., Blinou D.O., Efimov N.N., Dorovatovskii P.V., Kiskin M.A., Eremenko I.L., Vologzhanina A.V. Design and synthesis of copper(ii) malonates with N,N′-containing linkers. CrystEngComm, 2023, 25, 2859-2870.

[2]. Blatov V.A., Shevchenko A.P., Proserpio D.M. Applied Topological Analysis of Crystal Structures with the Program Package ToposPro. Cryst. Growth Des. 2014, 14, 7, 3576–3586.

[3]. (a) Alexandrov E.V., Shevchenko A.P., Nekrasova N.A., Blatov V.A. Topological methods for analysis and design of coordination polymers. Russ. Chem. Rev. 2022, 91 RCR5032. (b) Shevchenko A.P., Blatov V.A. Simplify to understand: how to elucidate crystal structures? Struct. Chem. 2021, 32, 507–519. (c) Alexandrov E.V., Virovets A.V., Blatov V.A., Peresypkina E.V. Topological Motifs in Cyanometallates: From Building Units to Three-Periodic Frameworks. Chem. Rev. 2015, 115, 22, 12286–12319.

[4]. Mitina T.G., Blatov V.A. Topology of 2-Periodic Coordination Networks: Toward Expert Systems in Crystal Design. Cryst. Growth Des. 2013, 13, 4, 1655–1664.

[5]. Serezhkin V.N., Vologzhanina A.V., Serezhkina L.B., Smirnova E.S., Grachova E.V., Ostrova, P. V., Antipin M.Y. Crystallochemical formula as a tool for describing metal–ligand complexes–a pyridine-2, 6-dicarboxylate example. Acta Crystallographica Section B: Structural Science, 2009, 65, 1, 45-53.

[6]. (a) O'Keeffe M., Peskov M.A., Ramsden S.J., Yaghi O.M. The Reticular Chemistry Structure Resource (RCSR) Database of, and Symbols for, Crystal Nets. Acc. Chem. Res. 2008, 41, 12, 1782–1789. (b) Blatov V.A., O'Keeffe M., Proserpio D.M. Vertex-, face-, point-, Schläfli-, and Delaney-symbols in nets, polyhedra and tilings: recommended terminology. CrystEngComm. 2010, 12, 44-48.

Table S11.1.2. Crystal parameters and refinement details for B–C

CIF Datablock	xe159	spk6161	spk6212	spk7724	co253k_a
MOF	B	B1	B2	B3	C
CCDC number	2353519	2353522	2353520	2353517	2353518
Brutto formula	$C_{150}H_{179}Cu_4N_{14}O_{35}Si_{16}$	$C_{60}H_{86}Cu_2N_4O_{18}Si_8$	$C_{61}H_{76}Cu_2N_4O_{18}Si_8$	$C_{70}H_{209}Cu_2N_6O_{18\cdot5}Si_8$	$C_{35}H_{43}CoN_3O_9Si_4$
Formula weight	3441.66	1503.2	1503.56	1783.22	821.01
Diffractometer	Bruker APEX DUO	Bruker APEX-II CCD	Bruker APEX-II CCD	Marexperts dtb goniostat	Marexperts dtb goniostat
Scan mode	ω and ϕ scans	ω and ϕ scans	ϕ and ω scans	ϕ scans	ϕ scans
Anode [Wavelength, Å], X-ray source	CuKα [1.54178] microfocus X-ray tube	MoKα [0.71073] sealed tube	MoKα [0.71073] sealed tube	synchrotron [0.7527]	synchrotron [0.9699]
Crystal Dimensions, mm	0.31 × 0.36 × 0.39	0.26 × 0.28 × 0.37	0.25 × 0.34 × 0.39	0.05 × 0.07 × 0.12	0.34 × 0.36 × 0.39
Crystal color	blue	blue	blue	blue	red
Crystal system	monoclinic	orthorhombic	monoclinic	triclinic	tetragonal
a, Å	21.8520(10)	23.0414(13)	18.463(12)	11.030(2)	17.522(3)
b, Å	18.2435(8)	20.7854(12)	12.247(6)	18.120(4)	17.522(3)
c, Å	48.809(2)	31.9741(18)	37.31(2)	23.800(5)	42.933(9)
α, °	90	90	90	93.40(3)	90
β, °	93.177(3)	90	91.77(2)	94.20(3)	90
γ, °	90	90	90	98.69(3)	90
Volume, Å³	19428.3(15)	15313.2(15)	8433.(8)	4677.5(17)	13182.(5)
Density, gcm^{-3}	1.177	1.304	1.184	1.266	0.827
Temperature, K	120	100	100	100	253
T_{min}/T_{max}	0.5327/0.7536	0.6665/0.7461	0.5963/0.7453	0.712/1.000	0.834/1.00
μ, mm^{-1}	1.978	0.744	0.676	0.718	0.882
Space group	P12$_1$/n1	Pbca	P12$_1$/c1	P$\bar{1}$	P4/ncc
Z	4	8	4	2	8
Reflections collected	160449	218326	46026	71842	96034
Independent reflections	37490	15078	16489	24797	7177
Reflections (I>2σ(I))	13245	7136	9198	16017	2933
Parameters	2013	903	886	962	254
R_{int}	0.1985	0.193	0.055	0.0893	0.1272
$2\theta_{min}$ - $2\theta_{max}$,°	4.344 - 145.400	3.536 - 52.044	3.978 - 52.152	4.504 - 61.978	4.486 - 76.982

wR$_2$ (all reflections)	0.3574	0.2504	0.2378	0.244	0.3063
R$_1$(I>σ(I))	0.1251	0.0764	0.0929	0.0797	0.1129
GOF	1.049	1.007	1.005	1.084	1.012
ρ$_{min}$/ρ$_{max}$, eÅ^{-3}	-0.7255	-0.7374	-0.5914	-1.108	-1.0906
Restraints	492	209	375	42	143

wR$_2$ (all reflections)	0.3574	0.2504	0.2378	0.244	0.3063
R$_1$(I>σ(I))	0.1251	0.0764	0.0929	0.0797	0.1129
GOF	1.049	1.007	1.005	1.084	1.012
ρ$_{min}$/ρ$_{max}$, eÅ^{-3}	-0.7255	-0.7374	-0.5914	-1.108	-1.0906

Table S11.1.3. Crystal parameters and refinement details for G–F.

CIF Datablock	xe1552	spk9156fin	znmof_a	spk6122	spk3062
MOF	G	E	D	H	F
CCDC number	2353515	2353521	2353513	2353514	2353516
Brutto formula	$C_{60}H_{74}Co_2N_4O_{17}Si_8$	$C_{143}H_{97}Cd_4N_{13}O_{33}Si_{16}$	$C_{64.5}H_{76.5}N_5O_{16}Si_8Zn_2$	$C_{65}H_{80}LiN_5O_{18}Si_8Zn$	$C_{67.5}H_{79.5}Hg_2N_{5.5}O_{16}Si_8$
Formula weight	1465.81	3424.04	1531.86	1516.37	1849.88
Diffractometer	Bruker APEX-II CCD	Marexperts dtb goniostat	Marexperts dtb goniostat	Bruker QUEST	Bruker APEX-II CCD
Scan mode	ω scans	φ scans	φ scans	ω and φ scans	ω and φ scans
Anode [Wavelength, Å]	MoKα [0.71073] sealed X-ray tube	synchrotron [0.7527]	synchrotron [0.9699]	MoKα [0.71073] microfocus sealed X-ray tube	MoKα [0.71073] sealed tube
Crystal Dimensions, mm	0.24 × 0.25 × 0.36	0.03 × 0.05 × 0.07	0.22 × 0.25 × 0.29	0.13 × 0.22 × 0.24	0.24 × 0.27 × 0.35
Crystal color	red	colourless	blue	colourless	colourless
Crystal system	orthorhombic	triclinic	triclinic	triclinic	monoclinic
a, Å	21.9244(16)	14.880(3)	12.982(3)	10.9120(9)	19.2731(14)
b, Å	22.2302(15)	25.590(5)	14.749(3)	18.6410(19)	23.3848(16)
c, Å	31.501(2)	27.680(6)	23.936(5)	19.974(3)	18.5671(13)
α, °	90	114.04(3)	80.25(3)	85.626(7)	90
β, °	90	98.30(3)	79.42(3)	76.013(7)	95.013(4)
γ, °	90	90.96(3)	64.36(3)	84.230(6)	90
Volume, Å³	15352.9(18)	9492.(4)	4040.5(18)	3916.9(7)	8336.1(10)
Density, gcm⁻³	1.268	1.198	1.259	1.286	1.474
Temperature, K	120	100	100	100	120
T_{min}/T_{max}	0.6292/0.7453	0.712/1.000	0.854/1.000	0.6038/0.7453	0.5096/0.7453
μ, mm⁻¹	0.618	0.702	1.795	0.502	3.855
Space group	Pbca	P1̄	P1̄	P1̄	P12₁/c1
Z	8	2	2	2	4
Reflections collected	53603	153806	32184	53456	54333
Independent reflections	15100	48944	15367	15538	16482
Reflections (I>2σ(I))	5678	23986	8565	12397	9580
Parameters	851	1955	932	912	966
R_{int}	0.1797	0.0759	0.1462	0.052	0.0806
2θ$_{min}$ - 2θ$_{max}$,°	2.912 - 52.046	1.942 - 61.780	6.064 - 73.552	3.936 - 53.032	3.400 - 52.854

wR$_2$ (all reflections)	0.2234	0.3422	0.3219	0.1941	0.1372
R$_1$(I>σ(I))	0.0866	0.0988	0.1131	0.0852	0.0545
GOF	0.964	1.065	0.967	1.138	1.032
ρ_{min}/ρ_{max}, eÅ^{-3}	-0.688	-0.6493	-0.9462	-0.6498	-1.0546
Restraints	80	985	193	4	198

CCDC 2353513-2353522 contains the supplementary crystallographic data. These data can be obtained free of charge from the Cambridge Crystallographic Data Centre via https://www.ccdc.cam.ac.uk/structures.

MOF B

x

y

z
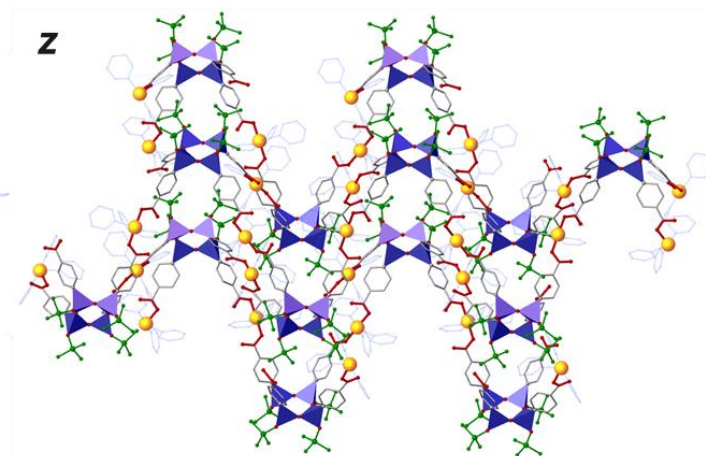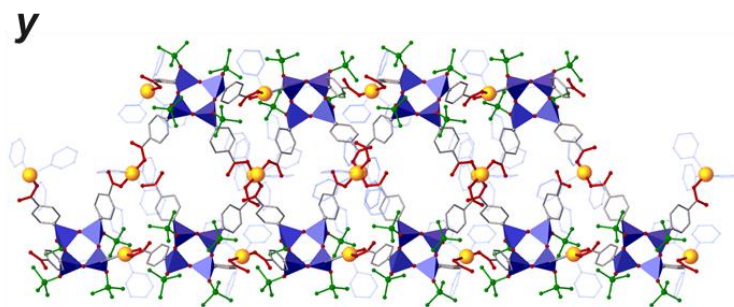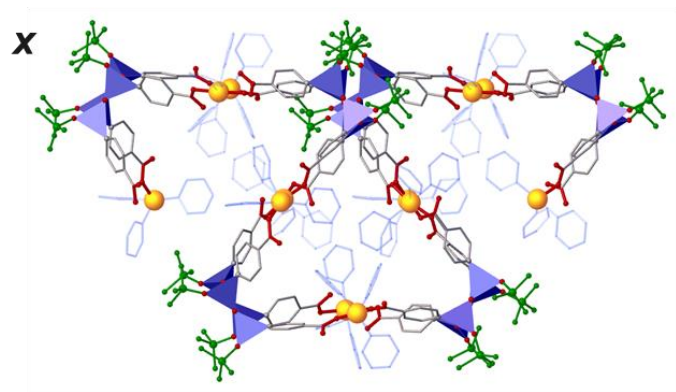
Structure of Cu-unit in MOF B

Relative ligand orientation in MOF B

Conformations of A in MOF B

Simplified structure of MOF B

☐ A
🟠 Cu-unit

🟢 TMS or Me   🟠 Cu²⁺   ⚫ C
🔴 O or C(O)O   🔵 Li⁺   DMF
🔺 Si *in cycle*   Py   🔵 [N]
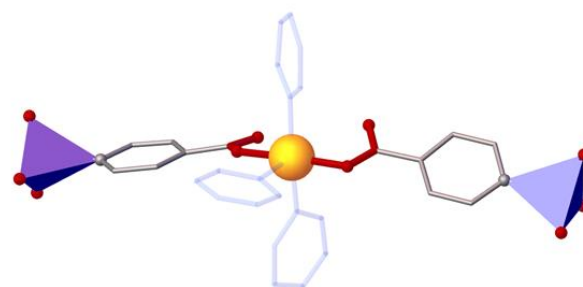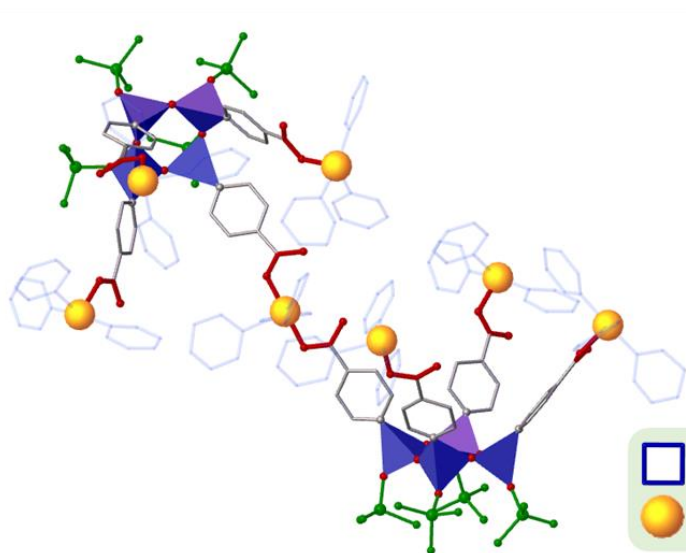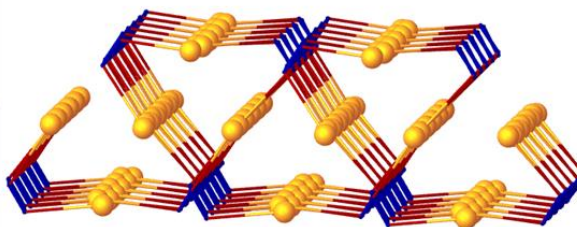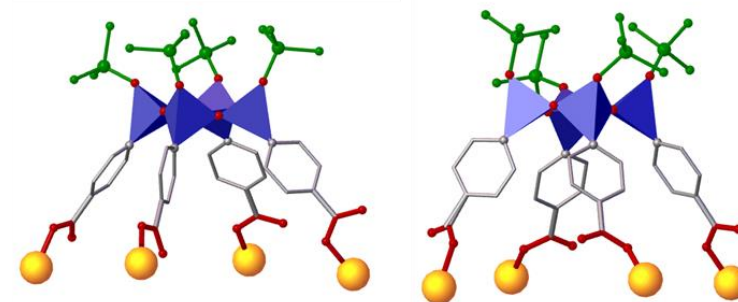
Figure S11.1.2. XRD structure of MOF B
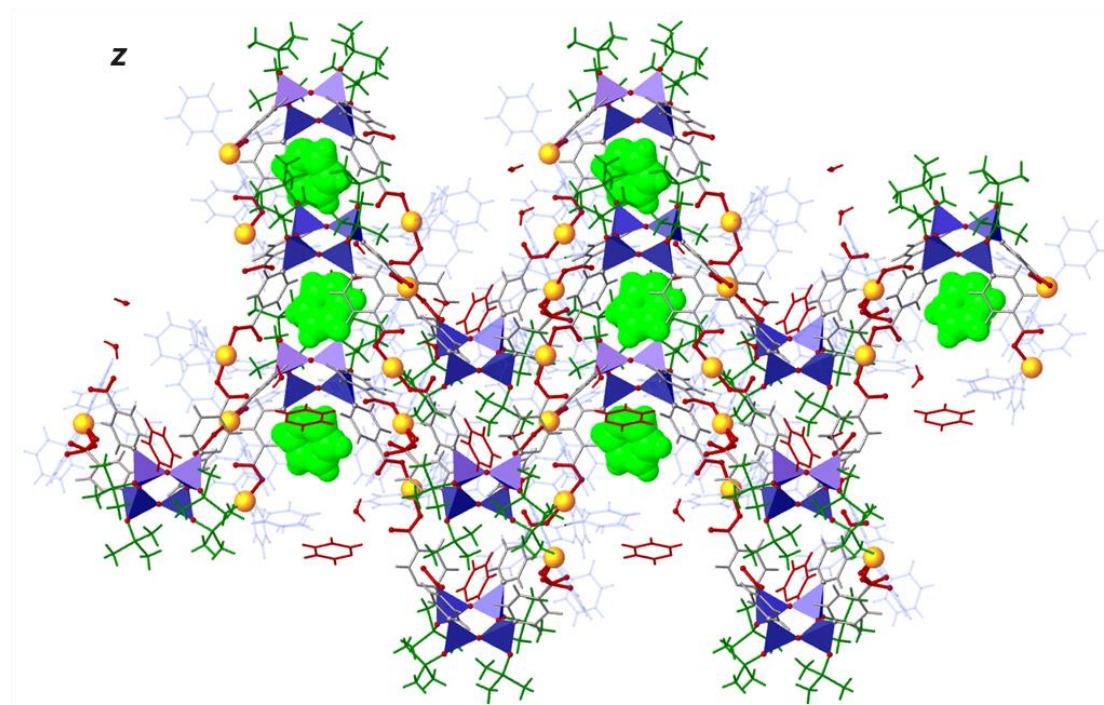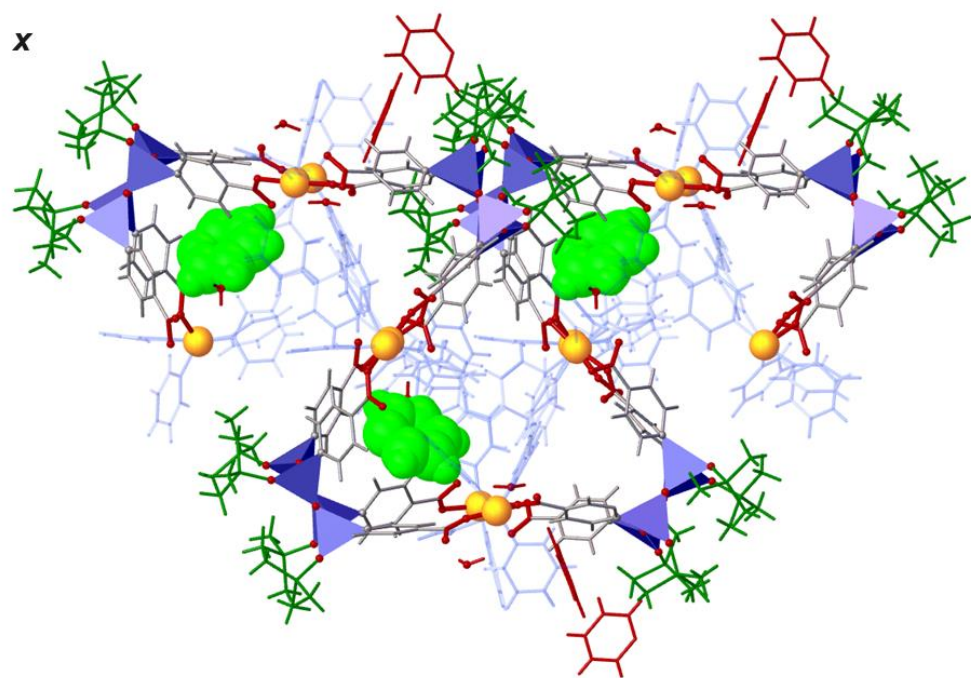
Figure S11.1.3. Non-coordinated pyridine in MOF B (highlighted, sphere-packing representation).
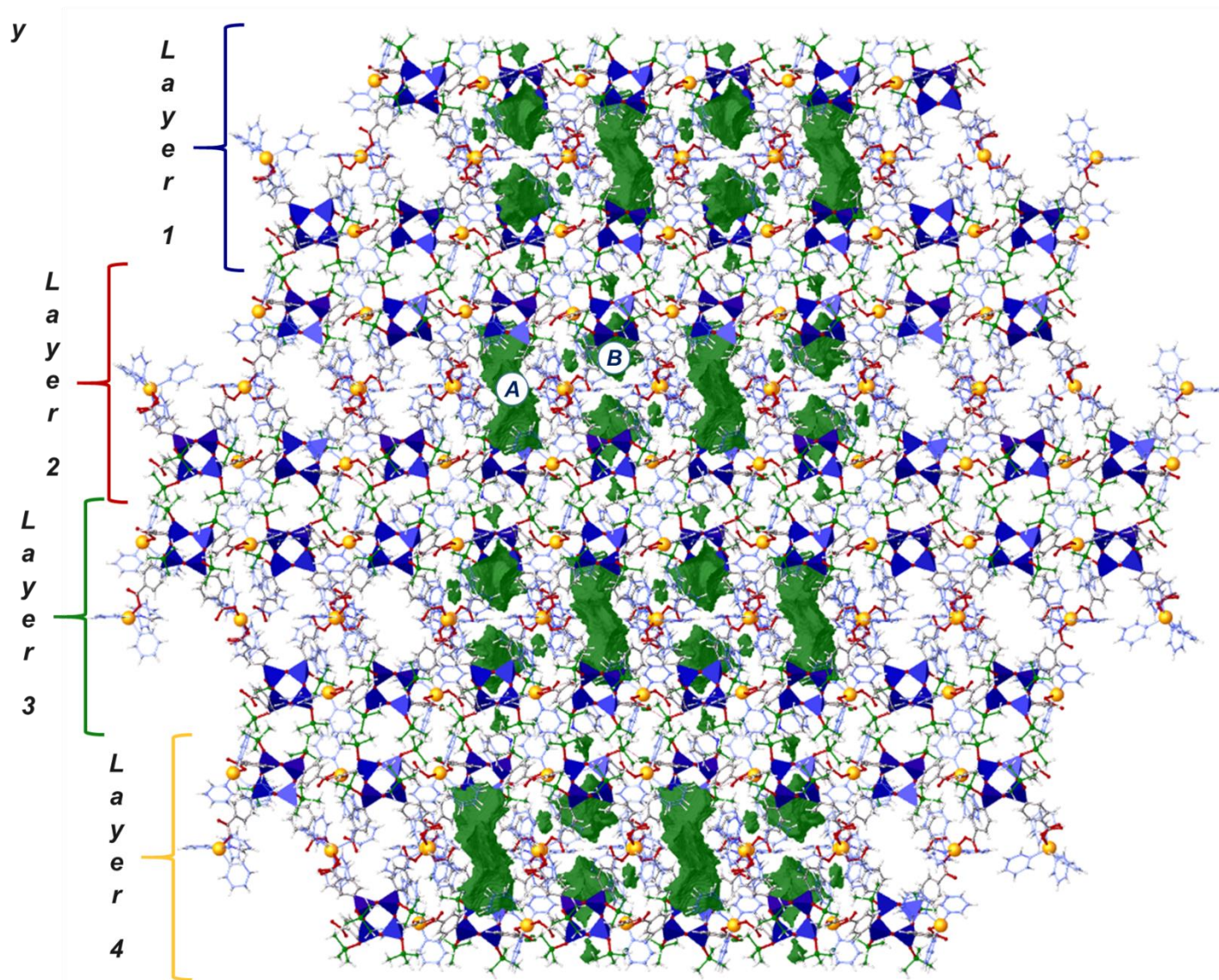
Figure S11.1.4. Voids in MOF B (all non-coordinated solvent molecules within layer are removed; total solvent accessible volume per cell, probe R/Å = 1.2 Å: 16%) *A.* **Continuous channel along *y* direction.** *B.* **Isolated solvent-filled void.**
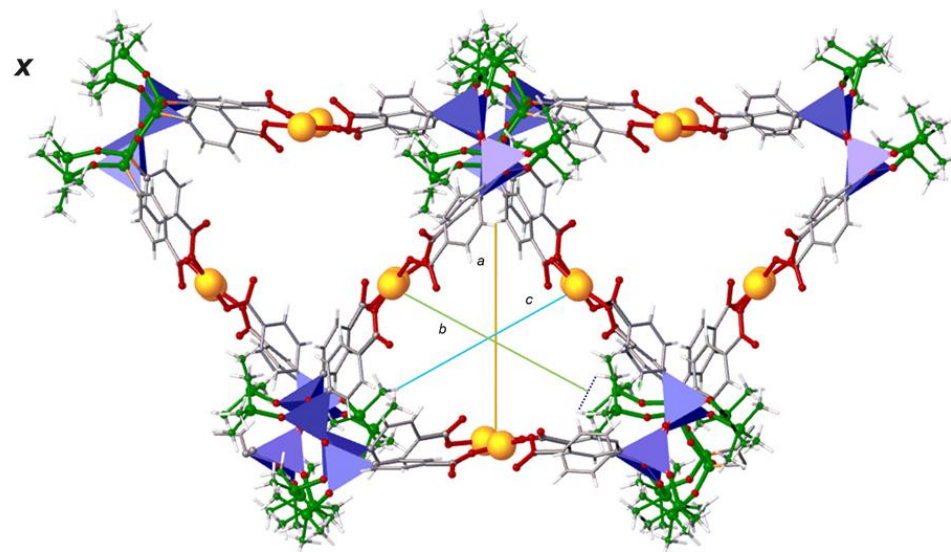
a d[(H105)-plane(Cu2-Cu3-Cu2)] = 10.478 Å;
b d[(Cu1)-plane(H50B-H55B-H50B)] = 11.13 Å;
  d[(Cu4)-plane(H50B-H55B-H50B)] = 11.065 Å;
c d[(H11R)-plane(Cu1-Cu4-Cu1)] = 10.065 Å.
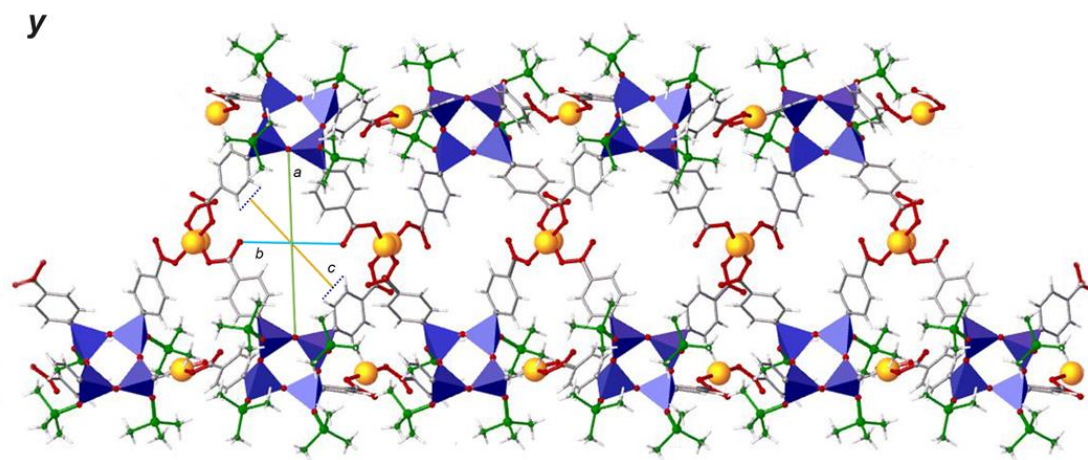
a d[lines(O3-O3)] = 11.641 Å;
b d[lines(O15-O15)] = 6.409 Å;
c d[plane(H21-H22-H21)] = 7.701 Å.

Figure S11.1.5. MOF B. Potential void parameters in carboxylate-only idealized coordination network (both coordinated and non-coordinated solvent molecules are omitted).

MOF B1

x

y

z
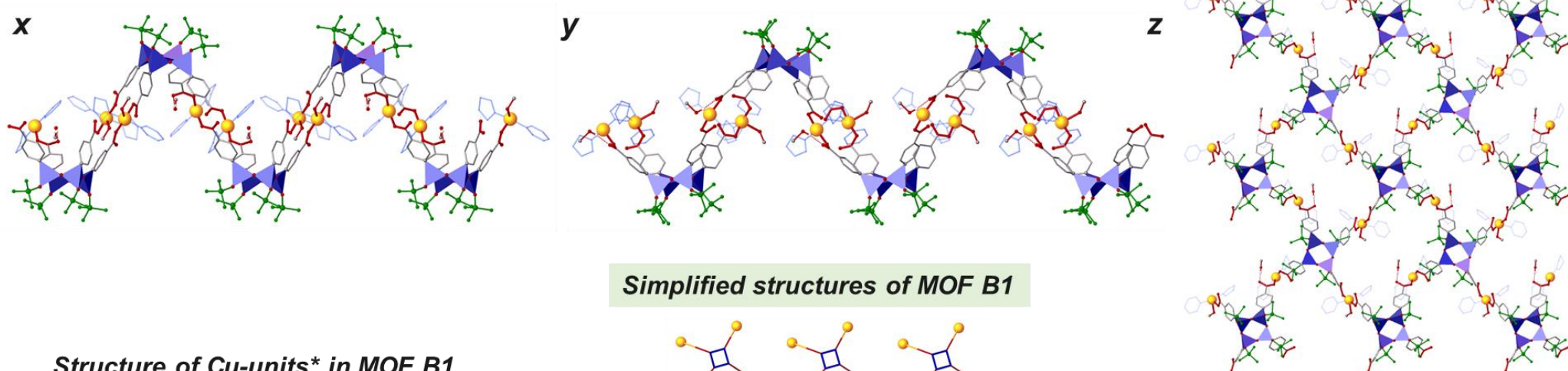
Simplified structures of MOF B1

Structure of Cu-units* in MOF B1

Conformation of A in MOF B1

☐ A

● Cu-unit
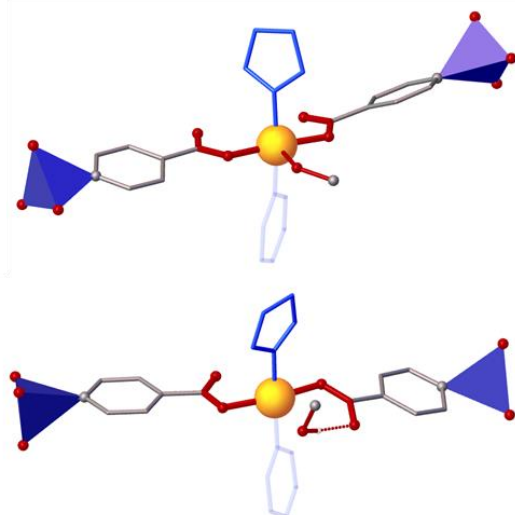
* ligand disorder was omitted for clarity

● TMS or Me	● Cu²⁺	● C
● O or C(O)O	● Li⁺	● DMF
◢ Si *in cycle*	● Py/[N]	● [N]**
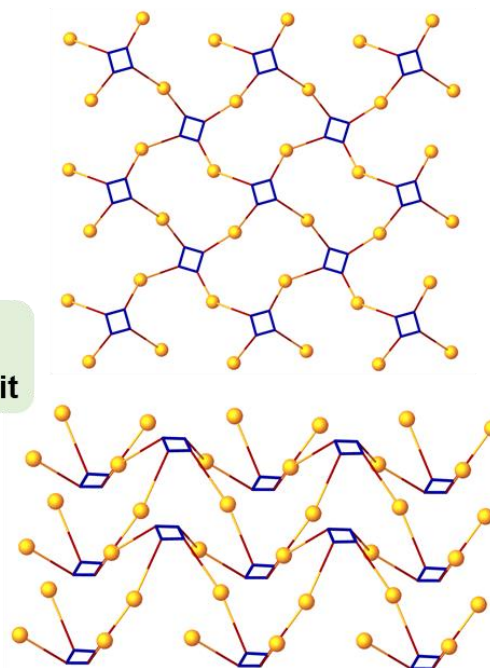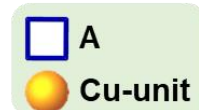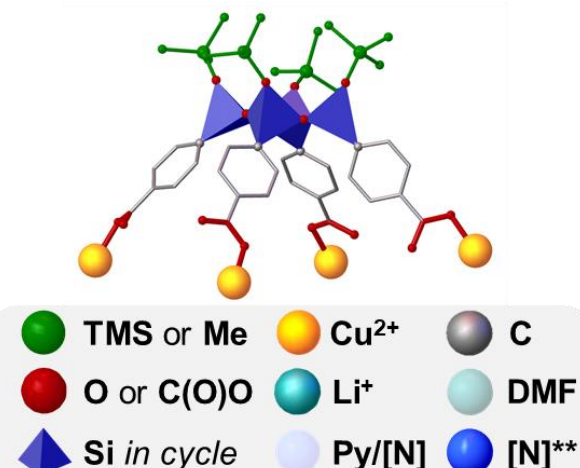
**highlighted in units*

Figure S11.1.6. XRD structures of MOF B1
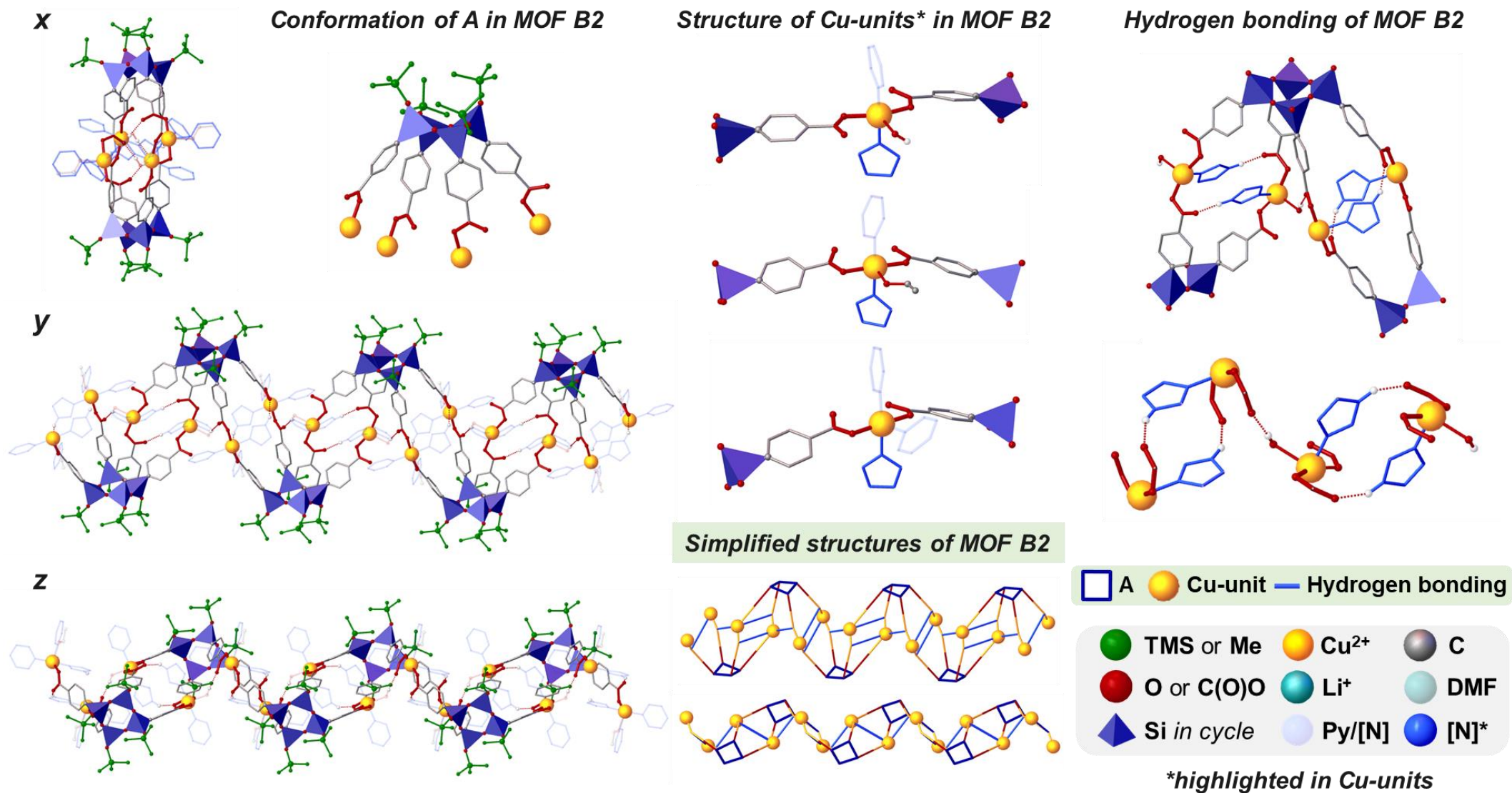
Figure S11.1.7. XRD structures of MOF B2

MOF B3

Supramolecular 2D structure of MOF B3

x

y

z

Conformation of A in MOF B3
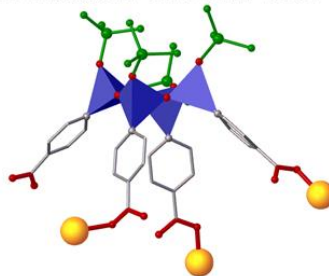
Simplified supramolecular structure of MOF B3
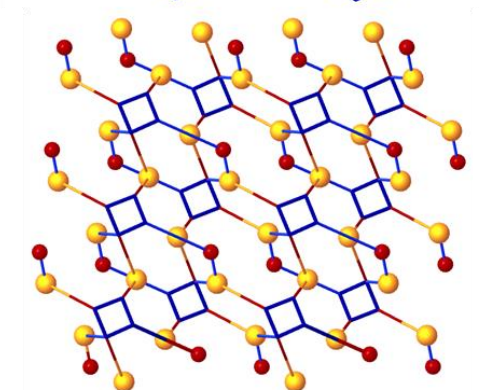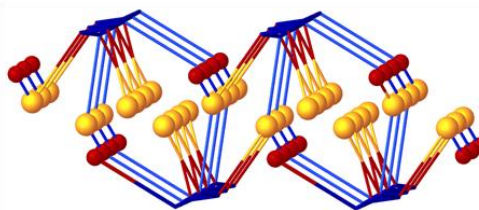
☐ A 🟡 Cu-unit — Hydrogen bonding

Structure of binding Cu-unit* in MOF B3
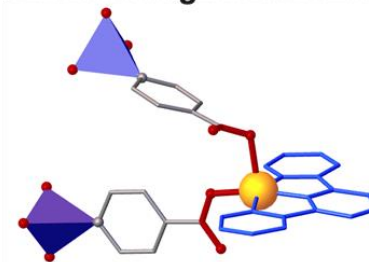
Structure of 1D chain in MOF B3

Simplified structure of 1D chain in MOF B3

🟢 **TMS** or **Me**   🟡 **Cu²⁺**   ⚫ **C**

🔴 **O** or **C(O)O**   🔵 **Li⁺**   **DMF**

🔷 **Si** *in cycle*   **Py/[N]**   🔵 **[N]***
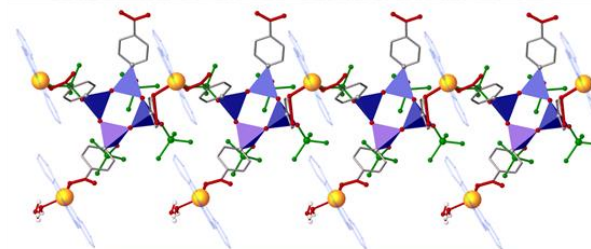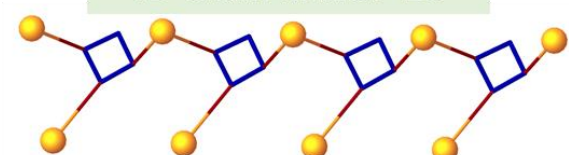
highlighted in units

Figure S11.1.8. XRD structure of MOF B3

MOF C

x

y

z
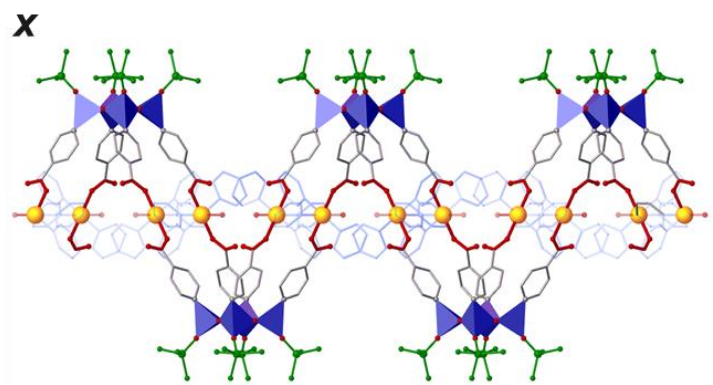
Relative ligand orientation in MOF C
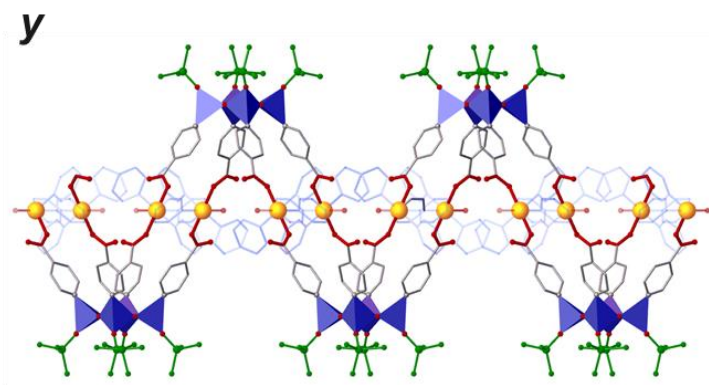
Structure of Co-unit in MOF C
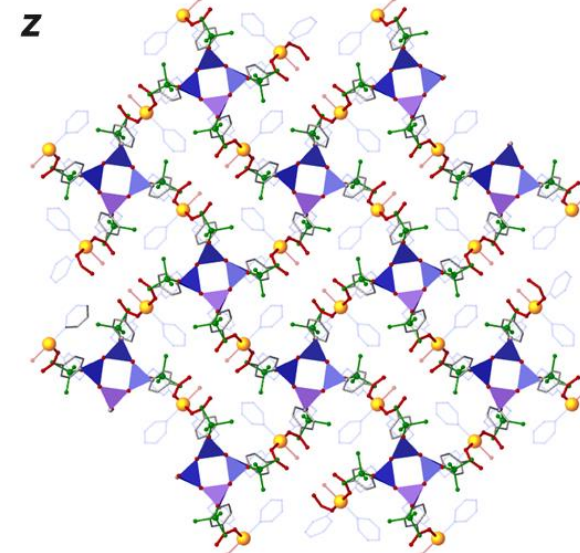
Conformation of A in MOF C

□ A

● Co-unit
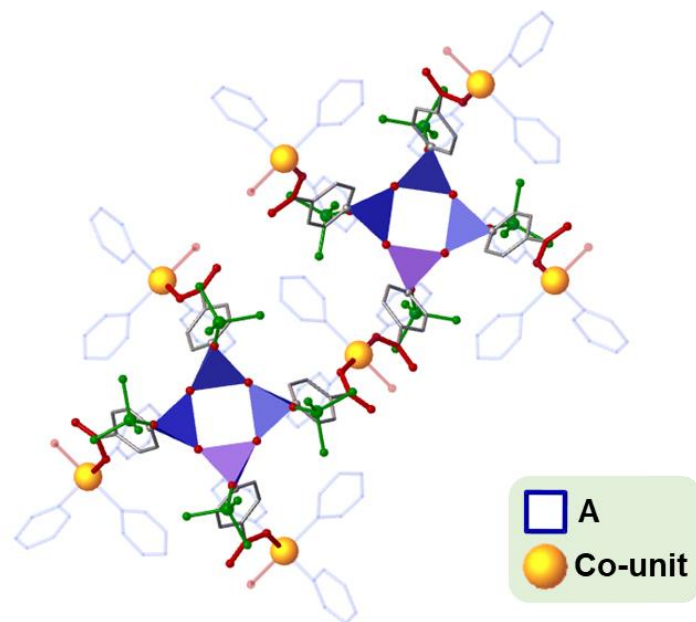
Simplified structure of MOF C
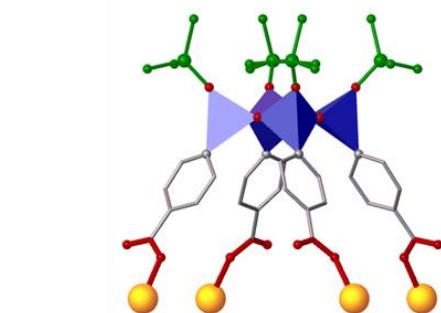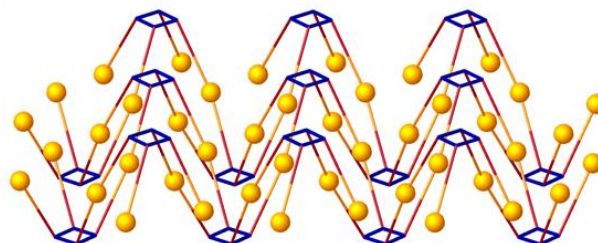
Figure S11.1.9. XRD structure of MOF C

● TMS or Me   ● Co²⁺   ● C

● O or C(O)O   ● Li⁺   ● DMF

▲ Si *in cycle*   ● Py   ● [N]

MOF D

x

y

z

Relative ligand orientation in MOF D

Structure of Zn-units in MOF D

Conformation of A in MOF D

□ A

🟠 Zn-unit

Simplified structure of MOF D

🟢 **TMS** or **Me**	🟠 **Zn²⁺**	⚪ **C**
🔴 **O** or **C(O)O**	🔵 **Li⁺**	⚪ **DMF**
🔷 **Si** *in cycle*	⚪ **Py**	🔵 **[N]**
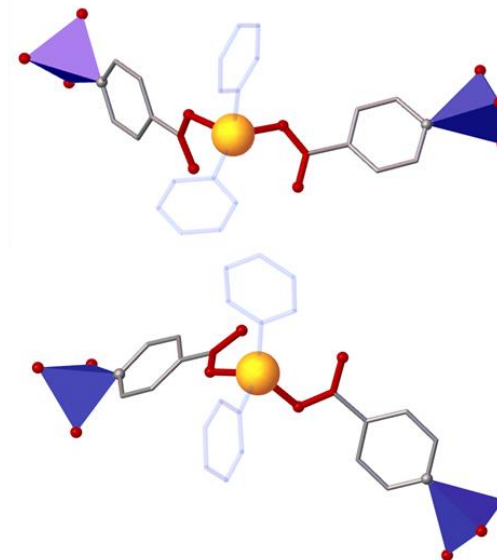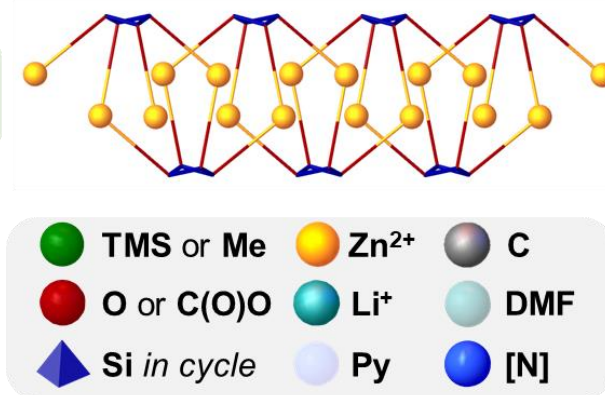
Figure S11.1.10. XRD structure of MOF D

MOF E

Relative ligand orientation in MOF E

x

y

z

Conformations of A in MOF E

Simplified structure of MOF E

☐ A

⬤ Cd-unit

Structure of Cd-unit in MOF E

⬤ TMS or Me   ⬤ Cd²⁺   ⬤ C
⬤ O or C(O)O   ⬤ Li⁺   ⬤ DMF
🔺 Si *in cycle*   ⬤ Py   ⬤ [N]
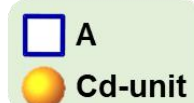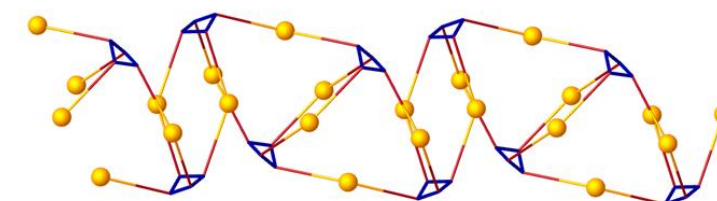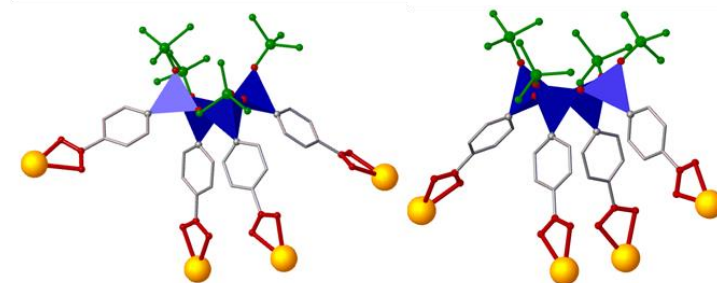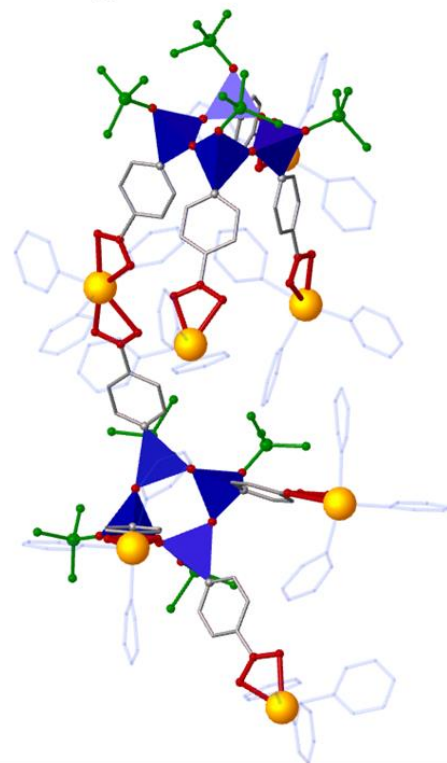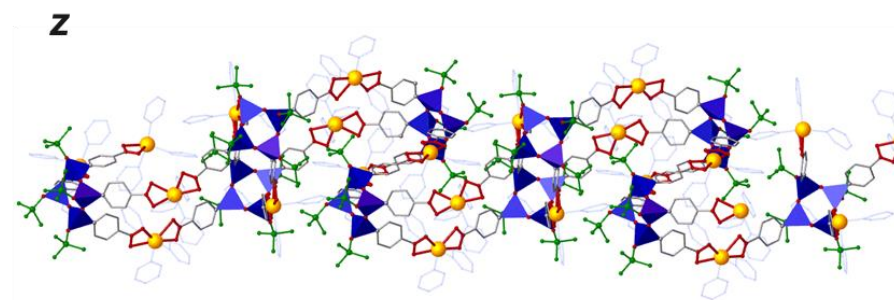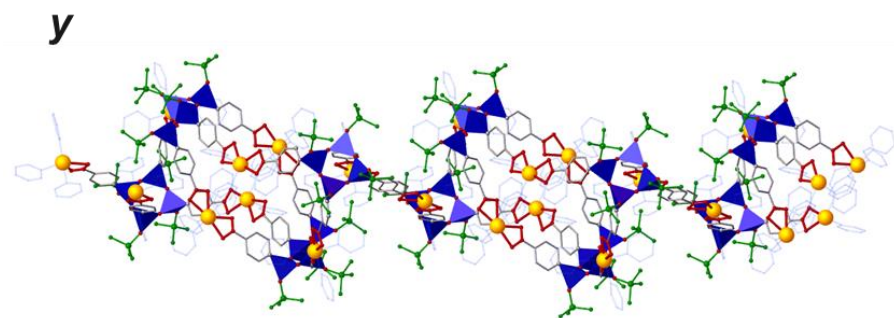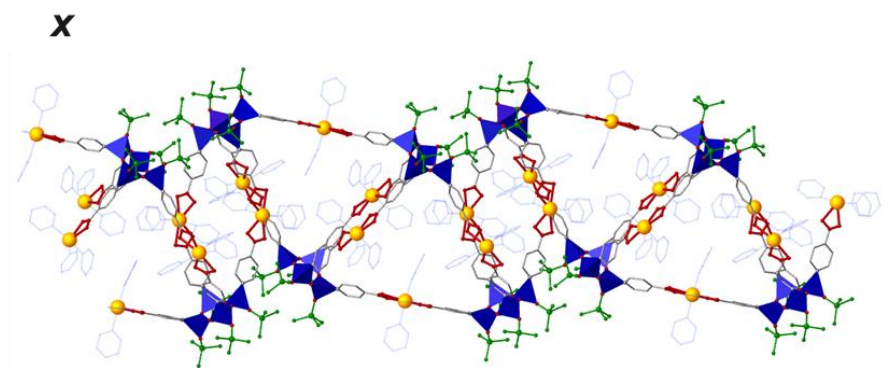
Figure S11.1.11. XRD structure of MOF E

MOF F

x

y
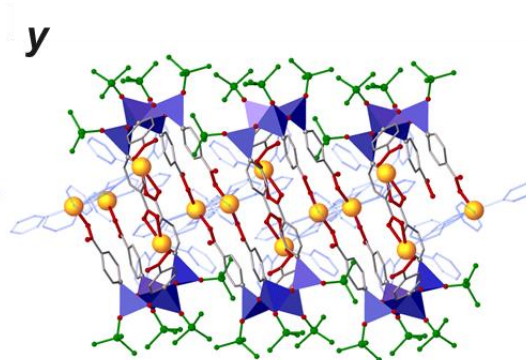
Structure of Hg-unit in MOF F

z

Simplified structure of MOF F

Relative ligand orientation in MOF F

Conformation of A in MOF F

☐ A

🟠 Hg-unit

🟢 **TMS** or **Me**	🟡 **Hg²⁺**	⚪ **C**
🔴 **O** or **C(O)O**	🔵 **Li⁺**	🔵 **DMF**
🔺 **Si** *in cycle*	⚪ **Py**	🔵 **[N]**
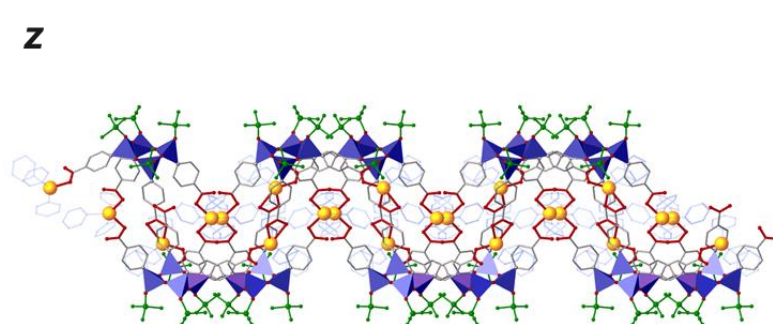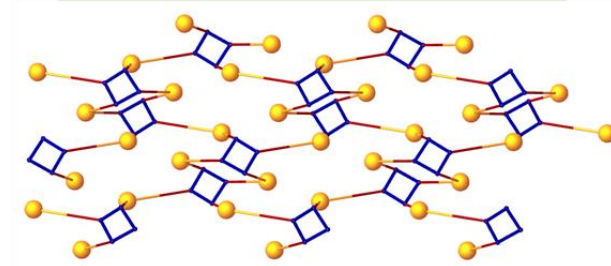
Figure S11.1.12. XRD structure of MOF F

MOF G

x

y

z
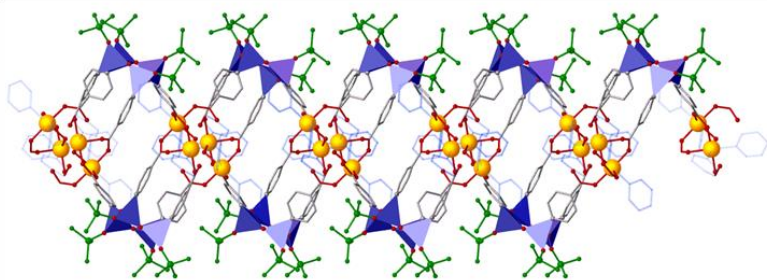
Relative ligand orientation in MOF G
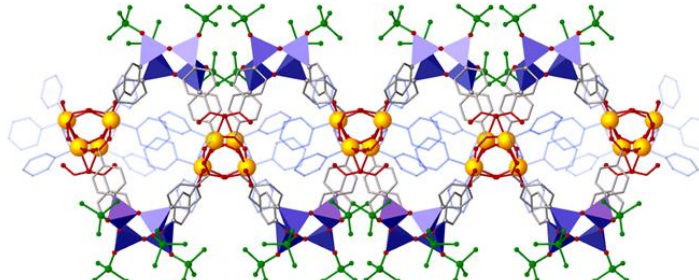
Structure of Co-SBU in MOF G
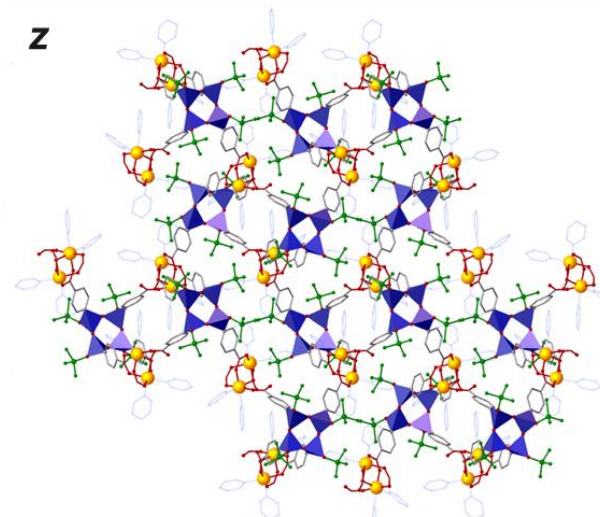
Simplified structure of MOF G

Conformation of A in MOF G

□ A
🟠 Co-unit

🟢 **TMS** or **Me**	🟠 **Co²⁺**	⚪ **C**
🔴 **O** or **C(O)O**	🔵 **Li⁺**	🔵 **DMF**
🔺 **Si** *in cycle*	🔷 **Py**	🔵 **[N]**
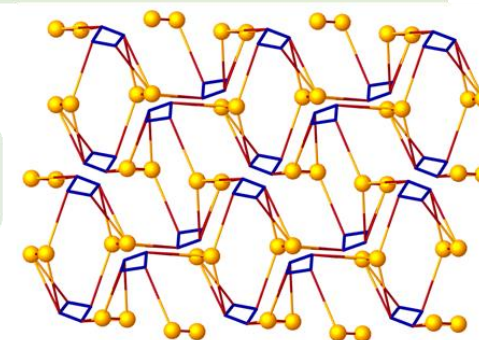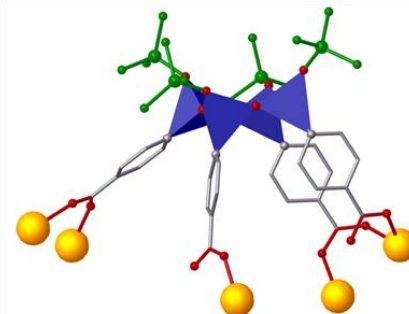
Figure S11.1.13. XRD structure of MOF G

MOF H

x

y

z
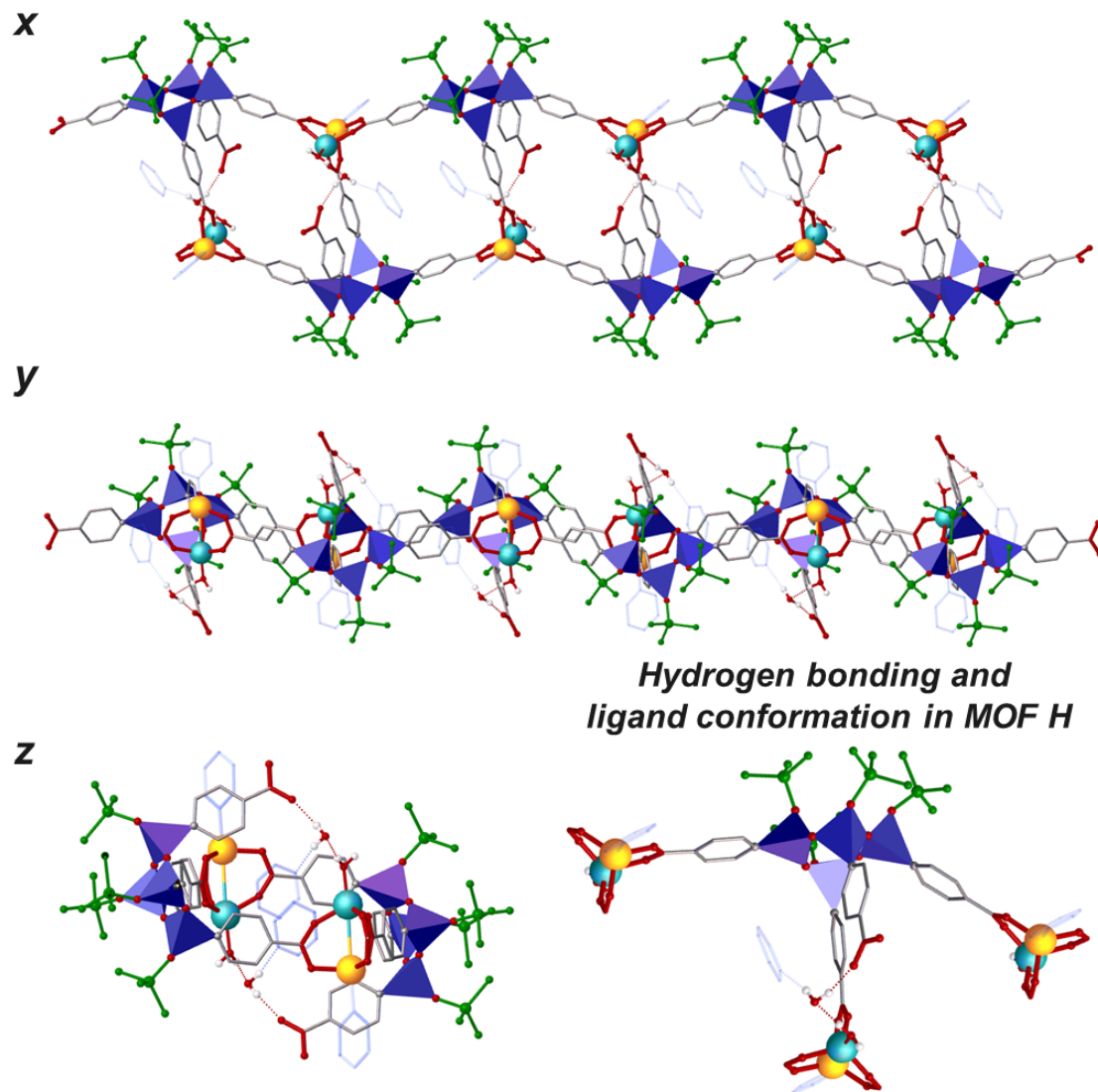
Structure of Zn/Li-SBU in MOF H

Hydrogen bonding and ligand conformation in MOF H

Simplified structures of MOF H

☐ A

🟠 Zn-unit

🔵 Li-unit

🟢 **TMS** or **Me**   🟠 **Zn²⁺**   ⚫ **C**

🔴 **O** or **C(O)O**   🔵 **Li⁺**   ⚪ **DMF**

🔺 **Si** *in cycle*   ⚪ **Py**   🔵 **[N]**
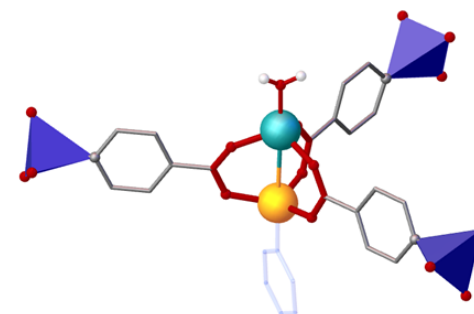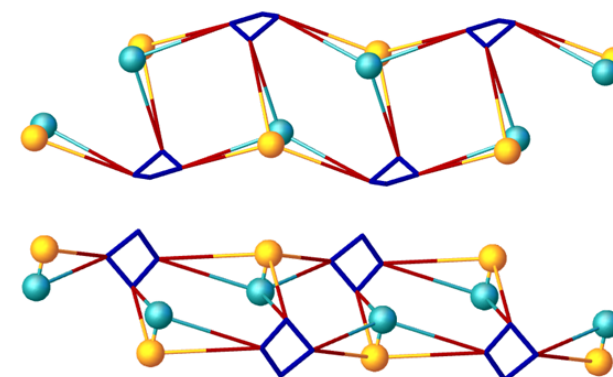
Figure S11.1.14. XRD structure of MOF H

S11.2. PXRD

The comparison of XRD patterns of **B5**, **B4** and **B4'** (**Figure S11.2.1**) has shown that two latter samples belong to phase that can be described as amorphized. Indeed, the XRD patterns of **B4** and **B4'** demonstrated the presence of only two wide maxima.
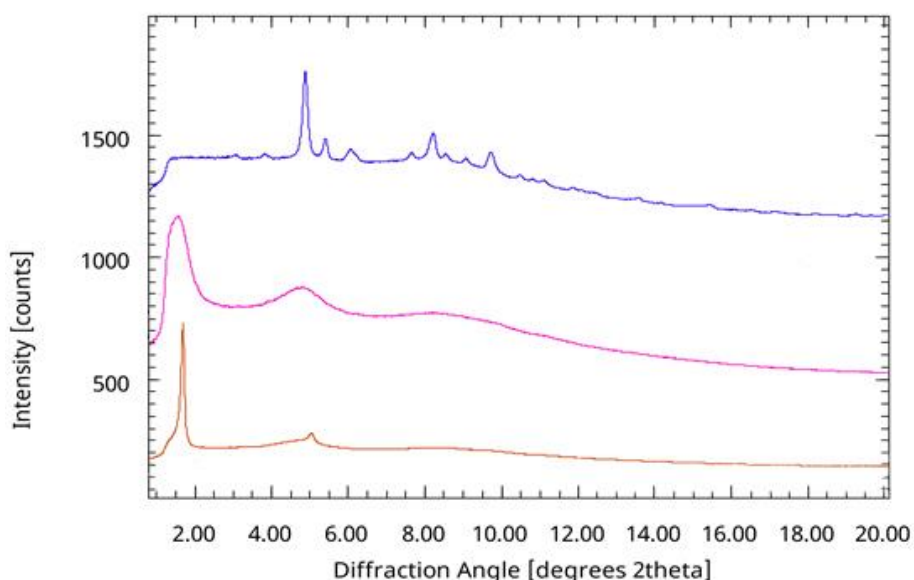
Figure S11.2.1 PXRD spectra: blue – **B5**; pink – **B4**; brown – **B4'**

Moreover, the XRD patterns of **B4** and **B4'** according to positions of their maxima can be described as amorphous phases derived from **B**. On the other side, the XRD patterns for **B** and **B5** are different.

The stability of MOA **B5** was studied in a climate chamber at various temperatures (ranging from 30 to 70 °C) and humidity (from 20 to 90%). It was found that MOA **B5** did not interact with water (neither chemically or physically). Hydrolytic stability was estimated by the PXRD (*see below,* **Figure S11.2.2**).
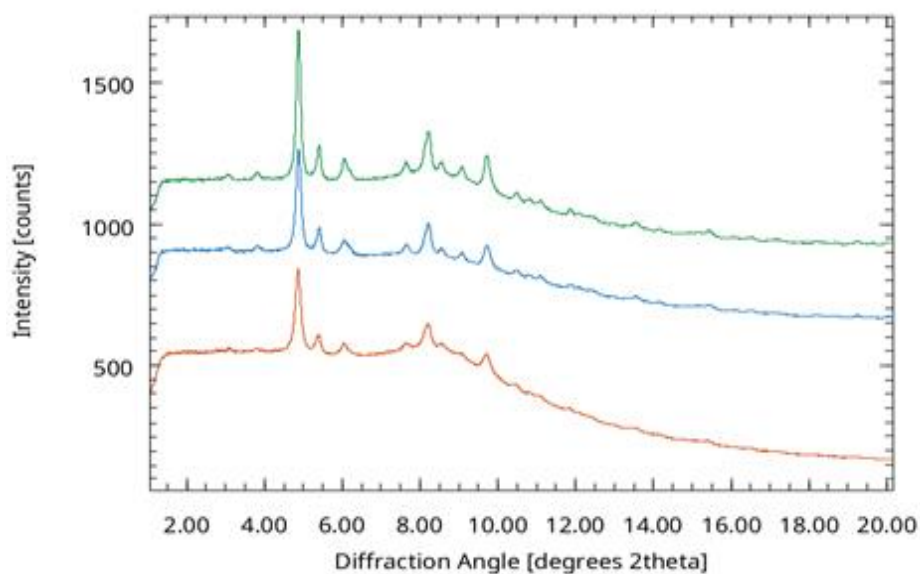
Figure S11.2.2. PXRD spectra MOA **B5**: green – freshly obtained (activated by SCD, next it was thermally activated (20 mbar, 200 °C, 2 h) and subsequently stored in air (2 h)); blue –after aging in a climatic chamber (humidity – 80%, T – 30 °C, 10-12 h); red – after catalytic reaction, aerobic oxidation (separated from the reaction mass and dried by SCD)

S11.3. *In situ* X-ray study of crystallization using the example of MOF B

The MOF growth is a complex process that depends on many thermodynamic and kinetic parameters.

As follows from **Figure 2 B** (Manuscript), both Pyr and H_2O had a prominent effect on the resulting crystallinity of the product **B**. According to Cu K-edge EXAFS (extended X-ray absorption fine structure, see below in Section S12.1) studies of $Cu(OAc)_2$ dissolved in pure Pyr or H_2O, four equally short distances between the Cu(II)-centers and N-/O-containing molecules in the equatorial plane of Cu(II)-center were formed [1]. However, in the Pyr/H_2O (4/1) two distinct Cu(II)–N/O-distances have been found: short (1.94 Å, 2.00 Å) and one longer axial bond (2.13 Å). Such parameters indicate joint coordination of H_2O and Pyr upon interaction with Cu(II)-ions. The formation of such pre-activated Cu(II)-units may play an important role in the controlled formation of crystalline MOF (**B**). Crystallization for MOF **B** was also studied *in situ* by means of time-resolved synchrotron XRD (**Figure S11.3.1**). The indexing of crystallographic planes in **Figure S11.3.1 A** is based on theoretically computed peak positions for crystalline structure of MOF **B**.
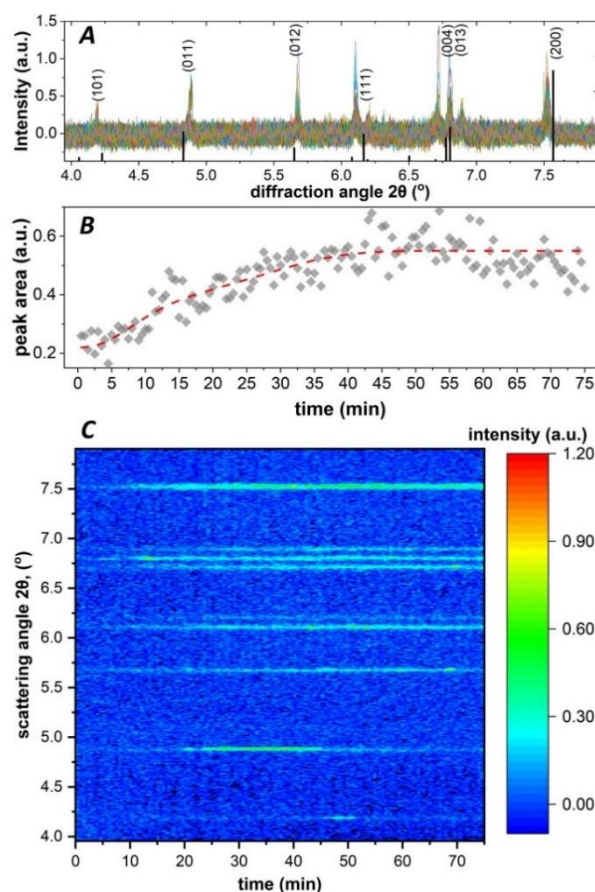
Figure S11.3.1. *In situ* X-ray study of crystallization. *A*. Dataset of diffraction patterns obtained after integration of 2D scattering maps and background subtraction. Black bars show theoretically computed peaks from CIF file of MOF **B** single crystal. *B*. Quantitative estimation of the volume of crystalline phase obtained from integrated peak intensities in XRD pattern (gray symbols) and fit with Gualtieri model (red dashed line). *C.* Two-dimensional representation of diffraction patterns collected during MOF **B** crystallization process.

The crystallization starts after short induction period (5-10 min) and crystallinity of the sample maintained till the end of observation (**Figures S11.3.1 *B* & *C***). The increase in intensity of XRD signals after induction period can be described by monotonic growth (within next 45 min), followed by plateau region and further small negative slope (after 1 h). Interplay between two stages of MOF formation, namely nucleation and crystal growth, is commonly described by Gualtieri model [2], shown as red dotted line in **Figure S11.3.1 *B*** for our data. After fitting, the rate of nucleation was found to be ~2 times faster than crystal growth. Previous studies report that kinetics of nucleation and growth depend on the composition of reaction mixture and MOF type [3]. Another observation is related to the nonmonotonic evolution of scattering intensity at ca 4.8° (**Figure S11.3.2**). As can be seen, this peak reaches maximum amplitude at 35 min and then becomes smaller. These changes were likely related to the preferred orientation of crystallites in the reaction cell at a certain stage of particle growth. They could also be due to the formation of intermediates consisting of Cu(II)-units, Pyr/H_2O and the ligand **A.** A similar effect was observed in the study of other MOFs [4].
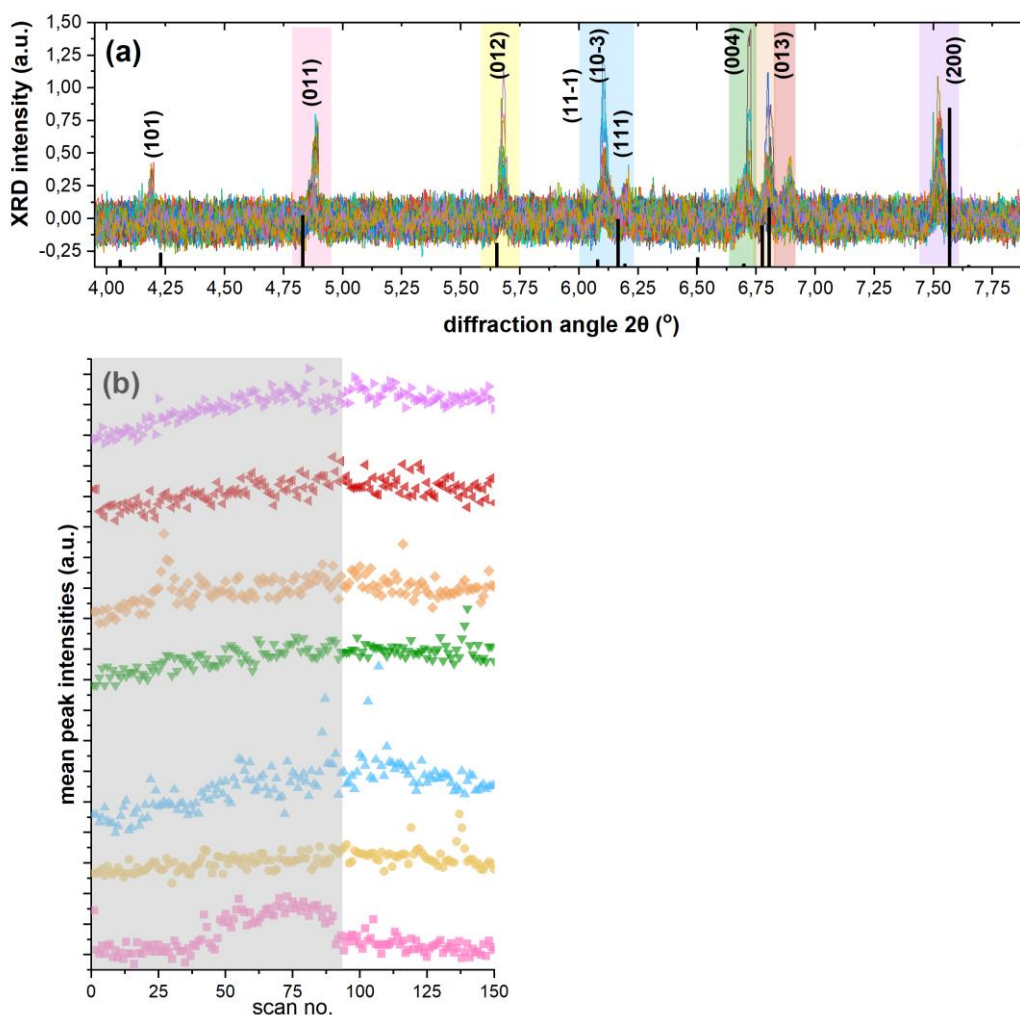
Figure S11.3.2. *A*. Data intervals selected for quantitative evaluation of time evolution for different peak intensities. *B*. Corresponding values of peaks intensities estimated as a mean intensity values over the intervals highlighted in part *A*. Grey rectangle represents the area where linear growth trend is observed for different peaks with the exception of (011) peaks. The lines are shifted vertically for better visualization.

Additional description for the Figure S11.3.2. Collected dataset of scattering patterns is presented in **Figure S11.3.2 *A*** along with tentative indexing of crystallographic planes from computed peak positions in VESTA software for CIF file of MOF **B**. **Figure S11.3.2 *A*** shows time of evolution of individual peaks in the XRD pattern. Both time evolution of particular peaks and their integrated intensity assume linear crystalline MOF **B** growth within first 45-50 minutes of observations followed by the plateau region and further small negative slope after 1h. The only exception was the time evolution of the peak centered at *2θ* = 4.83 ° and associated with (011) reflection, which appears only in the time interval around 20 – 45 minutes. Time evolution of different diffraction peaks reported at **Figure S11.3.2 *B*** might assume anisotropic crystallization character. Rare sharp increase in the intensity of particular reflections might be related with temporary preferred orientation of the MOF crystallites upon their growth. Intensity decrease in the end of observation period might be explained by precipitation process which occurs once the MOF crystallites gain critical mass/size.

Summarizing all data obtained from Section 2.2.1 (Manuscript) and Section S11.3 (Supp. Inf.), the main functions of Pyr and H_2O, which provide the high efficiency of the method developed in the preparation of crystalline MOFs, can be highlighted:

– Pyr and H_2O perform as modulators providing more controlled and relatively slower growth of MOF crystals compared to the other solvents (and conditions) studied.

– Pyr is an activator of metal building blocks [5, 6], facilitating the replacement of AcO-anions; it enhances the nucleophilicity of carboxyl groups in ligand (**A**) thus favoring their more efficient interaction with M-blocks and also binds the acetic acid (AcOH) produced.

– H_2O, on the one hand, increases the solubility of M-salts, and on the other hand, facilitates the formation of MOFs crystallization centers, being poor solvent for (semi-)products based on ligand (**A**) and M-units.

– In addition, H_2O and Pyr almost always coordinate the M-units, thus stabilizing them and the MOF structure (Section S11, Supp. Inf.).

References**:**

[1] Persson, I.; Lundberg, D.; Bajnóczi, É. G.; Klementiev, K.; Just, J.; Sigfridsson Clauss, K. G. V. EXAFS Study on the Coordination Chemistry of the Solvated Copper(II) Ion in a Series of Oxygen Donor Solvents. *Inorganic Chemistry* **2020**, *59* (14), 9538-9550. DOI: 10.1021/acs.inorgchem.0c00403.

[2] Gualtieri, A. F. Synthesis of sodium zeolites from a natural halloysite. *Physics and Chemistry of Minerals* **2001**, *28* (10), 719-728. DOI: 10.1007/s002690100197.

[3] Salionov, D.; Semivrazhskaya, O. O.; Casati, N. P. M.; Ranocchiari, M.; Bjelić, S.; Verel, R.; van Bokhoven, J. A.; Sushkevich, V. L. Unraveling the molecular mechanism of MIL-53(Al) crystallization. *Nature Communications* **2022**, *13* (1), 3762. DOI: 10.1038/s41467-022-31294-4.

[4] Godfrey, H. G. W.; Briggs, L.; Han, X.; Trenholme, W. J. F.; Morris, C. G.; Savage, M.; Kimberley, L.; Magdysyuk, O. V.; Drakopoulos, M.; Murray, C. A.; et al. Analysis by synchrotron X-

ray scattering of the kinetics of formation of an Fe-based metal-organic framework with high CO2 adsorption. *APL Materials* **2019**, *7* (11), 111104. DOI: 10.1063/1.5121644 (acccessed 4/23/2025).

[5] Godfrey, H. G. W.; Briggs, L.; Han, X.; Trenholme, W. J. F.; Morris, C. G.; Savage, M.; Kimberley, L.; Magdysyuk, O. V.; Drakopoulos, M.; Murray, C. A.; et al. Analysis by synchrotron X-ray scattering of the kinetics of formation of an Fe-based metal-organic framework with high CO2 adsorption. *APL Materials* **2019**, *7* (11), 111104. DOI: 10.1063/1.5121644 (acccessed 4/23/2025).

[6] Aggett, J.; Billinghurst, M. W. Solvent extraction of pyridine complexes of copper(II). *Journal of Inorganic and Nuclear Chemistry* **1969**, *31* (2), 513-525. DOI: https://doi.org/10.1016/0022-1902(69)80495-1.

S12. X-ray absorption spectroscopy (XAS)

S12.1. Analysis of the local atomic environment of Cu(OAc)$_2$ in solution

Cu K-edge X-ray absorption spectra (XAS) of Cu(OAc)$_2$ solutions in Pyr or in Pyr/H$_2$O indicate Cu^{2+} oxidation state. Comparison with the spectrum of CuO (planar 4-coordinated environment of the Cu-ion) indicates a higher intensity of the white line in the spectra of solutions at 8998 eV and the absence of a shoulder at 8986 eV (**Figure S12.1.1**). This indicates a larger number of neighbors in the first coordination sphere and a violation of the planar environment, likely a transition to pyramidal or distorted octahedral coordination.
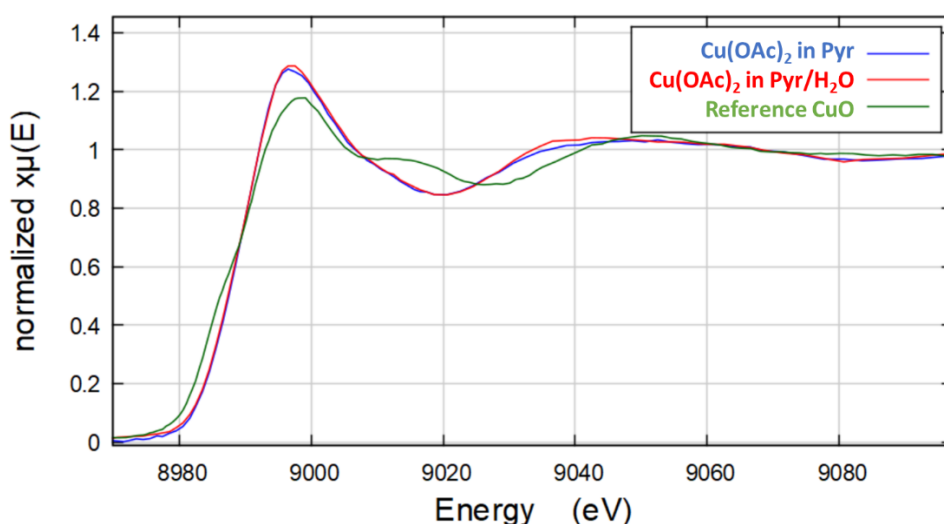
Figure S12.1.1. Comparison of Cu K-edge XANES for Cu(OAc)$_2$ solutions and CuO

When comparing the spectra of the reference compounds with the spectrum of MOF **B**, the overall shapes of the spectra are similar, indicating pyramidal or distorted octahedral coordination, but there are subtle differences in the spectrum of MOF **B** (**Figure S12.1.2**).
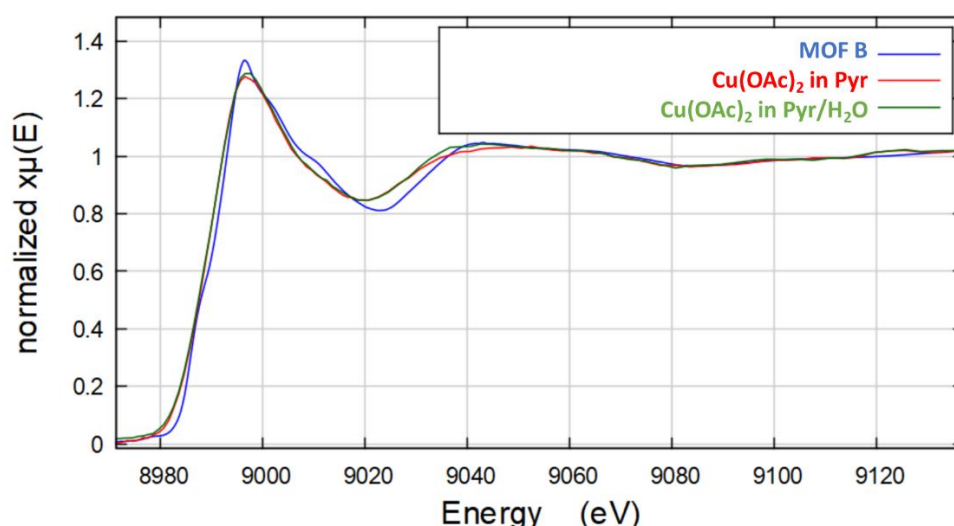
Figure S12.1.2. Comparison of Cu K-edge XANES for MOF B and Cu(OAc)$_2$ solutions

Next, we performed a quantitative fitting of the EXAFS spectra for the measured solutions in the range R = 1.05 - 2.00 Å and k = 2 - 10 Å^{-1}. The fitting results are shown in **Table S12.1.1**.

Table S12.1.1. Structural data of the local atomic environment of the Cu-atom in Cu(OAc)$_2$ obtained from fitting EXAFS data (R-interatomic distances, N-coordination number, σ^2-Debye-Waller factor, R-factor fit quality function. $S_0^2 = 0.9$)

Compound, model	Coordination sphere	N	R, Å	σ^2, Å^2	E0	R-factor
Cu(OAc)$_2$*H$_2$O in Pyr 5-coordinated model	Cu-O/N	2	1.98	0.002	0.6	0.009
	Cu-O/N	2	1.98	0.002		
	Cu-O/N	1	2.15	0.002		
Cu(OAc)$_2$*H$_2$O in Pyr 4-coordinated model	Cu-O/N	2	1.97	0.0020	-1.2	0.012
	Cu-O/N	2	1.99	0.0020		
Cu(OAc)$_2$*H$_2$O in Pyr/H$_2$O 5-coordinated model	Cu-O/N	2	1.94	0.002	1.3	0.011
	Cu-O/N	2	2.00	0.002		
	Cu-O/N	1	2.13	0.002		

Measurements on a laboratory device allow a reliable analysis of only the close environment of the Cu-atom. For the Cu(OAc)$_2$*H$_2$O solution in Pyr, the nearest four N-atoms are located at the same distance from the Cu-atom and describe the radial Fourier transform function well (**Figure S12.1.3**). The addition of a fifth N-atom at an increased distance improves the quality of the fit, and its presence also follows from the increased intensity of the main maximum in the XANES spectrum and the absence of a shoulder at the absorption edge (such a shoulder at 8986 eV is characteristic of a flat or linear configuration).
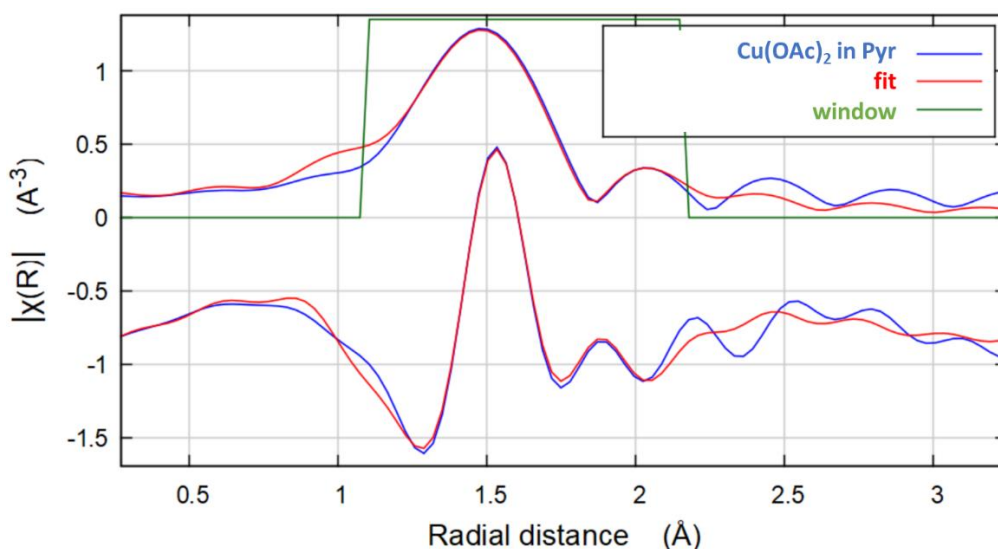
Figure S12.1.3. Fitted EXAFS of Cu(OAc)$_2$ in Pyr

When fitting the spectrum in a mixture Pyr/H$_2$O, a fundamental difference is observed, i.e. the presence of two different distances in the first coordination sphere of Cu-atom at distances of 1.94 and 2.00 Å. The overall quality of the fit in the Pyr/H$_2$O mixture is slightly worse than for pure Pyr, which is likely due to the competing interaction of H$_2$O-molecules and Pyr with Cu-atoms (the presence of a mixture of different coordinations, **Figure S12.1.4**).
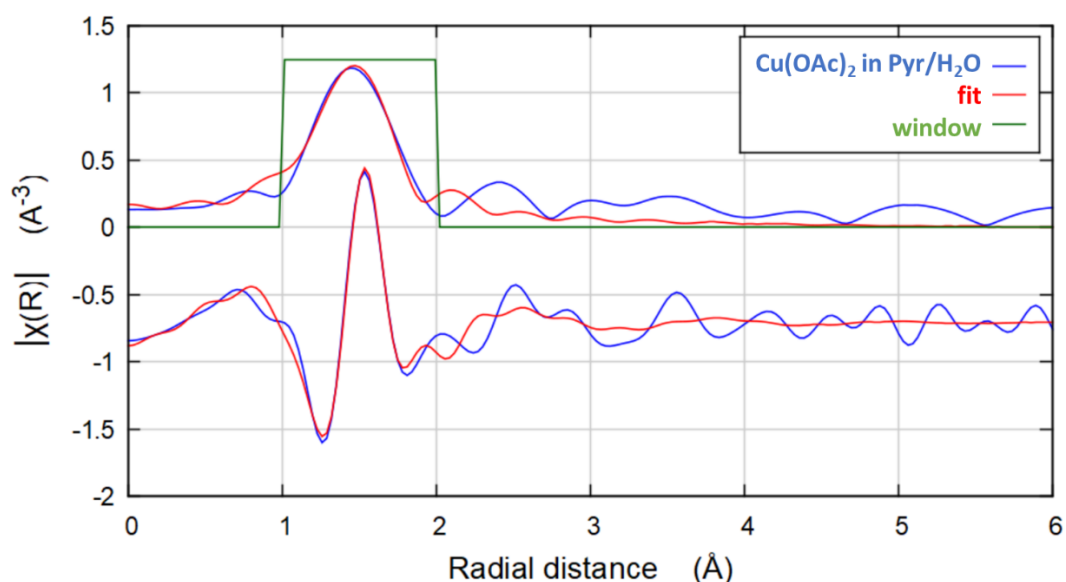
Figure S12.1.4. Fitted EXAFS of Cu(OAc)$_2$ in Pyr/H$_2$O

DFT geometry optimization further supports results of EXAFS analysis. Calculations indicate the stability of both 4- and 5-coordinated models with Pyr ligands (**Figure S12.1.5**). In the solution, there is probably a dynamic equilibrium between such configurations, and the fifth Cu-N bond is longer than 2.3 Å, which do not make a significant contribution to the EXAFS spectrum.

Cu-N = 2.01, 2.01, 2.01, 2.01 Å	Cu-N = 2.04, 2.04, 2.05, 2.06, 2.27 Å
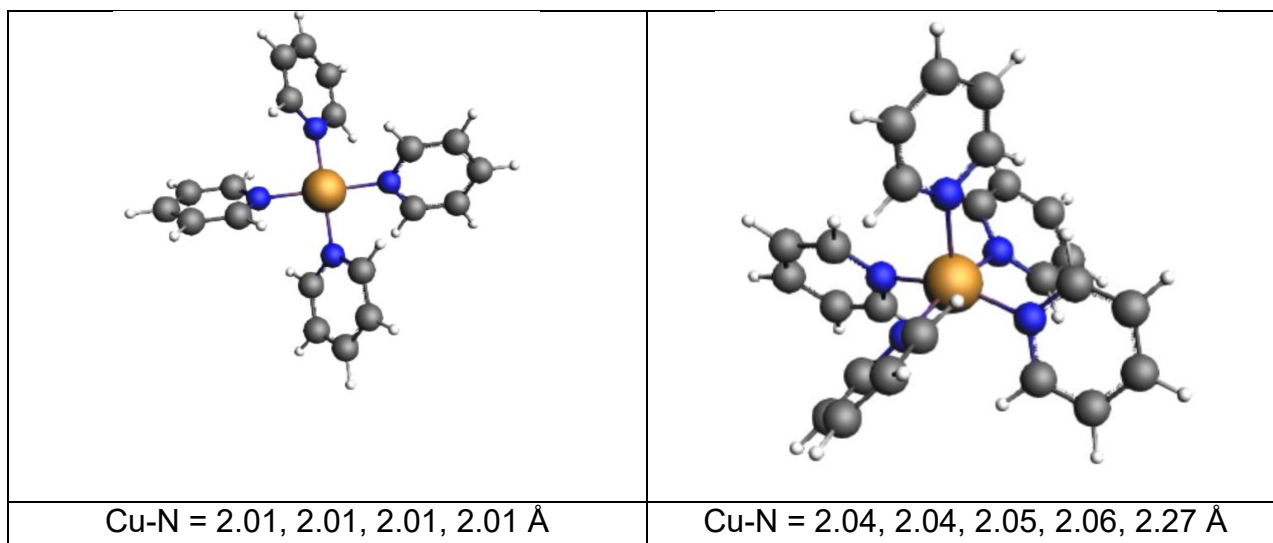
Figure S12.1.5. Calculated 4- and 5-coordinated Cu^{2+} models with Pyr ligands

For mixed Py/H$_2$O coordination, distortions in the geometry of the first coordination sphere and the presence of both two different Cu-O/N distances. Thus, the EXAFS results obtained for a sample in a pyridine/water mixture most likely indicate the presence of a statistical mixture of coordinations with different numbers of water and pyridine molecules (**Figure S12.1.6**).

Cu-N = 1.95 Å, Cu-O = 1.96, 1.98, 2.02 Å	Cu-N = 1.99, 1.99, 1.99 Å, Cu-O = 2.11 Å

Cu-O = 2.0, 2.0, 2.0, 2.0, 2.31, 2.31 Å
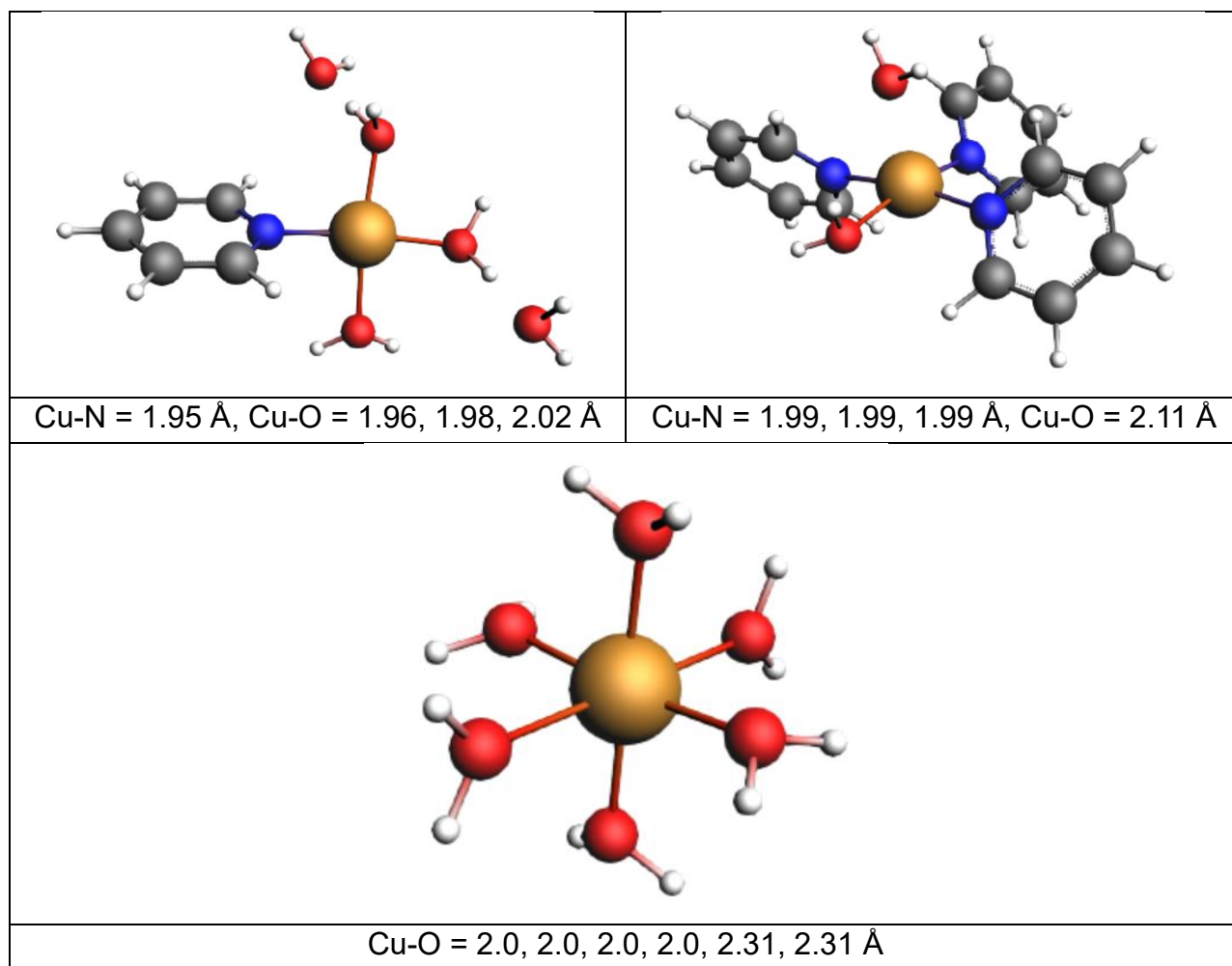
Figure S12.1.6. Optimized geometries with Pyr and H_2O ligands

S12.2. Analysis of the local atomic environment of Cu-ions in MOFs B, B4, B4' & B5

Tables S12.2.1 and **S12.2.2** show results of quantitative EXAFS refinement. The local environment around copper ions is represented by several Cu-O/N distances and thus different models can adequately describe experimental data with similar R-factor. However, there are common trends in all good fits. The distances in the first coordination sphere after refinement can be described by two pairs of Cu-O/N bonds with length in the range 1.90 … 1.98 Å. The fifth atom is likely present at elongated distance that is refined from EXAFS at ca. 2.1 Å versus 2.26 Å from XRD data. Such discrepancy may be explained by several factors, including disorder of solvation molecules that influence both XRD analysis and EXAFS fits.

Table S12.2.1. Structural data of the local atomic environment of the copper atom in MOFs **B, B4** and **B5**, obtained from multi-sphere fit of the k^3-weighted $\chi(k)$ EXAFS data in the range of 3–13 Å^{-1} (R – interatomic distances, CN – coordination number, σ^2 – Debye-Waller factor, Q – fit quality function)

MOF	Neighbor atom	CN	R, Å	σ^2, Å^2	Q, %	XRD data
B	O/N	2	1.91	0.0037	1.2	O 1.95 Å
	O/N	2	1.99	0.0037		O 1.97 Å
	O/N	1	2.07	0.0037		N 1.99 Å
						N 2.02 Å
						N 2.26 Å
B4	O/N	2	1.92	0.0037	0.3	N/A
	O/N	2	1.97	0.0037		
	O/N	1	2.07	0.0037		
	Cu	0.4	2.61	0.0065		
B4 Fit#2	O/N	2	1.94	0.0037	1.4	
	O/N	2	1.98	0.0037		
B5	O/N	2	1.90	0.0037	0.2	
	O/N	2.5	1.98	0.0037		
	Cu	0.3	2.61	0.0065		
B5 Fit#2	O/N	2	1.93	0.0037	0.6	
	O/N	2	1.97	0.0037		

Refinement of data for **B4'** showed obviously smaller Cu-O/N distances in the first coordination sphere (**Table S12.2.2**).

Table S12.2.2. Structural data of the local atomic environment of the Cu-atom in MOF **B4'** obtained from the first coordination sphere fit of the k^3-weighted $\chi(k)$ EXAFS data in the range of 2–9 Å^{-1}. Smaller wavenumber region for this sample was chosen due to smaller amount of powder available for XAS measurements and thus lower quality of the data at high k-values.

MOF	Neighbor atom	CN	R, Å	σ^2, Å^2	Q, %
B4'	O/N	2	1.87	0.005	
	O/N	1	1.91	0.005	1.8
	O/N	2	1.99	0.008	
B4' fit#2	O/N	2	1.92	0.005	1.8
	O/N	2	1.93	0.005	

Another interesting observation follows from the analysis of second coordination shell. The second coordination shell in the FT EXAFS (peak at 2.1 Å of the phase uncorrected data in Figure 9b, main text) corresponds to the scattering from carbon atoms in the RC(O)O- and Pyr-ligands. Increased intensity of this peak for **B4** and **B5** may indicate additional scattering from Cu–Cu-pairs as evidenced from wavelet transformation (WT) analysis which represent the distribution of photoelectron scattering in both R- and k-space. Due to the different values of the maximum of the scattering amplitude function for light atoms (about 5 Å^{-1} for C/O/N) and heavy atoms (about 10 Å^{-1} for Cu), it is possible to separate such coordination spheres of mixed composition in k-space. We obtained WT maps for EXAFS of all studied compounds, which are shown in **Figure S12.2.1**. The complex structure of the intensity distribution on WT maps is explained by interference effects arising from the presence of several scatterers at slightly different distances [1].
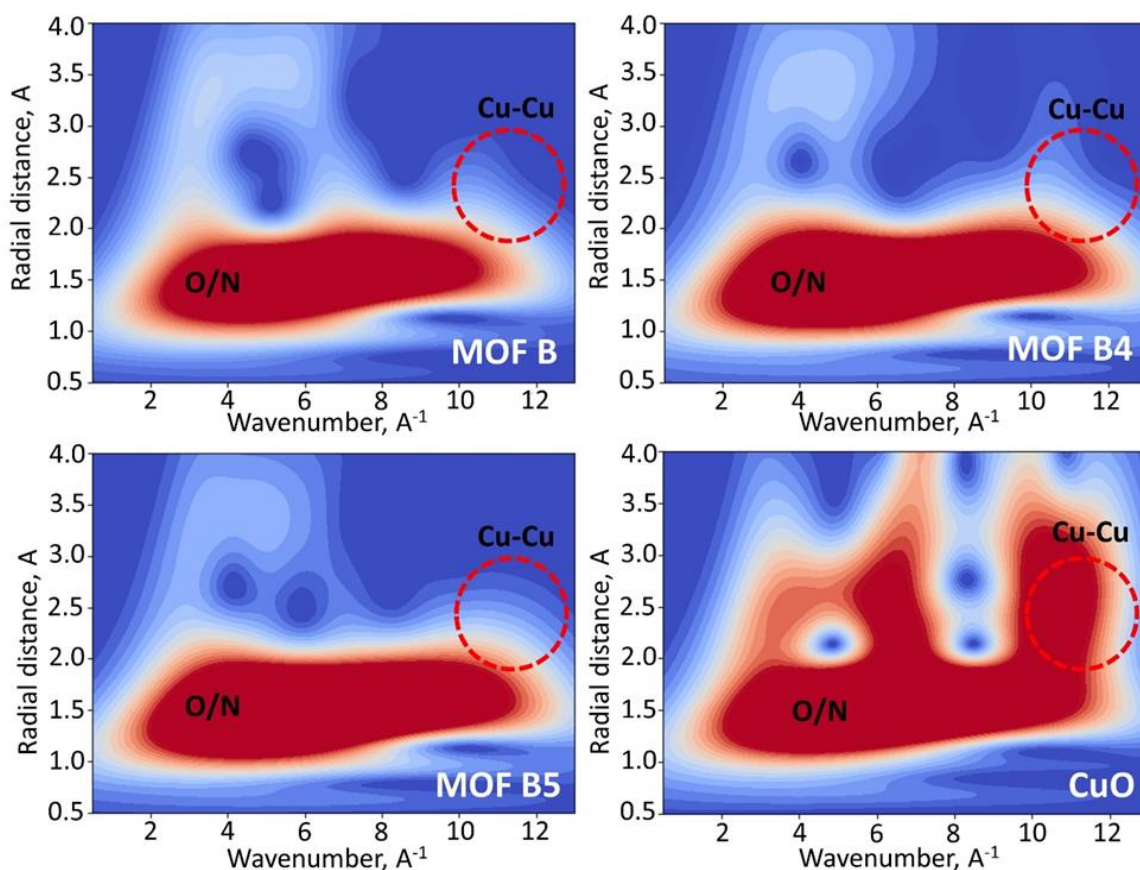
Figure S12.2.1. WT maps for EXAFS

As evidenced from integrated WT maps in **Figure S12.2.1, B4** and **B5** show enhanced scattering in the distance region R > 2 Å (phase uncorrected) for the wavenumbers k > 9 Å^{-1} indicating contribution from heavy neighbors (compare with the reference CuO and Cu(OAc)$_2$ samples in **Figure S12.2.2**).
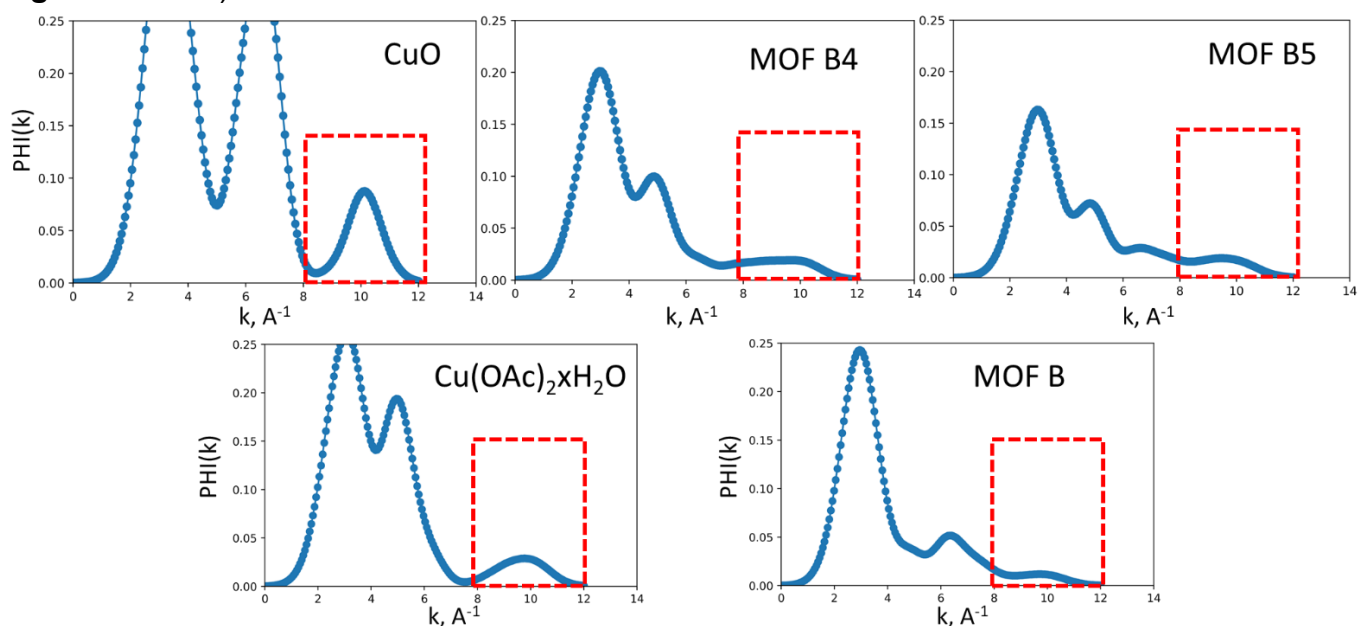
Figure S12.2.2. Integrated WT maps. The integrals are evaluated in coordinates k, PHI(k) wavelet-transform area at R > 2.0 Å for reference and MOF **B**, **B4**, **B5** samples. The Cu-Cu scattering region is highlighted.

The largest contribution of Cu-Cu can be noticed for **B4** and **B5** MOF samples, so we believe that for these structures the Cu-Cu coordination sphere should be included for the fit of **B4** and **B5** MOFs. In contrary, presence of copper atoms can be excluded for 2nd coordination sphere of MOF **B**. It should be noted that analysis of the X-ray absorption spectra indicates a multicomponent composition of samples **B4, B4'** and **B5**. For these, we were able to obtain a very good description of the spectra based on a linear combination of the spectra of the reference compounds (**Figure S12.2.3** and **Table S12.2.3**). This further indicates that **B4**, **B4'** and **B5** are a mixture of phases in which the local environment of copper corresponds to a superposition of coordinations observed in copper oxide, hydroxide, acetate, formed during manipulations during sample synthesis and drying. According to the fit **B4** has highest fraction of highly coordinated sites (78% contribution from $Cu(OAc)_2$ x H_2O phase), while **B4'** has the lowest amount of such sites.
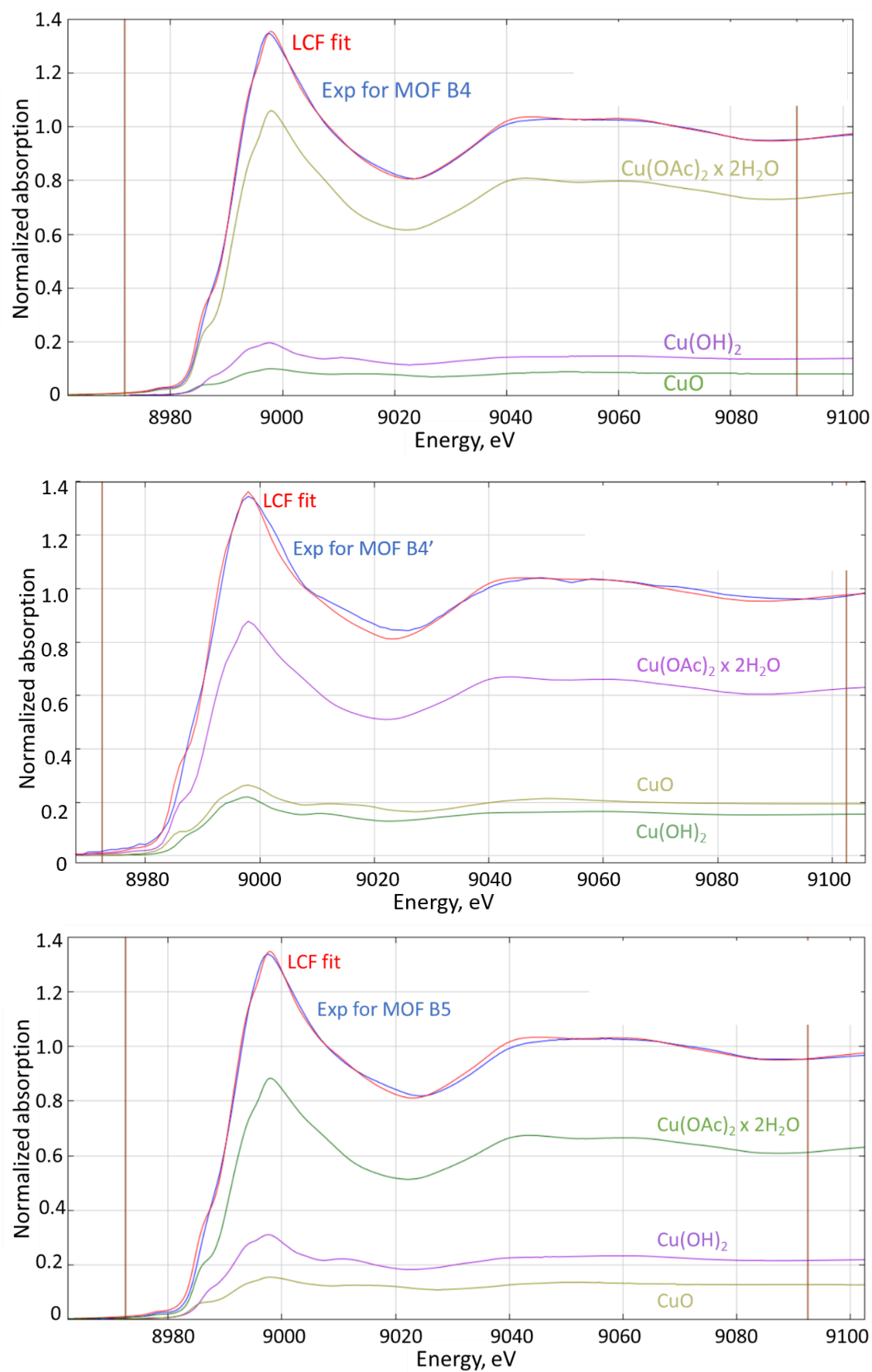
Figure S12.2.3. Results of fitting by the method of linear combination of the spectra of MOFs **B4**, **B4', B5** using the experimental spectra of comparison samples.

Table S12.2.3. Concentrations of components of the spectra of reference samples obtained by fitting by the linear combination method for MOF **B4**, **B4'**, **B5**.

	MOF **B4**	MOF **B4'**	MOF **B5**
Component 1 $Cu(OAc)_2$	78%	64%	67%
Component 2 $Cu(OH)_2$	15%	16%	24%
Component 3 CuO	7%	20%	9%

S13. Solid-state NMR analysis of MOF powder structure

S13.1. Methodology of signal assignment and analysis of spectra

The presence of paramagnetic Cu(II)-units in the framework of **B**, **B4**, **B4**' and **B5** significantly complicates the structure determination due to strong broadening and paramagnetic shifts of signals in the spectra, even under MAS conditions. Because of this, paramagnetic MOFs are quite rarely studied using NMR spectroscopy, and the necessary structural information becomes much more difficult to extract from the spectra. Also, literary methodologies do not always work and are not always applicable to new classes of objects.

To study Cu-MOFs using SSNMR, we modified and used more specialized approaches to analyze broad overlapping signals. The general strategy for assigning SSNMR spectra was as follows. First, a complete assignment of ^{13}C signals on the original ligand **A** was performed (in the solution and in the solid, using a standard set of 1D and 2D experiments). This assignment of ^{13}C chemical shifts can generally be transferred to the spectra of the MOF, however, it is necessary to take into account rather significant paramagnetic signal shifts, which also provide additional information about the structure. Resolving overlapping wide signals unambiguously is a challenging task, nevertheless, this can be successfully addressed using 2D ^{13}C-^{1}H CP-HETCOR methodologies with the use of FSLG spin-lock narrowing, which significantly increases the resolution in the spectra. The use of CP and CP-NQS in comparison with HPDEC and Spin-Echo-based pulse sequences allows for the unambiguous assignment of different types of the quaternary carbons and protonated carbons, and also 2D ^{13}C-^{1}H CP-HETCOR experiments with varying CP pulse duration (from 0.3 msec to 2 msec) allow to make a complete assignment of CH and quaternary-carbons, since changing the duration of CP allows to estimate the distances between H and C in space. In general, these approaches are fairly standard for SSNMR, but they have been adapted for paramagnetic Cu-MOFs – a class of objects under study. The complete final assignment and deconvolution of ^{13}C signals for all three MOFs is shown in Figures below and also in the main text of the manuscript.

A more detailed methodology for assigning signals in ^{13}C SSNMR spectra can be described as follows. At the first stage, the signals are preliminarily assigned based on the position of the chemical shifts, taking into account its broadening, which, when comparing the spectra with the initial ligand **A**, quite accurately describe the spectrum. At the next step, a series of edited ^{13}C spectra is made with observation of individual types or groups of signals. Using ^{13}C CP experiments (typical contact times of 2-5 msec) allows one to observe protonated carbons and closely related quaternary carbons (e.g., *ipso*), and to isolate by comparison the missing more distant quaternary carbons (e.g., C(O)O and partially *para*). Using ^{13}C CP with short contact pulse times (typically 300-800 usec) one can selectively observe only the signals from protonated carbons. Using ^{13}C CP NQS, on the contrary, one can selectively observe only quaternary carbons, while strongly broadened quaternary carbons with too short T_2 relaxation times (such as C(O)O or *para*) may not be visible and also be edited in this way. ^{13}C Spin-Echo techniques with different spin-echo times allow one to edit the spectrum with adjustment to specific T_2 relaxation times, including for broad signals, or, on the contrary, to partially narrowing the signals. Finally, a series of ^{13}C-^{1}H 2D HETCOR experiments with different parameters allow to refine the assignment made and to isolate individual strongly overlapping signals due to narrowing of signals with the help of FSLG spin-lock, including distant quaternary C(O)O carbons when using longer contact pulses (longer than 300-

500 usec). Also, two-dimensional ^{13}C-^{1}H experiments allow to refine the assignment due to observation of more distant H-C contacts through 2-3 bonds and further.

S13.2. General discussion of the analysis and assignment of A, B, B4, B4', B5 MOF

The main technique was based on a detailed analysis of the signal parameters of solid-state ^{1}H, ^{13}C, ^{29}Si NMR spectra. These parameters depend on the general and fine structure of the products, the influence of paramagnetic Cu(II)-centers, and their solvation environment. The paramagnetic shifts are nevertheless quite weak in absolute terms and the broadening is not so strong, due to the relative symmetrical environment of single copper(II) cations in the near coordination sphere (compared for example to the same dicopper tetraacetate $Cu_2(OAc)_4$). Combined with a range of 1D and 2D SSNMR experiments, this provides important structural information. Significant refinements to the structural analysis were provided by SSNMR experiments with MOF **B** and ligand **A**, the structure of which was unequivocally confirmed using XRD, NMR, HRMS ESI, etc.

As a result, structure models for **B**, **B4**, **B4**', and **B5** were proposed. All four products, despite significant external differences, are based on the same general skeleton and have similar structures. They contain one Cu(II)-center coordinated with two ArC(O)O-groups of ligand **A**. The main difference between the four structures (**B**, **B4**, **B4**' and **B5**), which was established using SSNMR, lies in the presence of monodentate ligands (Pyr, ROH or H_2O) in coordination spheres of Cu-centers, as well as disorder/heterogeneity and amorphous structures of **B4** and **B5**, compared to more crystalline **B** and **B4**'.

In the MOF **B**, there are three Pyr molecules in the nearest coordination sphere of Cu(II)-center, which matches the XRD (Section S11, Supp. Inf.) and XANES/EXAFS data (Section S12, Supp. Inf.). The pores also contain a significant amount of Pyr molecules and, apparently, H_2O. Excess of Pyr in pores is strongly disordered and influenced by paramagnetic copper(II), and it appears in the ^{13}C SSNMR spectra as a wide intense background hump under the main **B** signals with width ca. 300 ppm. When Pyr molecules evaporate from the pores in air, the ordered crystal structure of **B** begins to be disrupted, followed by amorphization. The structure of **B** becomes similar to **B4**, **B4**' and **B5**. Although significant disorder occurs, the basic framework of MOF **B** is retained.

The structure of product **B5** was studied in most detail using SSNMR. It is actually a completely amorphous structure. This amorphous aerogel structure leads to a surprisingly significant narrowing of the signals in the MAS SSNMR spectra, even taking into account the significant paramagnetic broadening due to the presence Cu(II)-ions. Apparently, despite the amorphizm, the disordering of the structure in the immediate environment is quite small, and the main amorphization occurs in the distant environment; in addition, the high degree of aerogelity can lead to additional narrowing of the signals. This allows us to study its structure in more detail. It is also shown that pores constitute a significant volume of the **B5** structure. Despite supercritical drying, a small amount of MeOH molecules coordinated with Cu-centers remains in **B5**. A rough estimate is approximately one MeOH molecule per Cu-center and two ArC(O)O groups. Apparently, the rest of the coordination sphere of Cu-centers in **B5** is occupied by H_2O molecules (see below).

The structure of **B4** is also largely amorphous and is generally similar to **B5**. However, it is significantly denser, more heterogeneous and may contain residual crystalline phases (from MOF **B**) that have not completely converted to amorphous form (**B4**), which results in an overall highly disordered structure. As a result, the **B4** signals are much more broadened compared to **B5** in the SSNMR spectra, although they do not change their position. Also, **B4** does not contain visible solvent residues (^{i}PrOH, Pyr); perhaps there are few of them and/or they are highly disordered.

The structure of **B4** is denser than **B5** and contains fewer pores, which is consistent with other experimental data (see below).

For all four types of structures (**B**, **B4**, **B4'**, and **B5**) ^{1}H, ^{13}C, ^{13}C-^{1}H correlation SSNMR spectra are very similar in chemical shifts description terminology due to the similarity of the structures of the main framework (with the exception of coordinated solvent molecules). However, they differ in a large extent in the width of the signals, which increases when moving from **B5** to **B4** and **B**. Moreover, compared to the original ligand **A**, ^{13}C SSNMR chemical shifts undergo significant changes due to coordination with paramagnetic Cu(II)-centers. In this case, paramagnetic shifts are observed, which are most significant for C-centers close to paramagnetic Cu(II)-centers, and weaken with distance from it. Thus, the description of paramagnetic shifts allows us to observe coordination with Cu(II)-centers.
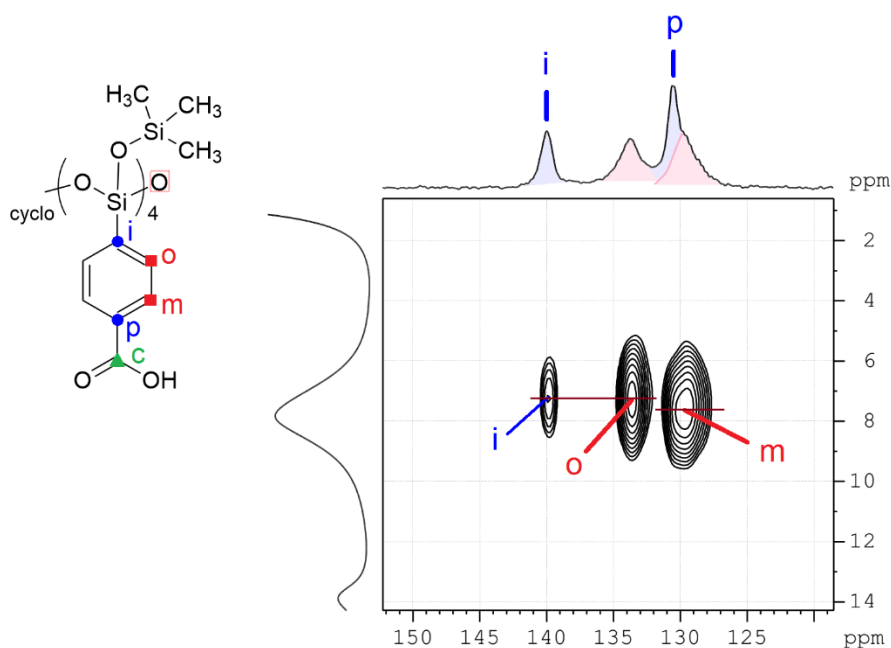
Figure S13.2.1. Assignment of SSNMR MAS spectra of compound **A**
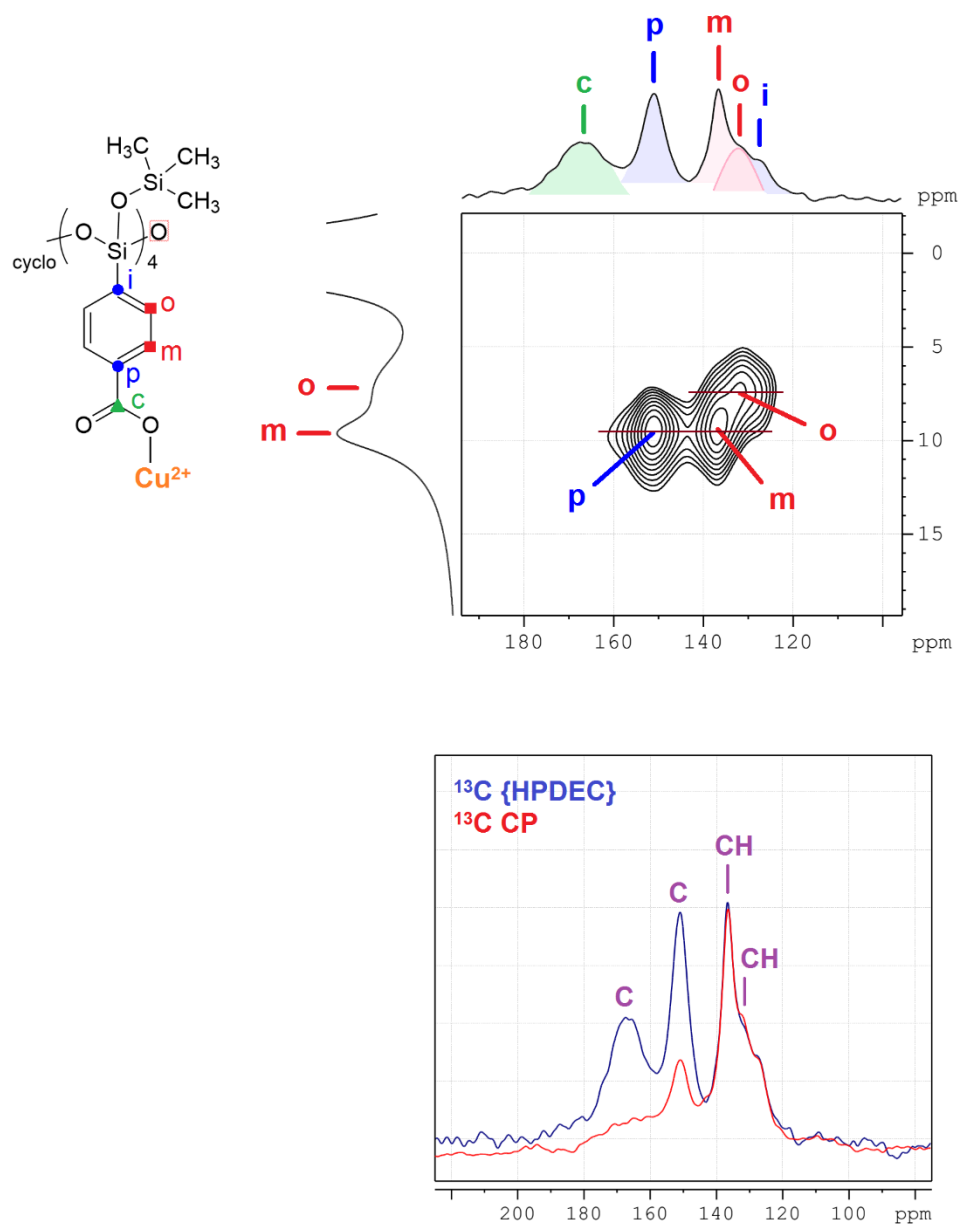
Figure S13.2.2. Assignment of SSNMR MAS spectra of MOF **B5**
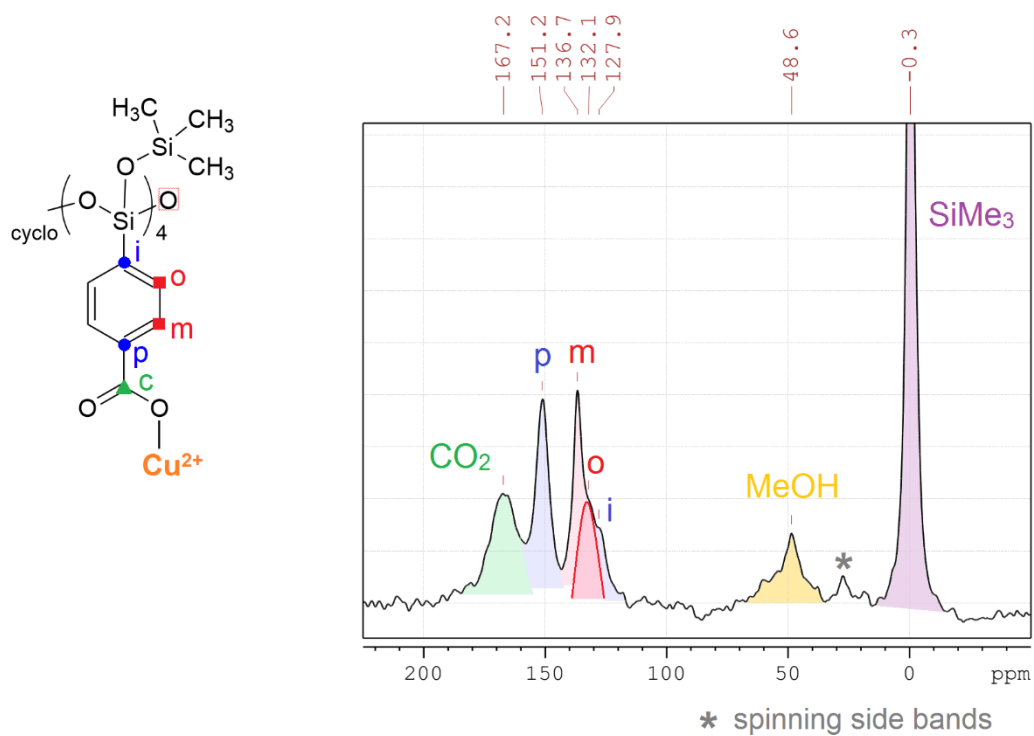
Figure S13.2.3. ^{13}C HPDEC SSNMR MAS spectrum of MOF **B5** with assignment
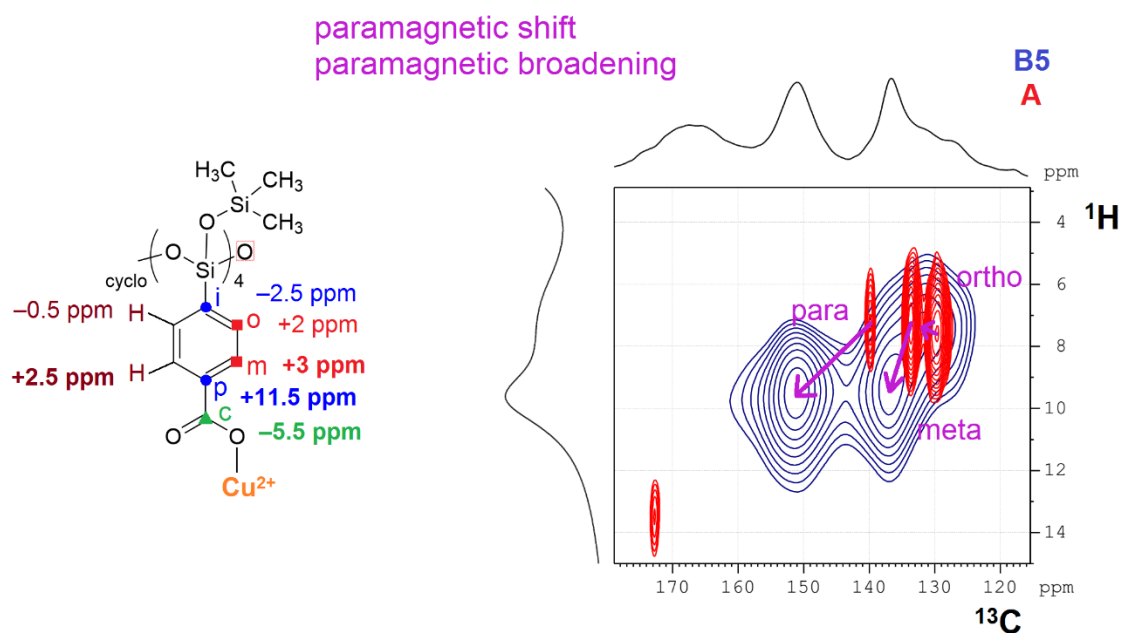
Figure S13.2.4. Paramagnetic shifts (^{13}C, ^1H) in MOF **B5**
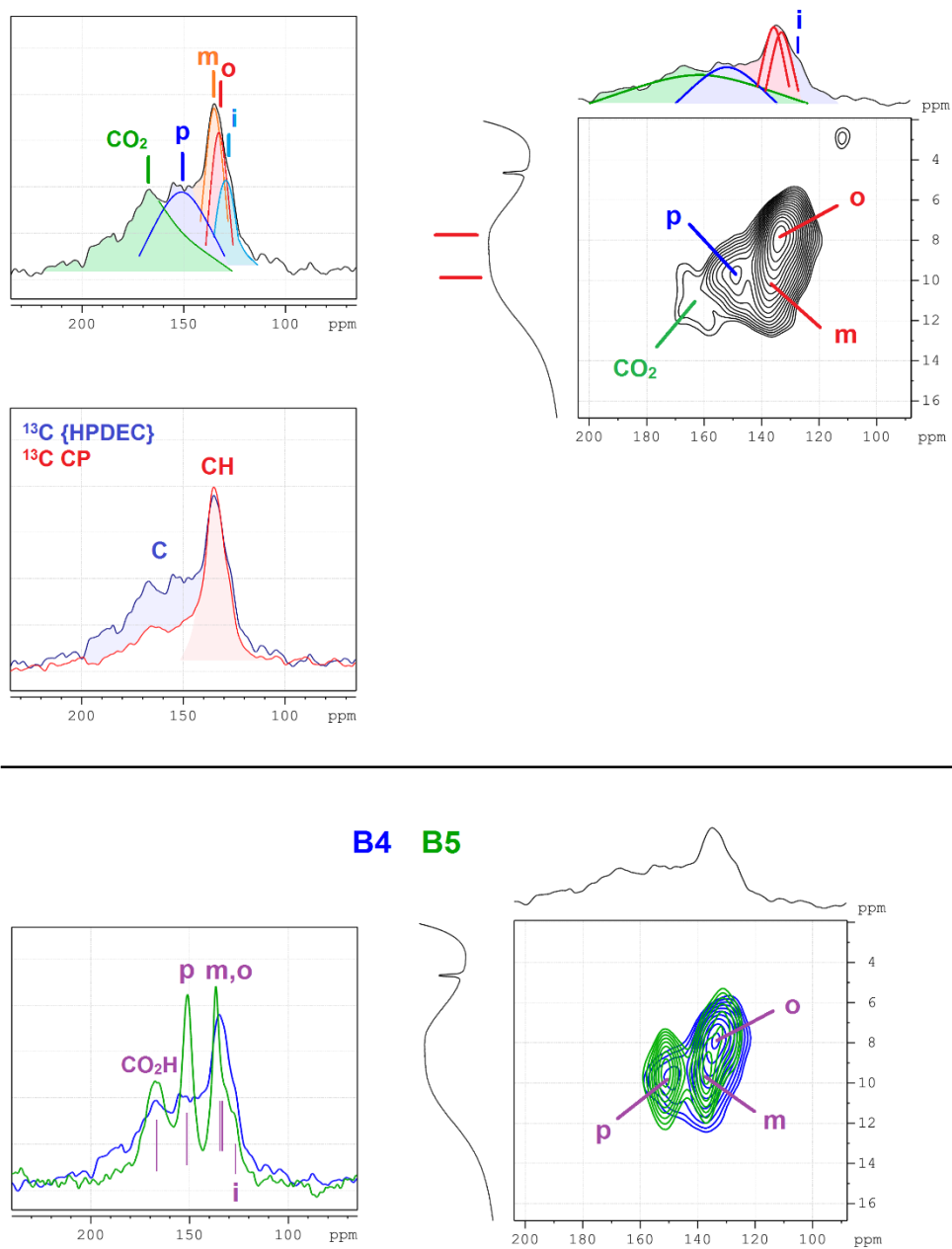
Figure S13.2.5. Assignment of SSNMR MAS spectra of MOF **B4** (top) and comparison with MOF **B5** (bottom)
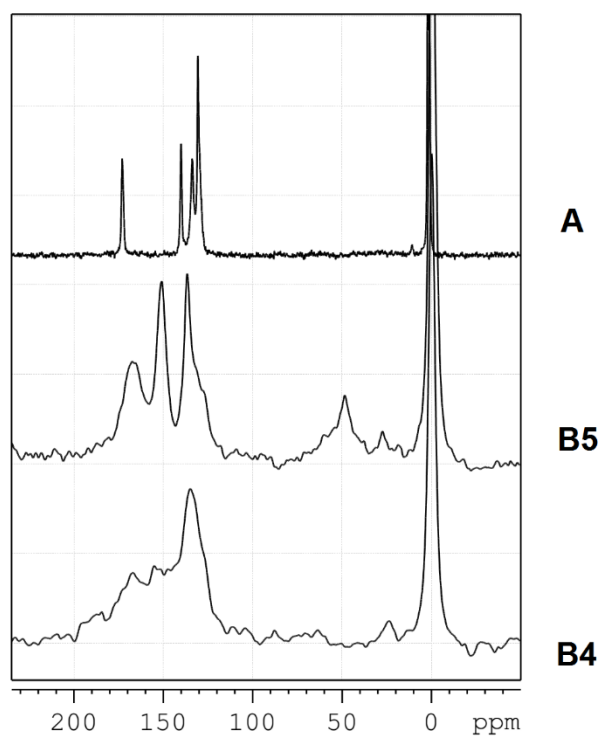
Figure S13.2.6. Comparison of ^{13}C SSNMR MAS spectra of **A, B4, B5** MOF
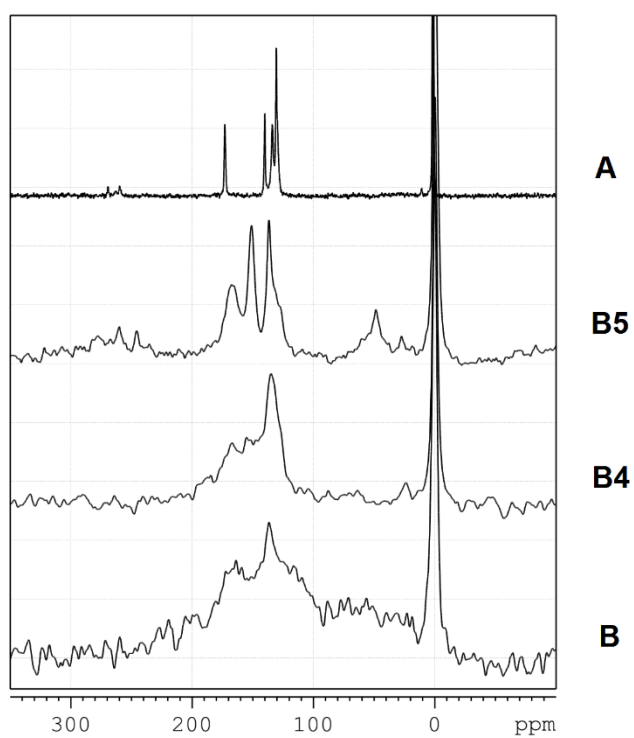
Figure S13.2.7. Comparison of ^{13}C SSNMR MAS spectra of **A, B, B4, B5** MOF

¹H MAS 14 kHz SSNMR
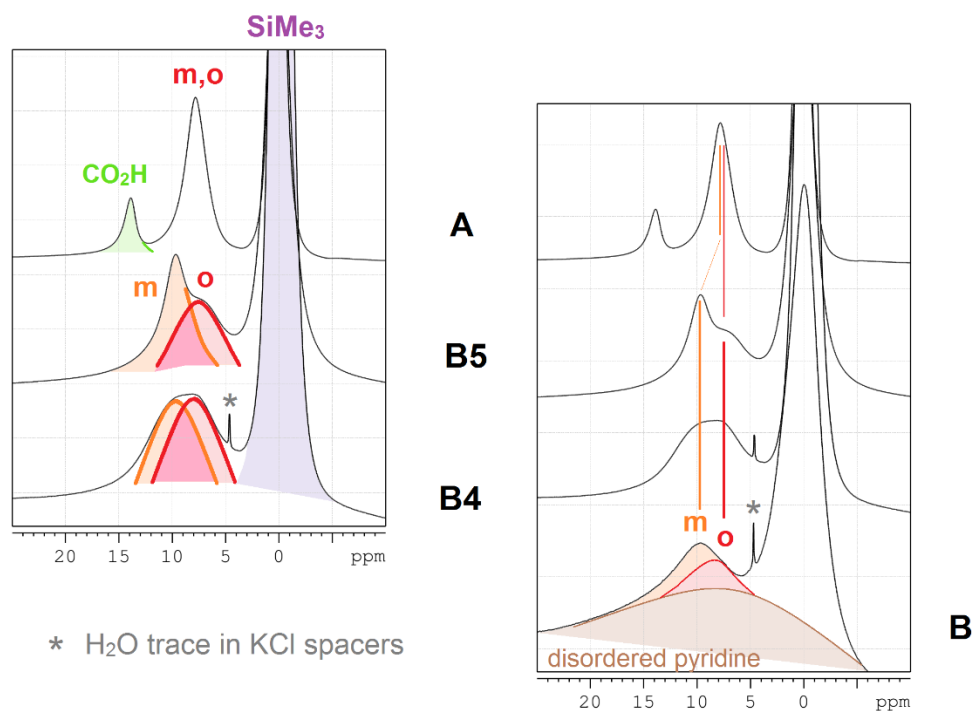
Figure S13.2.8. Comparison of ¹H SSNMR (14 kHz MAS) spectra of **A, B, B4, B5** MOF with assignment

²⁹Si–¹H HETCOR MAS SSNMR
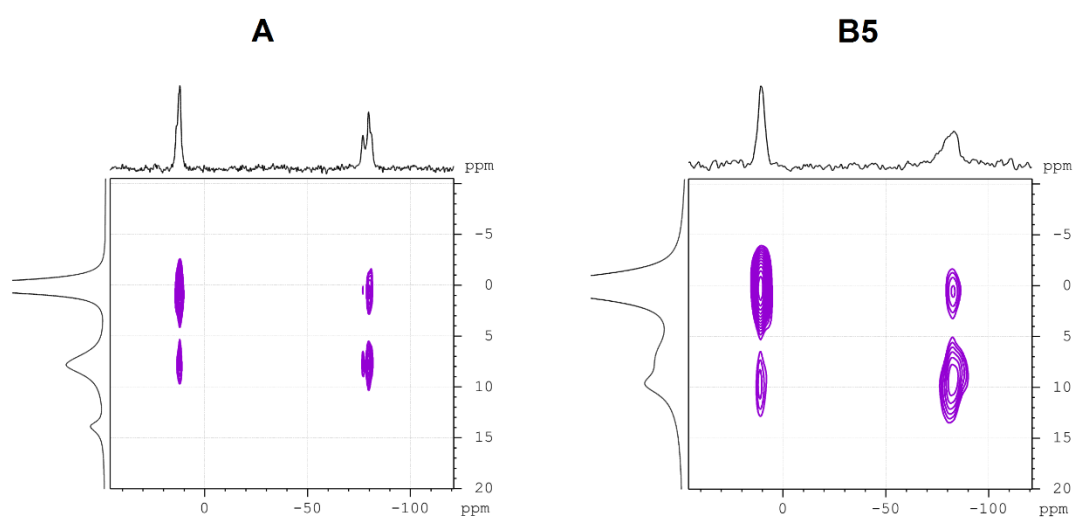
Figure S13.2.9. Comparison of ²⁹Si-¹H HETCOR SSNMR MAS spectra of **A, B4, B5** MOF with assignment

B5
^{13}C MAS SSNMR
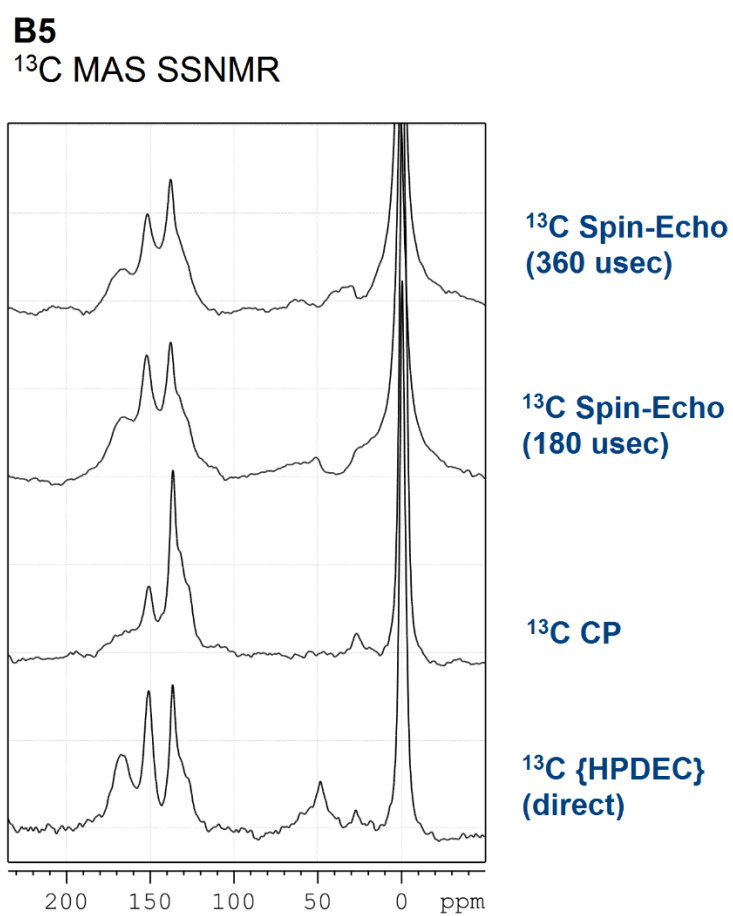
Figure S13.2.10. ^{13}C SSNMR MAS spectra for MOF **B5** recorded in different modes
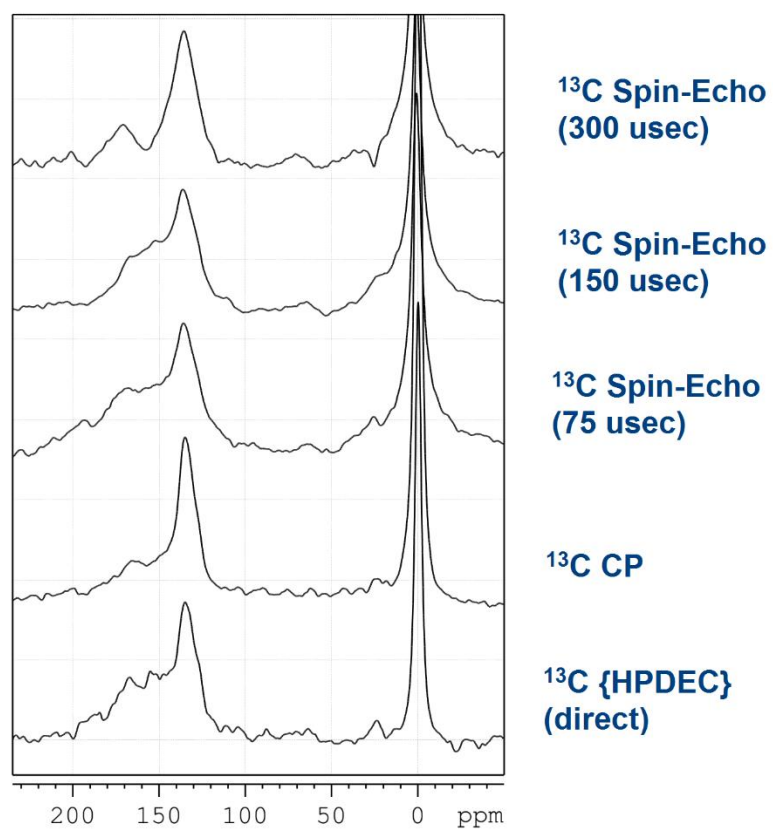
Figure S13.2.11. ^{13}C SSNMR MAS spectra for MOF **B4** recorded in different modes

B
^{13}C MAS SSNMR

^{13}C Spin-Echo (170 usec)

^{13}C Spin-Echo (85 usec)

^{13}C CP

300   200   100   0   ppm
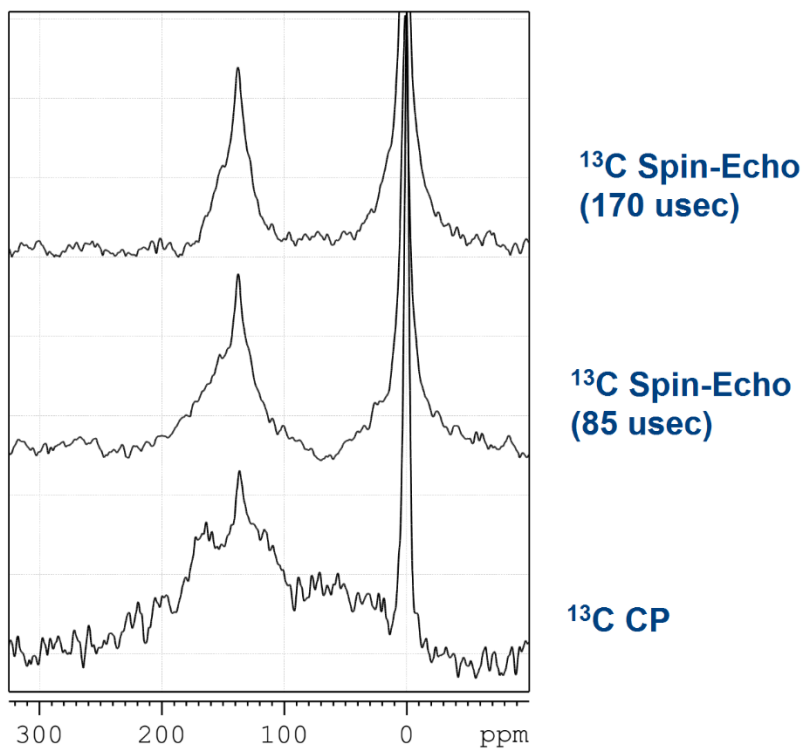
Figure S13.2.12. ^{13}C SSNMR MAS spectra for MOF **B** recorded in different modes

¹³C–¹H HETCOR MAS SSNMR

A

B5

B4
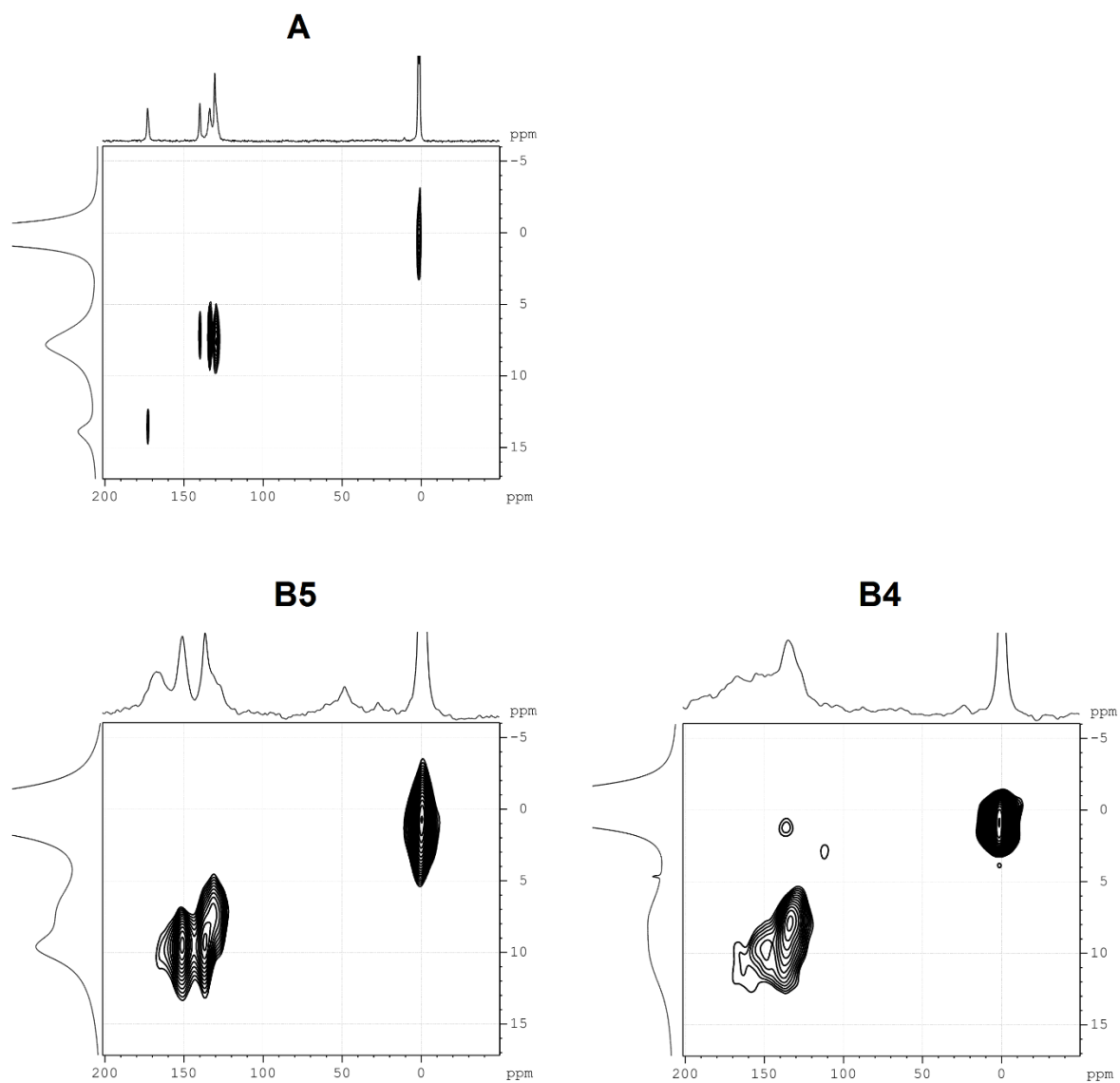
Figure S13.2.13. 2D ¹³C-¹H HETCOR SSNMR MAS spectra of **A, B4, B5** MOF

^{13}C–^{1}H CP FSLG HETCOR MAS SSNMR 2D spectra
with full assignment of the signals
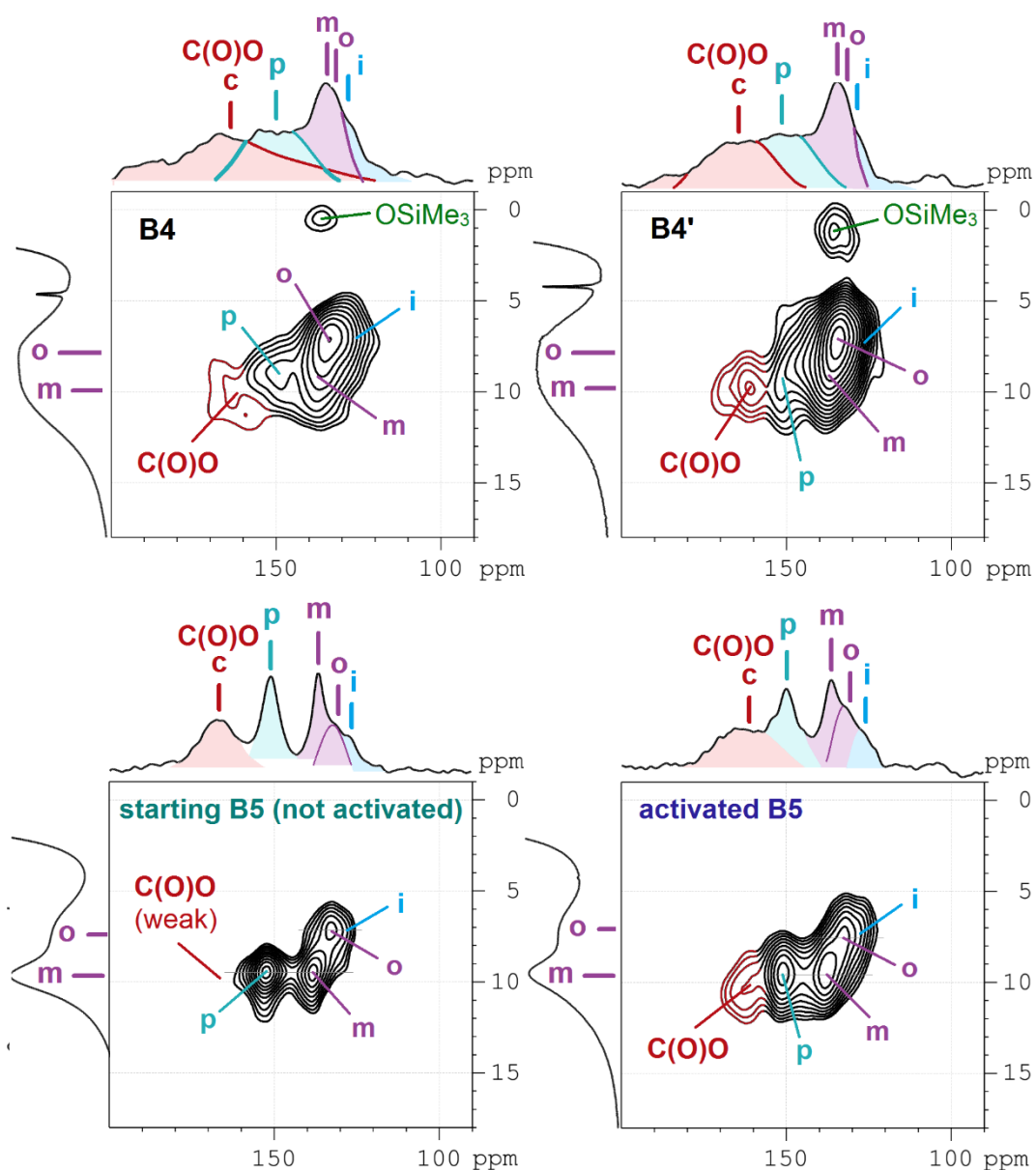
Figure S13.2.14. Comparison of the 2D ^{13}C-^{1}H CP FSLG HETCOR SSNMR spectra (13 kHz MAS) for four different MOF **B4**, **B4'**, not activated **B5**, activated **B5**

S13.3. Solid-state NMR analysis of copper coordination sphere in MOF B5

At the next step, we studied the Cu-coordination sphere in more detail using solid-state NMR (SSNMR) approaches.

Since copper is coordinated only with two carboxylate groups, for coordination saturation of its sphere, copper must be coordinated with three other additional ligands. In MOF **B** it is pyridine, in aerogel MOF **B5** it is water or methanol. By additionally drying (activation) the **B5** [conditions: heating (at 80-100 °C and 1 atm) or vacuum treatment (at <300 mbar and r.t.), fast H_2O release occurs (from a second to a minute)], it is possible to completely remove all ligands and make the copper center coordinatively unsaturated. In this case, the color of the MOF changes from blue to blue-violet.

In the SSNMR spectra, a change in the copper coordination sphere can be clearly observed. In the initial **B5**, according to the SSNMR spectra, there are on average three water molecules per Cu-center (the amount of water was determined by quantitative integration of D-signal from D_2O in ^2H SSNMR using an external standard (glycine-d2)), or two water molecules and one methanol molecule (the amount of methanol was approximately determined by quantitative integration of ^{13}C signals using single-pulse direct acquisition of the spectra); both **B5** variants were obtained. After drying the **B5** and packing it into a rotor in a glove box, a significant broadening (up to 2.4 kHz) of the ^{13}C signal of the C(O)O-carboxylate groups bound to copper and an additional paramagnetic shift to a strong field (–6 ppm) occur in the ^{13}C SSNMR spectra, since the effect of copper increases due to the absence of ligands and CSA (chemical shift anisotropy) also increases significantly. Also, a weaker shift is experienced for the next atom signal from the copper (*para*-carbon aromatic atom). All other signals remain in place and are somewhat broadened due to the increase of CSA. The signal of coordinated methanol completel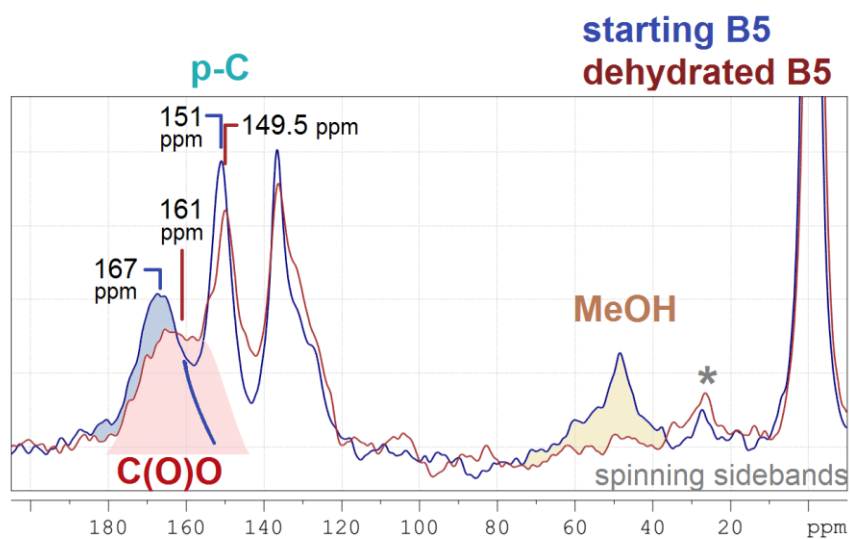y disappears. Thus, SSNMR spectroscopy is a very sensitive method for detecting fine parameters of the structure and changes in the copper coordination sphere. MOF **B5** after drying in a coordinatively unsaturated state is very hygroscopic and instantly adsorbs moisture in the air, turning into the initial state of MOF **B5**. Despite the fact that this MOF is strongly hydrophobic, it combines these two properties. Nevertheless, high hydrophobicity prevents it from absorbing much moisture from the air, only to fill the coordinatively unsaturated copper sphere. According to SSNMR spectra, slightly less than in the initial **B5** before drying, approximately 2.5 water molecules per copper center, which leads to slightly wider C(O)O signals in the ^{13}C spectra compared to the initial **B5**, due to the increased disorder of the ligands and greater CSA. Due to direct coordination with paramagnetic copper atom, water signal in ^1H SSNMR spectra is too broad (more than spectral range) and cannot be directly observed in ^1H spectra (other signals and probe background completely block it). To observe coordinated water and its dehydration in vacuum, we used D_2O isotopic labels to observe water on ^2H. In the ^2H spectra, water gives a very broad signal due to paramagnetic broadening with a width of about 180 ppm and a chemical shift of about +9 ppm, control experiments and spinning sidebands unambiguously confirm the belonging of this signal.

Figure 13.3.1. Visual photo of MOF **B5** used for SSNMR studies: starting, activated (dehydrated), and with subsequent sorption of water (heavy water)

Figure 13.3.2. ^{13}C HPDEC SSNMR spectra for starting and activated (dehydrated) MOF **B5**

$^{13}C–^1H$ CP FSLG HETCOR MAS ssNMR 2D spectra
contact time 1 msec
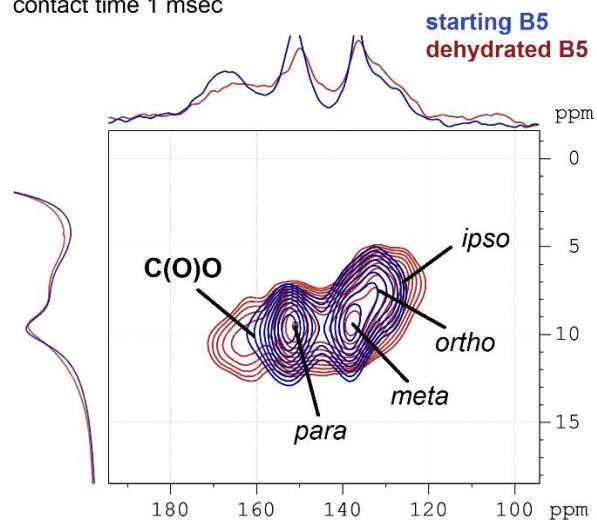
Figure S13.3.3. ^{13}C-^1H CP FSLG HETCOR SSNMR spectra for starting and activated (dehydrated) MOF **B5**

Difference in coordination of ligands and parameters of key ^{13}C signals

A	**B5** ·MeOH ·2H$_2$O	**B5** dehydrated	**B5** ·2.5D$_2$O
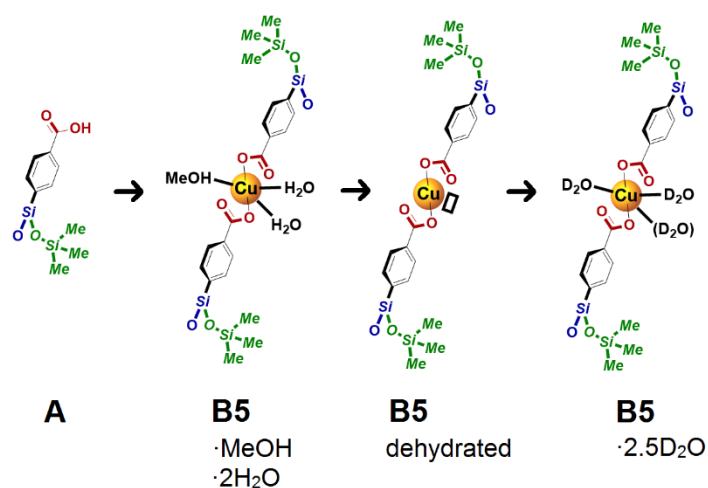
C(O)O	δ, ppm	W$_{1/2}$, Hz		
173 ppm 140 Hz	**167 ppm** 1500 Hz	**161 ppm** 2400 Hz	**167 ppm** 1700 Hz

paramagnetic shift, Δ, ppm

	–6 ppm	–12 ppm	–6 ppm

para-C   δ, ppm

139.5 ppm	151 ppm	149.5 ppm	151 ppm

Figure S13.3.4. Difference in coordination of ligands and parameters of key ^{13}C signals of the MOF **B5**: starting, activated (dehydrated), and with subsequent sorption of water (heavy water)

S13.4. Solid-state NMR analysis of supramolecular packing and copper coordination sphere in MOF B4' crystals

<u>General description of the study of the MOF **B4'** structure based on the results of SSNMR in combination with data from other methods</u>

B4' has an apparent crystalline structure, but in reality, it is highly disordered but not completely amorphous. Compared to related **B4**, which is amorphous to a large extent (but may contain residual crystalline phases), the structure of **B4'** is significantly more ordered.

Thus, the most revealing comparison is with this related **B4**, which has also been studied in detail by SSNMR. The **B4** has a mainly amorphous and a highly disordered structure, and, as a consequence, highly broadened signals. **B4'**, on the contrary, has narrower signals (especially the key signal of C(O)O carboxylate groups), which is a direct consequence of the partial ordering and crystallinity of the structure.

On the contrary, the spectra of **B4'** are significantly inferior in signal width to amorphous **B5**. However, it is necessary to take into account that **B5** is a low-density aerogel (and this already leads to some narrowing of the signals), and **B5**, despite its amorphous nature, also apparently has a fairly ordered structure at the molecular level. Against, **B4'** has a larger chemical shift anisotropy due to its crystallinity and numerous surface defects (see below).

Unfortunately, it is not possible to directly compare the SSNMR spectra with crystalline MOF **B**, since its crystals are significantly degraded under packing and MAS conditions, resulting in completely broadened and difficult to analyze spectra, apparently containing several different overlapping disordered phases. For **B4'**, special additional stabilizing conditions were used during spectra recording to avoid similar problems with partial destruction of the structure.

<u>Experimental description of spectra recording of the **B4'**</u>

For **B4'**, although its crystals are much more stable, there was a risk of partial destruction of the structure, since MOFs are sensitive to increased pressure and stresses that occur during pressing and grinding (MAS rotation even at high speeds has significantly less impact). Therefore, a gentle approach was taken for the **B4'** packing, using the minimum possible force to create the required homogeneity in the rotor and without grinding the crystals. During long-term structural MAS SSNMR experiments, additional fast ^{13}C SSNMR monitoring was carried out to control a possibility of the destruction of the supramolecular structure of MOF and for the comparison of the spectra before and after. Only 10-15 mg of **B4'** was used for the 4 mm rotor, owing to the packing with KCl spacers with a thin layer of target unpressed **B4'** in the center of the rotor homogeneity zone. Using this allows avoiding problems associated with filling the 4mm rotor entirely with MOF.

The structure of the **B4'** MOF was studied in detail using a set of SSNMR experiments (4 mm MAS probe, 9-14 kHz MAS) – ^{1}H, ^{13}C HPDEC, ^{13}C CP with different CP-pulse times, ^{13}C CP-NQS, ^{13}C Spin-Echo sequences, ^{13}C-^{1}H CP-HETCOR with different parameters, ^{29}Si CP. The use of a set of methodologies with different parameters (with special attention paid to ^{13}C spectra) allows to separate and identify individual overlapping broad signals and to carry out a detailed analysis of the spectra.

Analysis of supramolecular packing of **B4'**

The MOF **B4'** is intermediate and differs from the others (**B, B4, B5**), and has partial ordering and crystallinity. In the SSNMR studies of **B4'**, special attention was paid to the investigating the spatial intermolecular arrangement of distant groups using CP-based experiments to reveal the features of structure organization and packing at the supramolecular level. According to electron microscopy data (SEM, Section S14, Supp. Inf.) the high-level structure **B4'** is represented by a set of long thread-like 30-40 nm diameter fibers, packed in parallel into layers and a layered structure as a whole, which form macroscopic crystals. Other **B**-series MOFs do not have this structure, but show some characteristic features: they also have a layered structure and have the beginnings of splitting into individual fibers (**B, B4$_{sol}$, B4'$_{sol}$**). Compared to others, **B4'** has closer molecular chains at the supramolecular level, due to compression and a controlled formation of numerous defects on the surface of the threads. All this is manifested in a number of spatial and other effects in the SSNMR spectra. According to SSNMR data, this makes the protons become closer in space and a significantly increases the efficiency of ^{1}H-^{13}C cross-polarization (CP) for the internal quaternary carboxylate C(O)O-groups distant from the protons, which are indicative in this regard. Apparently, due to the convergence of molecular chains, the structure in the **B4'** MOF crystal is stretched in length into a thread-like packing, and also due to compression, the controlled formation of numerous surface defects (on the surface of the threads) and the final formation of long individual threads (or fibers) occurs. The initial layered crystal packing results in the multi-scale **B4'** structure observed by SEM during formation. At the same time, the orderliness of the crystal structure is partially preserved, and the structure does not turn completely into amorphous. Also, coordinated pyridine is observed by SSNMR, which, due to the paramagnetic influence of Cu(II), has very strong signal broadening and an order of magnitude shorter T_2 relaxation times, and can therefore be distinguished from the signals of the MOF skeleton by a set of experiments. Due to the very strong broadening of the signals, it is difficult to estimate the quantitative content of pyridine, but apparently there is not much pyridine there (significantly less than 3 coordinate molecules) and the coordination sphere of copper(II) is partially unsaturated, because some of the pyridine evaporates during supercritical drying, and this appears to be the driving force behind the compression of the molecular structure and the formation of surface defects that lead to the final **B4'** filamentary structure. When pyridine is removed from the Cu coordination sphere, its compression is observed, i.e., the carboxylate C(O)O-ligands become somewhat closer to the Cu(II). A similar effect was observed by SSNMR upon dehydration of **B5** (see the corresponding section in the main text), but in that case it was reversible. For **B4'** this effect is irreversible and leads to controlled deformation of the structure upon its production. In the SSNMR spectra this is manifested as an increase in the paramagnetic shift of the ^{13}C(O)O signal due to the proximity to Cu(II) (additionally by 4 ppm to a strong field, from 167 ppm to 163 ppm). This is also confirmed by the EXAFS data.
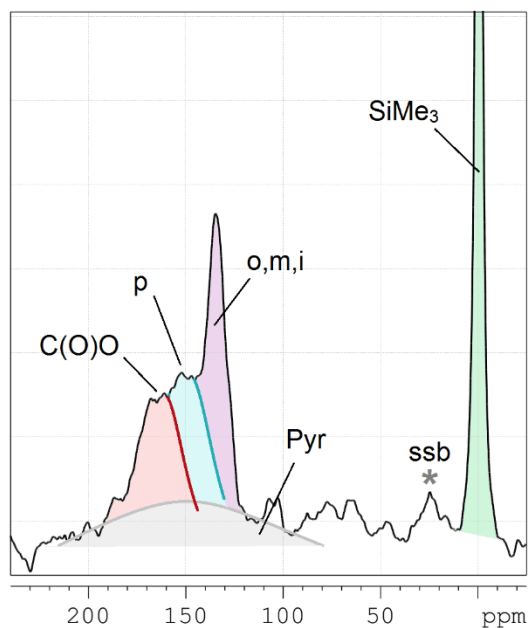
Figure S13.4.1. Visual photo of MOF **B4'** crystals used for SSNMR studies
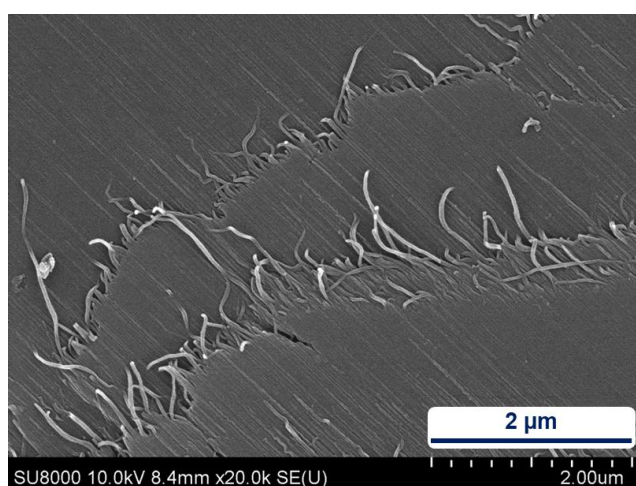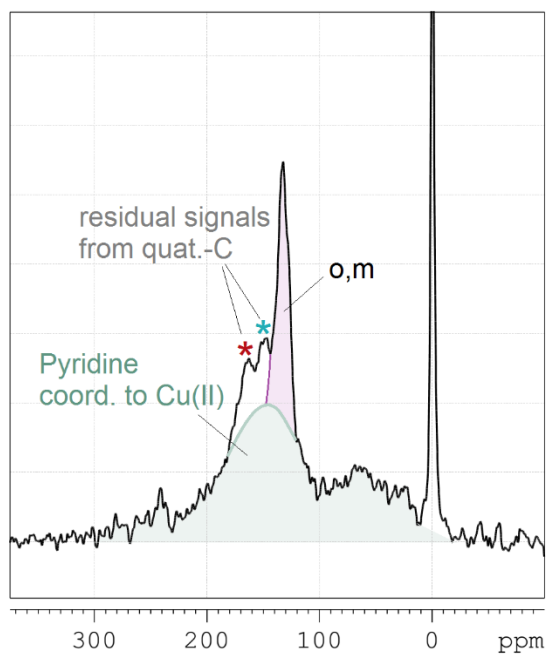

Figure S13.4.2. SEM imaging of MOF **B4'** crystals used for SSNMR studies, showing filamentous layered 3D packing with fibers of 30-40 nm diameter
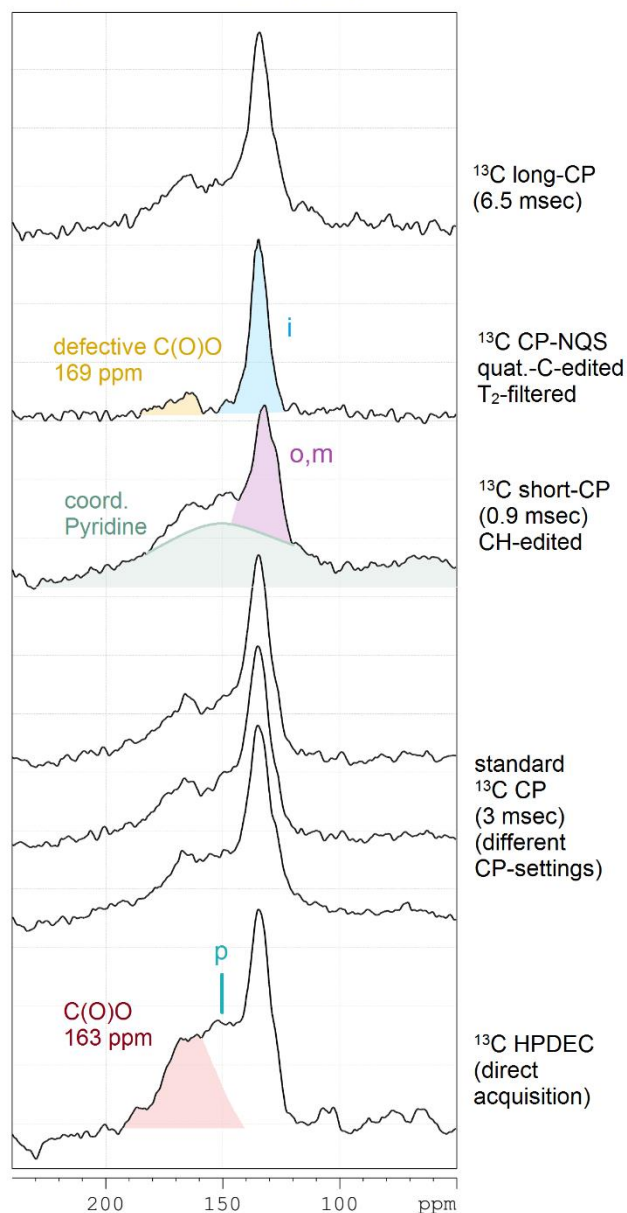
Figure S13.4.3. ^{13}C HPDEC MAS SSNMR spectrum (direct acquisition) with assignment

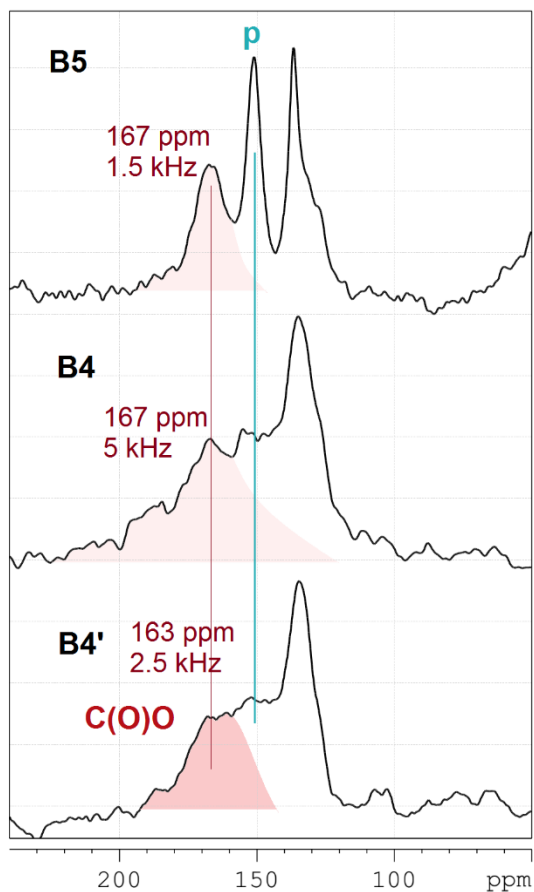**Figure S13.4.4.** Wideline CH-edited ^{13}C short-CP MAS SSNMR spectrum for assignment of pyridine coordinated to paramagnetic Cu(II)
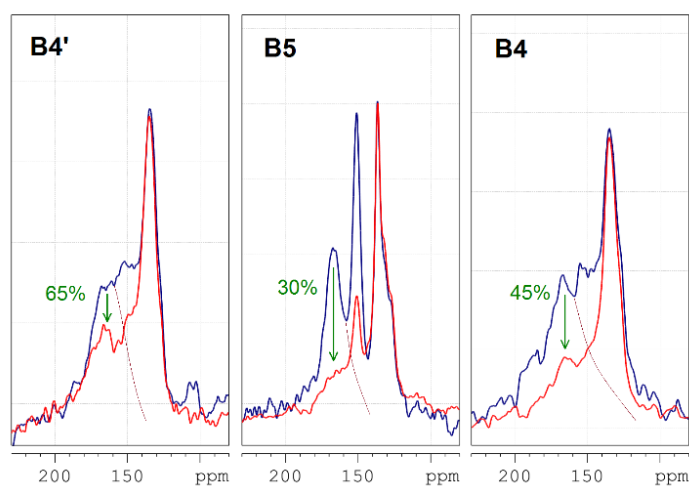
Figure S13.4.5. ^{13}C MAS SSNMR spectra recorded in different modes for assignment and detailed analysis of structure on supramolecular level

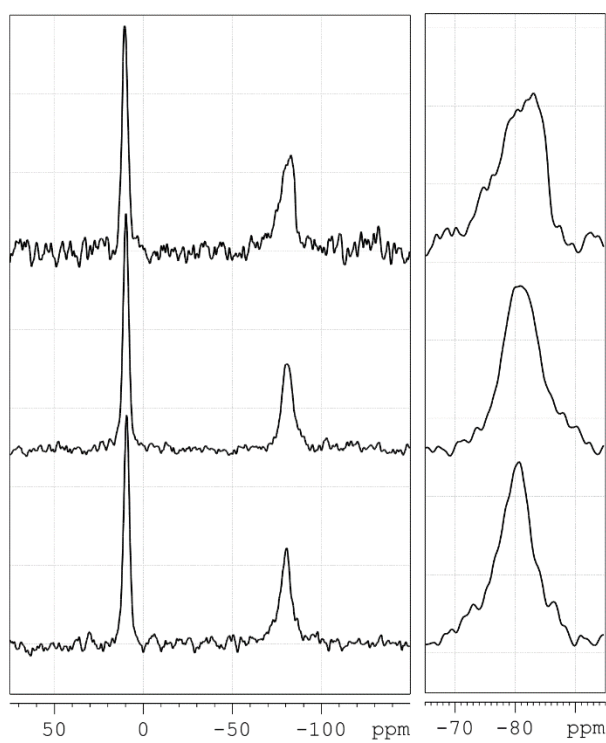^{13}C HPDEC MAS ssNMR spectra

Figure S13.4.6. ^{13}C HPDEC MAS SSNMR spectra (direct acquisition) of MOF **B4', B4, B5** – comparison and analysis of key C(O)O signal parameters

^{13}C HPDEC (dark blue), ^{13}C CP (3 msec) (red)
efficiency of CP to C(O)O compared to CH-signals (green)

Figure S13.4.7. Intensity difference of ^{13}C CP and HPDEC MAS SSNMR spectra of MOF **B4', B4, B5** for detailed analysis of structure, efficiency of CP-transfer to C(O)O compared to CH for different MOF

Figure S13.4.8. ^{29}Si CP MAS SSNMR spectra of MOF **B4', B4, B5** – comparison and analysis of cyclic-Si signal parameters
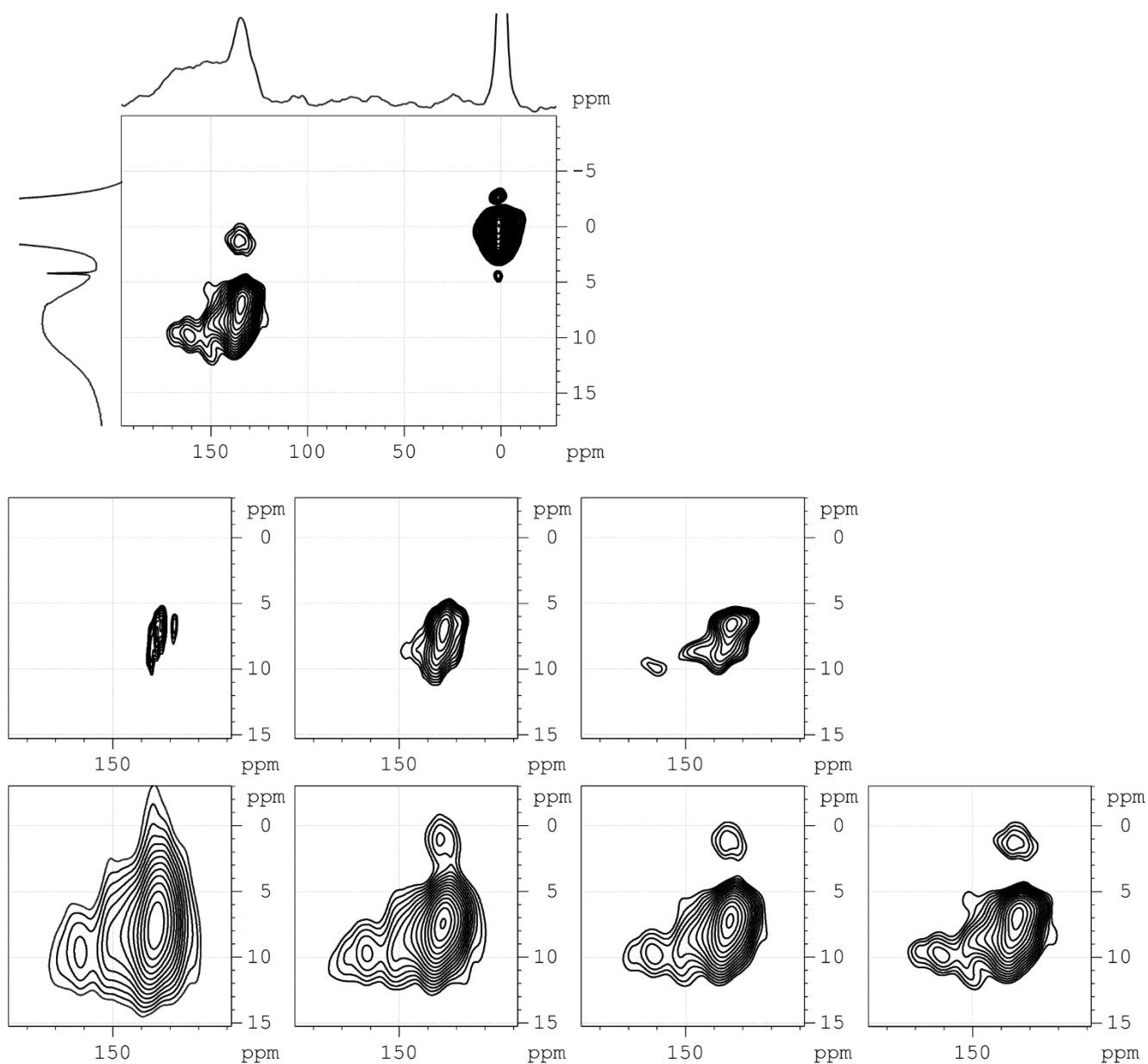
Figure S13.4.9. 2D ^{13}C-^{1}H CP FSLG HETCOR SSNMR spectra (13 kHz MAS) in different modes and processing parameters for assignment and detailed analysis of structure **B4'** on supramolecular level

S13.5. References for SSNMR Section.

General references for SSNMR method description:

1. B. Reif, S. E. Ashbrook, L. Emsley, M. Hong, *Nat Rev Methods Primers* **2021**, *1*, 2.

References for SSNMR studies of MOF:

2. C. He, S. Li, Y. Xiao, J. Xu, F. Deng, *Solid State Nucl. Magn. Reson.* **2022**, *117*, 101772.

3. B. E. G. Lucier, S. Chen, Y. Huang, *Acc. Chem. Res.* **2018**, *51*, 319-330.

4. S. Li, O. Lafon, W. Wang, Q. Wang, X. Wang, Y. Li, J. Xu, F. Deng, *Adv. Mater.* **2020**, *32*, 2002879.

5. E. Brunner, M. Rauche, *Chem. Sci.* **2020**, *11*, 4297-4304.

6. Y. Fu, H. Guan, J. Yin, X. Kong, *Coord. Chem. Rev.* **2021**, *427*, 213563.

7. Y. Fu, Y. Yao, A. C. Force, J. Li, K. Mochizuki, J. R. Long, J. A. Reimer, G. D. Paepe, X. Kong, *Nat. Commun.* **2023**, *14*, 2386.

8. A. A. Gabrienko, S. Chaemchuen, Z. Kou, N. Ogiwara, H. Kitagawa, A. E. Khudozhitkov, A. G. Stepanov, D. I. Kolokolov, F. Verpoort, Angew. Chem. Int. Ed. 2025, 64, e202414823

9. A. J. Rossini, A. Zagdoun, M. Lelli, A. Lesage, C. Coperet, L. Emsley, *Acc. Chem. Res.* **2013**, *46*, 1942-1951.

References for SSNMR of Paramagnetic MOF:

10. C. A. Klug, M. W. Swift, J. B. Miller, J. L. Lyons, A. Albert, M. Laskoski, C. M. Hangarter, *Solid State Nucl. Magn. Reson.* **2022**, *120*, 101811.

11. D. M. Dawson, L. E. Jamieson, M. I. H. Mohideen, A. C. McKinlay, I. A. Smellie, R. Cadou, N. S. Keddie, R. E. Morris, S. E. Ashbrook, *Phys. Chem. Chem. Phys.* **2013**, *15*, 919-929.

12. Y. Jiang, J. Huang, B. Kasumaj, G. Jeschke, M. Hunger, T. Mallat, A. Baiker, *J. Am. Chem. Soc.* **2009**, *131*, 2058-2059.

References for SSNMR of Paramagnetic Cu$_2$(O(O)CR)$_4$-units in MOF:

13. Z. Ke, L. E. Jamieson, D. M. Dawson, S. E. Ashbrook, M. Buhl, *Solid State Nucl. Magn. Reson.* **2019**, *101*, 31-37.

14. F. Gul-E-Noor, B. Jee, A. Poppl, M. Hartmann, D. Himsl, M. Bertmer, *Phys. Chem. Chem. Phys.* **2011**, *13*, 7783-7788.

15. G. W. Peterson, G. W. Wagner, A. Balboa, J. Mahle, T. Sewell, C. J. Karwacki, *J. Phys. Chem. C* **2009**, *113*, 13906-13917.

16. M. Rauche, S. Ehrling, L. Abylgazina, C. Bachetzky, I. Senkovska, S. Kaskel, E. Brunner, *Solid State Nucl. Magn. Reson.* **2022**, *120*, 101809.

17. D. M. Dawson, L. E. Jamieson, M. I. H. Mohideen, A. C. McKinlay, I. A. Smellie, R. Cadou, N. S. Keddie, R. E. Morris, S. E. Ashbrook, *Phys. Chem. Chem. Phys.* **2013**, *15*, 919-929.

18. L. N. McHugh, M. J. McPherson, L. J. McCormick, S. A. Morris, P. S. Wheatley, S. J. Teat, D. McKay, D. M. Dawson, C. E. F. Sansome, S. E. Ashbrook, C. A. Stone, M. W. Smith, R. E. Morris, *Nat. Chem.* **2018**, *10*, 1096-1102

19. D. M. Dawson, C. E. F. Sansome, L. N. McHugh, M. J. McPherson, L. J. McCormick McPherson, R. E. Morris, S. E. Ashbrook, *Solid State Nucl. Magn. Reson.* **2019**, *101*, 44-50.
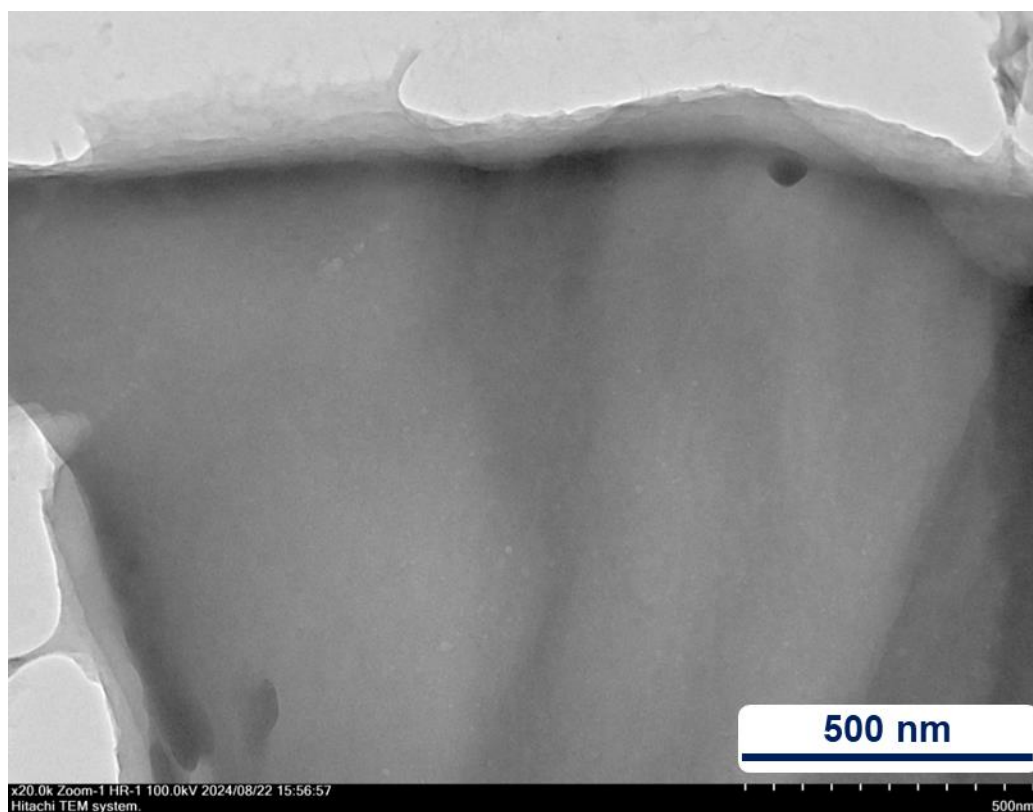
References for SSNMR studies of filamentous structure:

20. T. Kress, M. J. Duer, *J. Am. Chem. Soc.* **2025**, *ASAP*, 10.1021/jacs.4c13930.

S14. SEM and TEM
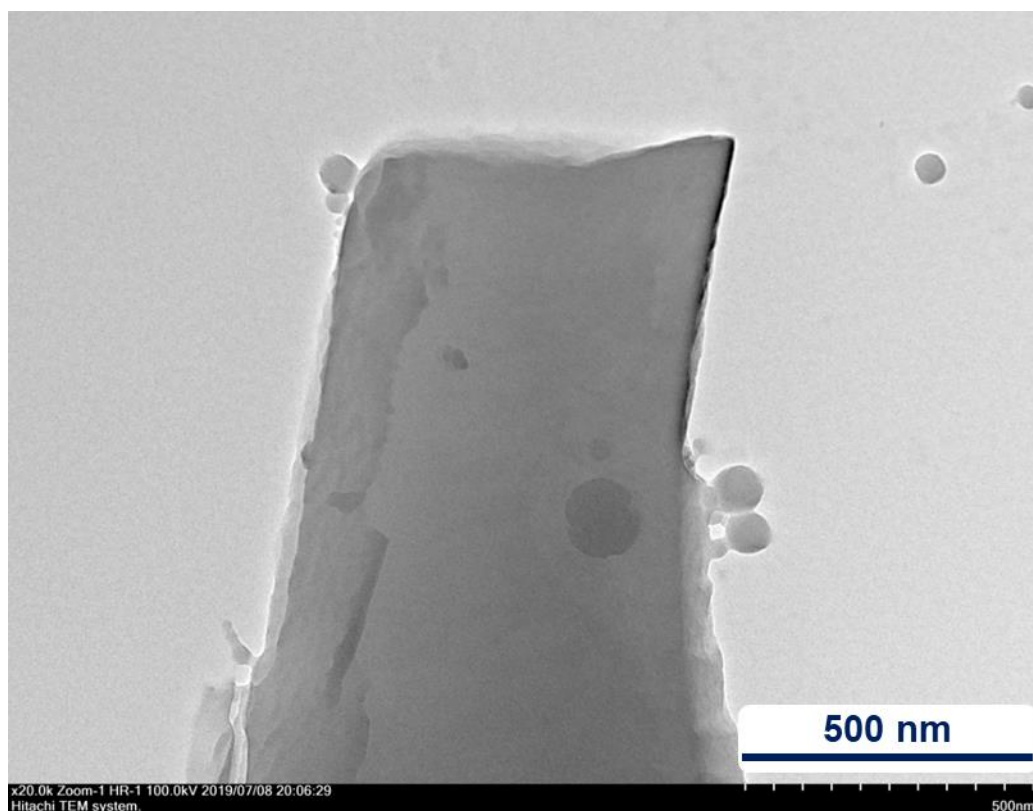
Figure S14.1. Full size TEM image of the crystalline sample **B** stored in the mother liquor

Figure S14.2. Full size TEM image of the crystalline sample **B4$_{sol}$** stored in the mother liquor
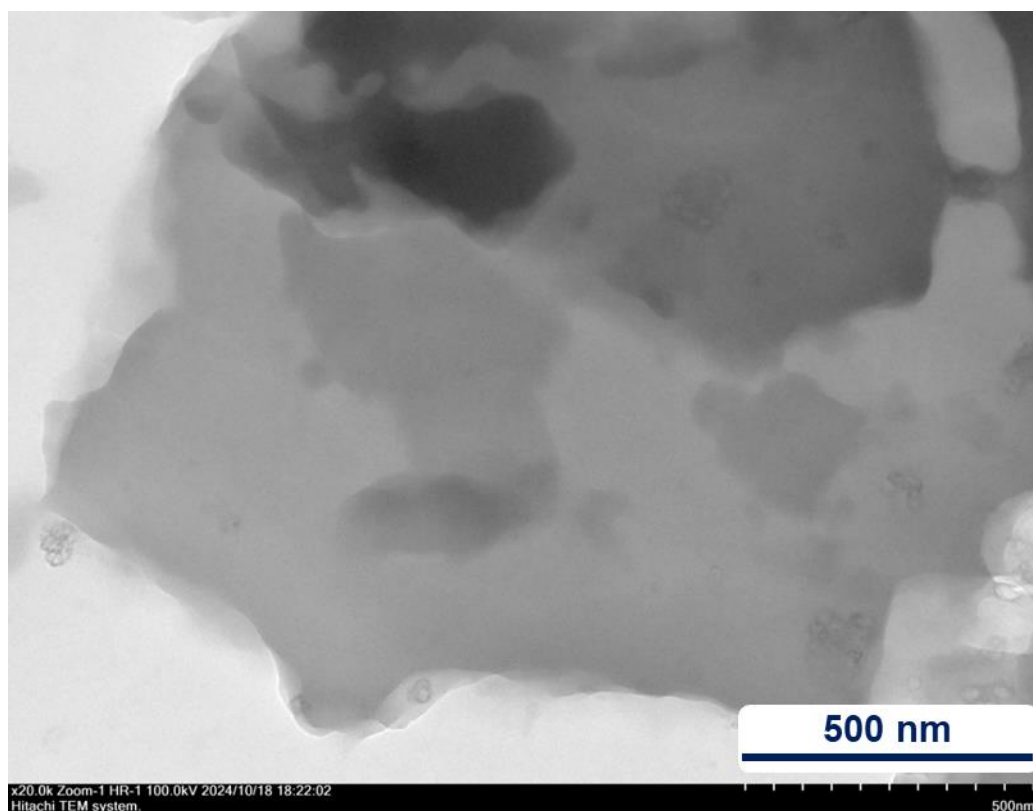
Figure S14.3. Full size TEM image of the crystalline sample **B4'sol** stored in the mother liquor
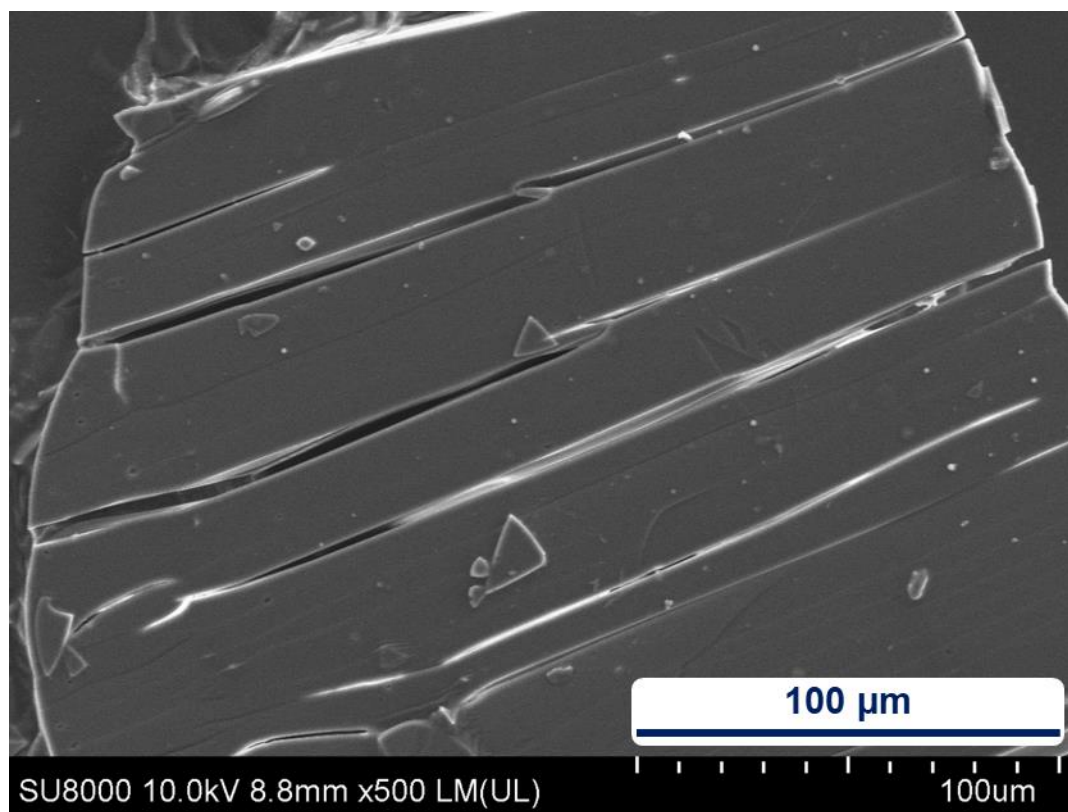
**Figure S14.4.** Full size SEM image of the crystalline sample **B** stored in the mother liquor
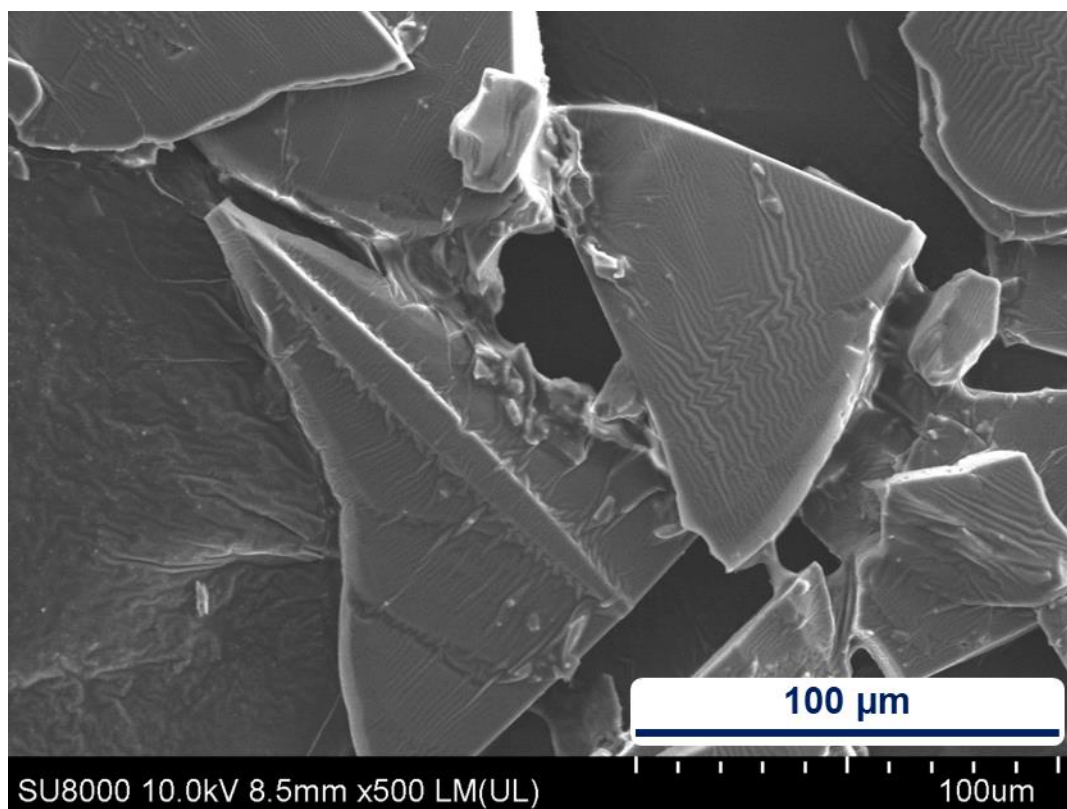
Figure S14.5. Full size SEM image of the crystalline sample **B4$_{sol}$** stored in the mother liquor
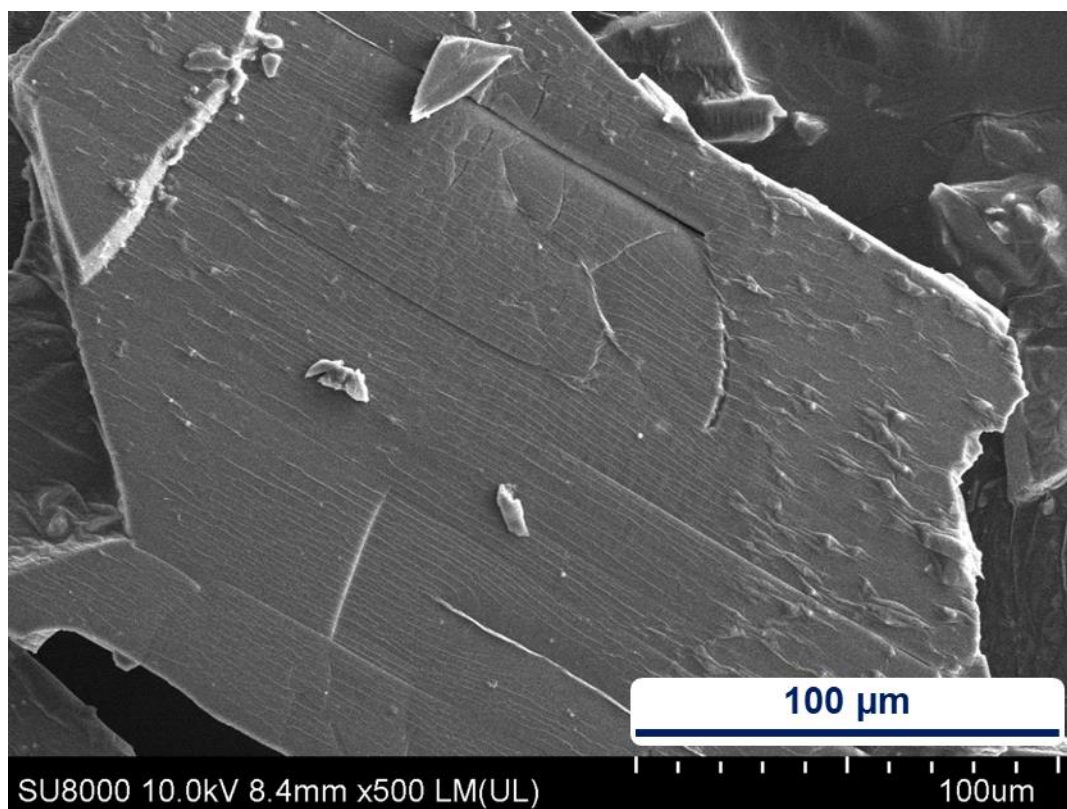
Figure S14.6. Full size SEM image of the crystalline sample **B4'$_{sol}$** stored in the mother liquor
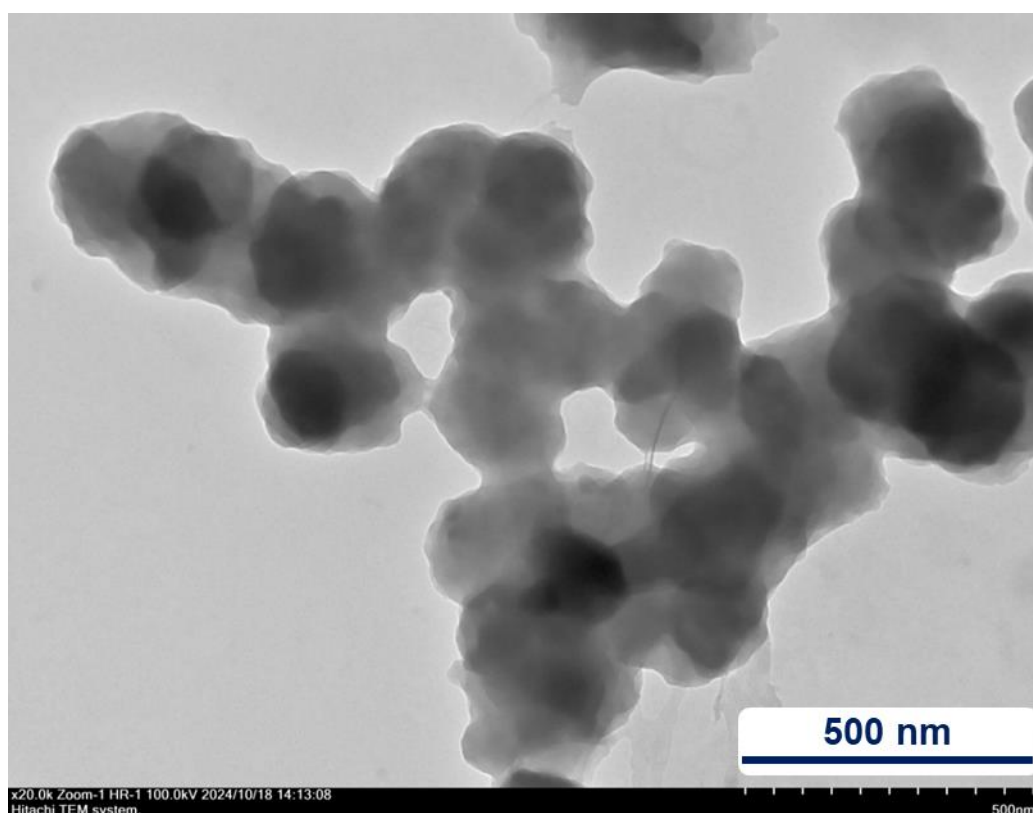
Figure S14.7. Full size TEM image of the solid sample **B4** obtained after solvent replacement and supercritical drying
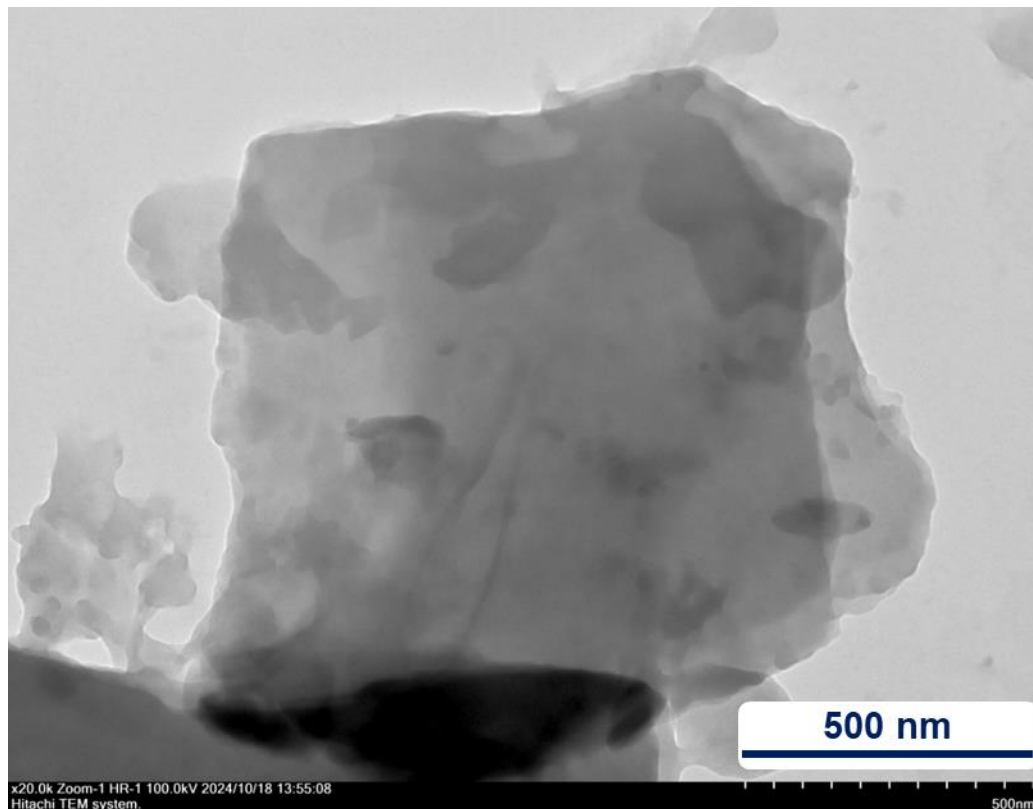
Figure S14.8. Full size TEM image of the solid sample **B4'**obtained after solvent replacement and supercritical drying
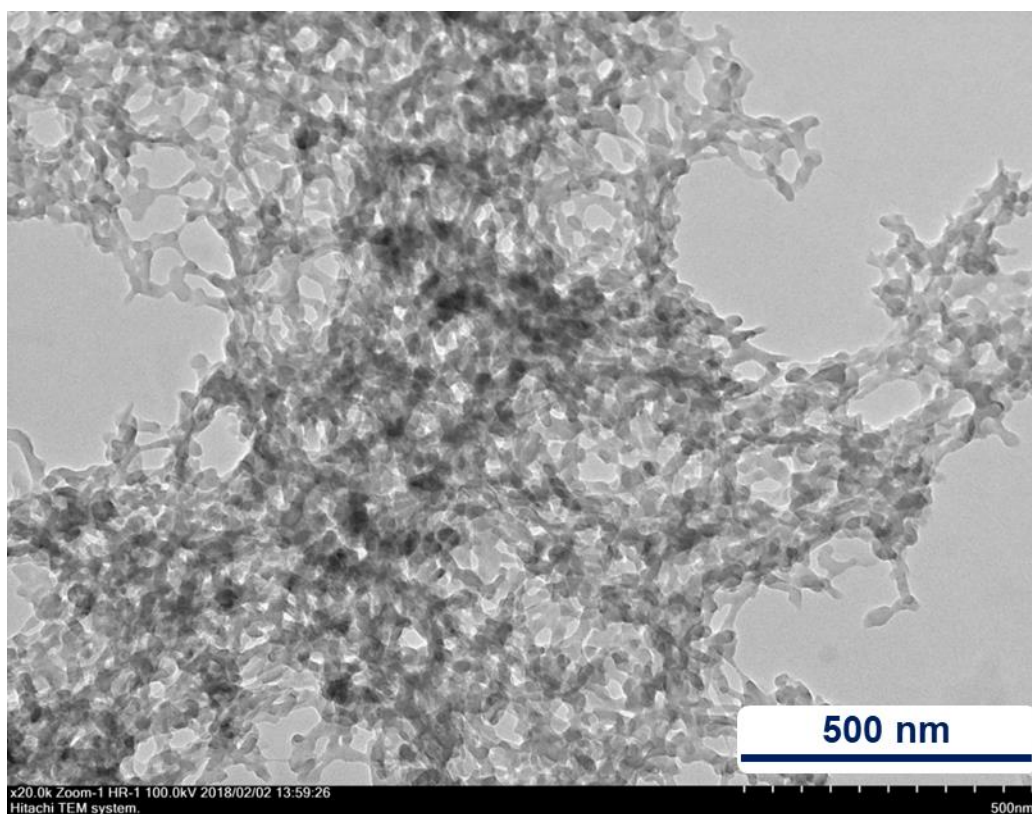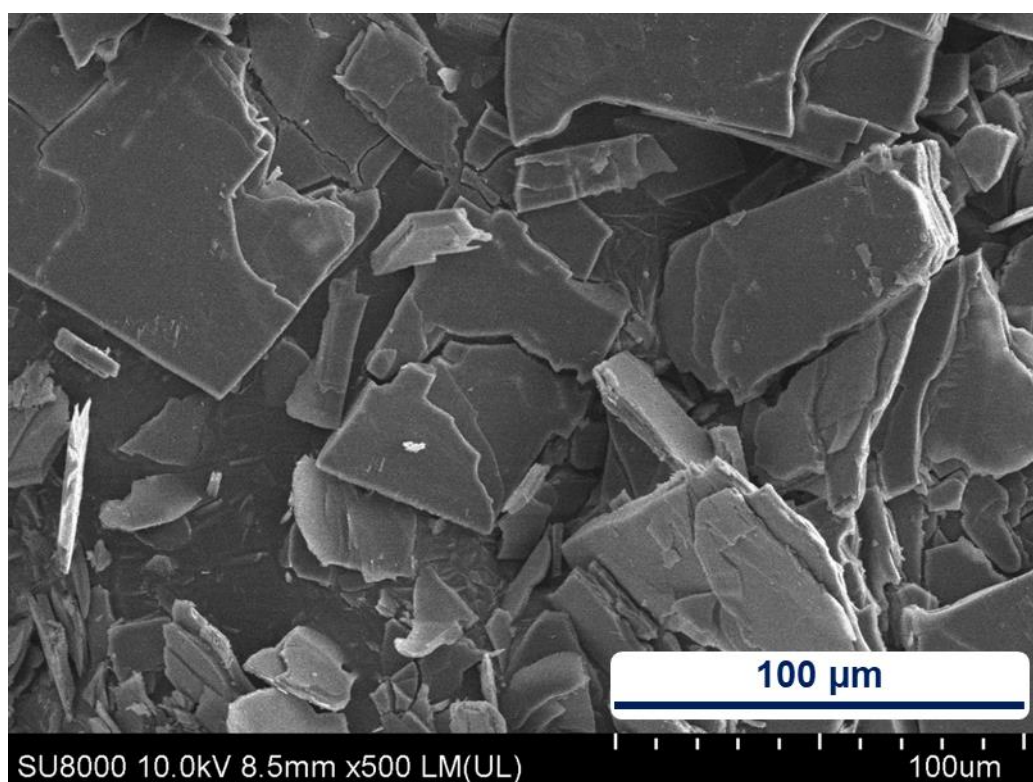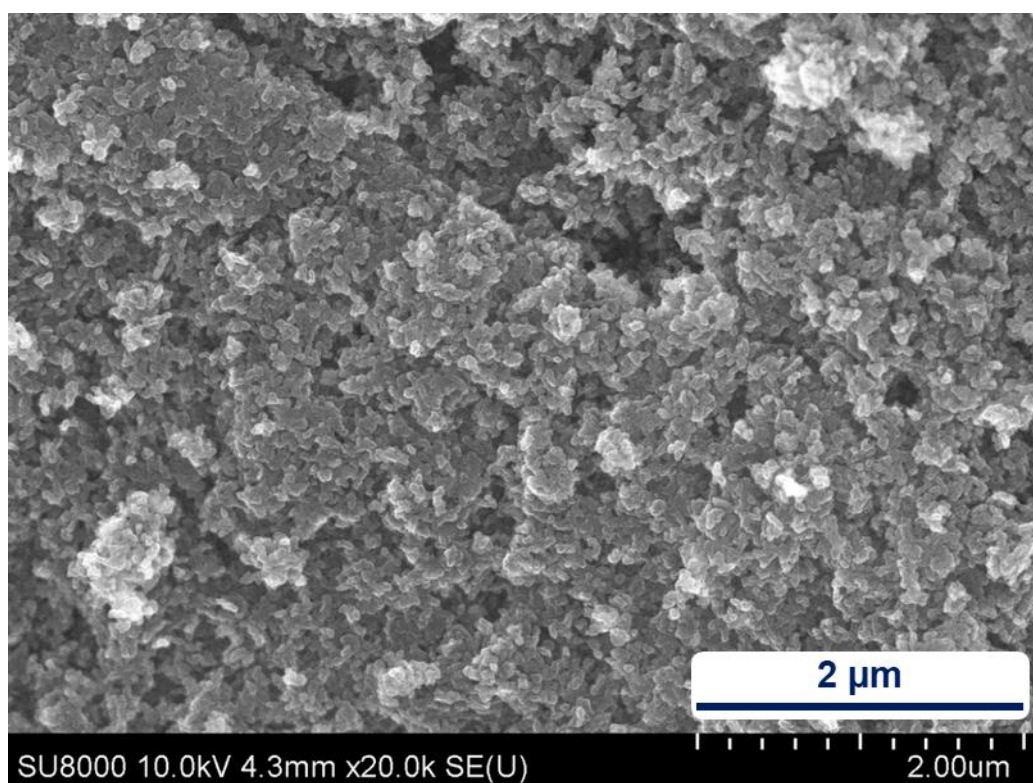
Figure S14.9. Full size TEM image of the solid aerogel sample **B5**
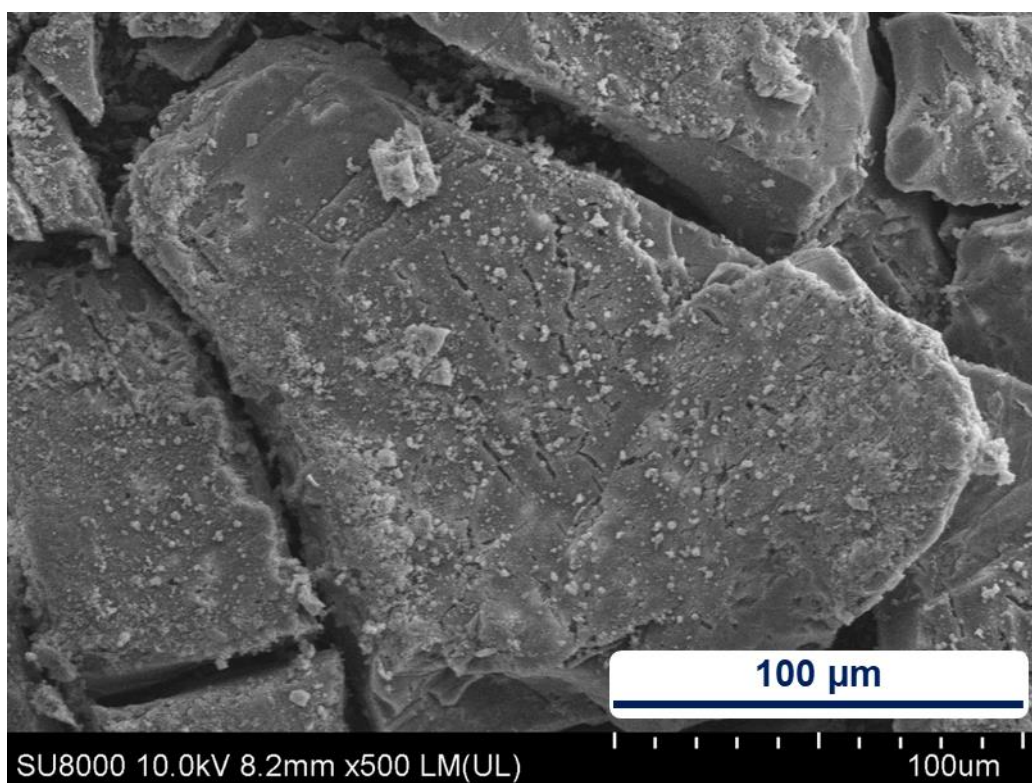
Figure S14.10. Full size overview SEM image of the solid sample **B4** obtained after solvent replacement and supercritical drying
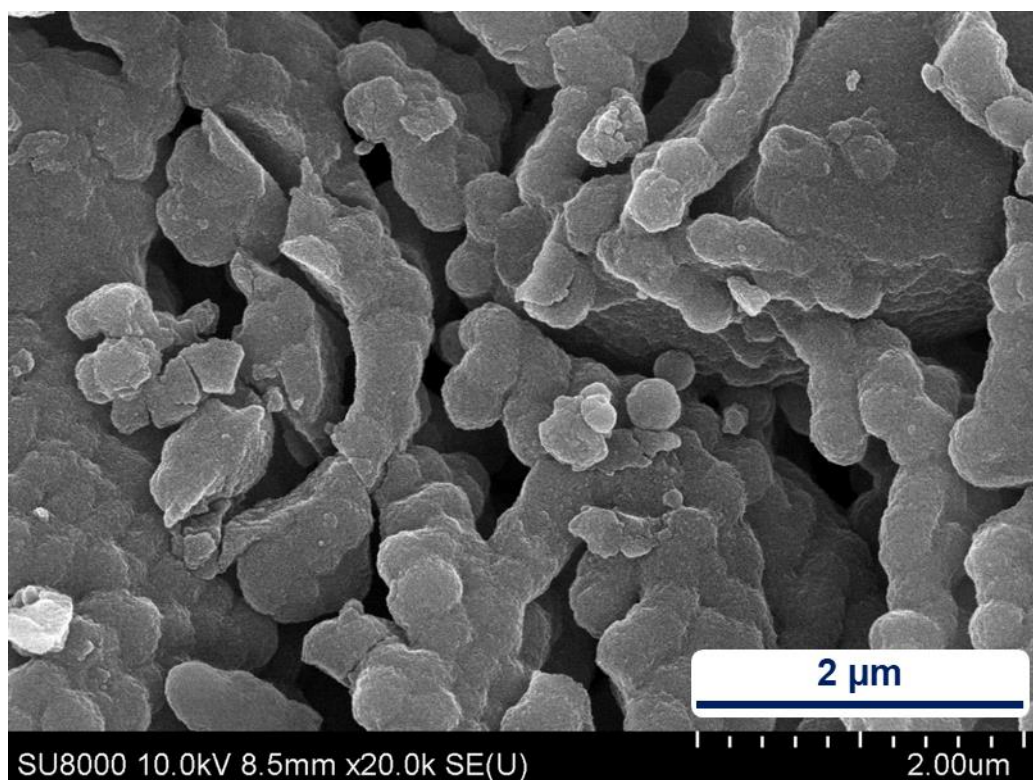
Figure S14.11. Full size overview SEM image of the solid sample **B4'**obtained after solvent replacement and supercritical drying
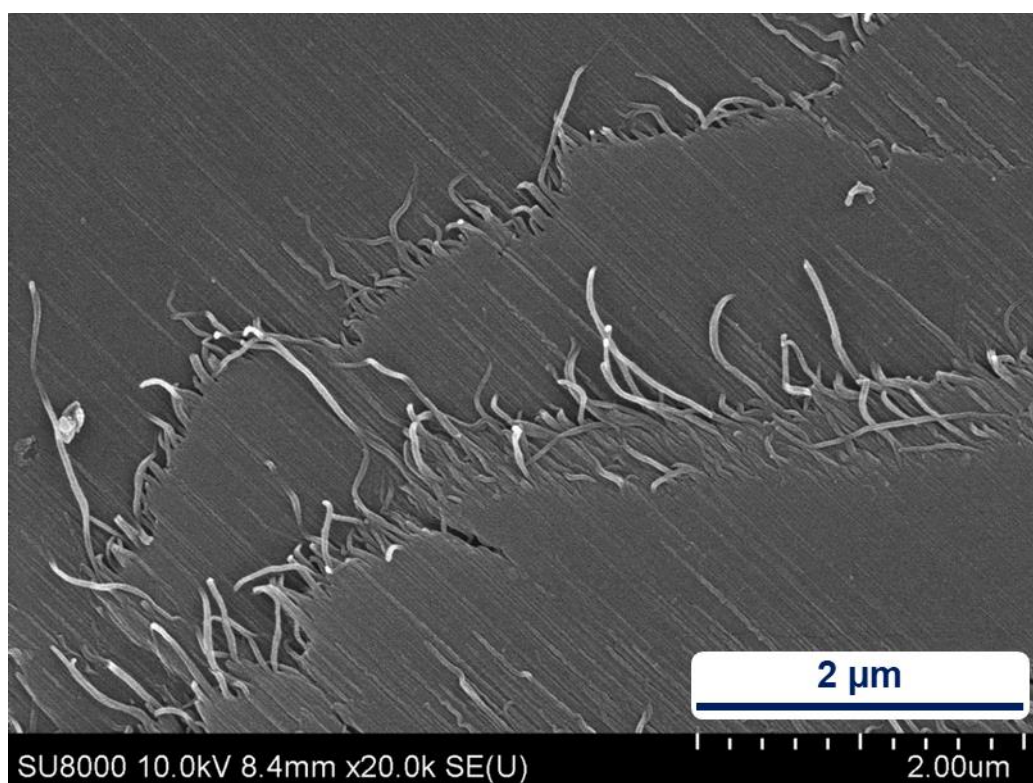

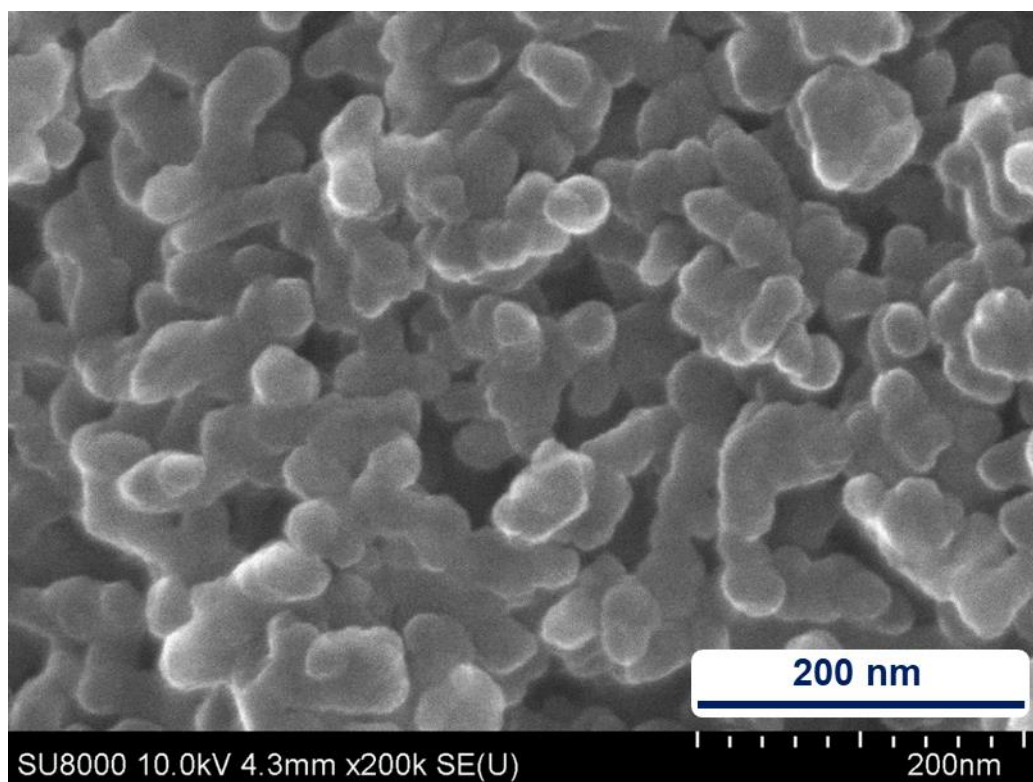**Figure S14.12.** Full size overview SEM image of the solid aerogel sample **B5**

Figure S14.13. Full size detailed SEM image of the solid sample **B4** obtained after solvent replacement and supercritical drying

Figure S14.14. Full size detailed SEM image of the solid sample **B4'**obtained after solvent replacement and supercritical drying
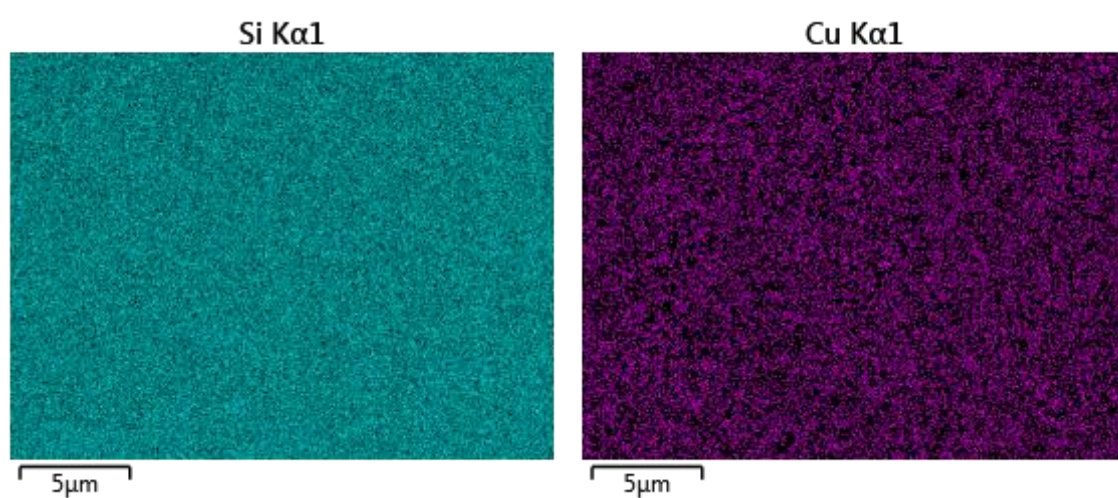
Figure S14.15. Full size detailed SEM image of the solid aerogel sample **B5**
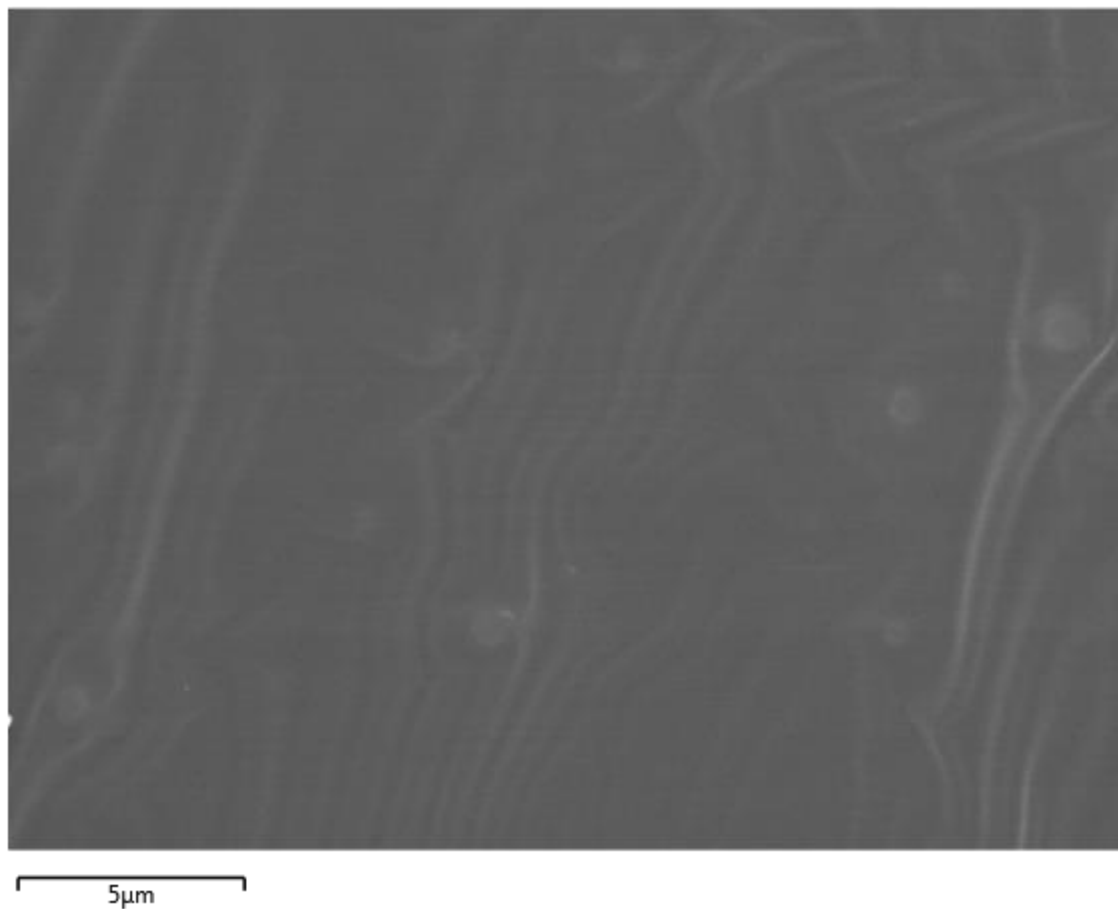
Electron Image 1

5μm

Figure S14.16. SEM image of the area of sample **B** selected for SEM-EDX elemental mapping
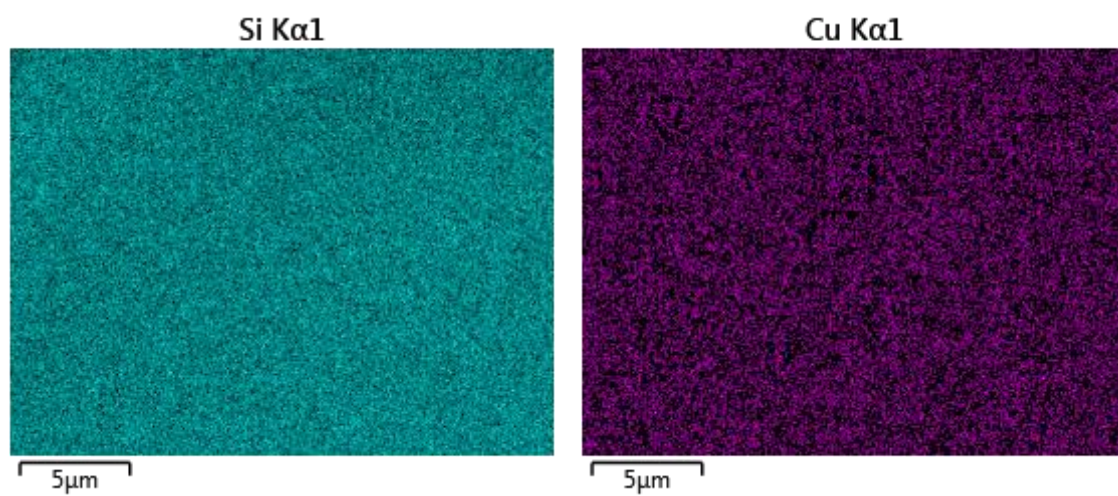
Si Kα1   Cu Kα1

5μm   5μm

Figure S14.17. Silicon (left) and copper (right) distribution maps within the selected area of sample **B** recorded using the SEM-EDX method
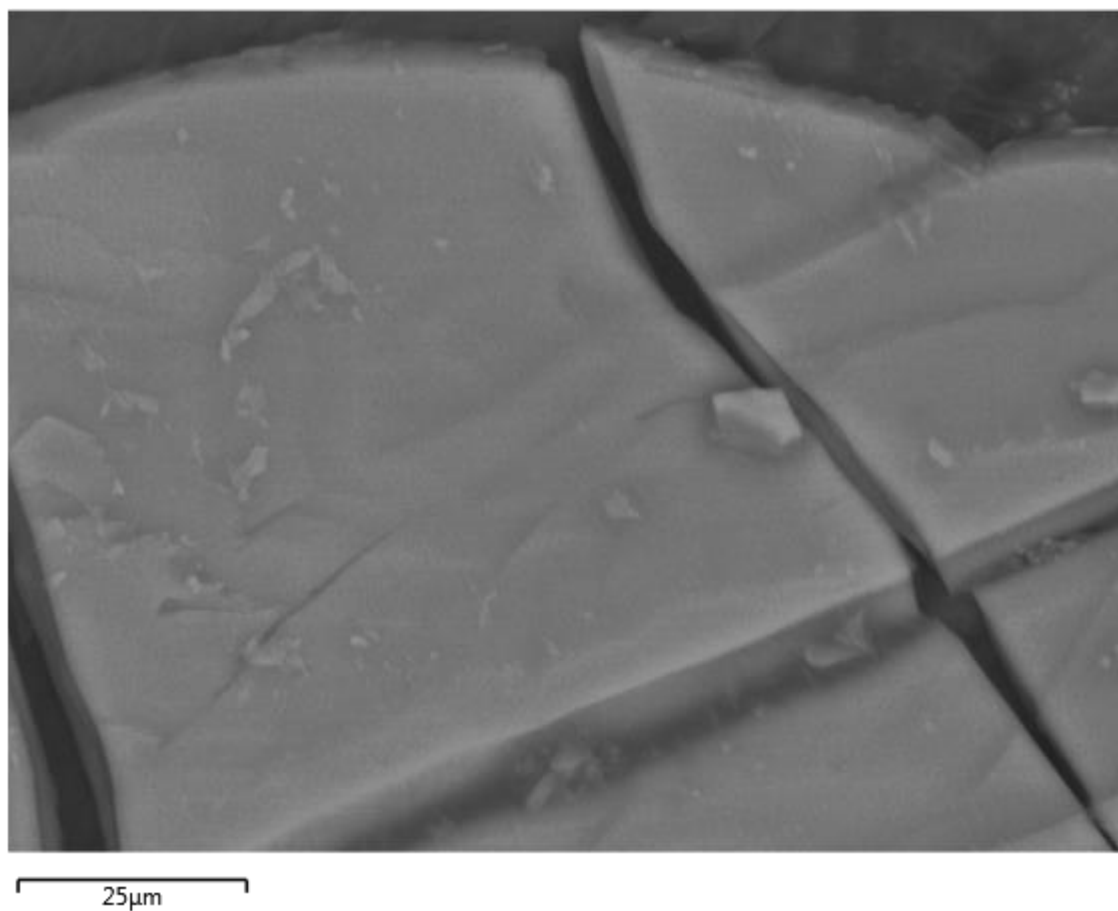
Electron Image 1

5μm

Figure S14.18. SEM image of the area of sample **B4$_{sol}$** selected for SEM-EDX elemental mapping
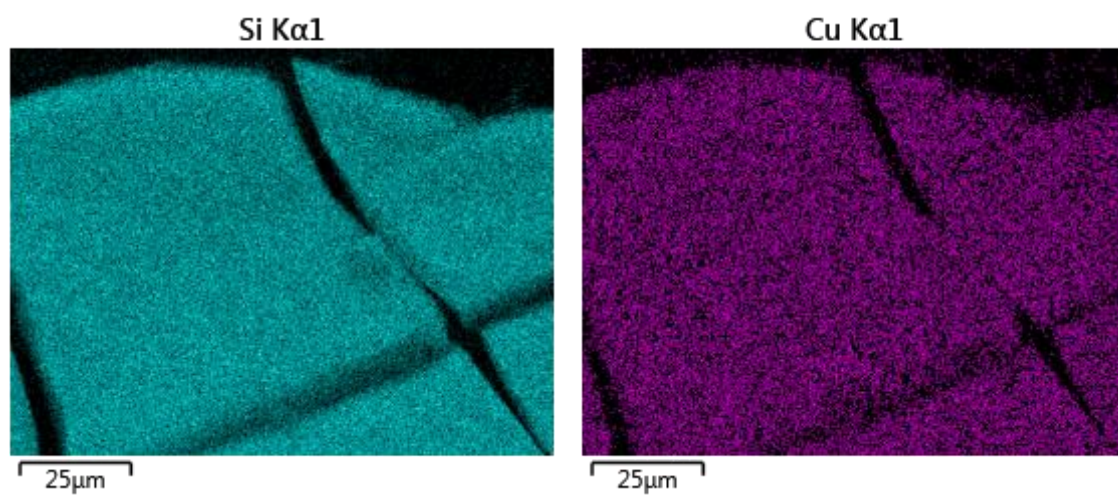
Si Kα1

Cu Kα1

5μm

5μm

Figure S14.19. Silicon (left) and copper (right) distribution maps within the selected area of sample **B4$_{sol}$** recorded using the SEM-EDX method

Electron Image 1

25μm

Figure S14.20. SEM image of the area of sample **B4'ₛₒₗ** selected for SEM-EDX elemental mapping

Si Kα1

Cu Kα1

25μm

25μm

Figure S14.21. Silicon (left) and copper (right) distribution maps within the selected area of sample **B4'ₛₒₗ** recorded using the SEM-EDX method
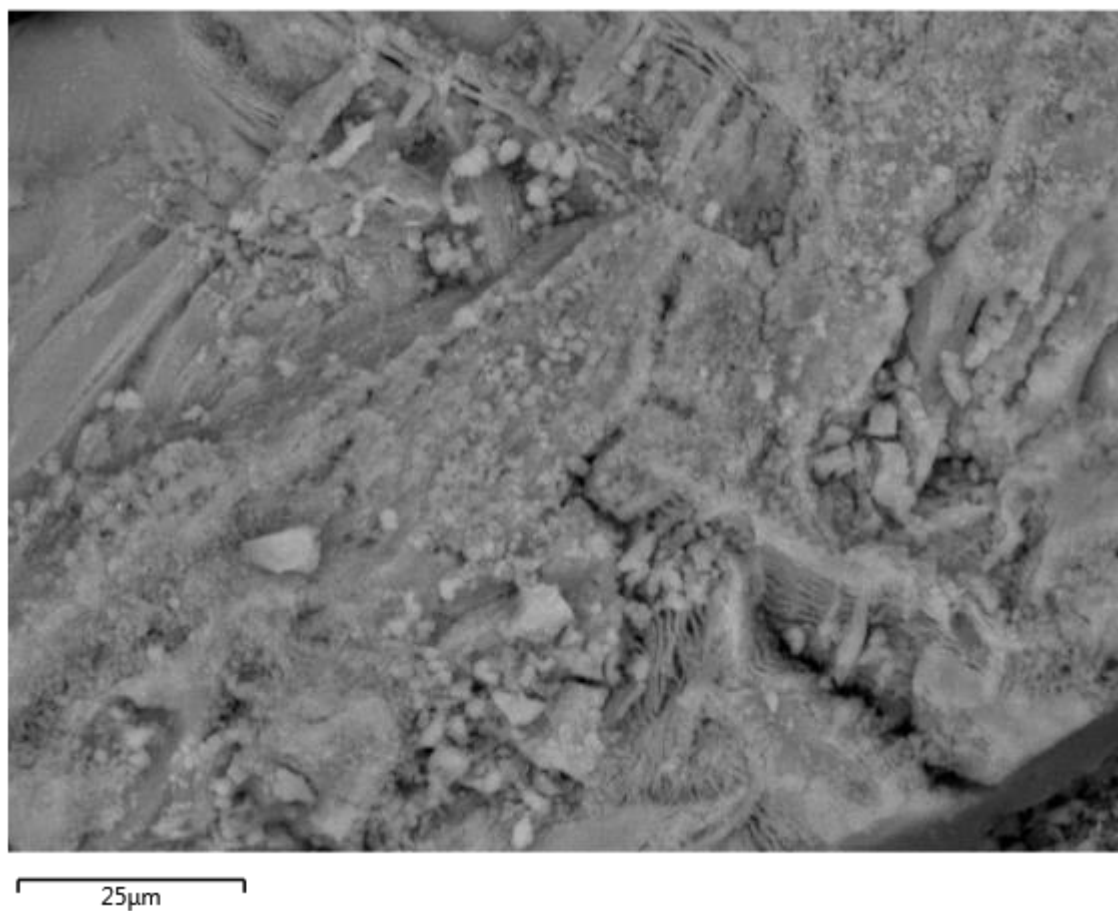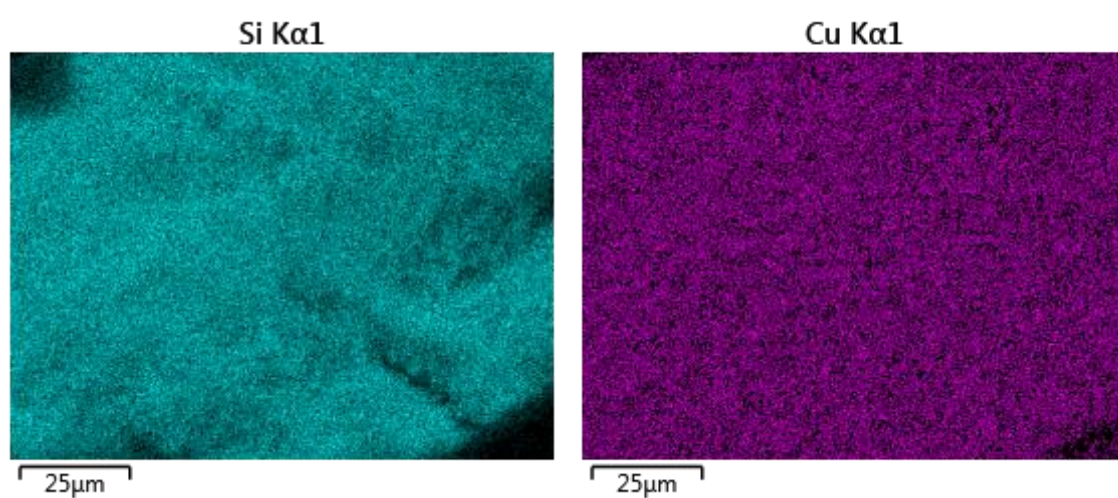
Electron Image 3

25µm

Figure S14.22. SEM image of the area of sample **B4** selected for SEM-EDX elemental mapping

Si Kα1

Cu Kα1

25µm
25µm

Figure S14.23. Silicon (left) and copper (right) distribution maps within the selected area of sample **B4** recorded using the SEM-EDX method

Electron Image 5

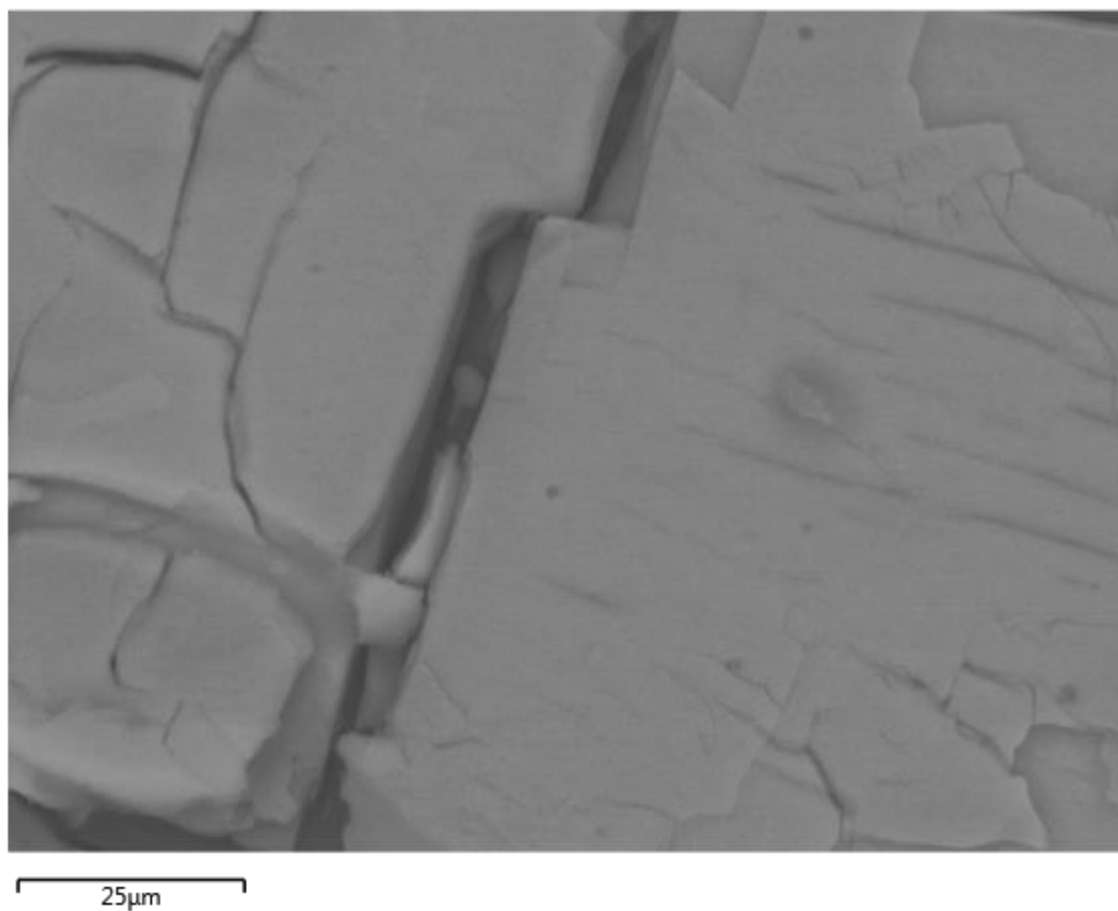25μm

Figure S14.24. SEM image of the area of sample **B4'** selected for SEM-EDX elemental mapping
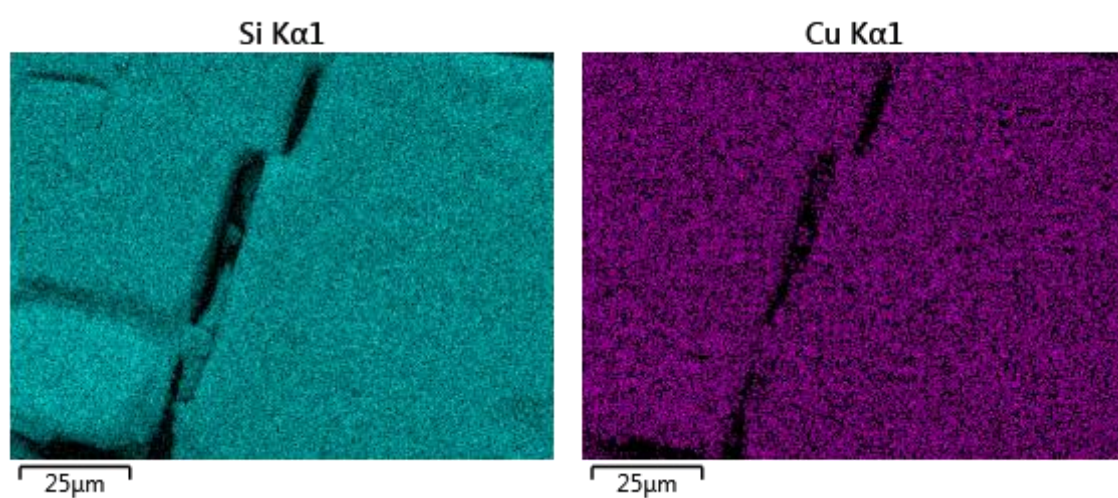
Si Kα1

Cu Kα1

25μm

25μm

Figure S14.25. Silicon (left) and copper (right) distribution maps within the selected area of sample **B4'** recorded using the SEM-EDX method
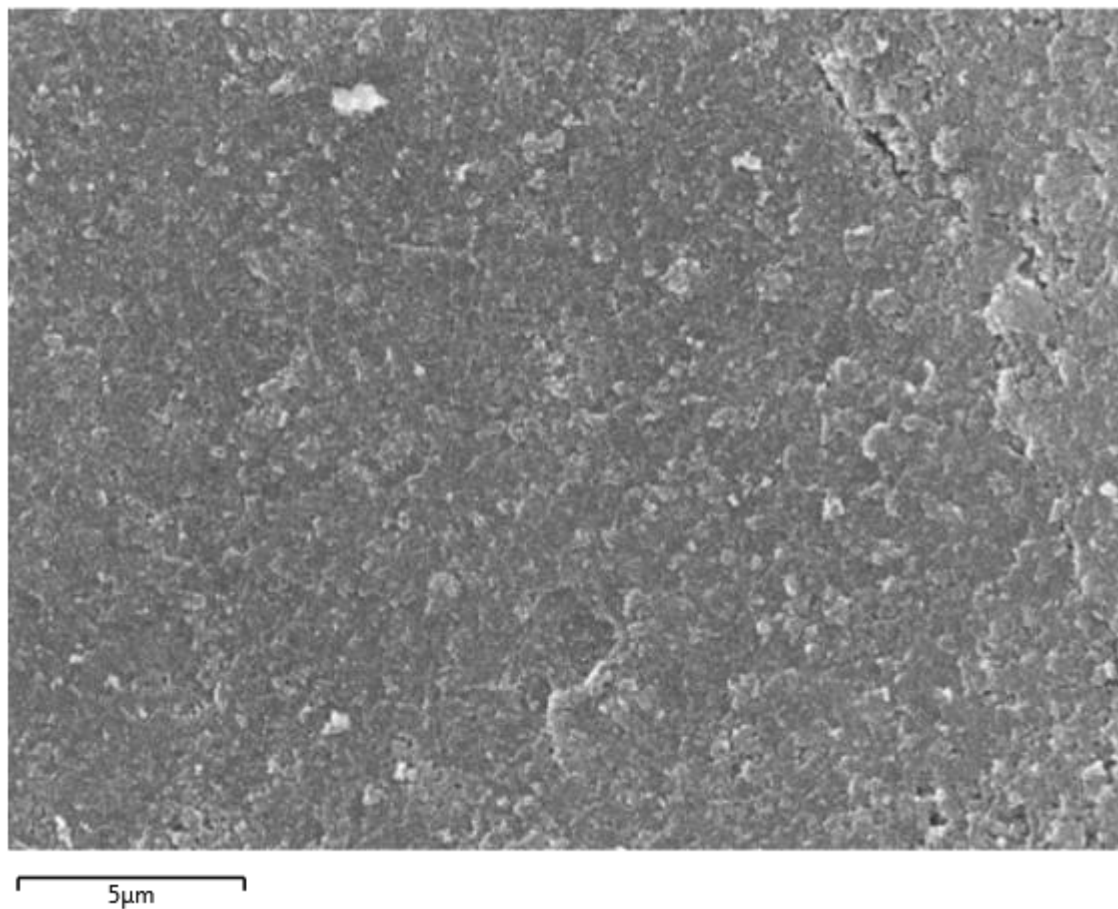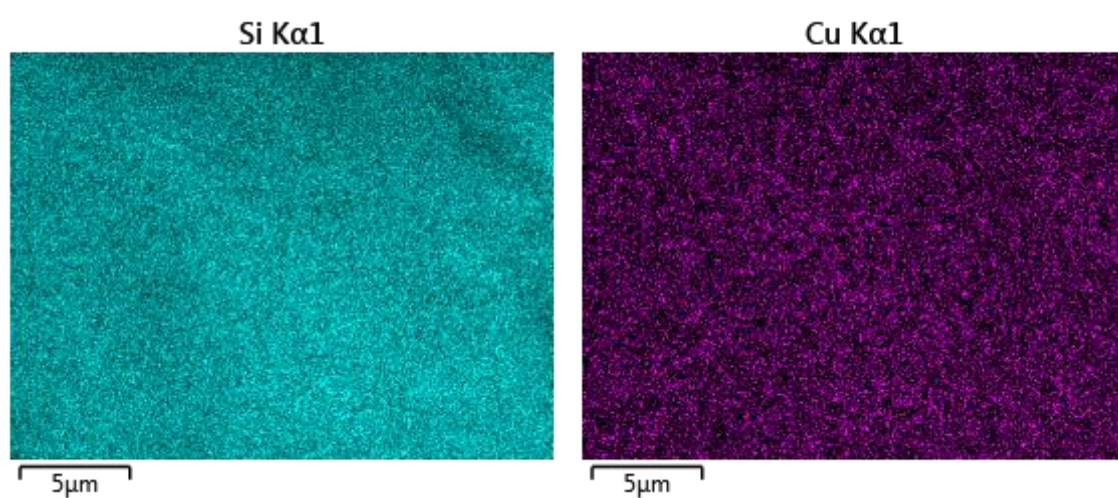
Electron Image 1

Figure S14.26. SEM image of the area of sample **B5** selected for SEM-EDX elemental mapping

Figure S14.27. Silicon (left) and copper (right) distribution maps within the selected area of sample **B5** recorded using the SEM-EDX method

S15. Gas adsorption on B5

Porous structure (Textural properties)

Measured isotherms of nitrogen adsorption at 77 K are represented in **Figure S15.1**. Compounds under investigation are possessing type II isotherm. The inflection point lies at low relative pressure, which is corresponded to presence of micropores. Calculated parameters of porous structure are given in **Table S15.1**.
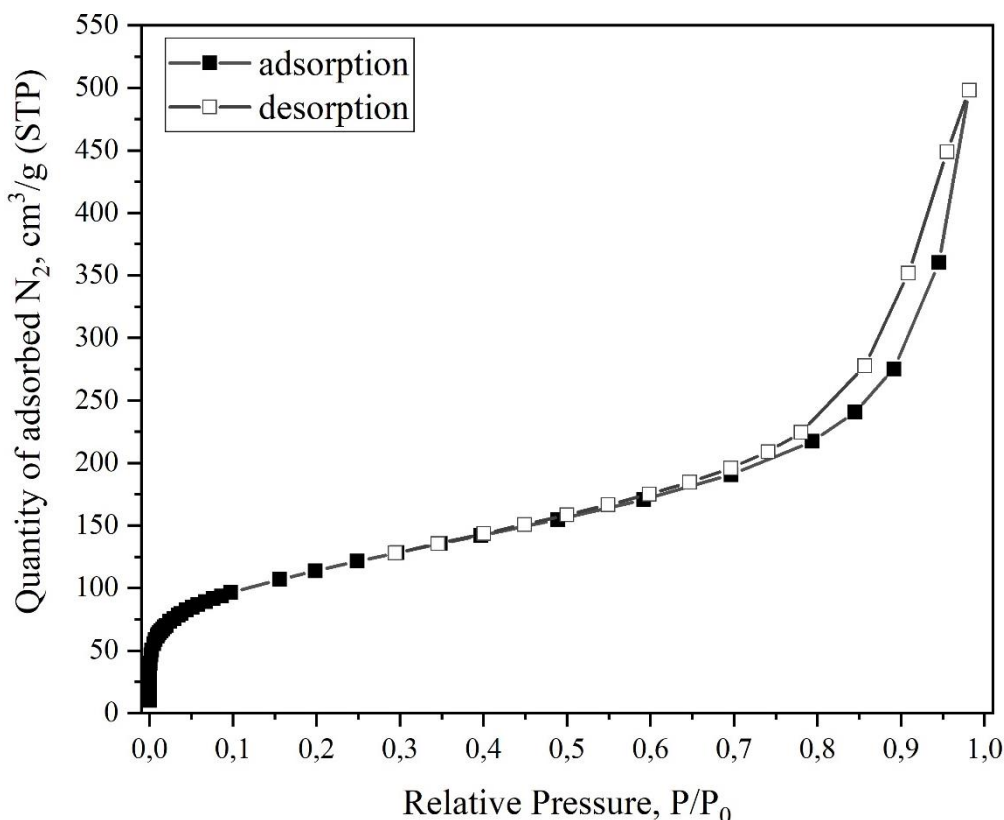
**Figure S15.1. Nitrogen adsorption-desorption isotherm of B5 sample at 77 K**

Table S15.1. The parameters of porous structure of samples under investigation.

Sample	Specific surface area, m^2/g		V $_{pore}$, cm^3/g		V $_{ads}$(N$_2$)^b, cm^3(STP)/g
	BET	BJH $_{ads}$	Total^a	BJH $_{ads}$	
B5	341.5	400.6	0.771	0.782	360.1

^{a} measured at 0.99 P/P$_0$

^{b} measured at 0.95 P/P$_0$

Pore size distribution plot (**Figure S15.2, a**) shows the predominance of mesopores, as well as the presence of macropores. Estimation of the micropores range by the Dubinin-Astakhov and Horvath–Kawazoe methods (**Figure S15.2**, **b and c**) demonstrates the presence of micropores with an average size of 1.1 nm, which was confirmed by the inflection point in the low P/P$_0$ region (**Figure S15.1**).
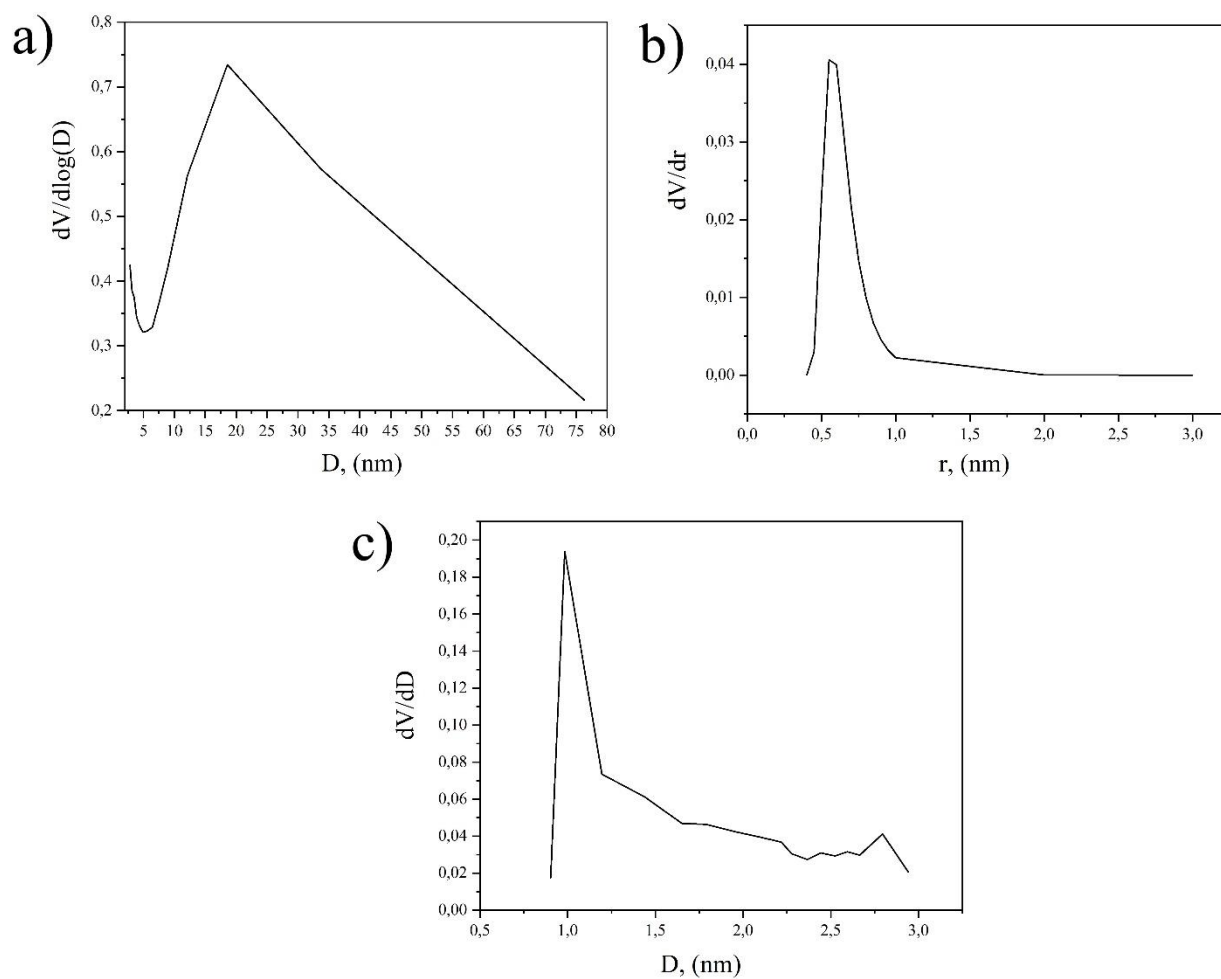
Figure S15.2. Calculated pore size distributions for B5: a) in meso- and macroporous range according to BJH$_{des}$ calculations; b) in microporous range by Dubinin–Astakhov (DA) method; c) in microporous range by Horvath–Kawazoe (HK) method